Institut für Photogrammetrie und Kartographie

The Application of Advanced Interferometric Radar Analysis for Monitoring Ground Subsidence: A Case Study in Bangkok

Jirathana Worawattanamateekul

Vollständiger Abdruck
der von der Fakultät für Bauingenieur- und Vermessungswesen
der Technischen Universität München
zur Erlangung des akademischen Grades eines
Doktors der Naturwissenschaften (Dr.rer.nat.)
genehmigten Dissertation.

Vorsitzender:

Univ.-Prof. Dr.rer.nat. K. Thuro

Prüfer der Dissertation:

1. Univ.-Prof. Dr.-Ing.habil. R. H. G. Bamler
2. Prof. Dr.rer.nat. Dr.rer.nat.habil. W. Altermann,
   Ludwig-Maximilians-Universität München

Die Dissertation wurde am 13.2.2006 bei der Technischen Universität München eingereicht und durch die Fakultät für Bauingenieur- und Vermessungswesen am 10.3.2006 angenommen.

Gedruckt mit Unterstützung des Deutschen Akademischen Austauschdienstes

Zusammenfassung

Die vorliegende Arbeit untersucht die Anwendbarkeit der 'Persistent Scatterer' Interferometrie (PSI) zur Vermessung der Landsenkung in Großraum Bangkok (Thailand). Es ist gezeigt worden, dass PSI die Möglichkeiten der konventionellen differenziellen Interferometrie zur Ableitung hoch präziser Bewegungsmessungen erweitert und viele der typischen Einschränkungen umgeht. Aber sie erfordert typischerweise eine große Zahl von SAR (Synthetisches Apertur Radar) Akquisitionen.

Landsenkungsmessungen mit konventionellen Methoden sind zwar hoch genau, aber durch große Messpunktabstände und seltene Messungen limitiert. Engere und häufigere Senkungsmessungen sind wesentlich um die Charakterisierung und das Verständnis der Landsenkung zu verbessern, die durch die Volumenabnahme in Bangkoks Grundwassersystem verursacht wird. Im Prinzip können mit satelliten-gestützter PSI Senkungskartierungen mit hoher Messpunktdichte und häufigen (z.B. 35 Tage für die ERS-1/2 Satelliten) Messungen auf Flächen bis etwa 10000 Quadratkilometer durchgeführt werden.

Für diese Untersuchung wurde die PSI mit ERS-1/2 C-Band Daten unter schwierigen Bedingungen angewandt um Oberflächensenkungen zu messen. Diese schwierigen Bedingungen waren insbesondere die starken atmosphärischen Einflüsse auf das Signal, die hohen und zeitlich veränderlichen Senkungsraten sowie die Tatsache, dass nur 20 SAR Akquisitionen für den Zeitraum von 1996 bis 2000 verfügbar waren vergleichsweise wenige für eine PSI Auswertung. Meine Ergebnisse zeigen dennoch, dass es möglich ist, mit der PSI Methode Senkungsraten mit einer Genauigkeit von mm/a zu bestimmen.

Mit einer Punktdichte von 28 PS/km^2 stellt diese PSI-Messung die detaillierteste Information über das Absenkungsfeld in Bangkok dar, die derzeit verfügbar ist. Die verbesserte Charakterisierung zeigt deutlich, dass die Senkungsraten im Untersuchungsgebiet und -zeitraum von Westen nach Osten hin zugenommen haben. Maximale Senkungsgeschwindigkeiten von 42 mm/a werden im Nordosten der Kreuzung zwischen Srinakarin road und Teparak road gemessen. Ausserdem wurde eine statistische Beschreibung der Qualität der gemessenen Senkungsraten abgeleitet.

Ein Vergleich mit unabhängigen Nivellierungsmessungen bestätigt, dass die erreichte Genauigkeit, trotz der nicht idealen Bedingungen für die Untersuchung, an Orten die näherungsweise konstante Senkungsraten aufweisen besser als 1.5 mm/a ist. Die Unterschiede zwischen den aus der PSI-Analyse und den Nivellierungsdaten abgeleiteten Senkungsraten nehmen zu, wo sich die Senkungsraten zeitlich ändern. In Gebieten mit zeitlich linearem Senkungsverhalten stimmen die Senkungsraten für 6 von 10 Monumente innerhalb von $\pm\, 1.5\, mm/a$ überein.

Die PSI Senkungsraten werden zusammen mit in Brunnen gemessenen änderungen von Grundwasser-Pegeln genutzt, um einen Gesamt-Speicherkoeffizienten für das Bangkok Grundwassersystem an mehreren Stellen zu bestimmen. Diese Untersuchung stellt die erste Anwendung von PSI zur Ableitung von Speicherkoeffizienten dar. Sie ist damit ebenfalls die erste Beschreibung der elastischen Kompressibilität von Bangkoks Grundwassersystem mit diesen Mitteln. Die gemessenen Speicherkoeffizienten stimmen mit Messungen auf der Basis der Nivellierungsdaten und derselben Grundwasserpegel überein. Der maximale Unterschied der zwei Messungen ist etwa 3mm pro Meter Pegeländerung. Dies zeigt, dass PSI-Senkungsmessungen für Messungen der Speicherkoeffizienten in Aquifersystemen genutzt werden können, für die keine Nivellierungsdaten verfügbar sind.

Für den Zeitraum von 1992 bis 1995 waren keine SAR Daten verfügbar. Das Senkungs-Pegelängerungs-Verhältnis ($\triangle b/\, \triangle\, h$) wurde aus Nivellierungsdaten und Pegeldaten dreier Mess-Brunnen für diesen Zeitraum berechnet um Informationen über die inelastische Kompressibilität zu erhalten. Die für die drei Brunnen bestimmten Verhältnisse sind 0.01, 0.02 und 0.04 und nehmen von Westen nach Osten zu. Dies bestätigt, dass die Gebiete im Osten des Untersuchungsgebietes für Senkungen anfälliger sind als die im Gebiete im Westen.

Zusätzlich zu diesen Analysen habe ich eine Senkungs-Risikokarte und eine Vorhersage des künftigen Senkungsfeldes aus den historischen Senkungsraten abgeleitet. Hiermit sollen weitere mögliche Verwendungen der mit PSI gemessenen Senkungsraten im Kontext der Schadensbegrenzung demonstriert werden. Für die Senkungs-Risikokarte wurden die Senkungsraten klassifiziert um die Stärke der Senkung zu kategorisieren. Eine solche Abstraktion kann für die strategische Planung administrativer Körperschaften im Zusammenhang mit der Senkungsproblematik nützlich sein. Eine einfache empirische Vorhersage der Senkungen im Jahr 2025 und 2050 wurde mit Hilfe eines exponentiellen Modells zur Extrapolation der PSI-Messwerte erstellt. Die Ergebnisse erwarten eine maximale Senkung von 0,73 m bis 2025 und 1,14 m bis 2050 in diesem Gebiet.

Diese Arbeit stellt den ersten erfolgreichen Versuch dar, Senkungserscheinungen im Stadtgebiet einer asiatischen 'Mega-City' mit PSI zu quantifizieren. Hiermit kann bestätigt werden, dass die PSI Technik auch unter schwierigen Bedingungen präzise Ergebnisse erreichen kann. Obwohl das Untersuchungsgebiet in dieser Studie auf etwa 100 km^2 begrenzt war, ist die beschriebene Methode auch für größere Gebiete und unter vergleichbar schwierigen Bedingungen einsetzbar.

Abstract

This thesis examines the applicability of Persistent Scatterer Interferometry (PSI) for determining subsidence in the Bangkok Metropolitan Area (Thailand). Although PSI has been shown to extend the capability of conventional differential interferometry (DInSAR) for deriving highly precise displacement measurements and avoiding many of the typical constraints, it typically requires a large number of acquisitions.

Subsidence measurements by conventional means are very accurate, but limited by their spatially sparse and infrequent sampling. Denser and more frequent subsidence observations are crucial for an improved characterisation and understanding of the ground subsidence attributable to the compaction of the Bangkok aquifer system. In principle, satellite-based PSI is capable of providing dense and frequent (e.g. 35 days for the ERS-1/2 satellites) subsidence observations covering areas of approximately ten thousand square kilometres per observation.

In this investigation I apply PSI using ERS-1/2 C-band data to quantify surface subsidence under difficult conditions, namely a strong atmospheric signal contribution, high and temporally varying subsidence rates and the fact that only 20 radar acquisitions were available covering the time period between 1996 and 2000 relatively few for a PSI analysis. Nevertheless, my results demonstrate the feasibility of deriving subsidence rates at a precision of mm/yr using the PSI technique.

With a density of 28 PS/km^2 the PSI estimate represents the most detailed subsidence information currently available for Bangkok. The improved characterisation of the spatially variable subsidence field clearly demonstrates that the subsidence rates in the study area increased from the west to the east during the period studied. Peak subsidence rates of up to 42 mm/y are observed at the northeast of the intersection between Srinakarin and Teparak roads. I also obtained statistics describing the quality of the PS subsidence rate estimates.

A validation conducted against independent leveling data for the same period confirms that the precision achieved is better than 1.5 mm/yr for locations that exhibit approximately constant subsidence rates, even under the less than ideal conditions that

prevailed here.

The differences between subsidence rates estimated from PSI and the reference leveling data increase where the subsidence rates varied over time. For areas showing temporally linear subsidence the subsidence rates agreed within $\pm$ 1.5 mm/yr for 6 out of 10 benchmarks.

I used the PSI subsidence rate estimates together with aquifer head changes in individual wells to estimate overall storage coefficients for the Bangkok aquifer system at several locations for the period between 1996 and 2000. This study represents the first application of PSI to derive storage coefficient estimates. As the hydraulic heads increased between the stated time periods, the derived storage coefficient estimates indicate the elastic compressibility of the Bangkok aquifer system. The estimated storage coefficients agree with measurements obtained from using the reference leveling data together with the same aquifer head changes. The maximum discrepancy between the two measurements is of the order of +3 mm per 1 metre of hydraulic head change. This implies that the subsidence rates derived from PSI may be used for estimating the storage coefficient of aquifer systems for which leveling data is unavailable.

Synthetic Aperture Radar (SAR) data were unavailable between 1992 and 1995. Subsidence to head decline ($\triangle b/ \triangle h$) ratios of three groundwater monitoring wells for this period were estimated from hydraulic head changes in conjunction with geodetic leveling. The hydraulic heads decreased between the stated periods, thus the derived subsidence to head decline ratios provide information on the inelastic compressibilities. The estimated ratios for the three wells are 0.01, 0.02, and 0.04 increasing from west to east. This confirms that areas in the east of the study site are more susceptible to subsidence than are those located towards the west.

In addition to these analyses, a subsidence risk map and predicted subsidence fields are derived from the historic subsidence rates to demonstrate further applications of PSI subsidence rate estimates in the context of damage mitigating. For the subsidence risk map the subsidence rates are classified to provide information on the severity of subsidence. Such an abstraction may be useful for strategic planning of administrative bodies. A simple empirical prediction of subsidence by the year 2025 and 2050 was carried out by extrapolating the PSI measurements assuming an exponential model. The results anticipate a maximum subsidence of 0.73 m and 1.14 m by the year 2025 and 2050 in this area.

This study represents the first successful attempt to quantify urban subsidence in one of Asia's mega cities using PSI, validating it as a technique for achieving high precision even under a set of difficult conditions. While the study itself was limited in extent

to about 100 km^2, the method described here is applicable to other and larger areas under similarly difficult conditions.

Acknowledgements

During the 4-years time of completion this dissertation, many people have contributed to this work in their unique ways. Initiation of this work could not be realized without the support from Prof. Dr. Wladyslaw Altermann, Dr. Harald Mehl, Mr. Robert Schumann, Dr. Kiyoshi Honda and Dr. Phisan Santithamnont.

I profoundly thank to my Doktorvater, Prof. Dr. Wladyslaw Altermann for his constant guidance and support. His suggestions do not only concern on academic issues but also on 'How to live a research's life in Germany ?'. I gratefully thank to Prof. Dr. Richard Bamler for his kind support and many valuable comments. Although he is very busy, I highly appreciated his 'always accessible' character. I am indebted to Dr. Jörn Hoffmann, my advisor at DLR-DFD, for his valuable comments, 'hundreds' of guidances and discussions. Many times, your ideas turned me to see things in a completely new and more concrete way. Jörn, thank you very much.

This work was financially supported by the German Academic Exchange Program (DAAD) for 3.5 years. I gratefully thank DAAD for giving me this opportunity and privilege. Additional financial support was granted as a student assistantship at the section Geology, Department for Earth and Environmental Science, Ludwigs-Maximilians University of Munich (LMU). A field investigation in Bangkok and vicinity conducted in 2002 was kindly supported by DFD-UG.

During my research time, I sincerely thank to Dr. Stefan Dech, Dr. Harald Mehl at the German Remote Sensing Data Center (DFD), German Aerospace Center (DLR) for their hospitality and for giving me an opportunity to work as a guest scientist in such an outstanding research institute. A special thanks goes to all colleagues in the SAR-TOPO working group supervised by Achim Roth. I thank you all for providing me all kind of support, cooperation and friendship. I always appreciate the support from Detlev Kosmann as he is a very efficient system administrator in DFD. Detlev, you helped me many times to survive from computer troubles !!!

At DLR, It was a privilege to work with Nico Adam and Bert M. Kampes from the Remote Sensing Technology Institute (IMF), who have developed the Persistent Scat-

terer Interferometry (PSI) processing system I used in this study. Bert, Nico, thank you for your many explanations, comments and valuable discussions. Additionally, I thank Nico for his critical comments on my dissertation writing that finally turned into many improvements.

The ERS-1/2 SAR data used for this study had been kindly supported by the European Space Agency (ESA) under the AOE. 762. The support data of groundwater level, well information and subsidence measurements from leveling were obtained from the Department of Mineral Resources (DMR), Thailand. I specially thank Dr. Somkid Buapeng, Mr. Sutthipong, Dr. Oranuj and Mr. Therdsak at DMR. I thank Dr. P. H. Giao for several comments on the subsidence analysis of Bangkok. The vector data of subsidence measurements in 1997 was provided by Dr. Sombat Yoomuang. For other support data, I would like to thank Dr. Surat, Mr. Sawang, Ms. Wandee and Ms. Supawan. I thank Robert Schumann and Robert Klus for the proofreading of this work. Additionally, I would like to thank for the contribution of the authorities of these properties/assets presented in the section 2.5 and fig. B.1 on page 154. I declare that presentation of these photos aims only for educational purpose.

Many friends have shared parts of my memorable time inside and outside the working place. I thank Katja, Zsofia, Somphop and Pae, they have given me the pleasant time to remember; parties, having fun together, and the unforgettable friendship. Also, I thank other Thai friends in Munich, friends at the section Geology, LMU with whom I shared my first and very impressive geological fieldwork in Germany. I sincerely thank Margot and Heinz Pfeil for the countless meals, coffees at their place and their friendship. With Wolfgang and Yaroslav I shared the lunchtime for years at DLR. 'Who knows that the conversation from DFD to the 'Casino' everyday can make friends?' I appreciate Tin Aung Moe, Wandee, Charimarn, Somnik, Thitinan, Sopa and Siriporn for their every communications and support. They are the distant friends but very close in my mind.

I would like to personally thank to the 'Dittrich' family for their cheerful support by all means. I thank Ilona Dittrich for continuous support of her 'selfmade Jam' that has always made my breakfast healthy and special. It plays an important role for a good start of my day. Danke Loni! I gratefully thank Steffen Dittrich for his steady understanding, support in all terms, his love and patience. Thank you for being by my side through the way to the completion of this work.

Finally, I would like to thank my 'Worawattanamateekul' family. I am indebted to my parents for they have given me a great opportunity to be their daughter. I proudly appreciate their love, constant support, teaching and steady understanding. I greatly

thank my four sisters; P' Nacha, Kritsana, Rattana, Pojana, my two brothers; H. Suwit and Dr. Wanchai, my nephew; Tairo and my brother-in-law; Kageyama san for they have always given me unforgettable times we have shared together. I appreciate the long-lasting inspiration provided by my 'beloved' father that accompanies me along my entire way. Without your support, alone I cannot stand at this point. Thank you all!

München, 2005

After all, it is the journey, not the destination that matters most

Acronyms

APS - Atmospheric Phase Screen

DIFGM(s) - Differential Interferogram(s)

DEM - Digital Elevation Model

DMR - Department of Mineral Resources (Thailand)

ERS - European Remote Sensing satellite

ESA - European Space Agency

GPS - Global Positioning System

IFGM(s) - Interferogram(s)

ILS - Integer Least-Squares

InSAR - Interferometric Synthetic Aperture Radar (also radar interferometry)

JICA - Japan International Cooperation Agency

LOS - Line of Sight direction of the satellite (also slant range direction)

MWA - Metropolitan Waterworks Authority (Thailand)

PS - Permanent Scatterer

PSC - Permanent Scatterer Candidate

PSI - Persistent Scatterer Interferometry

PWA - Public Works Department (Thailand)

RCS - Radar Cross Section

RMS - Root Mean Square

SCR - Signal to Clutter Ratio

SNR - Signal to Noise Ratio

SLC - Single Look Complex

SRTM-(X) - Shuttle Radar Topography Mission (X stands for x-band of the microwave wavelength)

Contents

List of Figures

List of Tables

Chapter 1

Introduction

Extensive overdrafting of the aquifers in the Bangkok metropolitan area during the past decades has led to widespread ground subsidence (AIT, 1981, 1982). An attempt to restrict the amount of groundwater extraction in central Bangkok by the Metropolitan Waterworks Authority[1] (MWA) in conjunction with the launch of groundwater control regulation over the last 20 years has succeeded in stabilizing groundwater levels in this part of the city (Suzuki, 1991; DMR, 1997). Consequently, subsidence trend in central Bangkok has slowed. However, despite this success the total quantity of groundwater abstraction in the greater metropolitan area[2] has continued to increase. An increasing demand by the private sector (e.g. industries, table 2.1 on page 15) particularly outside the MWA service area has offset the overall effect of limited pumping by MWA. This has led to recent subsidence in the suburban areas and adjacent provinces (JICA et al., 1995; Duc, 1999; RTSD, 2002). Damages caused by active subsidence were documented during field investigations in the study area (section 2.5). Ground subsidence frequently damages engineering structures such as roads, railways, pipelines and tunnels. More importantly, Bangkok and its vicinity are situated in the flat terrain with the minimum elevations of only about 1 meter or less above mean sea level (Nutalaya et al., 1989; JICA et al., 1995). Therefore subsidence can lead to an increased risk of flooding (the New Orleans catastrophe is a good recent example that coastal subsidence can pose in terms of increased vulnerability to flooding) and saltwater intrusion into the freshwater system, which have already been observed in a few low-lying areas (Worawattanamateekul, 2002). A two-year plan (2004-2006) to expand the surface water distribution system to the outskirt of Bangkok is under way (MWA, 2003). One

[1] an organization responsible for water supply of the Bangkok, Samut Prakarn and Nonthaburi provinces

[2] covers the area of Bangkok and its surrounding provinces; Samut Prakarn, Samut Sakhon, Nonthaburi, Pathumthani and Ayuthaya

important objectives of this plan is to reduce groundwater consumption in the critical subsidence areas. It is expected that surrounding areas including Muangmai Bangplee (part of the study site of this work), the new international airport, and Bang Khun Thien beach road are to be served by MWA by the end of this project in 2006.

Despite this ongoing effort to tackle the subsidence problem, an effective tool to support long-term monitoring and sustainable mitigation of subsidence by providing basic and reliable subsidence information with sufficient detail is indispensable and unavailable to date.

Quantitative determination of land subsidence in Bangkok was first carried out by AIT (AIT, 1981, 1982) in surveys based on repeated benchmark levelling. Sungkhaburana (1983), Duc (1999), and Thepparak (2001) augmented these levelling surveys in subsequent studies with the installation of compression indicators at different depths. Although these methods provide highly accurate subsidence or compaction measurements their deployment is limited to only a handful of locations, yielding very few measurement points. Generally, direct measurements are very time consuming to acquire and a deployment over large areas is often prohibitively costly, especially if a high density of observations is to be achieved. These sparse and infrequent subsidence measurements are insufficient to represent the spatial and temporal surface subsidence changes above a complex aquifer system.

Satellite-based Interferometric Synthetic Aperture Radar (InSAR), developed during the 1980-90s (Gabriel et al., 1989; Massonet et al., 1993; Zebker et al., 1994), offers the potential for acquiring displacement observations over wide areas with a high resolution both spatially and temporally. A SAR scene from existing sensors like ERS-1/2 or ENVISAT typically covers an area of 10,000 km^2. The re-visit frequency is 35 days for the ERS and ENVISAT satellites. The highly accurate and spatially detailed deformation measurements obtainable from InSAR makes these data ideal for improving the characterisation of surface subsidence processes over a wide area. The ability for repeat acquisitions at regular intervals opens up the opportunity to compile time-variable as well as spatial variable subsidence information at resolutions that would be unattainable or unaffordable by traditional methods a potential of high practical interest.

The principles of the InSAR and DInSAR techniques have been well established within the field of radar remote sensing of the Earth (Massonet et al., 1993, 1994; Zebker et al., 1994). Applications of these techniques have been demonstrated in several projects and studies on topographic mapping including the Shuttle Radar Topographic Mission (SRTM) (DLR, 2001; NASA, 2005), earthquake monitoring, glacier and ice sheet veloc-

ity mapping, surface displacement monitoring and atmospheric mapping (see reviews and references therein (Henderson and Lewis, 1998; Hanssen, 2001)). The development of the Permanent Scatterer (PS) technique[3] at POLIMI[4] (Ferretti et al., 1999, 2001) has extended the ability of deriving highly precise displacement information by InSAR methods. Permanent Scatterer Interferometry (PSI) relies on the interpretation of differential phases at a set of selected points, called permanent or persistent scatterers. A persistent scatterer is a radar scatterer that maintains phase coherence over a long time. Permanent scatterers in the reality often correspond to man-made features including buildings (roofs and walls), electricity poles, etc. that reflect radar signals strongly and consistently. A PSI system for the exploration of different geophysical applications was developed at DLR-IMF (Adam et al., 2003, 2004; Kampes, 2005).

This study applies the DLR PSI system to the characterisation of ground subsidence in the Bangkok Metropolitan area. The analysis presented in this thesis tested the limits of PSI analysis under a set of challenging conditions, namely the strong influences of a variable atmospheric phase signal contribution, strongly non-linear ground motion, high rates of subsidence, and a limited number of SAR scenes available for the area of interest.

PS analysis obtains motion estimates by parameter estimation using an interferogram stack (time-series of interferograms of the same area). The reliability of the derived estimates is highly dependent on the number of images, and interferograms, used. Previous studies on displacement estimation using PSI have achieved estimates of displacement rates at a precision of 1 mm/yr or better, but have used phase time series of at least 25 interferograms, often significantly more, in order to do so (table 1.1). In this study I have attempted to achieve reliable and accurate displacement measurements in a PSI analysis with fewer available interferograms, which were acquired under unfavourable atmospheric conditions.

A key factor for measuring and controlling subsidence successfully is the establishment of a monitoring system with the responsibility for providing reliable measurements, reports on current and past subsidence status, and periodic observations of supported field data including levelling surveys and groundwater level etc. A robust and cost effective tool for measuring subsidence is a pre-requisite to the development of such a capability and it is suggested that a PSI based system providing detailed and regularly repeatable subsidence measurements over wide areas could be well suited for this purpose. Long-term sustainability of such a system seems likely through current and

[3]The term PS technique is a registered trademark.
[4]Politechnico di Milano, Italy.

Table 1.1: Examples of past studies exploiting PS analysis for ground displacement monitoring

Author	Area	Specific applications	Baseline (m)	Temp. Baseline (yrs)	No. of images
Walter et al., 2004	Ruhr region (DE)	underground mining	7-1000	8	78
Ketelaar et al., 2003	Rotterdam (NL)	gas extraction	-	8	32,72
Colensanti et al., 2003	California	linear, nonlinear	-	8	46
Fruneau et al., 2003	Paris	urban subsidence	-	6	76
Colensanti et al., 2002	1) Lorraine (FR)	mining induced	-	5	56
	2) San Jose, CA	seasonal displacement	-	8	46
Ferretti et al., 2001	Ancona (IT)	slow surface motion	max. 1600	5	34
Colensanti et al., 2000	California	seismic fault	-	7	54
Ferretti et al., 2000b	Pomona, CA	Urban subsidence	$\pm$1100	< 6	40

planned radar satellite missions.

1.1 Objectives and contributions

Strong atmospheric signals, high and temporally varying subsidence rates, and a limited number of radar images provide the challenging boundary conditions for the PS analysis in this study. The limited number of radar images resulted from the availability of only 35 ERS-1/2 scenes acquired over the Bangkok study site. These scenes were used to construct two interferogram stacks, comprising 19 and 15 interferograms, respectively. These were analysed using the DLR PSI system to characterise surface subsidence across the study site in the period 1996 to 2000.

The primary objective of this study was to

- quantify the subsidence rates for the study site, the southern part of Bangkok covering Bangna and Samrong area , averaged over the period from 1996 to 2000 at high spatial detail.

In addition, this study addresses the following primary research questions:

- Is it feasible to obtain robust linear displacement rate estimates by PSI under the boundary conditions stated and what is the attainable accuracy?
- What are the key factors influencing a successful subsidence estimation by means of PS analysis under these constraints?
- How can PS subsidence estimates in Bangkok be used to support the monitoring and mitigation of subsidence?

In succeeding to derive a detailed map of subsidence rates for the study area this study demonstrates the feasibility of using PSI even under the difficult set of boundary conditions.

The main results are:

- the most spatially detailed subsidence information to date for the area under study,
- a demonstration that, despite a nominal requirement for large number of interferograms, under certain data configuration it is feasible to use PSI for deriving highly precise subsidence estimates at locations subsiding at approximately constant rates with a limited number of scenes (20 scenes),

- the first successful attempt to quantify urban subsidence in one of the Asia's mega-cities by applying C-band SAR in a PSI analysis.
- In addition, my experience in using the prototypical PSI software as a test user has helped in the development of the code.

1.2 Outline

Chapter 2 of this dissertation presents general information on different aspects of subsidence in Bangkok. Section 2.1 provides information on the physical setting including the geological and hydrogeological aspects necessary for understanding the subsidence mechanism of aquifer system compaction. Section 2.2 present reviews past studies of Bangkok subsidence. The following sections 2.3 and 2.4 provide information on existing methods for subsidence measurement and on the laws or regulations issued for the purpose of subsidence control and mitigation in Bangkok. Chapter 3 serves as a bridge to Chapter 4 demonstrating and discussing the difficulties in applying conventional DInSAR for displacement detection over Bangkok. The main part of this thesis, including the derivation of mean subsidence rates applying the persistent scatterer analysis is presented in Chapter 4. The principle of PS analysis is described in Section 4.2. The interferometric data configurations used for the analysis are shown in Section 4.3. Section 4.4 explains the pre-processing procedures required before PS analysis. Section 4.5 describes how the mean subsidence rate are derived in least-squares (LS) approach. The estimation results and their post processing are then presented in sections 4.6 and 4.7. The derivation of the Bangkok subsidence field by kriging interpolation of the PS estimates is presented in Section 4.8. The following Section 4.9 describes briefly how the quality of the derived subsidence estimates is assessed. Section 4.10 presents the validation of the estimates through a comparison with independent geodetic observations from levelling benchmarks and discusses the PSI capability for subsidence measurements under the study constraints. In Chapter 5, a temporal analysis of subsidence observations in conjunction with hydrogeological data available is conducted, demonstrating one application of mean PS estimates for subsidence monitoring. Section 5.2 presents some theoretical foundations necessary for the understanding of aquifer system compaction mechanisms causing subsidence. Subsidence to head decline ratios are computed through the temporal analysis of subsidence observations (from PS estimates and levelling data) and the change in hydraulic head in Section 5.3. Potential uses of PS estimates to aid subsidence strategic planning and future monitoring are then demonstrated in Section 5.4 through a subsidence risk

map and predicted subsidence maps for the year 2025 and 2050. Finally, Chapter 6 concludes the main findings of this study to with respect to the questions previously presented in Section 1.1.

Chapter 2

Land subsidence in Bangkok

2.1 Setting of Bangkok

2.1.1 Geographical setting

Bangkok, the capital of The Kingdom of Thailand, is situated on a low lying flat deltaic plain (Lower Central Plain) located between the latitudes 13°30′and 13°55′N and longitudes 100°15′and 100°55′E . Topography of the basin is flat with minimum elevations of about 1 m or less above MSL (Nutalaya et al., 1989; JICA et al., 1995). The country is located in the tropical and humid climate zone. Most of Thailand has abundant rainfall which is largely confined to the months of May to October. This constitutes about 85% of the annual rainfall. During this rainy season the weather is dominated by the southwest monsoon blowing in from the Indian Ocean and bringing with it warm, humid air and clouds. In the months of November to April the air is much drier due to the northeast monsoon blowing overland from China or Indo-China. The average rainfall is about 1200 mm per year. The primary drainage system consists of the Chao Praya (light blue in fig. 2.1), Thachin and Bang Pakong rivers with their tributaries. The total drainage area is 55,000 km^2(Giao, 1996). Fig. 2.1 shows a satellite image (Landsat-TM) of Bangkok and its vicinity. A portion of downtown Bangkok can be seen at the top-left of the image and the test area for PSI analysis is delineated by a dashed rectangle. The area is defined by a domination of sub-urban environments, with urban settlements mixed with industrial clusters along the main roads. The red areas in the image represent vegetation cover.

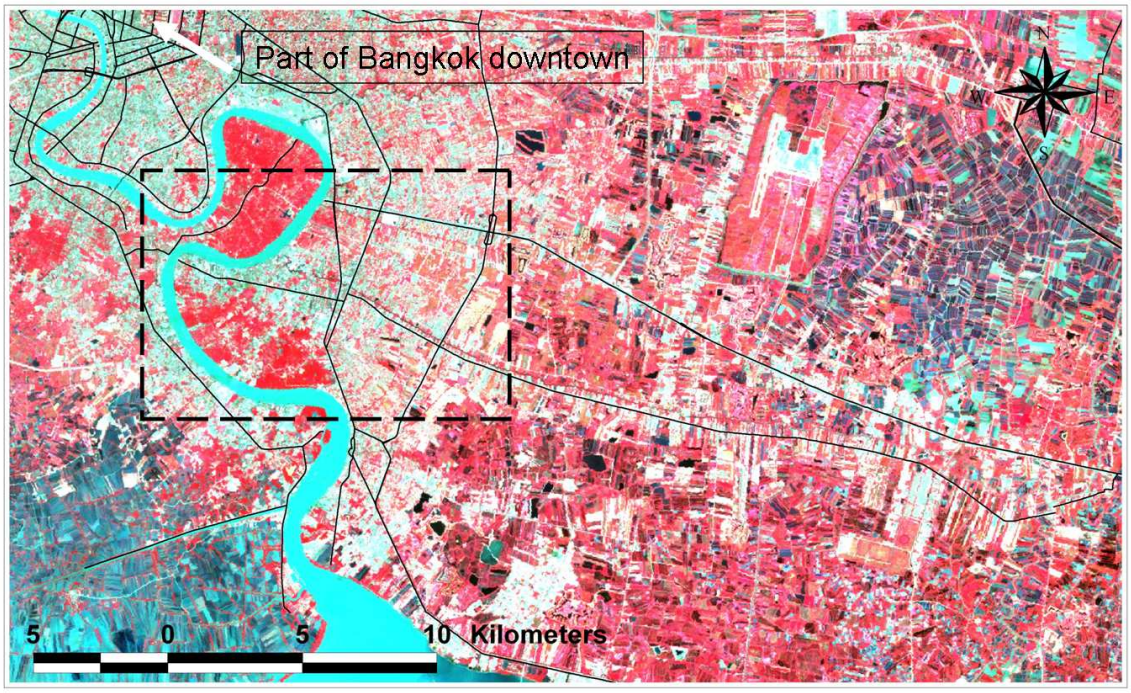

Figure 2.1: Landsat image of Bangkok and vicinity (RGB: 432)

2.1.2 Geological and hydrogeological setting

Geological setting

The lower central plain of Thailand is located along the north-south trending structural depression as a result of the crustal movements during the Mesozoic and Tertiary periods (Brown et al., 1951). According to Achalabuti (1974), aeromagnetic data indicated that the depression is underlain by various types of bedrock at a depth of 400 to 3,500 m. The basin floor slopes toward the central axis which is located more or less along the Chao Phraya river course and inclines southward to the Gulf of Thailand. Overlying the bedrock are the unconsolidated or semi-consolidated sediments deposited during the Tertiary and the Quaternary periods with a thickness of as much as 550 m (Sungkhaburana, 1983). The plain consists of a broad deep basin, filled with sedimentary soil deposits which form alternate layers of sand, gravel and clay (Piancharoen and Buapeng, 1973). Studies indicated that about 6,000 years ago the sea level in the Gulf of Thailand reached its maximum height of 4 m above the present level (Sinsakul, 2000). The coastline was located much further north than today, about 80 km north

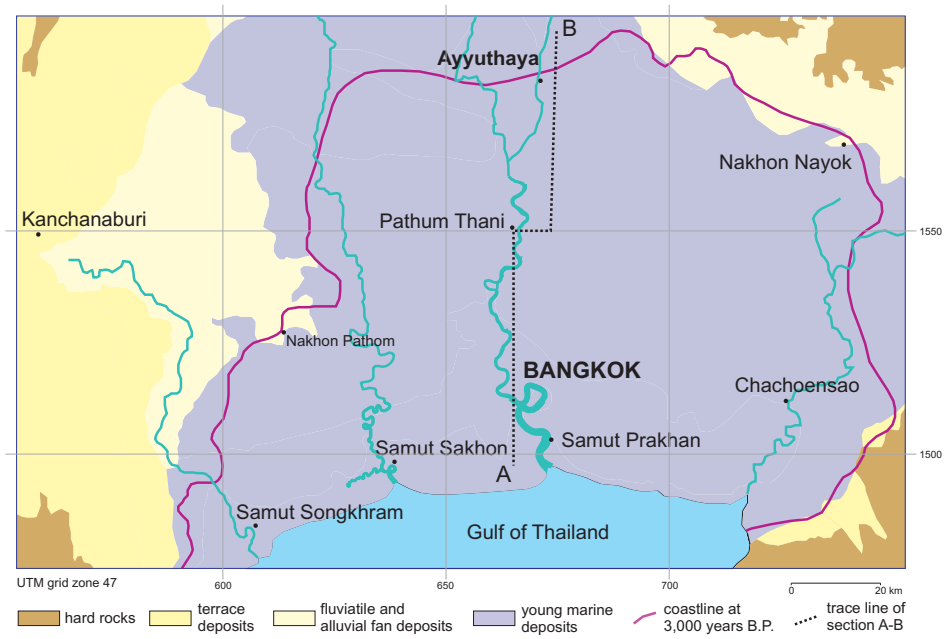

Figure 2.2: Geological map of the lower central plain and the location of the historic coastline. (after Kuehn et al. (2004))

of Bangkok (Woodrooffe, 2000). The top confining layer of soft marine clay, known as Bangkok clay, is thought to have been deposited during this marine transgression. Fig. 2.2 and 2.3 present the geological maps of the lower central plain.

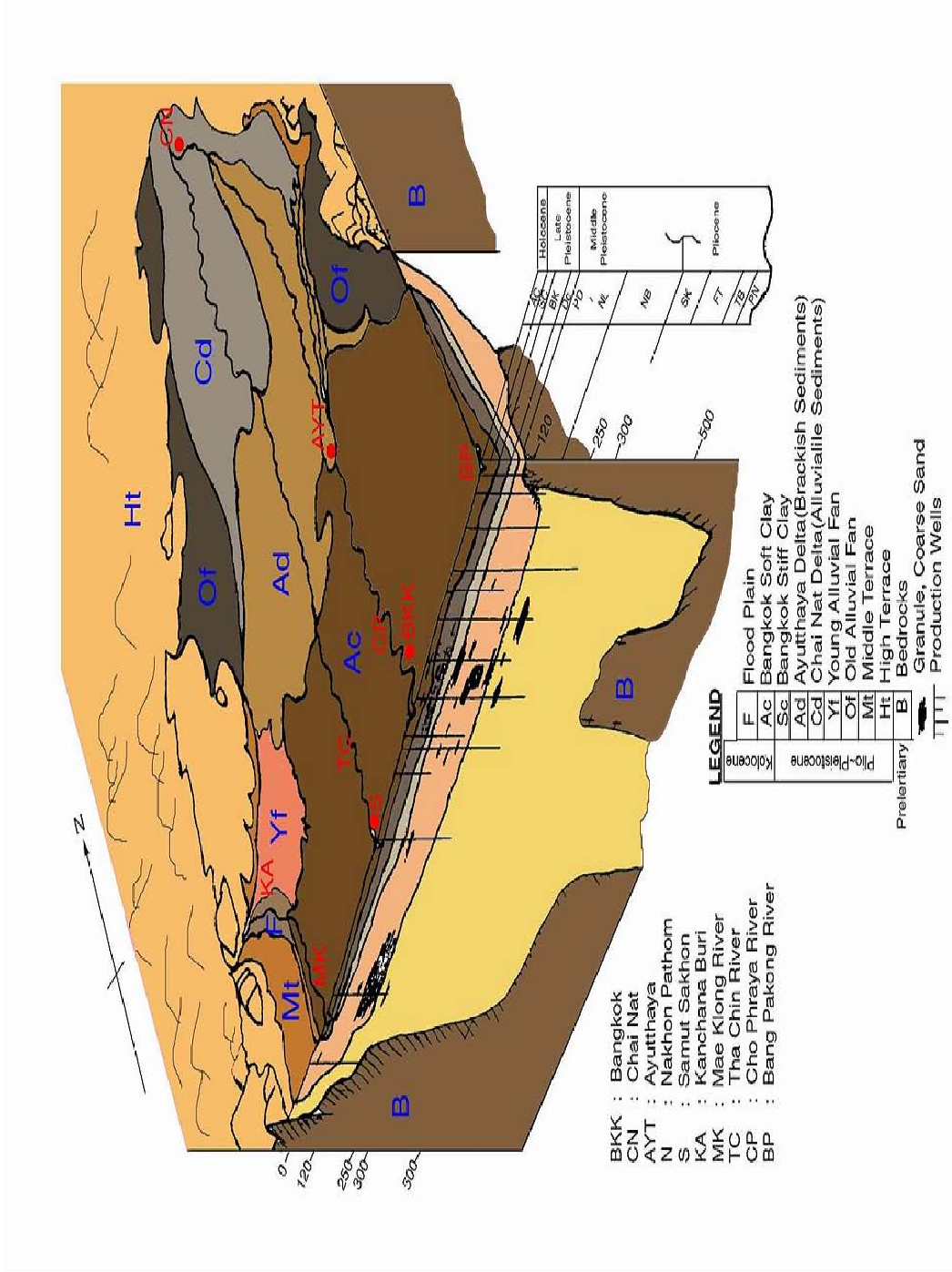

Figure 2.3: Geological setting of the lower central plain. Bangkok is situated on the east bank of the Chao Phraya (CP) river indicated with red letters (BKK). (after AIT (2004))

Subsoil strata

Subsoil characteristics have been studied and stratified primarily in the upper 30 m depth zone. The intensive studies on subsidence of Bangkok during 1978-1981 extended the investigation up to a depth of 400 m (AIT, 1981, 1982). The sequence of soil strata in the 30-50 m depth range are as follows:

- Top soil or weathered crust (1-3 m thick) with a yellowish brown to dark gray color.
- Very soft to medium clay, referred to as Soft Bangkok Clay (10-15 m thick) with an olive gray color and occasional shell fragments. The strata can extend up to the depth of 25-30 m.
- Stiff to very stiff clay, referred to as Stiff Bangkok Clay (5-10 m thick) with a light brown to gray color, sandy in some parts.
- Uppermost sand layer (8-16 m thick) with fine to medium sand and occasionally contains traces of clay or silt. It can be generally found at a depth of 20-30 m.

The deeper strata, they can be categorized into two major types namely:

- Sand layer with coarse grained soil, very small or no cohesion exhibiting high permeability and low compressibility
- Clay layer with fine grain soil of considerable cohesion exhibiting low permeability and a higher compressibility than sand layer.

Permeability tests in the laboratory showed the typical range for the permeability of clay samples to be $5 \times 10^{-8} - 10^{-6}$cm/sec while for the sand samples it varies from $10^{-5} - 10^{-4}$ cm/sec. Both samples were taken from 400 m deep boreholes.

Hydrogeological setting

According to their geoelectrical properties the sediments in the upper 550 m of the Lower Central Plain were identified and classified into 8 principle aquifers (fig. 2.4) (Piancharoen and Buapeng, 1973; Ramnarong and Buapeng, 1992). The aquifers consist mainly of sand and gravel separated by clay layers. Stratigraphically the components of the Bangkok multiaquifer system, aquifers and aquitards did not develop continuously.

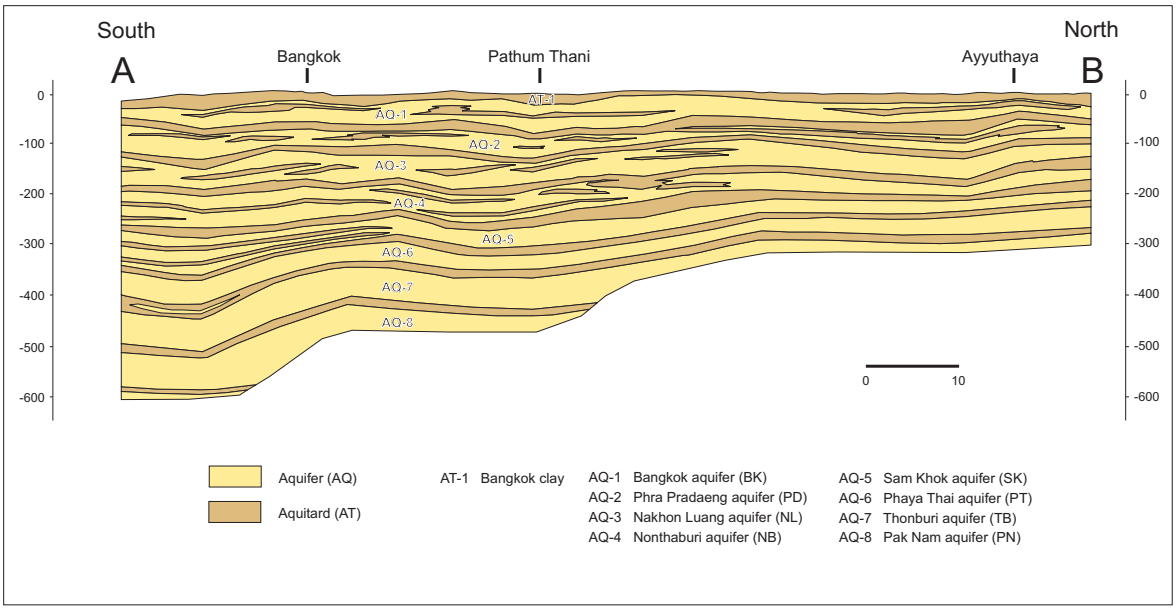

Figure 2.4: Hydrological profiles for N-S section of the lower central plain indicated by dotted line from A to B in fig.2.2. (after Kuehn et al. (2004))

Missing clay layers and interconnections between the aquifers were mentioned by AIT (1981); Premchit and Gupta (1981); AIT and DMR (1982); AIT (1992).

The sequence of the aquifer system from top to bottom can be classified as

1. Bangkok aquifer - BK (50 m zone)
2. Phra Pradaeng aquifer - PD (100 m zone)
3. Nakhon Luang aquifer - NL (150 m zone)
4. Nonthaburi aquifer - NB (200 m zone)
5. Sam Khok aquifer - SK (300 m zone)
6. Phaya Thai aquifer - PT (350 m zone)
7. Thon Buri aquifer - TB (450 m zone)
8. Pak Nam aquifer - PN (550 m zone).

Most wells in Bangkok penetrate to the second, the third, and the forth aquifers, because they are highly productive and yield water of excellent quality. Their coefficient transmissivities range from 40-130 m^3/hr.

Table 2.1: Records of groundwater discharge in cu.m per day for 4 provinces (Bangkok, Samut Prakarn, Nonthaburi and Pathumthani)

Year	MWA**	Private	Total
1993	134,368	944,200	1,078,588
1994	250,000	1,094,292	1,344,292
1995	250,000	1,215,864	1,465,864
1996	265,000	1,396,869	1,661,869
1997	265,000	1,405,702	1,670,702
2002	N/A	N/A	$2,250,000^*$

* from personal communication , N/A not available
** Metropolitan Waterworks Authority
Source: Department of Mineral Resources (DMR) 1997

2.1.3 Groundwater extraction

Expansion of urban areas and industrialization in mega cities have increased the simultaneous needs in water supply. Urbanization and the industries of the Bangkok metropolitan area had been heavily developed during the late 60s and 70s (Suzuki, 1991). Exploitation of groundwater on a large scale started with an extraction from NL aquifer in 1954. Groundwater from PD aquifer has been heavily pumped since 1960 mainly for industrial use and from NB aquifer since 1965. Extensive pumping during the 70s-80s have led to significant declines of piezometric levels with a maximum up to 40-50 m in each exploited aquifer and hence to the extensive land subsidence in Bangkok and vicinity (Giao, 1996). The maximum total subsidence observed during 1933-1987 (54 years) was 1.6 m, during 1978-1987 (9 years) it was 0.75 m and during 1978-1997 (19 years) it was 0.7 m (Nutalaya et al., 1989; Duc, 1999). Such figures evidenced that intensive subsidence had occurred during the 70s and 80s.

Although the present amount of pumping by the government sector, the MWA has been maintained ($\sim$16 % of total discharge in 1997) the total amount of discharge has still been increasing every year (table 2.1). Records of discharge also show that private sectors , domestic and industries, are the main groundwater users in the Bangkok metropolitan areas. The largest quantity of groundwater is extracted from the NL aquifer (49%) , followed by the NB aquifer (20.3%) and the PD aquifer (14.9%) respectively. And about 84% of all wells extract the water from the NL aquifer (JICA, 1993).

2.2 Previous studies on Bangkok subsidence

Previous studies have identified groundwater pumping as the primary cause responsible for widespread subsidence in Bangkok and vicinity. The subsidence magnitudes are apparently related to drops in piezometric levels (Duc, 1999). Subsidence in Bangkok was probably first mentioned by Cox (1968). He pointed out some similarities between the subsidence in Tokyo and Bangkok and recommended the phenomenon to be investigated. Worayingyong (1975) carried out a preliminary simulation of Bangkok's subsidence and estimated that the subsidence should not have started earlier than 1963. The cause of subsidence was found to be due to compression of the upper clay layers. A Finite Difference (FD) Quasi-3D model (groundwater model) was successfully developed and used to simulate land subsidence for Bangkok by Premchit (1978) and Premchit and Gupta (1981). Until early 1978, there have were no studies carried out to determine subsidence quantitatively. A long term project on investigation of Bangkok land subsidence due to deep well pumping was conducted by researchers at the Asian Institute of Technology (AIT). It remarked a comprehensive phase of subsidence investigation during 1978-1981 and is probably the first systematic study on Bangkok subsidence. A direct relationship between surface subsidence and declines of piezometric level was found. Recommendation to use artificial recharge to halt subsidence was proposed (AIT, 1981, 1982). The maximum subsidence rate of about 10 cm/y was observed in the suburb of Bangkok. Another cooperative study (AIT and DMR, 1982) of the same period cooperated between Water Resource Engineering Division, AIT and the Department of Mineral Resources (DMR) applied different models of pumping schemes to predict subsidence. As a result, reduction amount of groundwater extraction from 1.4 million m^3/day to 0.4 million m^3/day was proposed. An increase of surface water production and the extension of its distribution system to the MWA non-service areas were the possible solutions suggested. Also, the regular monitoring of piezometric heads and soil compression are necessary. In 1989, artificial recharge was tested practically for the first time both in and outside Bangkok (Nippitavasin, 1989; Ramnarong, 1989). The test results were not significant enough to derive meaningful conclusions. A full scale field test of artificial recharge, carried out in 1995, involved recharging to the shallow wells penetrating to the upper BK aquifer (AIT, 1995). Guidelines for design, instrumentation, monitoring and analysis of recharge data were obtained. A more recent comprehensive study on management of groundwater and land subsidence was conducted by JICA et al. (1995). They stated that groundwater level in central Bangkok was recovered from the year 1983 but it has continued to drop in the vicinity area. This implies that subsequent subsidence studies

for Bangkok should also include its surrounding provinces. Subsidence magnitude in central Bangkok was about 20 mm/y while it reached 50 mm/y in the vicinity, e.g. Samut Prakarn and Pathumthani (JICA et al., 1995). Giao (1996) conducted research on the operational aspects of artificial recharge through the uppermost aquifer to bring out possibilities of further applications to the deeper aquifers. Several schemes of artificial recharge were studied. The obtained results showed positive abilities of recharge to mitigate land subsidence. Duc (1999) analysed surface subsidence with the emphasis on the shallow soil settlement and concluded that most of the subsidence was subjected to compression of soils in the first 150 m depth zone. This is the zone where the majority of groundwater is extracted. He further stated that in the most subsiding area, about 50-70% of the compression occurs in the zone below the first sand layer (30 m depth and below) and about 50-30% of the compression occurs in the upper clay layer or Bangkok clay. In Bontenbal (2001), a summary on change of land subsidence in Bangkok over the last 25 years was reported. It was summarized that after the highly annual subsidence rate of about 10 cm/y in 1978 to 1981, subsidence decreased almost steadily until the beginning of 90s (maximum subsidence rate was 8.5 cm/y during 1981-1985, 3.5 cm/y during 1985-1988 and 3.0 cm/y during 1988-1991). Due to the economic boom, subsidence rate increased again until 1997 (the maximum subsidence rate was 4 cm/y during 1991-1994 and 5.5 cm/y during 1995-1997). After the economic crisis in 1997, subsidence slowed down and the maximum rate was approximately 3.5 cm/y (1997-2000).

2.3 Existing means to determine subsidence

Determination of ground subsidence in Bangkok has been achieved by measuring one or both of these two quantities.

- Absolute subsidence
- Compression of soil layers

Absolute subsidence determined by precise surface leveling

Precise leveling is the method to determine the elevation of the benchmarks at land surface using an engineer's level and a level rod. It is said to be the most practical method for measuring vertical displacement of benchmarks in subsidence monitoring (Poland, 1984). The benchmark net should be designed to cover the area of known or

suspected subsidence and to extend into a broader regional network of two or three reference benchmarks that are stable. The spacing of benchmark in the net is normally in the range of 400-1000 m or closer. In benchmark surveys of subsiding areas, the leveling can be of the first or second order. The suitable time for carrying out benchmark surveys is immediately following the rise of groundwater level, when compaction and subsidence are minimal.

The accuracy of the leveling observations used in this study is $\pm 2.33\sqrt{K}$ for line leveling and $\pm 4\sqrt{K}$ mm for loop leveling. K denotes the distance of a line or the perimeter of a loop in kilometers (DMR, 2002). The leveling survey is usually done annually to determine subsidence of the ground surface. At least two government agencies, the Royal Thai Surveys Department (RTSD) and the Department of Mineral Resources, conduct the leveling surveys annually to determine subsidence in the Bangkok area. Observation coverage varies depending on the budget available.

Compression indicators (CI)

Total subsidence of the multi-layer deposits is the summation of the compression of the component layers. It is essential to measure the compression of each of the individual layers. Compression of soils can be measured by three different types of deep compression indicators; the compression type, the extension type and the precision extensometer type (Thammakumpee, 1978). For Bangkok, the compression type has been used.

Measuring subsidence by any of the stated means is costly most likely due to the maintenance of the instruments, labour intensive and time consuming. Table 2.2 compares the advantages and disadvantages of different subsidence measurement methods. InSAR technique is included. Odijk et al. (2003) suggested that the combination to use both optical leveling and InSAR could possibly result in a more efficient monitoring strategy due to their different characteristics in measurements. InSAR provides temporal height differences for coherent resolutions while leveling measurements, if well founded, represent subsoil deformations. InSAR derived height changes can be subjected to deformations of surface, subsurface soils or buildings depending on the dominant source of radar reflection. InSAR is suitable for deriving large extent of subsidence information, while leveling is very precise for a local point measurement. Subsurface deformation, if of interest, can be well monitored using deep compression indicators but its areal resolution is low. These three methods provide comparable precision at sub-millimeter to millimeter level. In terms of measurement cost, comparing per area of coverage measurements InSAR could be more economical compared to

Table 2.2: Comparison of different means for measuring subsidence

Methods	Surface leveling	CI Extensometers	PSI
1.What is measured	surface	subsurface	surface
2. Measured values	absolute	relative	relative
3. Precision	sub-millimeter	sub-millimeter*	millimeter
4. Resolution in space	1 point /100km^2	N/A	**
5. Resolution in time	depends on frequency of surveys	depends on type of instruments	35 days (ERS-1/2 case)
6.Observation coverage	points along the profile line	at installation point	100x100 km
7. Cost	25 Euro/ 1 km line	∼200 - 5000 Euro*	50 Euro/ radar scene

* depends on instrument types based on Poland (1984)
** depends on the distribution of PS, in urban area PS density is higher than the density of the survey benchmarks
N/A not available

leveling survey. Therefore, subsidence analysis in an integrated fashion could yield a more preferable approach benefiting from each of the advantages.

2.4 Control and mitigation

Apart from damage to engineered structures such as buildings, roads, pipelines, well casings etc., subsidence may cause disturbance to the natural water system, to the saltwater-freshwater ecosystems and trigger intrusion of seawater into aquifers (Worawattanamateekul, 2002). As Bangkok is located in a low lying area, subsidence can enhance severe coastal or river flooding.

In an attempt to mitigate subsidence and control the use of groundwater two major regulations were launched. The first regulation, Groundwater law, issued in 1978 aimed to control groundwater usage and development primarily from the private sector. Six provinces were defined as effective areas for this law namely; Bangkok, Samut Prakarn, Samut Sakorn, Nonthaburi, Ayuthaya and Pathumthani. Permission to drill the well or withdraw groundwater had to be requested beforehand. The second regulation launched in 1983 divided subsidence critical areas into 3 zones depending on the level of severity, more than 10 cm/y, between 5-10 cm/y and less than 5 cm/y respectively. The main purpose of this law was to maintain the present level of groundwater

in the Bangkok and Samut Prakarn areas. It was also estimated that by the year 1988, groundwater level should increase by a few percent. Regulations for collecting a groundwater fee were issued in 1983 after three intensive subsidence studies during 1978-1981 (Suzuki, 1991). In February 1985 the ministry of industry began to collect the groundwater fee. The fee is waived when pumping amounts less than 25 m^3/day and for the areas where the public water system does not cover. As a result from the law, in 1987 the amount of groundwater pumping from the Metropolitan Water Works Authority (MWA) was reduced by almost 50% compared to its consumption in 1982. In 1989, recovering of the water level was recorded in some areas but decreasing in others. Although, the number of drilling wells had been decreased the total groundwater consumption had increased (Suzuki, 1991).

This proved that the control of groundwater use is effective only in central Bangkok, where the water distribution system has been well developed and is sufficient. On the other hand, drops of water level have been spread out to outside Bangkok where most of the users still rely on groundwater usage. Effective control of groundwater usage and subsidence would be successful when the distribution of surface-water supply system can cover the subsidence affected areas.

In mitigating adverse consequences from subsidence, artificial recharge could probably be considered as a solution. Two successful cases using artificial recharge to relieve subsidence are:

- The case at Wilmington oil field in Long Beach, CA. The re-pressuring of an oil reservoir was started in 1958 and by 1963 there had been a modest rebound in the subsiding area. The rates of subsidence were reduced elsewhere (Freeze and Cherry, 1979).

- Shang Hai case. The recharge was done in the winter to insert water back and use it in the summer. By this means, they can reduce groundwater usage from 0.55 million m^3/day to 80,000 m^3/day (Suzuki, 1991).

2.5 Evidence of subsidence

Photos presented in fig. 2.5 to fig. 2.7 were collected during the field investigations in 2002 (Worawattanamateekul, 2002).

(a) (b)

Figure 2.5: Evidence of subsidence in the study area. (a) shows the basement of a house separated from the ground. (b) shows cracks on the sidewall of the same house.

(a) (b)

Figure 2.6: (a) and (b) show the unnatural and strongly uneven road surface of the two sides of a main road (passing from north to south of the study site) found in the study area.

(a) (b)

Figure 2.7: Evidence of subsidence found at a site located southeast from Bangkok (outside the study site). (a) shows two different guard shelters that the basements were founded at different depths. The basement of the right shelter was founded in the shallower clay layer and therefore strongly affected by subsidence than the one founded deeper in the sand layer (left shelter). (b) damage of the engineering structures due to subsidence of the same site. The subsidence rate of approximately 11 cm/y was estimated for this location.

Chapter 3

Feasibility study of the classical differential interferometry (DInSAR) for subsidence detection in Bangkok

3.1 Introduction

Differential interferometry, a technique by which surface deformation is measured, is a powerful tool that can be used to obtain displacement information in the direction of radar line of sight. It is able to provide millimeter-scale precision and meter-scale resolution over kilometer-wide areas (Zebker and Goldstein, 1986; Massonet et al., 1993; Rosen et al., 1996). It is a unique means to perform low-cost and large coverage surface deformation monitoring (Ferretti et al., 1999). Apart from its remarkable potential in providing high resolution surface movement information, the application of DInSAR to some areas (particularly in the tropical environments) has still been limited primarily due to atmospheric disturbance and temporal decorrelation. In this chapter the feasibility of the classical DInSAR for subsidence detection in tropical environments will be investigated using SAR data sets. Decorrelations due to unsuitable baseline configuration and physical changes of the scatterers during the acquisitions contributing to the quality of the interferograms are primarily considered. The atmospheric effects on the interferograms will be demonstrated. The obtained results demonstrated that detectability of the displacement signals in the study area was hampered by decorrelation of signals (primarily by temporal decorrelation). In addition, the extensive

atmospheric artifacts in some of the available tandem interferograms prevents their usage as topographic interferograms.

3.2 Interferometric Synthetic Aperture Radar (InSAR) Technique

The principle of InSAR uses two or more SAR images either received by two different antennas simultaneously (single-pass) or by repeated acquisitions (repeat-pass) enabling the technique to obtain the distance as well as the angular measurements. The phase measurements permit the relative distance observations as a fraction of the radar wavelength while the difference in antenna locations enables the angular difference observations. Interferometric processing results in an important product called an *interferogram* in which every image element is generated by multiplication of the amplitude of two images and the subtraction of phase information. According to the application purpose and processing consideration, interferograms can then be employed for topographic mapping, surface movement or deformation detection and atmospheric studies.

InSAR method can be categorized as an across-track or an along-track SAR interferometry with respect to the orientation of the SAR antennas. Both across-track and along-track InSAR are applicable on the airborne SAR systems as well as on the space shuttle (SRTM-C/X) and the future radar satellite systems (TerraSAR-X). The position of the two SAR antennas mounted on the platform is perpendicular to the flight direction for across-track InSAR while it is parallel to the flight direction for the along-track InSAR. A different method that requires only one SAR antenna and hence well suited to the spaceborne SAR system currently available is *repeat-pass interferometry*. In this method, the two SAR images are acquired with a temporal difference that is equal to a satellite repeat orbit cycle (35 days for ERS-1/2) covering an area with a slightly different viewing geometry.

One very spectacular application of the repeat-pass InSAR configuration is that it allows one to detect and monitor ground surface changes that have taken place during the acquisitions i.e. the deformation monitoring. Therefore, geodynamic phenomena like volcanic deflation, co-seismic deformation, glacier motion and urban subsidence can be mapped and quantified. A problem in this application is that for the normal baseline[1] larger than zero, the deformation signal will be mixed with the topographic

[1]The normal or perpendicular baseline is the distance separation (m) between two SAR antennas

signal (Massonet et al., 1993, 1994; Hanssen, 2001). The suitable solution is the *Differential Interferometry (DInSAR)*, in which the topographic phases (either derived from other interferograms or an external Digital Elevation Model (DEM) are scaled into the baseline conditions of the deformation interferogram. The scaled phases are then subtracted from the deformation interferogram, yielding a differential interferogram consisting of merely a deformation signal (Gabriel et al., 1989). Massonet et al. (1993) firstly applied the two-pass method requiring an external DEM to observe co-seismic deformation on the scale of cm-m of the Landers earthquake. The results demonstrated well agreement with the estimated deformation from the model.

3.2.1 Development in SAR Interferometry

Development in interferometric SAR can be described primarily by three keywords: radar, synthetic aperture radar and interferometry. *RADAR* stands for RAdio Detection And Ranging . The radar instrument emits electromagnetic pulses at radio or microwave wavelengths and detects the reflections of the emitted pulses in the line of sight direction. Although the development of radar technology was highly boosted by the military applications during World War II, its applicability for civilian and scientific uses rose quickly afterwards. For example, for the study of celestial bodies such as Moon, Venus and Mars.

The earlier development of side-looking imaging radars, the *Real Aperture Radar (RAR)*, owed its name by which a physically long antenna was requisite to obtain the resolution in the flight direction (azimuth resolution). Such a practical constraint on the antenna length resulted in a very coarse resolution in the flight direction. A later development in the late 50s and early 60s at the universities of Illinois and Michigan, the *Synthetic Aperture Radar (SAR)* applied the concept of coherent radar in which phase as well as amplitude information are preserved for later processing. This technique utilized a moving antenna and combined the information from a multitude of returned signals within the synthetic antenna length to create an artificially long antenna. By this method, the azimuth resolution can be increased dramatically from the 4.5 km beam width for a single pulse to approximately 5 m for the full synthetic aperture (Wiley, 1954; Graham, 1974).

Experience on airborne and spaceborne SAR missions for earth observation probably started during the 60s to 70s. Seasat, the L-band SAR satellite launched in June 1978 primarily for ocean studies could provide spectacular SAR imageries and enabled SAR

in the direction perpendicular to the radar line of sight ($B_\perp$ in fig. 3.1).

systems to be included in many upcoming satellites (Elachi et al., 1982) even though the mission ended after only 100 days of operation. Plenty of geological information and ocean topographic information were retrieved during this mission. Success of Seasat triggered the Space Shuttle and satellite missions to carry a SAR. The Shuttle Imaging Radar (SIR-A) launched in 1981 orbited the earth for only 2.5 days. An improved version of SIR-A, SIR-B operated in 1984 and was able to steer its antenna mechanically to change the look angles. Both systems were equipped with L-band SAR. The very first S-band SAR satellites, Cosmos-1870 launched in 1987 and ALMAZ-1 launched in 1991 by the former Soviet Union operated for 2 and 1.5 years respectively. In July 1991, the European Space Agency (ESA) launched its first radar satellite, the European Remote Sensing satellite (ERS-1). It operated at C-band and was designed for polar oceans and ice applications. Observation from the steep look angle of 23° results in the strong topographic distortion. The twin satellite of ERS-1, the ERS-2, was launched in April 1995 enabling a tandem mode (24 hours time difference) operation of the two satellites. In spite of its steep look angle, the systematic data acquisitions, good orbit control and maintenance of the ERS satellites largely benefit by the improvement of radar interferometry technique. Unlike other SAR missions, the first Japanese Earth Resources Satellite (JERS-1) was planned for solid earth remote sensing and was equipped with an L-band SAR at a wavelength of 23.5 cm. The satellite orbited the earth since 1992 and operated until October 1998. The 35°look angle operation made JERS-1 more favorable regarding topographic distortion and hence more suitable for topographic mapping. SAR system observations on the Space Shuttle continued again in 1994 equipped with three frequencies L-band, C-band and X-band radar, the SIR-C/X SAR. The multi-frequency characteristic extended the capability and improved the interpretation of data dramatically (Lanari et al., 1996; Cotelli et al., 1996). The Canadian Space Agency started to operate Radarsat, their first radar satellite in 1995. Although the satellite is capable of interferometric applications, limitation in orbit control and maintenance hampered its interferometric capabilities. The single-pass interferometry configuration of the Shuttle Radar Topographic Mission (SRTM) eliminated the temporal decorrelation problem of repeat-pass InSAR. It operated for 11 days during February 2000 in C-band and X-band to map the land mass.

The first experiments using airborne (SAR) interferometry to obtain elevation information from the phase difference images was performed by the U.S. military. This technique was patented in 1971. In 1974, Graham reported the results using this method to generate topographic contours (Henderson and Lewis, 1998; Hanssen, 2001). Graham (1974) applied optical processing by coherent addition of the signals received by

two antennas. Dual antenna (single-pass) airborne interferometry matured in the 80s by use of digital processing and multiplicative interferometry. Zebker and Goldstein (1986) extended Graham's technique and applied digital processing to generate an interferogram in which for every pixel element the amplitude of the two images were multiplied and the phases were subtracted resulting in a topographic map with an accuracy of 10-30 m. Researchers at JPL (Li and Goldstein, 1987; Goldstein et al., 1988; Li and Goldstein, 1990) demonstrated firstly that the same technique could be used on the satellite SAR data acquired on separate pass leading to the existence of repeat-pass interferometry. A problem in InSAR processing, phase unwrapping, was also addressed in Goldstein et al. (1988) who developed a technique to determine the absolute interferometric phase. Using one known elevation within a scene, they determined this remaining constant from which the elevations of all other points within that scene could be estimated. The early applications of radar interferometry were focused on the topography estimation of the terrain. Nevertheless, the repeat-pass configuration demonstrated an even more interesting application, deformation monitoring. The relative displacement of the scatterers in the line of sight direction with respect to a location in the image could be measured at a the fraction of the L-band, C-band and X-band wavelength yielding accuracies at the cm to mm level (Gabriel et al., 1989). A problem encountered when the interferometric baseline is greater than zero is that the topographic and deformation signals will be mixed. Gabriel et al. (1989) was the first to apply differential interferometry to discern the deformation signal from the topographic signal. This was done by scaling the topographic phases into the baseline condition of the deformation interferogram and subtracting from it.

3.2.2 InSAR Geometry

Interferometric Synthetic Aperture Radar analyses follow from interpreting the precise time delays and differential phase shifts in radar echoes as distance measurements and relating those geometric distances to topography, motion, or deformation of the surface (Zebker et al., 1997). The geometric relations which define the displacement measurements in terms of viewing geometry and InSAR measurable distances are visualized in fig. 3.1. A radar antenna transmits the radar pulse and receives the backscattered echoes from the Earth surface permitting an understanding of the physical characteristics of the illuminated targets, e.g. target P. For repeat-pass interferometry, two radar images are acquired at different times t_1 and t_2 from slightly different satellite positions described by an interferometric baseline B. R and R'represent the radar range distance at t_1 and t_2 respectively. θ depicts the satellite look angle, α depicts the

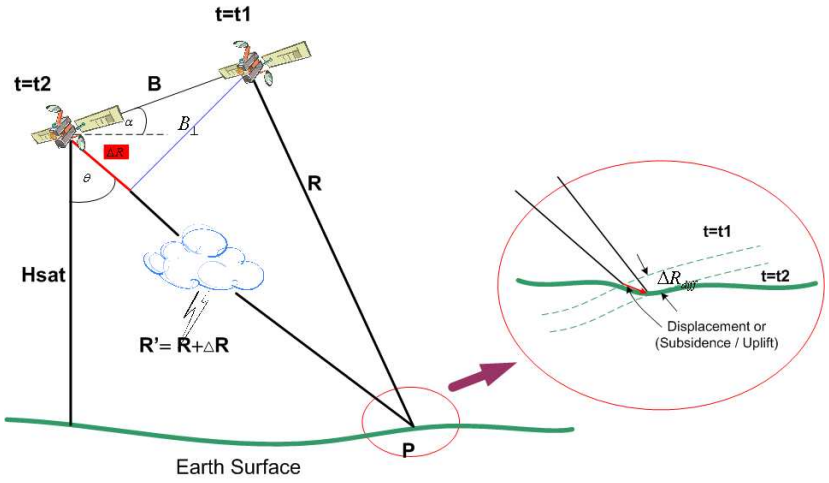

Figure 3.1: Illustration of InSAR imaging geometry in deformation interferogram (modified after Bamler and Hartl (1998)).

baseline orientation angle referenced to the horizontal. H_{sat} denotes the satellite altitude which is about 785 km (ERS-1/2). Basically, the observed interferometric phase ϕ_P can be expressed according to its deterministic component as the geometrical phase ϕ_{geom}, the scatterer phase component ϕ_{scat} and the stochastic component as noise (eq. 3.1). If a resolution element on the ground scatters identically for each observation ($\phi_{scat,t_1} = \phi_{scat,t_2}$) then the difference of the two phases at point P will depend only on the imaging geometry and can be expressed as in eq. 3.2. Note that the phase distortion due to the atmospheric path delay is included in the geometrical term.

$$\phi_P = \phi_{geom} + \phi_{scat} + noise \tag{3.1}$$

$$\phi_{geom} = \frac{4\pi}{\lambda} \triangle R; \qquad \text{for } \triangle \phi_{scat} = 0 \tag{3.2}$$

In the case of satellite-based InSAR, the distance to scatterer R is much larger than the interferometric baseline B and the far field approximation used by Zebker and Goldstein (1986) results in:

$$\triangle R = Bsin(\theta - \alpha) = B_\parallel \tag{3.3}$$

and thus eq. 3.2 can be rewritten as

$$\phi_{geom} = \frac{4\pi}{\lambda} B_\parallel \tag{3.4}$$

Extension of eq. 3.1 and representing an interferogram in the general terms according to its possible phase contributions leads to

$$\phi_P = \phi_{topo}(h, B_\perp) + \phi_{disp} + \phi_{atm} + \phi_{orbit} + \phi_{noise} \tag{3.5}$$

Where ϕ_{topo} denotes the phase component due to terrain topography which depends on terrain elevation h and the perpendicular baseline $B_\perp$. ϕ_{disp} represents displacement phase due to the scatterers motion. ϕ_{atm} denotes phase distortion due to the difference of atmospheric path delay during the two acquisitions. ϕ_{orbit} symbolizes phase contribution from orbit indetermination and ϕ_{noise} represents phase noise.

In the topographic interferogram, we can express the relationship between height h of the point P and the topographic phase as in eq. 3.6. $B^0_{\perp,P}$ denotes the perpendicular baseline component at point P, R_P represents path length from the sensor to the target and θ^0_P denotes the look angle for the pixel P. The zero superscripts symbolize the value that should be referred to the reference body e.g. ellipsoid. Detail derivation of this equation can be found in (Hanssen, 2001).

$$\phi_{topo} = \frac{4\pi}{\lambda} \frac{B^0_{\perp,P}}{R_P sin\theta^0_P} h_P \tag{3.6}$$

In case surface displacement $\triangle R_{diff}$ occurred over the period of time t_1 and t_2, the displacement phase adds into the observed interferometric phase as

$$\phi_P = \frac{4\pi}{\lambda}[B_\parallel + \triangle R_{diff}] \tag{3.7}$$

Using an external digital elevation model or multi-passes method to remove the topographic contribution phase, one can derive surface change over time i.e. in this study uplift and subsidence. Compared to the eq. 3.5, eq. 3.8 expresses phase contributions in a differential interferogram at point P after topographic phase removal. The last three contributions are considered as noise in this study. Eq. 3.9 expresses only the displacement phase component in relation to its displacement component $\triangle R_{diff}$.

$$\phi_P = \phi_{demerror} + \phi_{disp} + \phi_{atm} + \phi_{orbit} + \phi_{noise} \tag{3.8}$$

$$\phi_{disp} = \frac{4\pi}{\lambda} \triangle R_{diff} \tag{3.9}$$

3.2.3 Phase noise in interferograms

Coherent radar echoes will be correlated with each other if each one represents nearly the same interaction with a scatterer or set of scatterers (Zebker and Villasenor, 1992). The loss of coherence or decorrelation of two SAR signals which occurred through many driving mechanisms can be a significant impediment to repeat-pass interferometric analysis. Hanssen (2001) defines decorrelation as noise caused by error sources governing a correlation length smaller than the regular coherence estimation window[2] i.e. the high frequency noise. This implies that error sources with larger correlation length or low frequency noise such as orbit errors or atmospheric disturbances are not influenced in the estimation of coherence (see eq. 3.11).

One way to quantify the quality of an interferogram or fringe is by means of the coherence measurement. Phase noise in an interferogram can be expressed as a function of the absolute value of the complex coherence. The complex coherence can be estimated by use of eq. 3.10.

$$\gamma = \frac{\left|\langle c_1 c_2^{\star}\rangle\right|}{\left(\langle c_1 c_1^{\star}\rangle \langle c_2 c_2^{\star}\rangle\right)^{1/2}}, \tag{3.10}$$

when c_1 and c_2 denote the two complex values at the pixels of the two images that form an interferogram. The asterisk denotes complex conjugation. The angle brackets denote statistical expectation approximated by averaging with a rectangular filter when the interferometric phase varies slowly. The absolute coherence value ranges from 0 (uncorrelated signals) to 1 (completely correlated). An alternative expression of total coherence in terms of its different correlation terms can be written as (Hanssen, 2001)

$$\gamma_{tot} = \gamma_{geom} \times \gamma_{DC} \times \gamma_{vol} \times \gamma_{thermal} \times \gamma_{temporal} \times \gamma_{processing}. \tag{3.11}$$

Doppler centroid decorrelation γ_{DC} is caused by a difference in Doppler centroid frequencies between the two acquisitions. This effect is minimal for the ERS SAR data acquired before February 2000. Therefore, SAR data used to form the interferograms for this study are less affected by Doppler centroid decorrelation. The volumetric decorrelation originates from the penetration of the radar wave into the scattering medium. The amount of decorrelation depends significantly on the radar wavelength and the scattering medium (Hoen and Zebker, 2000). Co-registration and interpolation may

[2]In the estimation of the complex coherence, a rectangular filter (several or tens of pixels in size) or estimation window is placed on SAR images. The complex coherence of the centered pixel of this estimation window is obtained by averaging the terms according to eq. 3.10 of all pixels within this window.

result in processing induced decorrelation. Nevertheless, the impact can be alleviated by applying well-designed filtering procedures. In the next subsections three error sources; thermal decorrelation, geometrical decorrelation and temporal decorrelation, will be briefly described.

Thermal decorrelation

Theoretically, the influence of thermal and quantization noise in the radar receiver contributing to the interferometric phase can be normalized by determining the signal-to-noise (SNR) ratio. SNR value is influenced by two classes of parameters: those determined by the design of the radar system and those determined by the scene i.e. the normalized radar cross section σ_0. This effect, however, is easily evaluated and removed (Zebker and Villasenor, 1992). Eq. 3.12 expresses the derivation of $\gamma_{thermal}$ using SNR.

$$\gamma_{thermal} = \frac{1}{1 + SNR^{-1}} \tag{3.12}$$

Geometric decorrelation

Geometric or spatial decorrelation is caused by a difference in incidence angles of the two antennas at the earth's surface (Gatelli et al., 1994). Spatial decorrelation increases linearly with the amount of spectral shift between two acquisitions. This can also be physically inferred from the spatial baseline[3] extent of the interferometric pair (Zebker and Villasenor, 1992; Hanssen, 2001). Spectral shift originates from a difference between the object spectrum (object in reality) and the data spectrum (SAR image). The projection from ground range to slant range causes a wavenumber shift; the wavenumber of the object spectrum have shifted to other frequencies in the data spectrum.

The spatial extent of the baseline is one of the principle performance drivers in a interferometric radar system. When the baseline is too short the sensitivity to the elevation changes will be undetectable, while if the baseline is too long, spatial baseline decorrelation will create additional noise and corrupt the detection of the signal.

The critical baseline $B_{\perp,crit}$ is the baseline that causes the spectral shift equal to one bandwidth[4] B_R resulting in totally uncorrelated signals (coherence equals zero). It is

[3]Spatial baseline can be simply referred as the separation of SAR antennas during the first and the second acquisitions.

[4]Transmitted radar pulse covers a small band of frequencies called bandwidth. The pulse bandwidth

a function of the wavelength λ , the incidence angle θ_{inc} and the topographic slope ζ as expressed in eq. 3.13.

$$B_{\perp,crit} = \lambda\,(B_R/c)\,R_1 tan\,(\theta_{inc} - \zeta)\,. \tag{3.13}$$

Calculating using ERS parameters[5], the critical baseline under flat terrain becomes approximately 1100 m. Hence we can define the geometric decorrelation as

$$\gamma_{geom} = \begin{cases} \frac{B_{\perp,crit} - B_\perp}{B_{\perp,crit}} & ,|B_\perp| \leq B_{\perp,crit} \\ 0 & ,|B_\perp| > B_{\perp,crit} \end{cases} . \tag{3.14}$$

For slow displacement detection such as subsidence, the interferometric effective baseline $B_\perp$ of the deformation interferogram requires to be small $|B_\perp|_{defo} \ll B_{\perp,crit}$ in order to reduce the InSAR sensitivity to topographic signals and to obtain sufficient coherency. In a DLR InSAR processing system, this decorrelation effect is normally corrected by applying a spectral shift filtering prior to the generation of an interferogram. A reduction in the resolution is a trade-off from this correction. In corrugated terrain, the spectral shift filtering is not optimal. Slope-adaptive filtering can be another option which requires estimation of the terrain slope in the implementation.

Temporal decorrelation

This effect is a result from the random physical change with time of the scatterers presented in a radar resolution cell. The physical change can be implied as the difference in the distribution of the scatterers, or in their electrical characteristics (related to water content in the scatterers), during the two acquisitions.

Temporal effect in the interferogram has been difficult to quantify or describe by an analytical model. Its occurrence can be related to unpredictable phenomena such as anthropogenic changes due to agricultural activities, construction works and loading or even some specific weather conditions. Decorrelation due to these events differs considerably as a function of time even for interferograms of a few-days. A previous study (Zebker and Villasenor, 1992), nevertheless, quantified temporal decorrelation as the residual from the total coherence after the justification of other correlation terms i.e. spatial baseline decorrelation and thermal decorrelation. By assuming that temporal decorrelation is only induced by random scatterer motion, they derived the

determines resolution in the range direction. The higher bandwidth corresponds to finer resolution. The range bandwidth for ERS is 15.55 MHz.

[5] $B_R = 15.55$MHz, $\lambda \sim 5.6$ cm, $R = 847$ km and $\theta_{inc} = 23°$(mid-incidence angles)

statistical variation due to this temporal effect on the produced topographic map that was generated from SEASAT data over a lightly vegetated area and forest with RMS 1.5 and 2.5 m respectively.

Temporal baseline, the time separation between the two radar observations, may be optimized to achieve the preferable condition of InSAR depending on the application. Successful displacement detectability therefore depends on the displacement rate and the amount of temporal decorrelation. As mentioned previously, the spatial orbital separation between the two observations requires to be small. The long temporal baseline is preferable. This provides a sufficiently detectable displacement signal (depends on the displacement rate) but is a trade off to the level of coherency due to temporal change of the targets. A six-month time separation has a potential for surface deformation measurements e.g. volcanic deformation, while a 1-day InSAR can be used for topographic mapping , coherence map, and glacier motion studies (Rosen et al., 1996).

Atmospheric disturbance and orbit inaccuracies

Atmospheric artifact and orbit error are examples of the low frequency phase noise affecting the interferograms. Although they do not influence in the estimation of coherence (see eq. 3.11), these artifacts can compromise the accuracy of InSAR phase measurements. Although atmospheric phase contribution in the interferograms can also be regarded as signal in atmospheric studies. For displacement monitoring, it is considered as disturbance and is one of the primary limitations for accurate InSAR measurements.

There are two types of atmospheric disturbances frequently observed in interferograms. First, the one originates from turbulent mixing process in the atmosphere. This process results in the three dimensional spatial variation of refractivity during both SAR acquisitions. The effect can be encountered in the flat as well as mountainous terrain. The second type is correlated to the topography and is a result of the difference in the vertical refractivity profiles during two SAR acquisitions (Hanssen, 2001). The latter type of disturbance affects only the mountainous area. Its effect is therefore insignificant in case of flat terrain such as Bangkok and will not be further discussed.

Propagation of the electromagnetic radiation in a three dimensional space for every moment in time is governed by the refractive index n of the medium. The phase velocity v of the radio wave can be defined as $v = \frac{c}{n}$; where c is the electromagnetic velocity in the vacuum. Propagation of a radar signal through the atmosphere which has slightly higher refractive index than the vacuum (the refractive index n of the vacuum = 1), therefore slow down its propagation velocity. This generates a time delay

which is measured by the radar systems. The one-way slant atmospheric path delay $S_k^{t_i}$ at acquisition time t_i for pixel k due to atmospheric refractivity N , $(N = (n-1)10^6)$, can be expressed as

$$S_k^{t_i} = 10^{-6} \int_0^H \frac{N}{cos\,\theta_{inc}} dh. \tag{3.15}$$

where H is height of the satellite above the scatterer. θ_{inc} is the incidence angle. The refractivity N depends on the atmospheric pressure, temperature, amount of water vapour, the electron number density and the liquid water content (Smith and Weintraub, 1953). Past studies indicated that the dominant atmospheric disturbances in the interferograms is caused by the water vapour distribution in the lower troposphere (Goldstein, 1995; Zebker et al., 1997; Hanssen, 1998; Hanssen et al., 1999). As atmospheric pressure and temperature usually slightly change over time, the resulting slant atmospheric delay strongly depends on changes in water vapour distribution between two SAR acquisitions. Hanssen (2001) has shown that despite the different atmospheric conditions encountered in the observed interferograms, the shape of the power spectrum of the atmospheric disturbances can be modeled by three different scaling regimes which are remarkably similar, as supported by Kolmogorov turbulence theory.

In the case of surface deformation, the true motion of the ground between observations can be falsely indicated in the interferogram by an amount equal to the difference of the excess propagation length $(S_k^{t_1} - S_k^{t_2})$ through the atmosphere on the two passes.

Solutions to reduce these undesired atmospheric artifacts in the repeat-pass interferogram have not yet been well-established. Support data from GPS campaigns and from distributed meteorological stations in the study area might assist in the understanding and modeling the atmospheric characteristics. Nonetheless, the spatial distribution of these measurements is usually not sufficient to correct spatially detail interferometric phase effectively (Zebker et al., 1997; Fruneau et al., 1999). Averaging multiple independent interferograms is one possible solution to reduce such artifacts as applied by (Zebker et al., 1997; Fruneau et al., 1999). If two images have the same noise level then statistically their average will have less noise by a factor of $\sqrt{2}$.

For orbit errors, inaccuracy in the estimated baseline can introduce small linear and possibly quadratic distortions of low spatial frequency to the interferometric phase (Zebker et al., 1994). Interferometric processing at DLR uses the precise orbit information. Therefore, this additional artifact could be expected to be minimal. For precise orbits determined from tracking data and gravity models, the accuracies in across-track and

vertical direction are about 8 cm and 5 cm respectively (Scharoo et al., 1998).

3.3 Model definition for repeat pass interferometry

Radar interferometry can be considered as a parameter estimation problem. It is an inverse problem by which the model parameter is estimated from the observable data i.e. the wrapped interferometric phase. Interferometric phase, the phase difference between two coregistered complex signals, forms the observation space. While the parameters of interest could be the topographic height, the LOS displacement rate or the slant atmospheric phase delay depending on the applications. The model definition presented in this section applies the geodetic adjustment theory to the interferometric case. It is also a background for the model definition for PSI used in chapter 4. In this definition, a generic Gauss-Markoff model is applied to describe the functional and the stochastic relations for two-pass interferometry. The advantage of describing the problem of parameter estimation in a systematic model are two folds; 1) different physical and geometrical aspects of the problem can be reduced to relatively simple mathematical equations, and 2) it provides a structural approach and a variety of standard techniques for adjustments, quality description and hypothesis testing. As a result, such a technique can provide a quantitative measure of accuracy for the estimated parameters (Hanssen, 2001).

Interferometric phase φ_k observations form a real random vector of observations $\varphi \in \mathbb{R}^m$, characterized by the first moment $E\{\varphi\}$ and the second moment $D\{\varphi\}$. The relation between the observations and the unknown parameters can be expressed as a Gauss-Markoff model (Koch, 1999; Hanssen, 2001):

$$\begin{array}{ccccccccccc} E\{\varphi\} & = & A & \mathtt{x}; & D\{\varphi\} & = & C_\varphi & = & \sigma^2 & Q_\varphi & (3.16) \\ m \times 1 & & m \times n & n \times 1 & m \times m & & m \times m & & 1 \times 1 & m \times m & \end{array}$$

where A is the design matrix, C_φ is the variance-covariance matrix, $Q_\varphi \in \mathbb{R}^{m \times m}$the real positive-definite $m \times m$ cofactor matrix, and $\sigma^2 \in \mathbb{R}^+$ matrix the a priori variance factor. The vector of parameters $\mathrm{x} \in \mathbb{R}^n$is assumed to be real and non-stochastic. The first part of 3.16 is defined as the *functional model* or model of observation equations describing the physical and geometrical relationship between observations and the un-

known parameters. Whereas the second part is referred to as the *stochastic model* describing the dispersion of the observations in terms of variance and covariances.

The functional model can also be written as

$$\varphi = A\mathbf{x} + \varepsilon \tag{3.17}$$

where $\varepsilon \in \mathbb{R}^m$ and represents error of φ with $E\{\varepsilon\} = 0$. Design matrix A should be full rank[6] ($m \geq n$) to make the model solvable. The following equations 3.18 and 3.19 express the relation to obtain the estimates of unknown parameters and its covariance matrix. The best linear unbiased estimator of the unknown parameters $\hat{x}$ and the covariance matrix $C_{\hat{x}}$is given by

$$\hat{x} = \left(A^T Q_\varphi^{-1} A\right)^{-1} A^T Q_\varphi^{-1} \varphi \tag{3.18}$$

$$C_{\hat{x}} = \sigma^2 \left(A^T Q_\varphi^{-1} A\right)^{-1} \tag{3.19}$$

3.3.1 Generic functional model

Considering a single interferogram with M_1 rows and M_2 columns, a vector of interferometric observations for this interferogram can be written as φ_k , with $k = i+(j-1)\,M_1$, where $i = 1, ..., M_1$ and $j = 1, ..., M_2$ respectively. Despite of many parameters influence the interferometric phase, about five parameters are dominant (Hanssen, 2001). For every observation (pixel) k these parameters are:

- Topographic height H_k[m],
- Displacement in LOS direction D_k[m],
- Atmospheric path delay in slant direction during the first acquisition $S_k^{t_1}$[m],
- Atmospheric path delay in slant direction during the second acquisition $S_k^{t_2}$[m],
- and Integer ambiguity number $\omega_k \in \mathbb{Z}$.

When related to the above Gauss-Markoff model in eq. 3.16 , a generic linearized functional model for an interferogram and its related parameters can be expressed as (Hanssen, 2001)

[6]The problem is under determined when m < n.

$$E\begin{bmatrix}\varphi_1^w\\ \varphi_2^w\\ \vdots\\ \varphi_m^w\end{bmatrix} = \begin{bmatrix}A_1 & & & \\ & A_2 & & \\ & & \ddots & \\ & & & A_m\end{bmatrix} \begin{bmatrix}\mathtt{x}_1\\ \mathtt{x}_2\\ \vdots\\ \mathtt{x}_m\end{bmatrix} \tag{3.20}$$

where φ_1^w refer to as the wrapped phase observation. A_k is a part of the design matrix corresponding to observation k. It can be defined as follows:

$$A_k = \left[-\frac{4\pi}{\lambda}\frac{B_{\perp,k}}{R_k \sin\theta_k}, \frac{4\pi}{\lambda}, \frac{4\pi}{\lambda}, -\frac{4\pi}{\lambda}, -2\pi\right]. \tag{3.21}$$

$B_{\perp,k} = B\cos(\theta_k - \alpha_k)$ and is the perpendicular baseline at pixel k (see fig. 3.1). The corresponding parameter vector x_k for observation k is defined as

$$x_k = \left[H_k, D_k, S_k^{t_1}, S_k^{t_2}, \omega_k\right].^T \tag{3.22}$$

Note that in this case, the first four parameters of vector $x_k \in \mathbb{R}$ and $\omega_k \in \mathbb{Z}$. It is shown in eq. 3.22 that at least five unknown parameters are related with each observation k. This leads to the under determined problem. The following possibilities are addressed and commonly applied conjointly in order to effectively solve this problem: 1) more observations could be added into the model; this implies more interferograms should be used. 2) a priori information could be introduced e.g. using external DEM for deformation study, and 3) the model could be reformulated; relates to conceptual change of the model. Example cases are the use of three-pass, four-pass interferometry and interferogram stack for displacement detection.

3.3.2 Displacement mapping

For detection of line of sight displacement by mean of classical DInSAR the two-pass method in conjunction with the external digital elevation model acquired from SRTM mission was used. In this case, H_k in eq. 3.22 is known. The known topographic height was converted into phase information, projected in slant range direction and subtracted from the deformation interferograms. When there are no significant variabilities of the relative atmospheric conditions during the two observations $E\{S_k^{t_1}\} = E\{S_k^{t_2}\} = 0$, after phase unwrapping, the resulting phase in the differential interferogram is merely corresponded to displacement of the scatterer centers in the LOS direction D_k or $\triangle R_{diff}$.

Eq. 3.23 reveals the relation between LOS displacement $\triangle R_{diff}$ and displacement phase ϕ_{disp} in the differential interferogram (refer also to fig. 3.1 and eq. 3.9).

$$\triangle R_{diff} = \frac{\lambda}{4\pi}\phi_{disp} \tag{3.23}$$

3.4 Implementation and results

SAR data listed in table 3.1 and 3.2 were employed to investigate the effect of spatial baseline decorrelation and temporal decorrelation on coherence and thus on the detectability of the displacement signal by means of DInSAR. A common master orbit was selected for each data stack (5111 for the right stack and 13900 for the left stack[7]) and 36 interferograms were processed. The classical interferometric processing procedures were applied including coarse and fine co-registration between two complex images, complex multiplication of the coregistered signals to obtain an interferogram as expressed in eq. 3.5. Subsequently the external DEM from the SRTM-X data was used to synthesize the topographic phase. These synthetic topographic phases are then subtracted from the interferograms. As a result, the differential interferograms containing the possible displacement signals were obtained (see eq. 3.8).

Geometric and temporal decorrelation

A test area for this investigation was selected covering the southern part of Bangkok and some parts of Samut Prakarn. Fig. 3.2 shows a radar image of the test area representing in amplitude of the radar backscatter. The test area is characterized by a suburban environment, the settlements (houses and man-made features) are clustered near to the main roads and mixed with agriculture fields (the east side of the image). The bright areas or points in the amplitude image correspond to high radar reflectance features such as buildings, dense blocks of houses or man-made features. While the agriculture fields reflect low backscatter and thus appear dark in the image. The main river in central part of Thailand, the Chao Phraya river passes through the area from the northwest to southeast direction (highlighted in blue).

Fig 3.3 visualizes the derived DIFGMs together with their corresponding ensemble coherence images (under the DIFGM itself). The absolute coherence values (black to white: 0 to 1) can be used as quality indicators for DIFGMs to demonstrate the level

[7]The left and the right stacks refer to the time-series of SAR data acquired from the satellite tracks covering the west(left) and the east (right) sides of Bangkok (see also fig. 4.2).

Table 3.1: SAR data acquisitions (Track 247 Frame 3328: Right stack) ordered by date , Master acquisition 12-APR-1996

Orbit	Acq. Date	Baseline (m)	Time Baseline (days)	Satellite
11414	21-SEP-1993	254.59	-934	E1
11915	26-OCT-1993	190.99	-899	E2
12416	30-NOV-1993	87.23	-864	E1
4109	02-FEB-1996	72.11	-70	E2
24283	07-MAR-1996	61.13	-36	E1
4610	08-MAR-1996	-46.95	-35	E2
24784	11-APR-1996	99.75	-1	E1
5111	12-APR-1996	0	0	E2
25285	16-MAY-1996	17.88	34	E1
5612	17-MAY-1996	-119.84	35	E2
7115	30-AUG-1996	-864.78	140	E2
8117	08-NOV-1996	812.07	210	E2
43822	02-DEC-1999	-748.17	1329	E1
24149	03-DEC-1999	-964.23	1330	E2
24650	07-JAN-2000	-72.19	1365	E2
29660	22-DEC-2000	-310.53	1715	E2

E1 refers to SAR data acquired from ERS-1 satellite
E2 refers to SAR data acquired from ERS-2 satellite

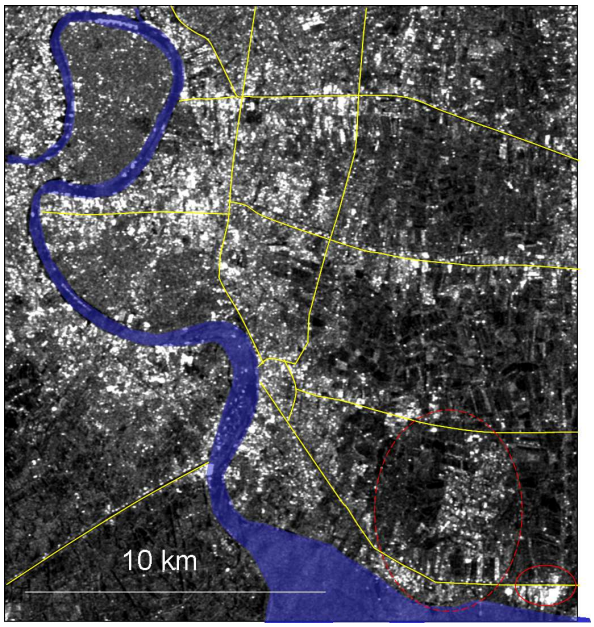

Figure 3.2: Radar image of the test area presented in amplitude of the backscattered signals. The yellow lines indicate main roads. Red ellipses present areas corresponding to where the possible subsidence in fig. 3.3 and 3.4 were found.

Table 3.2: SAR data acquisitions (Track 018 Frame 3327: Left stack) ordered by date, Master acquisition 17-DEC-1997

Orbit	Acq. Date	Baseline (m)	Time- Baseline (days)	Satellite
22050	03-OCT-1995	473.55	-806	E1
24054	20-FEB-1996	805.01	-666	E1
4381	21-FEB-1996	768.49	-665	E2
24555	26-MAR-1996	-806.43	-631	E1
4882	27-MAR-1996	-900.33	-630	E2
25056	30-APR-1996	1021.54	-596	E1
5383	01-MAY-1996	909.77	-595	E2
5884	05-JUN-1996	-980.19	-560	E2
6385	10-JUL-1996	311.74	-525	E2
6886	14-AUG-1996	-483.44	-490	E2
7387	18-SEP-1996	-6.17	-455	E2
7888	23-OCT-1996	744.59	-420	E2
10894	21-MAY-1997	59.24	-210	E2
13399	12-NOV-1997	-454.36	-35	E2
13900	17-DEC-1997	0	0	E2
14401	21-JAN-1998	-563.06	35	E2
15403	01-APR-1998	-352.51	105	E2
16405	10-JUN-1998	610.42	175	E2
44094	21-DEC-1999	-279.72	734	E1
24421	22-DEC-1999	-80.63	735	E2
24922	26-JAN-2000	-97.51	770	E2

Table 3.3: summarizes spatial and temporal baseline information of the interferometric SAR data presented in fig. 3.3 and their corresponding ensemble coherence based on the master acquisition 17-Dec-97.

IFGM	Baseline(m)	Time baseline	Slave data	Ensemble coherence
a	352	3.5 M	1-Apr-98	0.26
b	59	7 M	21-May-97	0.33
c	6	1.2 Yrs	18-Sep-96	0.32
d	280	2.0 Yrs	21-Dec-99	0.20

of signal decorrelation. As the geometric induced decorrelation has been corrected, its effect is much less compared to the temporal decorrelation. It can be observed that coherence can be maintained only in the settlement areas due to coherent scattering characteristics of man-made features. It is here where surface change can be detected (see as fringe: 1 color cycle corresponds to 2π radians in IFGM). The rest of the area e.g. vegetated areas in a DIFGMs are relatively noisy primarily due to the physical changes at the radar wavelength scale of the radar scatterers during two radar acquisitions. These changes in scattering characteristics can be due to seasonal difference between slave and the master images, planting and anthropogenic activities which can deteriorate the ensemble coherence. Thus increasing of time separation between two observations can reduce the correlation between two radar signals resulting in lowering of coherence and increasing difficulty in the detection of the displacement signal. Apart from temporal decorrelation effect, the noisy DIFGMs presented in fig. 3.3 can be subjected to possible atmospheric disturbance as well as noise, provided that precise orbit information was used (see eq. 3.8).

Detectability of the small displacement does not only rely on noise level due to temporal decorrelation but also the displacement signal itself. For example, the subsiding of 28 mm (half of the C-band radar wavelength) for 1-year IFGM would generate one displacement fringe and probably detectable in the IFGM provided that temporal and atmospheric effects are not more dominant.

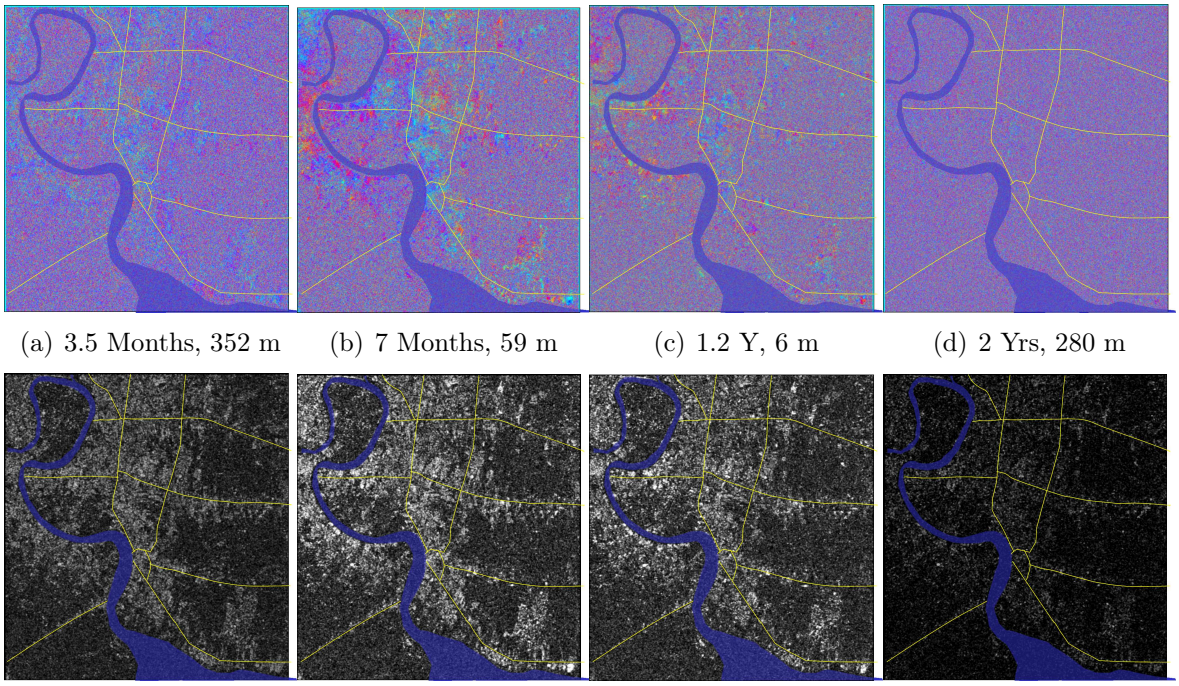

(a) 3.5 Months, 352 m (b) 7 Months, 59 m (c) 1.2 Y, 6 m (d) 2 Yrs, 280 m

Figure 3.3: Differential interferograms ordered by temporal baseline show primarily the effect of temporal decorrelation coupling with their coherence images underneath (see also table 3.3). The settlement areas are less affected by temporal decorrelation (bright dots in the coherence images), therefore in principle possible deformation could be detected. Deterioration of coherence was encountered in the other areas covered by vegetation fields and water bodies. As time baseline increases, temporal decorrelation is likely to increase. Captions of sub-figures a to d indicate time separation and the baseline extent in meter of the interferometric data respectively.

Possible deformation interferograms

Interferograms with short spatial baseline extent and long time separation are likely to be preferable for slow motion detection. Several interferograms from both data stacks with these configurations are presented in fig. 3.4 and 3.5.

Based on these interferograms, it was found that IFGMS with long temporal baseline can detect phase changes or fringes (areas indicated by red ellipse) only when baseline extent is relatively short (see IFGMs in fig. 3.4 (a) and (d)). The upper limit of temporal baseline for subsidence detection in this area could probably be about 2 years realizing from the undetectability transition from fig. 3.4 (d) to fig. 3.5 (a). However, a sufficiently fast subsiding location (small red ellipse) at bottom-right was able to be detected in all IFGMs. Although it can be argued that man-made features in urban areas could usually maintain their coherency for long period of time (Usai and F.Hanssen, 1997; Usai and Klee, 1999). The study area characterized by settlements

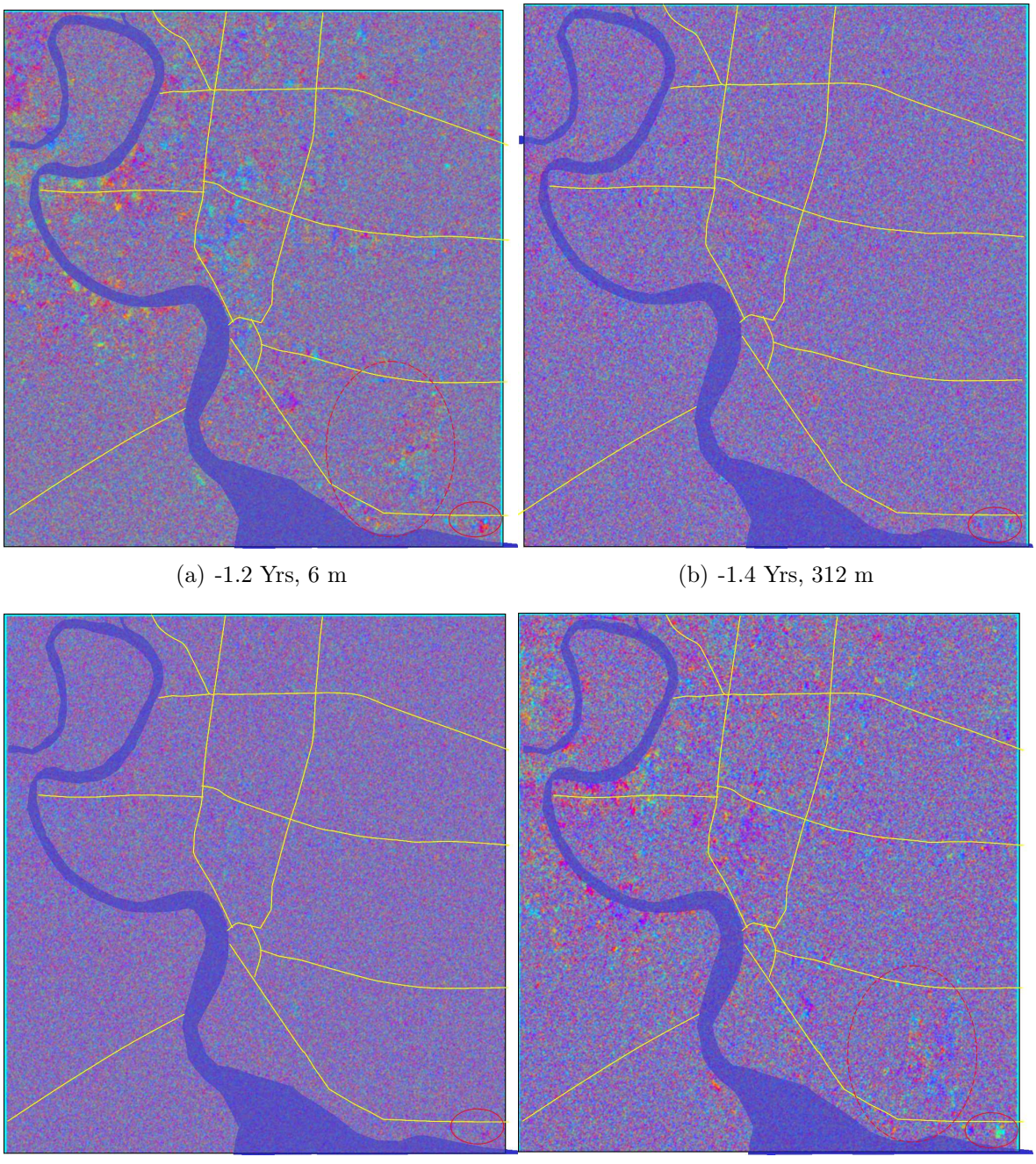

(a) -1.2 Yrs, 6 m

(b) -1.4 Yrs, 312 m

(c) 2 Yrs, 280 m

(d) 2.1 Yrs, 97 m

Figure 3.4: Possible deformation interferograms with short spatial baseline and long temporal baseline of the left data stack (ordered by temporal baseline).

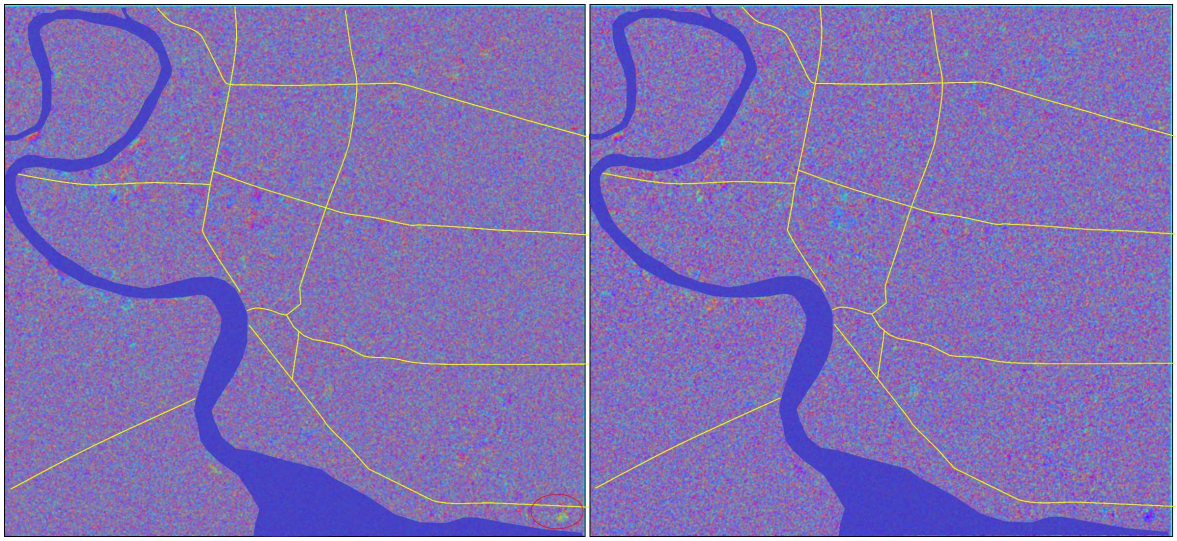

(a) - 2.4 Yrs, 87 m

(b) -2.5 Yrs, 191 m

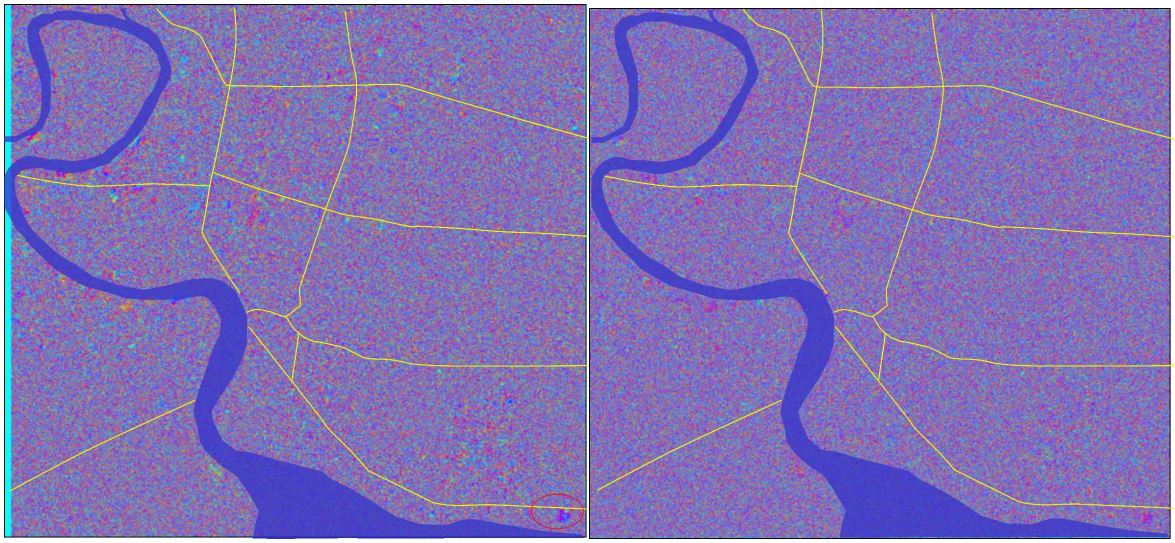

(c) 3.7 Yrs, 72 m

(d) 4.6 Yrs, 168 m

Figure 3.5: Possible deformation interferograms with short spatial baseline and long temporal baseline of the right data stack (ordered by temporal baseline) cover the same area as in fig. 3.4.

alternating with the vegetation fields could nevertheless deteriorate the ensemble coherence decreasing the signal's detectability. Although the deformation interferograms are able to provide displacement information where coherence has been preserved e.g. settlement area, the other areas in the interferograms are still noisy. This could effectively prevents the classical phase unwrapping procedure from achieving satisfied results.

Atmospheric artifacts in interferograms

The significant difference in the atmospheric path delays between both SAR acquisitions used to generate an interferogram could prevent DInSAR from accurate small displacement mapping. Strong atmospheric artifacts on the two tandem interferograms of Bangkok are presented to show strong atmospheric influence in the study area (fig. 3.6). As it is not possible to effectively separate these atmospheric artifacts from the useful displacement signal without knowledge of the atmospheric parameters at the SAR acquisition time. Such support data are either not available for Bangkok or it has insufficient resolution to correct atmospheric effects on the interferograms. These atmospheric disturbance is one of the primary limitation in accomplishing high accurate displacement mapping that is primarily required to the study of subsidence.

3.5 Summary

The results demonstrate principle limitations; the temporal decorrelation and atmospheric artifacts primarily encountered in the study area that prevent successful detection of subsidence by means of DInSAR. Physical changes of the scatterers due to seasonal changes, plantation and anthropogenic activities are important examples generating these temporal effects. As the long temporal baseline is usually preferable for the study of long-term displacement phenomenon like subsidence, the resulting high temporal effect is respectively inevitable in long-term deformation interferograms. From the 36 processed interferograms, it is relatively difficult to obtain interferograms that are optimal for subsidence detection. Most of the obtained differential interferograms are noisy and fringes are not clearly visible. Note that, it is possible to combine SAR images based on different master scenes. This could possibly results in the better deformation interferograms. Averaging several independent interferograms can reduce noise in interferograms. However, in this study I do not aim to further these examinations. In chapter 4, I present a systematic investigation to use interferogram stacks of the

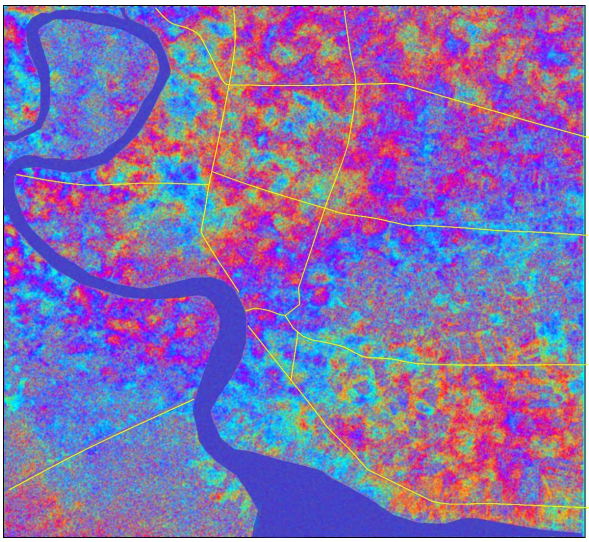

(a) Tandem pair of 11and 12-Apr-96

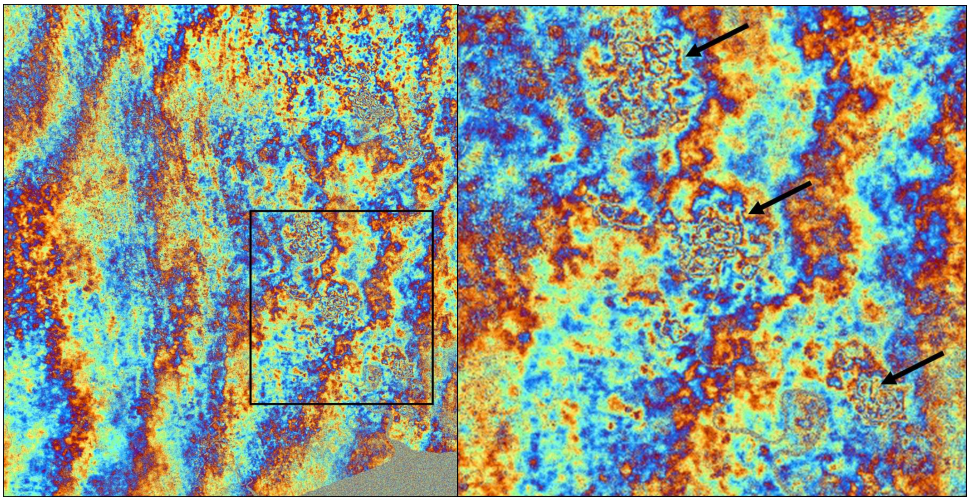

(b) Tandem pair of 26 and 27-Mar-96 (c) Zoom in of the area in black rectangle in (b) showing atmospheric generated phase

Figure 3.6: Significant atmospheric artifacts in the tandem interferograms of Bangkok

same data sets to derive subsidence information of the same area by means of PSI.

One possible solution to obtain more coherency from the signal is to use the longer wavelength radar e.g. L-band (24 cm) e.g. from the Japanese Earth Resource Satellite (JERS-1) mission. The longer wavelength reduces the signal's sensitivity to temporal backscatter changes. In the vegetated areas for example correlation of L-band signals has been proved to be far superior than of C-band. But the more inclined look angle (35°) compared to ERS system also reduces its sensitivity to deformation or subsidence. The lower sensitivity to noise of the L-band system nonetheless increase the possibility especially in the tropical environments to form the preferable interferograms.

Chapter 4

Derivation of subsidence estimates by means of persistent scatterer analysis

4.1 Introduction

In the last chapter, we have experienced some limitation of exploiting the conventional DInSAR technique for subsidence detection in Bangkok. This chapter focuses on the application of the phase time series of radar's point scatterers to derive the parameter of interest, the LOS subsidence rate, by means of persistent scatterer analysis. Most of the previous PS studies (table 1.1) used a large number of images (more than 30) to achieve the optimal accuracy at sub-millimeter level. Due to SAR data availability acquired over Bangkok, a PS analysis based on a much more limited number of scenes (20 and less) will be carried out. Moreover, high subsidence rates and strong atmospheric influence in the study area are additional challenging conditions. The goal is to answer two questions: *" How feasible is it to apply PS analysis under these challenging conditions? "* and if it is feasible *" How accurate are the resulting displacement estimates? ".* To assess the estimate's reliability independent leveling measurements from 12 benchmarks were used as the reference.

Due to interferograms limitations, two independent interferometric data stacks consisting of 15 and 19 interferograms from adjacent tracks[1] covering the same area of interest were analysed to enable cross-validation of both estimates. Nevertheless, results have proved that estimates from the smaller interferograms stack were insufficiently robust

[1]The satellite's paths on the ground (see fig. 4.2a).

to serve this purpose. The scientific PSI system (Adam et al., 2003; Kampes and Hanssen, 2004; Kampes and Adam, 2004) developed at DLR[2] was used to conduct all PS analysis in this study.

As it will be shown in the end, in spite of the limited number of interferograms used in the analysis, it is possible to derive reliable displacement estimates with an accuracy better than ±1.5 mm/y, where the linear displacement model is valid. Though subsidence detection over tropical Bangkok has been hardly achieved with the conventional DInSAR in the past, the forthcoming sections reveal that derivation of subsidence estimates by mean of persistent scatterer analysis over the same area become possible.

4.2 Persistent Scatterer Interferometry (PSI)

Geometric and temporal decorrelations are the key limitation that prevent the conventional differential interferometry technique from being used for successful small displacement detection. Additionally, atmospheric inhomogeneities during two SAR acquisitions contaminate interferometric signals leading to their misinterpretation as displacement. A relatively new InSAR technique called ' Permanent Scatterer Technique ' invented at POLIMI (Ferretti et al., 2000c, 2001) benefits from temporal phase information of the permanent scatterers to suppress these difficulties and is capable in principle of deriving displacement information at millimeter accuracy. Permanent scatterer (PS) can be defined as radar targets whose phases are consistent over long time. Examples of PSs in the reality are man-made features i.e. buildings, houses. An example of PSs found in the test area is shown in Appendix B. Due to their physical properties and orientation, PSs interact strongly with radar signals providing strong echoes back to the radar receiver. As their physical dimensions are smaller than a radar resolution cell, they are only slightly impacted by geometric decorrelation. Also, PSs are stable radar scatterers and their scattering characteristics usually do not change over time limiting temporal decorrelation. In addition, the atmospheric phase contribution can be estimated and removed from the signal of concern. Generally, only the radar point targets with high signal to noise ratio (SNR) can be exploited in the persistent scatterer analysis.

The principle of PSI relies on the multi-interferograms approach where a large number of SAR images acquired at different times over the same area are required. Also, a priori assumption of displacement behavior in the area is prerequisite i.e. in this study, the constant velocity model. The selected model should describe the actual behaviour

[2]Deutsches Zentrum für Luft und Raumfahrt e.V. - German Aerospace Center

reasonably well but small deviations from the model are acceptable. Assuming we have $N + 1$ SAR images, a series of N interferograms can be formed based on a common master scene. Based on the phase history of each PS, the spatial-temporal analysis is carried out and the relative LOS motion as well as DEM error on these subset of pixels can be both estimated.

Implementation steps of PSI can be generalized as follows:

1. Interferograms and differential interferograms[3] formation
2. PS identification
3. Preliminary estimate of parameters of interest e.g. LOS displacement, elevation (DEM) error and/or atmospheric phase contribution
4. Refinement of the estimate e.g. APS[4] removal applying suitable filter operations
5. Final estimate of the same set of parameters

The order of implementation might not be similar depending on the applied approach. Selection of PS should ensure that the good quality PS (affected by limited decorrelation noise, high SNR) can be identified. Because phase noise at the PS pixel is directly proportional to the standard deviation of the estimated parameters. To date, different approaches have been applied for PS selection namely coherence stability thresholding (Mora et al., 2002a), statistical analysis of calibrated amplitude more specifically, the dispersion index (Ferretti et al., 2000b, 2001), the radar cross section value thresholding (Kampes and Adam, 2003; Worawattanamateekul et al., 2003) and the signal-to-clutter (SCR) ratio (Adam et al., 2004).

Sufficient spatial density of PS in the area ($5 - 10\, PS/km^2$) (Colensanti et al., 2003a) and a sufficient number of available images guarantee a correct estimate and removal of atmospheric phase contribution. Ferretti mentioned in (Ferretti et al., 2000b) that about $100\, PS/km^2$ could be identified in urban areas of Milan, Paris and Los Angeles and could be exploited for terrain deformation monitoring with millimeter accuracy. In rural areas, Kircher et al. (2003) and Walter et al. (2004) demonstrate the applicability of PS technique for mining induced subsidence monitoring.

[3]Interferogram is a phase difference image in which every pixels is formed by multiplication of two complex signals. Differential interferogram results from a subtraction between two interferograms (topographic and deformation interferograms) to obtain surface change (displacement) information.

[4]Atmospheric Phase Screen (APS) is the phase delay generated due to the propagation of radar signal through the atmosphere. It is treated as disturbance for displacement study.

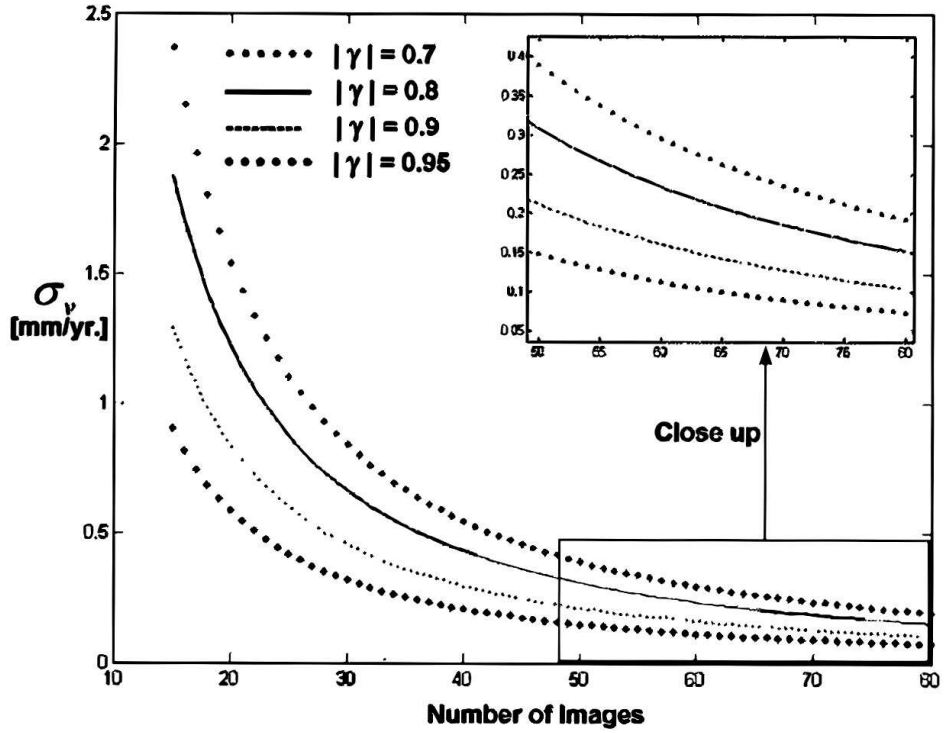

Figure 4.1: Precision of estimated mean velocity as a function of number of images (after Colensanti et al. (2003b))

With regard to the number of images required for a reliable PS analysis, past studies have cited the minimum number should be around 25-30 scenes (Ferretti et al., 2000b,c; Colensanti et al., 2002, 2003a). Fig. 4.1 reveals a an ideal relationship between precision of the estimated mean velocity as a function of number of images (regular temporal sampling of 35 days is assumed) at different coherence levels. It can be observed that the higher the number of images we analyze, the better the precision of the estimate we can obtain.

The algorithm to obtain the parameters of interest by PS analysis to date can be categorized into two main ideas, namely; the coherence-based approach (POLIMI) and the least-squares based approach (Kampes et al., 2001; Mora et al., 2002a; Kampes and Adam, 2003; Kampes and Hanssen, 2004; Kampes and Adam, 2004). From an applications point of view, a variety of applications have been studied and researched using PS technique. Table 1.1 lists examples of case studies of those dedicated to ground displacement monitoring either induced by natural or anthropogenic activities. An interesting, alternative approach requiring a small number of images working at a reduced resolution have also been researched (Lundgren et al., 2001; Usai, 2001; Berardino et al., 2002; Mora et al., 2002b). The principle of this approach benefits also from the consistent phase of the point scatterers but only small baseline interferograms

(more than one master image) are of interest. The use of small baseline interferograms ensure that possible spatial decorrelation noise is minimised. Other potential applications of PSI have also been demonstrated, for example the monitoring of landslides and tectonic motion (Colensanti et al., 2003b; Rocca et al., 2004; Colensanti et al., 2004; Strozzi et al., 2004) and identification of an individual building collapse (Ferretti et al., 2000a).

4.3 SAR Data and Area of Interest

Two adjacent tracks of synthetic aperture radar (SAR) data from ERS-1/2 missions were acquired for PS analysis. The number of image scenes acquired were 20 and 16 for the left (Track 018) and the right stacks (Track 247) respectively. The main ideas behind obtaining two adjacent scenes of SAR data are 1) accidentally no single frame that covers Bangkok area fully 2) to guarantee that there are as many scenes as possible available for the analysis, and 3) to investigate the possibility in integration of estimates from two different stacks. Therefore, the area located in the scene-overlapping (cyan rectangle) as shown in fig. 4.2(b) was selected as test area to serve this purpose.

Fig. 4.2(a) illustrates the ERS-1/2 coverage over Bangkok and its adjacent cities. A series of images from these two tracks (black frames) were obtained. Fig. 4.2(b) visualises the amplitude images from those tracks. Downtown Bangkok is easily distinguished due to its strong radar backscatter (bright) in the left amplitude image. The same SAR data sets were used for chapter 3 and chapter 4. Please refer to SAR data lists in table 3.1 and 3.2.

For the integer least-squares (ILS) estimation (see subsection 4.5.2), the smaller area of 8x12 km as indicated in fig. 4.3 was selected. As I focus on the feasibility study of the technique, it is better to start with a less problematic area where enough PS density can be expected.

4.4 Preliminary processing

This section presents a general InSAR processing procedure starting from importing a series of single look complex[5] (SLC) data to the selection of PS to obtain an initial set of so called potential persistent scatterers. Detailed procedures are explained in each forthcoming subsections 4.4.1 to 4.4.2. Fig. 4.4 illustrates the general processing flow

[5]A standard radar image used specially for interferometry application

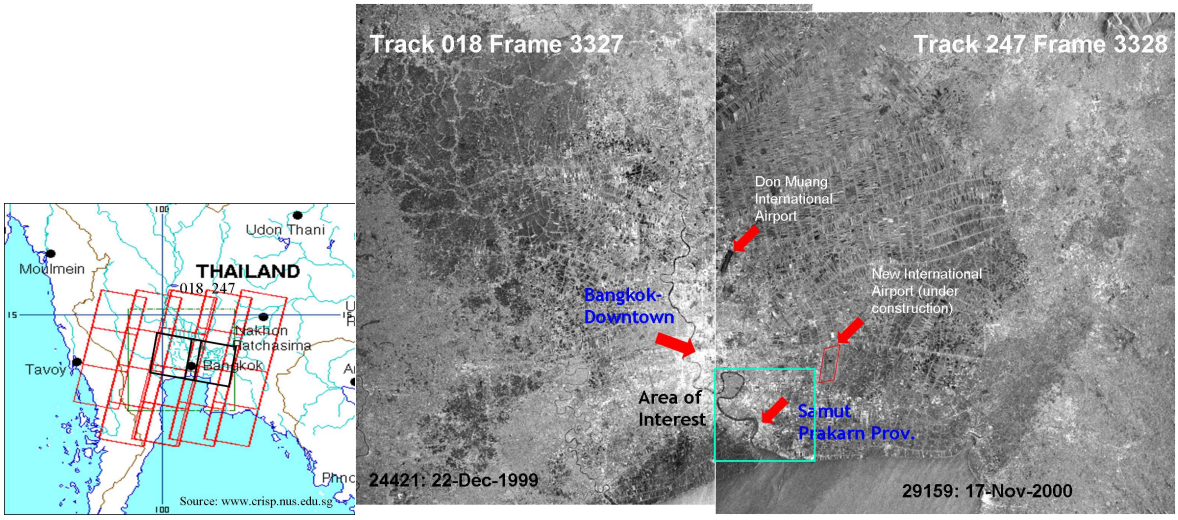

(a) (b)

Figure 4.2: a) ERS-1/2 coverage over Bangkok and its vicinity. Two adjacent tracks (the left and the right tracks represented by black frames) were acquired for this study. b) The corresponding amplitude images depict AOI (cyan rectangle) - situated in the overlapping area of these two scenes- and other important locations.

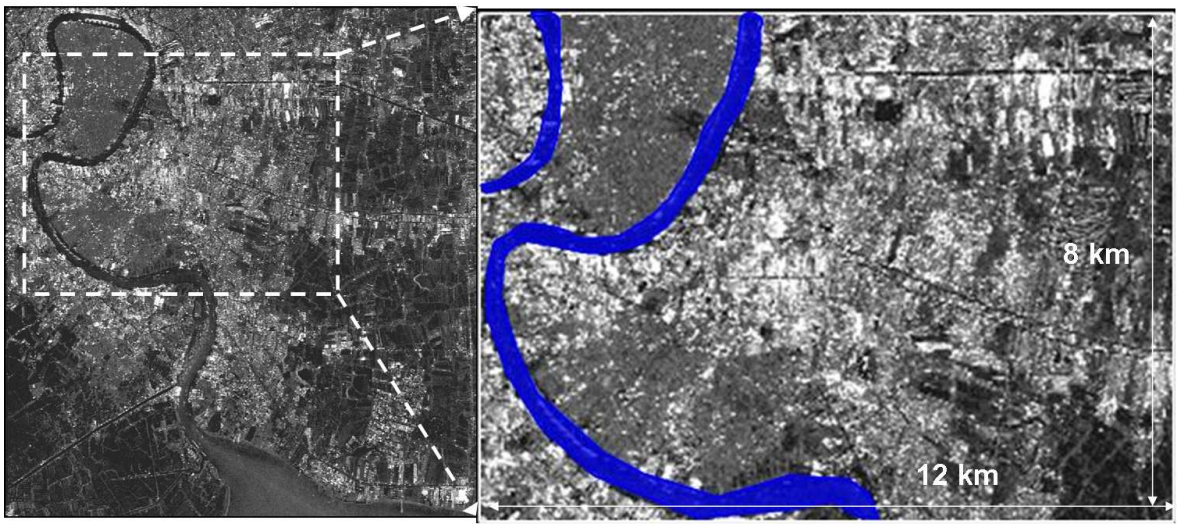

Figure 4.3: The Area Of Interest (AOI) for PS analysis

to obtain two main outputs prior to entering the ILS estimation, series of *differential interferograms* and the *persistent scatterer* map. The upper part starts with importing $N + 1$ SLC images into the InSAR processing system. After a master scene was carefully selected, all interferometric data were then oversampled twice, coregistered and resampled into the same master grid. Complex conjugate multiplication of the master and slave signals yields a product called ' an interferogram '. An independent SRTM-X generated DEM is used to remove the topographic phase contribution from interferograms resulting in N *differential interferograms*. The lower part of the flow chart shows that calibrated intensity image time series are utilized as the initial input. PSs can then be selected by thresholding one of these values, i.e. Radar Cross Section (RCS) , Signal to Clutter Ratio (SCR) or Dispersion index (D_A). In fig. 4.4, the RCS threshold is shown. Finally, a *persistent scatterer map* that contains good candidates of PS having a RCS higher than the set threshold with their corresponding coordinates is obtained. Since original phase information is required for PS analysis and has to be preserved, any filtering operations should not be applied to the interferograms.

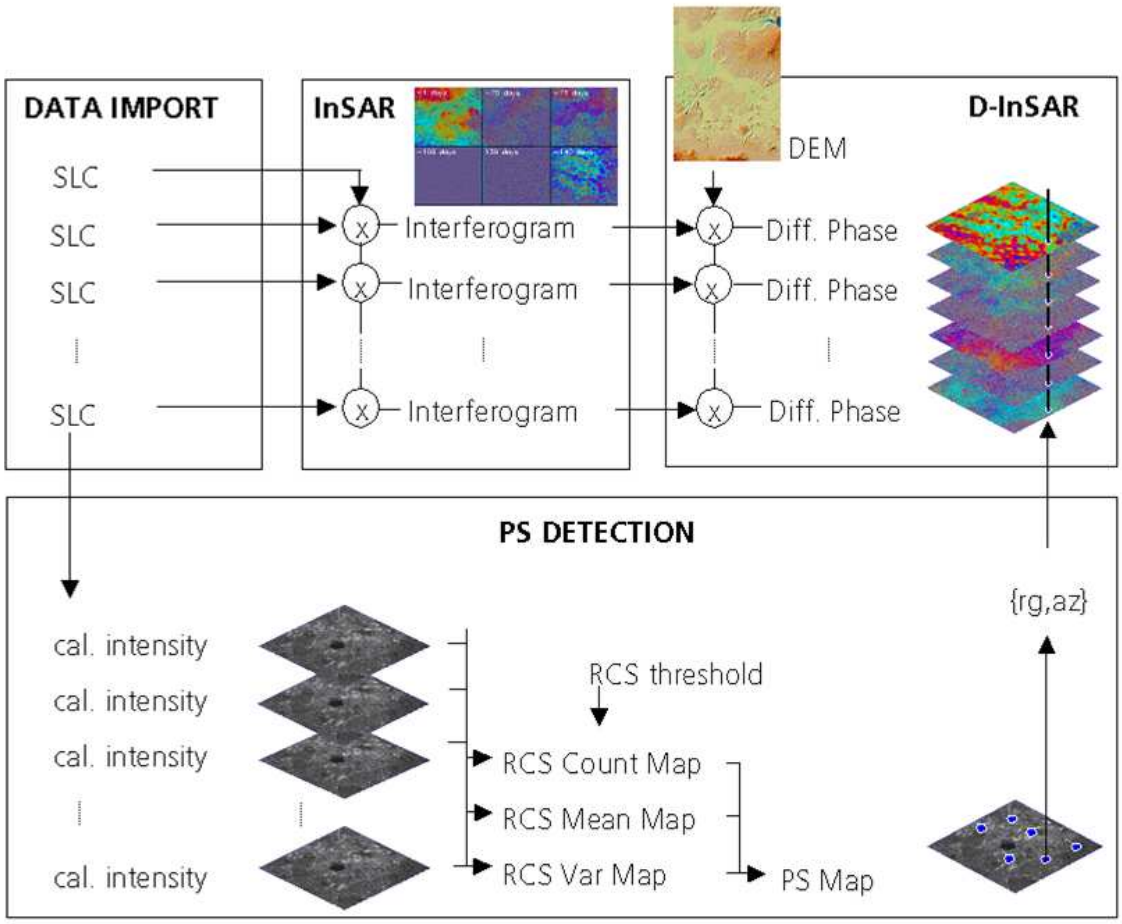

Figure 4.4: Processing flow to obtain possible PS (after Kampes and Adam (2003))

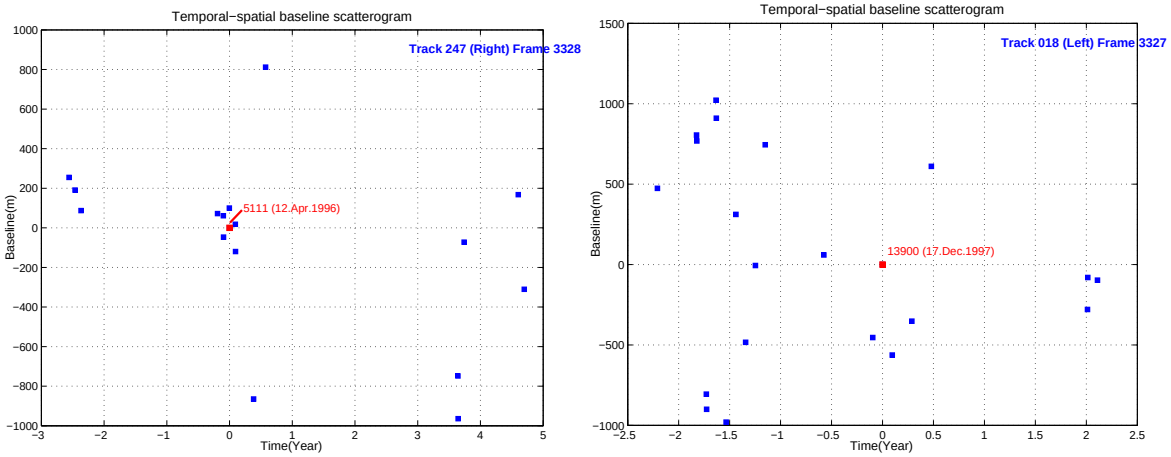

(a) Master orbit - 5111 (16 acquisitions) (b) Master orbit - 13900 (20 acquisitions)

Figure 4.5: shows temporal - spatial baseline scatterograms of 2 data stacks. The selected master orbit is indicated with a red square.

4.4.1 Differential interferogram generation

Master scene selection

In PS analysis, a series of SAR images should be coregistered and sampled into a regular grid based on a common master scene. A good master scene would lie in the middle position of the temporal- spatial baseline scatter plot (see fig. 4.5). This is to ensure that the dispersion of the time-spatial baseline of the data set is as low as possible.

The previously shown table 3.1 and 3.2 and fig. 4.5 provide the time and spatial baselines information of ERS-SAR data. For the left stack, data during 1995-2000 was acquired spanning a time of about 4 years with normal baseline range $\pm\,1000\,m$. For the right stack with a smaller data set, data during 1993-2000 was acquired with a time span of 7 years and a baseline range of about $\pm\,900\,m$. All baseline information is presented relative to the master scene (17.Dec.1997 for left stack and 12.Apr.1996 for the right stack) and shown in red in fig. 4.5. Note that the temporal data sampling of these two data sets is unfortunately not uniform and the normal baseline distribution is high. These data sets are not optimum for this investigation.

Phases in differential interferogram

The main goal of the PS technique is to separate different phase terms contributing to an interferometric phase utilizing phase information from a set of coherent radar targets (persistent scatterers) on an interferogram stack. After a series of interfero-

grams (IFGMs) were formed, an external DEM from the SRTM-X mission was used to remove the topographic phase contribution to obtain a set of differential interferograms (DIFGMs). In general, the relative vertical accuracy of the SRTM-X derived height information is about ± 6 m (Marschalk et al., 2004). In a flat area such as Bangkok the accuracy can be better.

Interferometric phase in a DIFGM ϕ_P at point P is composed of different phase terms namely from LOS displacement ϕ_{disp} , from uncompensated DEM error $\phi_{demerror}$, from difference of atmospheric phases between 2 acquisitions ϕ_{atm}, from orbit error ϕ_{orbit} and from decorrelation noise ϕ_{noise} (as expressed in eq. 3.8).

$$\phi_P = \phi_{demerror} + \phi_{disp} + \phi_{atm} + \phi_{orbit} + \phi_{noise}.$$

The displacement phase can be extended and written as

$$\phi_{disp} = \frac{4\pi}{\lambda} d_{LOS}. \tag{4.1}$$

For simpler understanding, $\triangle R_{diff}$ in eq. 3.9 is represented here as d_{LOS} and denotes as displacement in the line-of-sight direction. In PS analysis, the displacement rate, DEM error and the atmospheric phase contribution parameters can be estimated. The phase due to orbital indetermination can be minimised using precise orbit information. In addition, at the selected PS, its phase is expected to be slightly affected by decorrelation noise.

4.4.2 PS detection

Detection approaches

Three PS detection approaches are readily available in the DLR PSI system. These are the RCS, the SCR and the dispersion index (D_A) thresholding. Each method aims to identify pixels with high phase stability, an indicator for point scattering behavior. All methods require that the SAR images be calibrated prior to thresholding.

The *normalized radar cross section* σ^0 or radar backscattering coefficient describes mean reflectivity of an area of one square meter on the surface of the earth (Ulaby et al., 1982). It is commonly expressed in decibels. A pixel will be selected as a possible PS if its normalized radar cross section σ^0 i.e. its calibrated intensity follows

$$\sum_{k=0}^{K} a_k \geq N_1, \quad \text{with } a_k = \begin{cases} 1, & \text{if } \sigma_k^0 > N_2 \\ 0, & \text{otherwise} \end{cases} \tag{4.2}$$

where K denotes the total number of available images and $k = 1, 2, ..., K$. The two thresholds N_1 and N_2 have to be set. The typical value of $N_2 = -2\,dB$ ensures that all possible PSs in the interferograms can be detected (see Kampes (2005)). Here, the thresholds of $N_1 = 0.65K$ and $N_2 = 5\,dB$ were used. Assuming 10 SAR images are available, a pixel will be considered as a possible PS when 6.5 images or more have a σ^0 value higher than 5 dB. The higher threshold of $5\,dB$ was used to ensure that the selected PSs more likely behave as point scatterer and possess more phase stability.

Dispersion of phase (phase standard deviation) of a radar scatterer indicates its phase stability and therefore can be employed as a threshold in detecting possible PS. The concept of the *dispersion index* has been introduced in (Ferretti et al., 2000b, 2001) as a measure of phase dispersion based on the principle that at high SCR, the amplitude dispersion can be used as the estimate of the phase dispersion. D_A is related to the estimated phase dispersion ($\hat{\sigma}_\varphi$) as :

$$\hat{\sigma}_\varphi = \frac{\sigma_A}{m_A} = D_A, \tag{4.3}$$

where m_A is mean amplitude and σ_A is the standard deviation of the amplitude. It was mentioned in (Ferretti et al., 2001) that the dispersion index (D_A) threshold of 0.25 was proved to be sufficient to identify good PSs for PS analysis as an additional set of PS can be identified after atmospheric phase removal.

By *Signal-to-Clutter Ratio*[6] method, a pixel will be considered as a potential PS if its SCR is higher than a certain threshold. SCR is related to the phase dispersion $\hat{\sigma}_\varphi$ as (Adam et al., 2004):

$$\hat{\sigma}_\varphi = \frac{1}{\sqrt{2 \cdot SCR}}. \tag{4.4}$$

Fig. 4.6 illustrates the point scattering mechanism and its conceptual signal model. Fig. 4.6(a) visualizes a radar resolution cell consisting of a dominant point scatterer surrounded by background clutter. The actual complex signal Z that can be observed from this resolution cell is therefore an addition of signal components from the point scatterer (vector S) and from the background clutter (vector C) as illustrated in fig 4.6(b). σ_φ represents phase error due to the incoherent clutter C. The length of

[6]Clutter is the incoherent scatterer background surrounding the dominant scatterer (point scatterer) in a radar resolution cell.

vectors S and C is estimated using point target analysis. The method assumes that the power of the clutter around the pixel is equal to the clutter power inside the resolution cell. Based on this assumption, assessment of phase stability using SCR requires the application of spatial window. The threshold of $SCR = 2$ corresponding to a phase dispersion of 0.5 radian ($\sim 28°$) was used to identify potential PSs in this study. Eq. 4.3 and 4.4 indicate that the threshold $SCR = 2$ and $D_A = 0.5$ yield an equivalent phase dispersion of 0.5 rad. Detailed explanation on different PS detection approaches available in the DLR PSI system can be found in (Kampes, 2005).

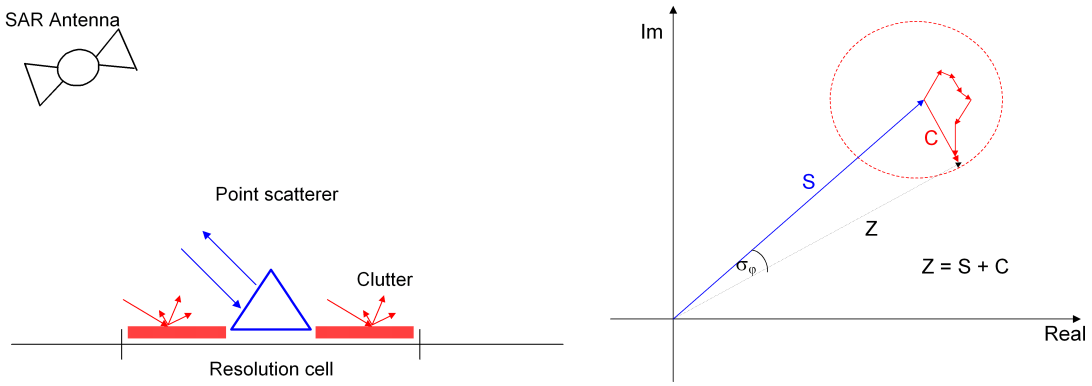

Figure 4.6: Conceptual signal model for a point scatterer observation (modified after Adam et al. (2004))

Comparison of PS detection approaches

The primary difference is that D_A estimates a phase dispersion temporally and on the other hand SCR approximates a phase error spatially. As a result, a reliable temporal phase dispersion estimate by the D_A approach highly depends on the number of SAR data samples available. The SCR can be estimated on every single SAR scene and the SCR time evolution of a PS can be obtained. Adam et al. (2004) showed that with more than 20 radar scenes, the estimation variance of D_A remains relatively constant. Based on this fact, 20 radar scenes could be an initial number of images for one to obtain an estimate of temporal phase error for a persistent scatterer. SCR method utilizes a spatial window to determine the signal and clutter power. Detectability of PS by this means is therefore compromised by the spatial window size. Due to an interferogram constraint, the SCR approach was considered suitable and was used for PS selection in this study.

Detected PS from RCS and SCR criteria are shown in fig. 4.7 and 4.8 respectively. Red

PSs indicate point scatterer whose property can fulfill the applied threshold criteria and are located inside the area of interest. Blue PSs represent the privileged radar point targets but only those that are lying outside the area of interest. The entire area shown in these figures can be determined as a semi-urban area i.e. consisting of settlement clusters or industrial clusters near and along the roads. The area is not as highly populated as in the Bangkok city center. The detected PS densities are different depending on the applied thresholds. The PS densities are 120 and 90 PS/km^2 by RCS and SCR respectively. The decreasing detectability of the SCR method is due to the exploitation of spatial window and the threshold value set. Distribution of selected PS by RCS are cluster-like, while the detected PSs by SCR are more isolated and better distributed (see fig. 4.7(b) and fig. 4.8(b)).

The estimated phase error (in radian) by SCR for the two data stacks are presented in 4.9 and 4.10. All shown PSs possess the SCR higher than 2 which correspond to phase error of less than 0.5 radian ($\sim 28\,degree$). The mean of phase standard deviation for these two stacks are relatively similar, both having about 0.4 radian ($\sim$ 23 $degree$). The relatively low phase error is an indication that the selected PS are less influenced by decorrelation noise and thus could be good PS. The number of PSs of these two stacks fulfilling the set up threshold are not identical which is likely due to a different SAR viewing geometry. PS densities are about 260 and 360 PS/km^2 for the left and the right stack respectively for $SCR \geq 2$. The larger look angle geometry ($\sim 22 - 23\,degree$) of the right stack appears to provide better interaction with the scatterers in the study area e.g. single bounce or multiple bounces with houses or buildings than the steeper look angle ($\sim 17 - 18\,degree$) of the left stack. Hence, a higher PS density could be obtained.

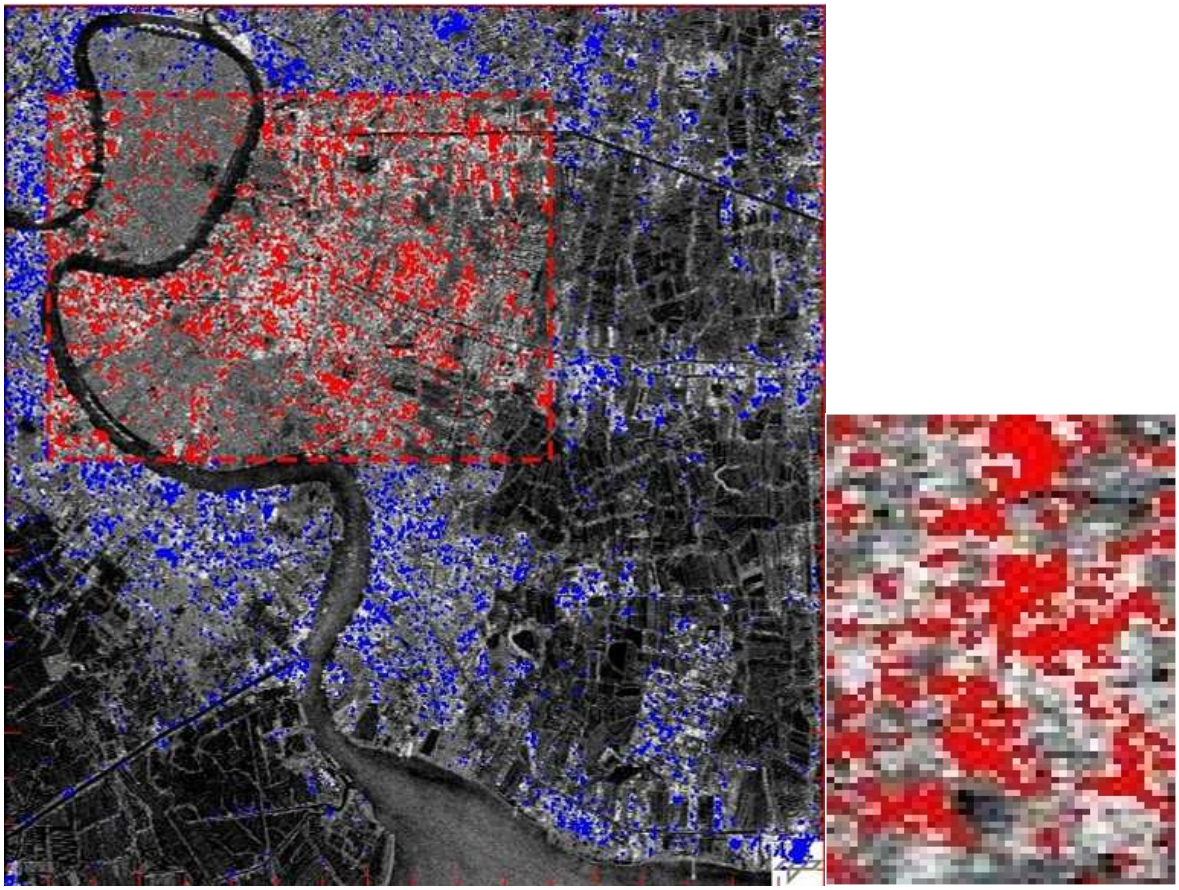

(a) (b)

Figure 4.7: PS detected by RCS thresholding and zoom-in of PS cluster

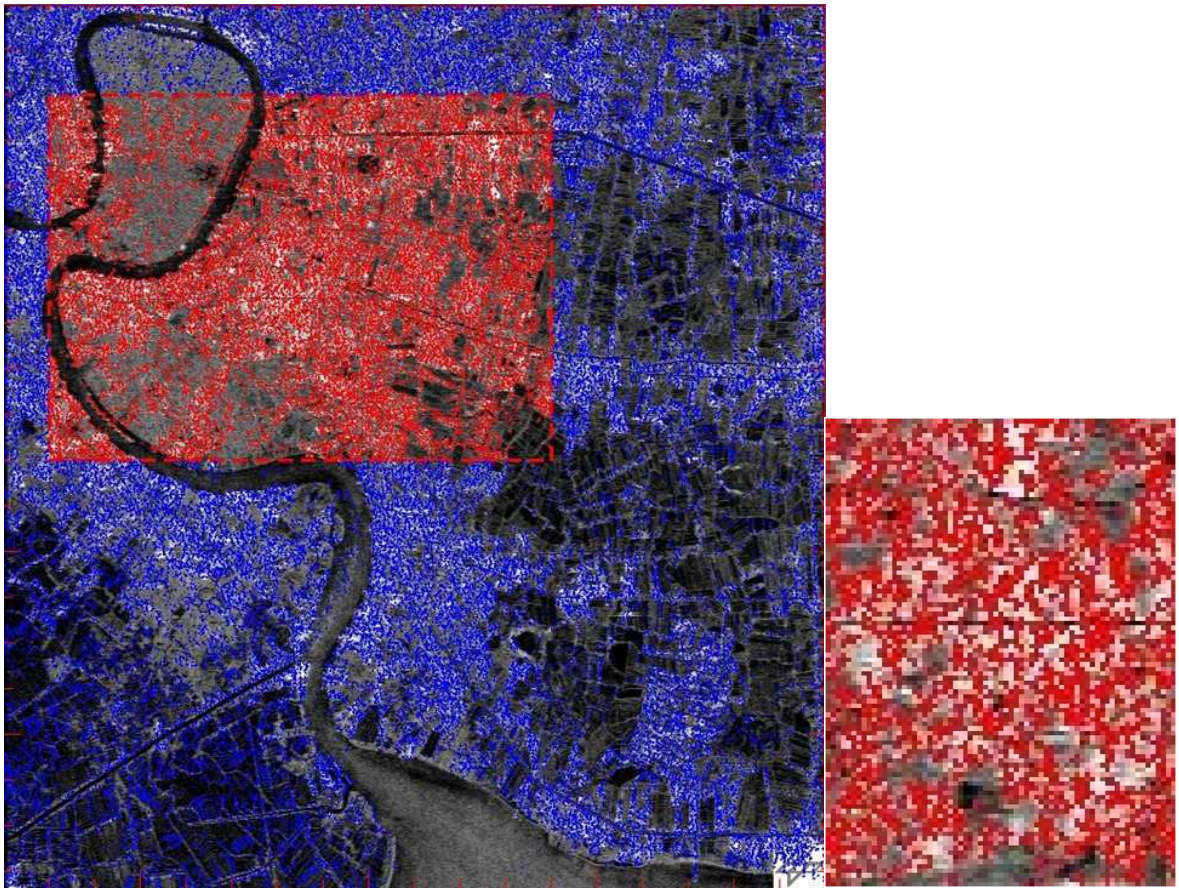

(a) (b)

Figure 4.8: PS detected by SCR thresholding and zoom-in of PS cluster

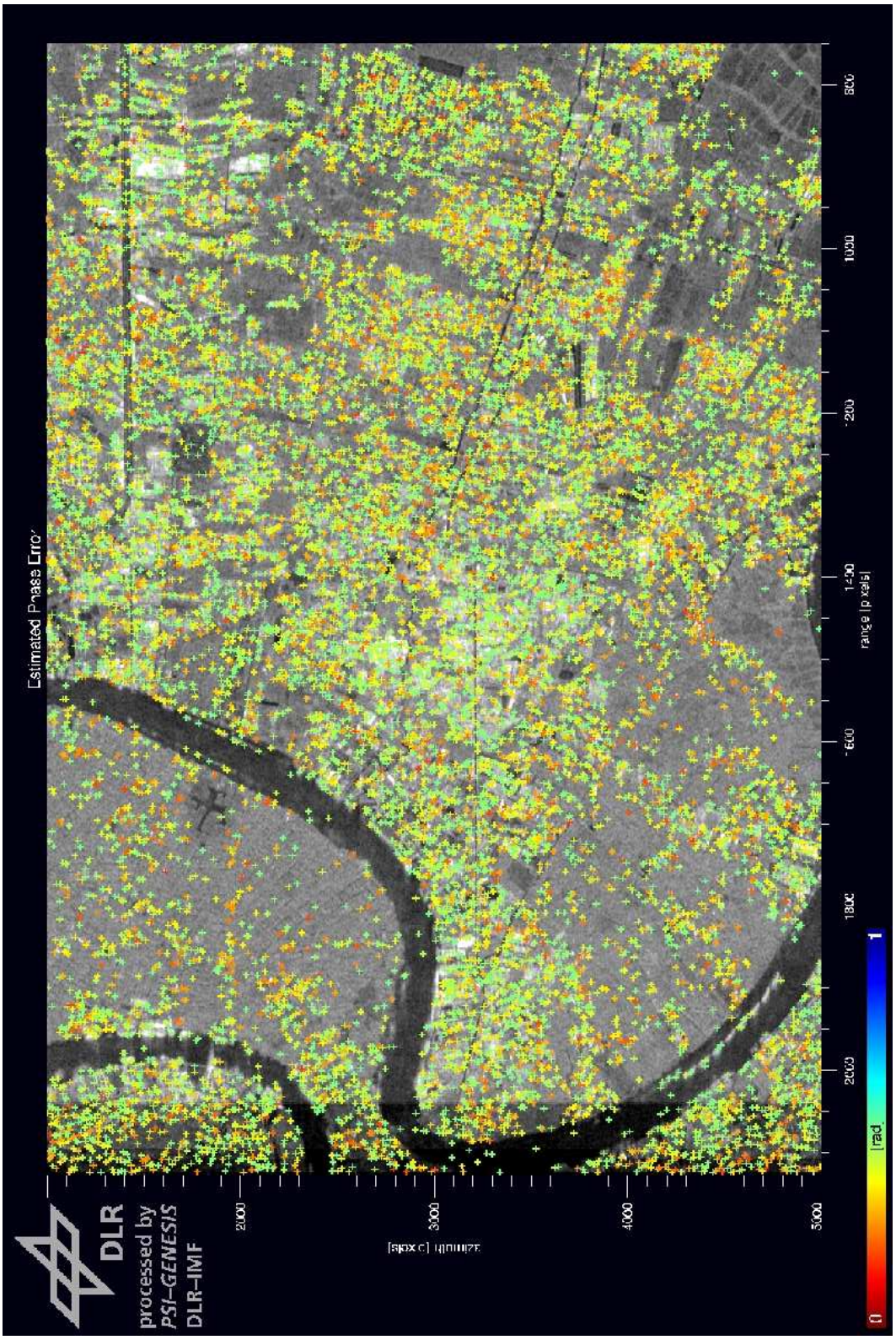

Figure 4.9: Estimated phase error at PS (SCR method) of the right stack data. Averaged PS density 360 PS/km^2.

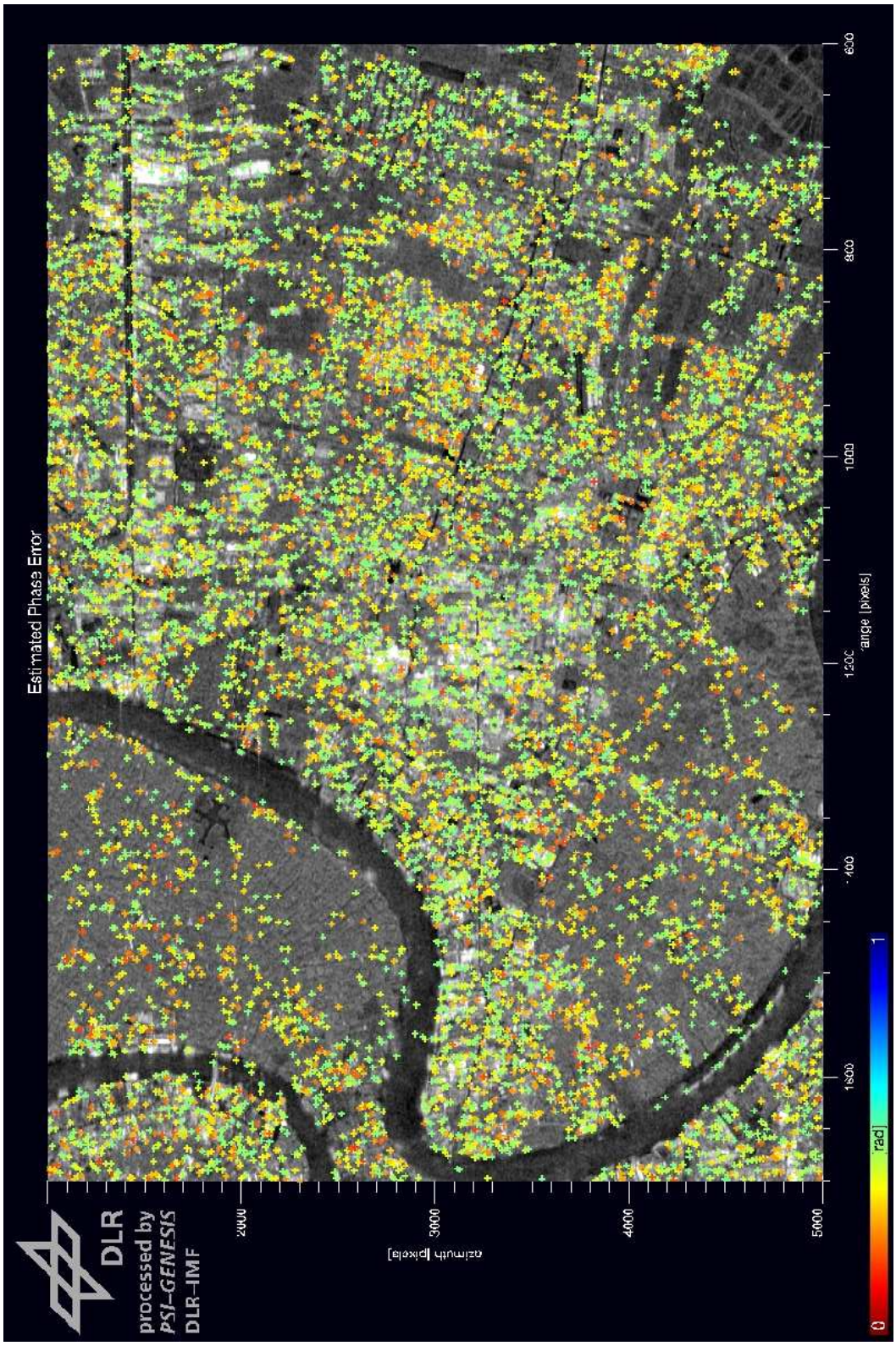

Figure 4.10: Estimated phase error at PS (SCR method) of the left stack data. Averaged PS density 260 PS/km^2.

4.5 Estimation of linear subsidence rates by Least-Squares method

4.5.1 Linear displacement model

The generic functional model for repeat-pass interferometry explained in section 3.3.1 illustrated that there are at least 5 unknown parameters related to each interferometric phase observation. In other words, it implies that this system of equations is an under-determined problem. Increasing the number of observations by using a stack of interferograms is a solution to decrease rank defect of this system. Furthermore, if the displacement behavior in the area can be explained by a mathematical function, the number of the unknown displacement parameters can often be reduced considerably (Hanssen, 2001).

In practice, the developed PS estimator of DLR facilitates the estimation of non-linear displacement parameters. However in this study a linear displacement model is exploited and of interest due to two reasons. Firstly, the geophysical processes like slow subsiding ground surface can be described using the uniform velocity model (Ferretti et al., 1999; Colensanti et al., 2003a). Secondly, under the constraint of number of interferograms, progressing from a linear to a more complicated non-linear displacement model implies that more parameters have to be estimated. This can introduce more rank defect into the system of equations. As a result, the obtained estimates might not be sufficiently robust.

The linear LOS displacement at a certain time at a location p $d(t,p)$ can be modeled as: (see also Kampes and Hanssen (2004))

$$d(t,p) = \alpha_1(p) \cdot f_1(t), \tag{4.5}$$

where $f_1(t)$ is linear base functions and $\alpha_1(p)$ is its corresponding amplitude. Note, that when the linear deformation model is utilized, one base function is used and only one unknown displacement parameter, $\alpha_1(p)$ is to be estimated. The linear base function used here can be expressed as a function of time t (in years) as

$$f_1(t) = t \tag{4.6}$$

(see also fig. 4.52). Therefore, the linear displacement signal at the coherent point scatterer p for interferogram i is the difference of LOS displacement at t^i and t^0 expressed as in eq. 4.7.

$$\Delta r_p^i = d(t^i, p) - d(t^0, p) \tag{4.7}$$

t^0 denotes acquisition time of the master scene ($t^0 = 0$). t^i denotes acquisition time of the slave scenes i , where $i = 1, 2, ..., N$. N represents total number of interferograms used for PS analysis. Recall eq. 4.5, eq. 4.7 can be rewritten as

$$\Delta r_p^i = \alpha_1 (p) \cdot \Delta f_1 \left(t^i\right). \tag{4.8}$$

4.5.2 Functional model between two points

As previously mentioned, interferometry can be considered as a parameter estimation problem. Unlike the forward problem, it is an inverse problem by which the model parameter i.e. the LOS subsidence rate, is estimated from the measurements or observable data i.e. the wrapped interferometric phase.

Section 3.3.1 defined a generic functional model for an interferogram, where the wrapped phase of every pixel k forms the observation space. For PSI, the wrapped phase differences (in the differential interferogram i) between two PSs $\varphi^i_{p,p'}$ form the observation space. A functional model is used to define the relation between phase difference of two PSs $\varphi^i_{p,p'}$with their unknown parameters e.g. the LOS displacement rate (difference) $\alpha_1 \left(p^{'}\right) - \alpha_1 (p)$. This concept is comparable to the principle of geodetic surveying where the height difference between points is the observable value and the elevation (difference) between points is the parameter of interest. An absolute elevation of a point is determined by relating the observed height differences to a reference point with known elevation through the leveling network. The functional relationship between two PSs p and $p^{'}$with their unknown parameters can be defined as (see also (Kampes and Hanssen, 2004)):

$$\begin{aligned} \varphi^i_{p,p'} \;=\; & -2\pi \cdot a^i_{p,p'} \\ & +\beta^i_p \cdot \left(\triangle h_p - \triangle h_{p'}\right) \\ & -\frac{4\pi}{\lambda} \sum \left(\alpha_1 \left(p^{'}\right) - \alpha_1 (p)\right) \cdot \triangle f_1 \left(t^i\right) \\ & +\left(\bar{S}_{p,p'}\right) + n^i_{p,p'}. \end{aligned} \tag{4.9}$$

$a^i_{p,p'}$denotes the integer ambiguities (difference) for each interferogram. β^i_p is the height conversion factor and can be defined as $\beta^i_p = -\frac{4\pi}{\lambda} \frac{B^i_{\perp,p}}{r^0_p \sin\theta^0_p}$. $\triangle h_p - \triangle h_{p'}$or $\triangle h_{p,p'}$denotes

the uncompensated topography related to DEM error (difference). $\alpha_1\left(p^{'}\right) - \alpha_1\left(p\right)$ or $\alpha_{1_{p,p'}}$ represents LOS displacement rate (difference) and $\bar{S}_{p,p'}$ represents the mean double difference[7] of atmospheric delay between points p and $p^{'}$ and between the master and all slave images. $\bar{S}_{p,p'}$ can be estimated using

$$\bar{S}_{p,p'} = S^0_{p,p'} - \frac{1}{N}\sum_{i=1}^{N} S^i_{p,p'} \tag{4.10}$$

where $S^0_{p,p'}$ is the atmospheric delay of the master scene ($i = 0$) and $S^i_{p,p'}$ is the atmospheric delay in the interferogram i. The last term $n^i_{p,p'}$ is the noise component.
Using the unwrapped phase differences between two nearby points and a model for displacement, the number of parameters (in eq. 4.9) that need to be estimated can be limited to 3 parameters. These parameters are uncompensated height with respect to the reference DEM (DEM error difference, $\triangle h_{p,p'}$) , the mean double difference atmospheric delay ($\bar{S}_{p,p'}$) , and the displacement rates difference ($\alpha_{1_{p,p'}}$) describing the displacement as a function of time.

Least-Square estimator

In radar interferometry, the observed phase can be only determined in the range of $[-\pi, \pi]$. Thus, a process to determine absolute phase Φ^i from this observed phase φ^i in order to reveal the actual distance measurement or phase unwrapping is required. The observed wrapped phase (difference) φ^i is unwrapped as

$$\Phi^i = \varphi^i + 2\pi \cdot a^i. \tag{4.11}$$

a^i is the integer ambiguities of interferogram i and has to be estimated or unwrapped.
The estimator implemented in the PSI processing system I used was adopted from the concept of the Least-Squares AMBiguity Decorrelation Adjustment (LAMBDA) estimator to PS interferometry case. The LAMBDA method was developed for the fast GPS[8] double difference integer ambiguity estimation. It is considered as the best integer least-squares (ILS) estimator in the sense that it provides the highest probability of correct integer estimation for the problems with a multivariate normal distribution (see Teunissen et al. (1995)). Adaption of ILS estimator to PSI application and its numerical definitions can be found in Kampes (2005).

[7]Double difference means difference that is occurred due to position difference ($p\,and\,p^{'}$) and due to time difference ($t^0\,and\,t^i$).
[8]Global Positioning System

4.5.3 Obtaining linear subsidence rate estimates

An initial set of PS points fulfilling the defined threshold explained in section 4.4.2 together with their phases from differential interferogram time-series constitute the starting point of the estimation. A flow diagram of the overall procedure applied to obtain the final line-of-sight (LOS) displacement estimate from PS analysis is illustrated in fig. 4.11. In the next subsections each processing step is explained in detail.

Sparsification of PS

The purpose of this step is to re-evaluate the PS resulting from the PS detection step in order to obtain the best PS. The best PSs selected here possess phases that are most likely stable over time and least affected by decorrelation noise. Also, they should be distributed regularly in the area. In order to obtain a regular distributed PS while preserving the distance among PS to within a few kilometers (e.g. less than 2 km. as the atmospheric signal will be usually still correlated), a grid size of a few hundred meters is placed on the generated differential interferograms and a temporal statistical analysis of amplitude values of these PSs is performed. The PS with the lowest dispersion index (D_A) will be considered as the best PS (red in fig. 4.12) of each grid. Since a higher density of PS is preferable in this study, the dispersion index of 0.56 is applied to allow more PS to be detected. The best PS from each grid forms the reference network skeleton. As a result of this step, the potential PS will be separated into two groups as the best PS and the other PS respectively. The former group of PS will be used to construct a reference network for the estimation. While the latter group will be integrated later and be estimated based on the reference network, once the parameters at the reference network points have been estimated. PS density at this step are found to be 5.9 and 6.8 PS/km^2 for the left and right stack respectively.

Reference network construction

A reference network for ILS estimation is formed by connecting the best PS with arcs. The number and length of each connecting arc can be determined. In principle, the distance between two points (arc) should not be larger than a few kilometers (e.g. 2 km.) as the atmospheric signal will no longer be correlated. The higher the number of connecting arcs per PS, the longer the computing time required. For the networks constructed, the mean distances of the generated arcs are 920 and 800 meter for the left and right data stacks. Fig. 4.13 visualizes the reference networks formed by connecting

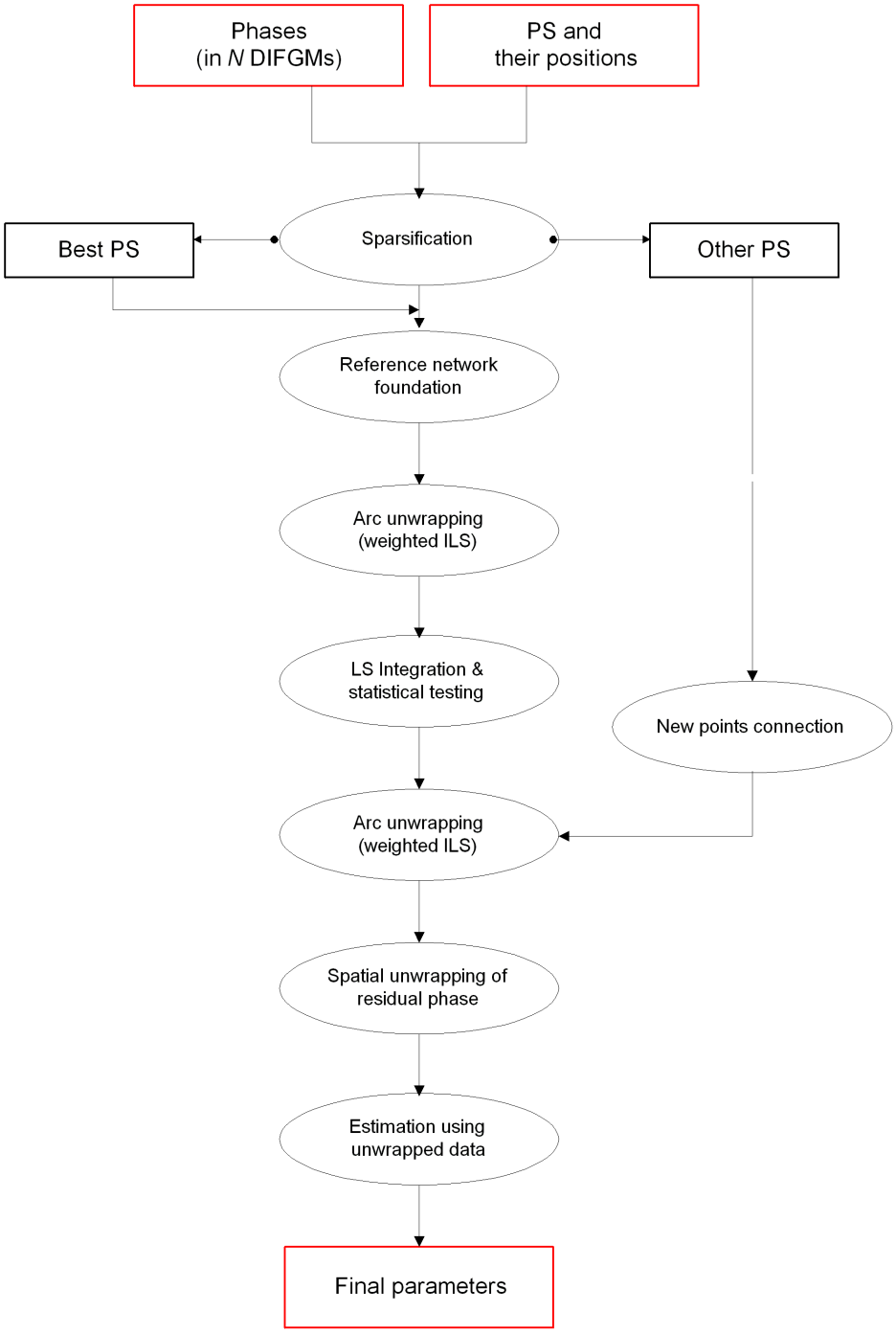

Figure 4.11: Flow diagram for PSI parameter estimation

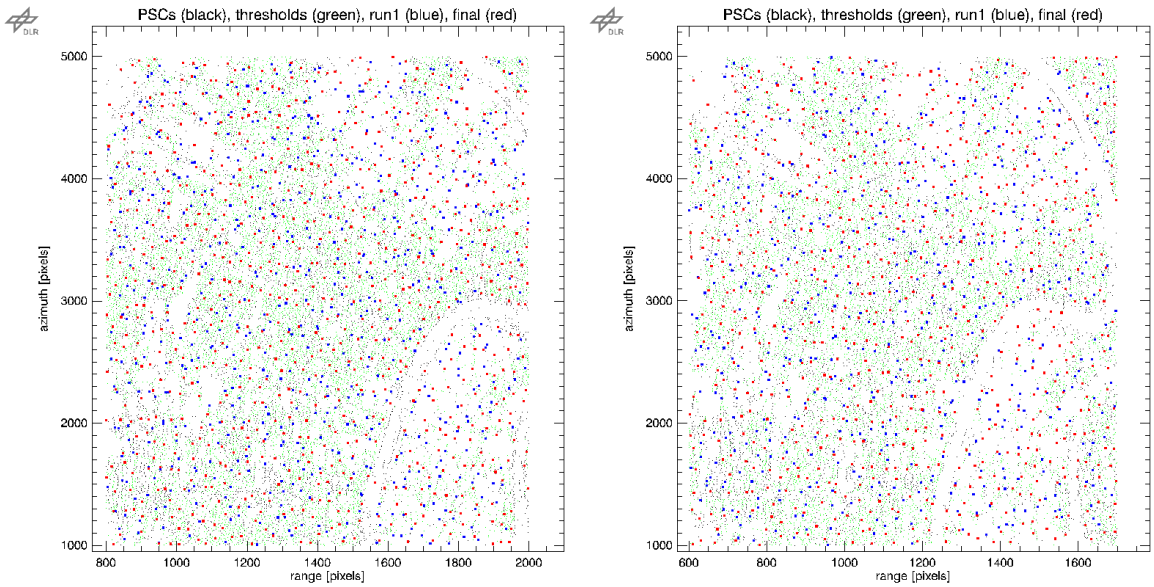

(a) Right stack (b) Left stack

Figure 4.12: Best PS (red) in the area of interest

the best PS in each grid and its close-up. An output of this step is the phase difference for each arc constituting the reference network.

Least-square estimation between two points

To obtain the quality description of the interferograms (observations) to use in the estimation, the variance factors were first estimated based on the residual phase derived from a number of established arcs in the reference network. Then, these quality factors were used as weights in the ILS estimation. At each arc, parameters of interest namely, the difference in DEM error and LOS displacement rate were estimated based on the principle of ILS. Note that in this study, the atmospheric phase contribution was not included in the functional model but the stochastic. This aims to reduce the number of unknown parameters (rank deficiency) in the system. This estimation procedure can be referred to as *temporal unwrapping* because the differential phase values are unwrapped through the temporal analysis in conjunction with a displacement model. The functional relation between the modeled phase $\phi^i_{p,p'}$between two points (p and $p^{'}$) and these parameters can be therefore expressed as in eq. 4.12. Subtraction of the modeled phase $\phi^i_{p,p'}$ from the observed phase $\varphi^i_{p,p'}$ yields the *wrapped residual phase* $\omega^i_{p,p'}$ as expressed in eq. 4.13.

$$\phi^i_{p,p'} = \phi_{topo_{p,p'}} + \phi_{disp_{p,p'}} \tag{4.12}$$

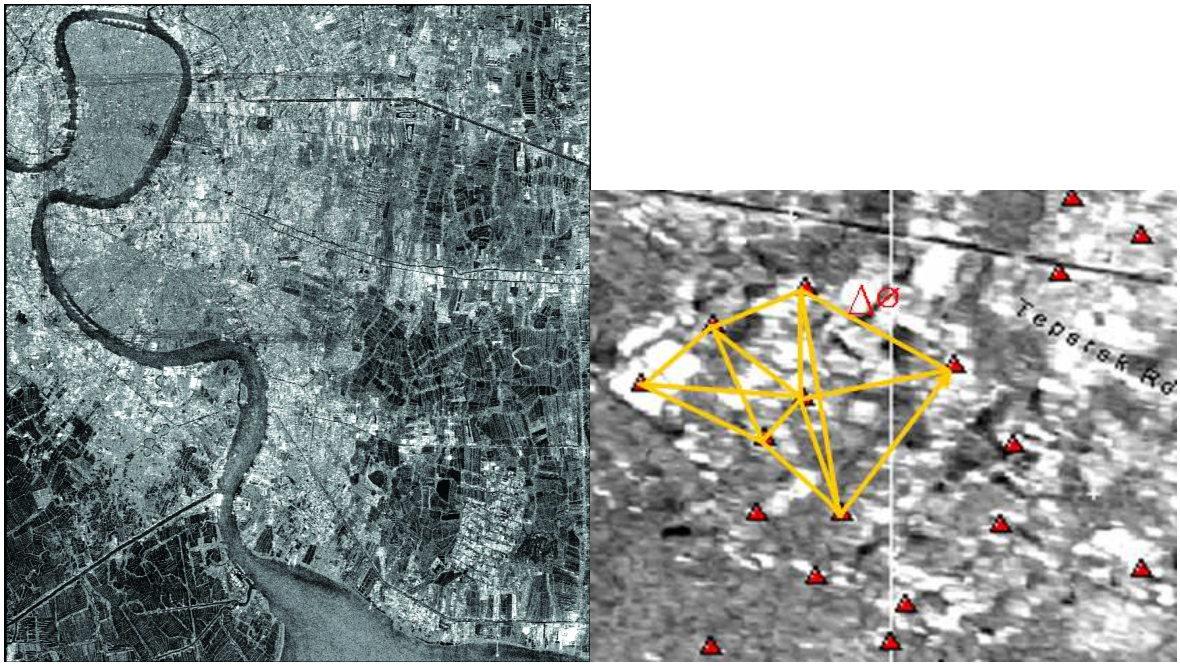

Figure 4.13: Constructed reference network on amplitude image background

$$\omega^{i}_{p,p'} = \varphi^{i}_{p,p'} - (\phi_{topo_{p,p'}} + \phi_{disp_{p,p'}}) \tag{4.13}$$

Therefore, the wrapped residual phase term contains other phase contributions e.g. the Gaussian distributed noise, (limited) temporal and spatial decorrelation, processing induced noise, atmospheric path delay and orbital error. Provided that good PS were selected and careful processing has been carried out, this residual phase is primarily composed of the atmospheric disturbance and orbital error (see also eq. 3.8).

Integration of parameters at points

Based on the estimated parameters at arcs, the estimates at PS points were obtained by *spatially integrating* estimates of the reference network targeting a closing error equal to zero. Identification of unqualified arcs and points were carried out by alternative statistical analysis. Those arcs and points identified were removed from the network and finally, a *stable reference network* is obtained. The following fig. 4.14 show the stable reference network with its estimated LOS displacement rate (mm/y) as a result from temporal unwrapping and LS integration of 15 and 19 IFGMs respectively. PS density of the resulted reference network in comparison to the density before the ILS estimation is provided in table 4.1. The green color arcs indicate high quality arcs with low LS error while the color of the points represent the magnitude of the displacement

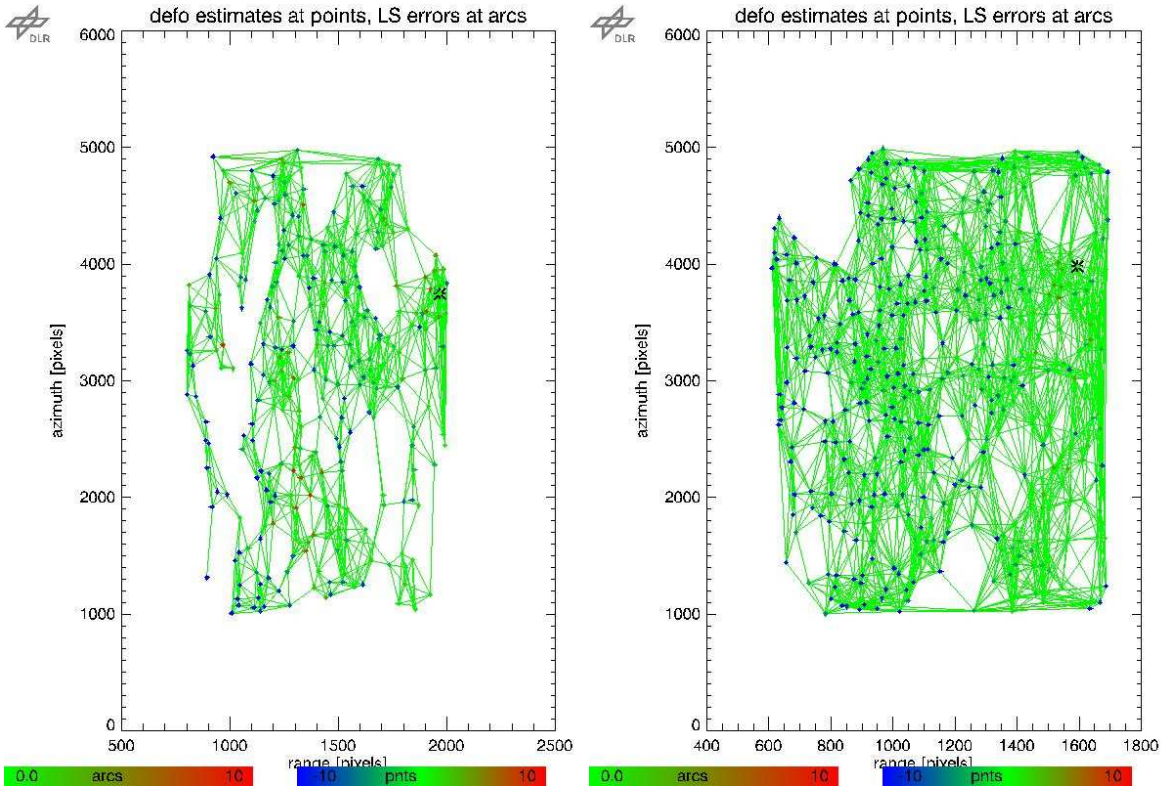

(a) (b)

Figure 4.14: Resulting PS reference network from (a) 15 IFGMs and (b) 19 IFGMs , the colors at the points denote the relative displacement rate while the colors at arcs denote the LS error

rate in relation to the reference point (black asterisk) from subside (blue) to uplift (red). It should be noted here that these subsidence rates are relative to the reference point movement velocity. If the reference point velocity is known, then the absolute subsidence velocity of other points can be revealed. Fig. 4.15 and fig. 4.16 depict the distribution of PSs in reality on an amplitude background those are left in the networks after LS integration and statistical testing. These PSs correspond to the same points in fig. 4.14.

Table 4.1: PS density before and after the ILS estimation and spatial integration in the reference network

IFGMs	Before ILS(PS/km^2)	After ILS ($PS:\ PS/km^2$)
15	6.8	299: 3.1
19	5.9	417: 4.3

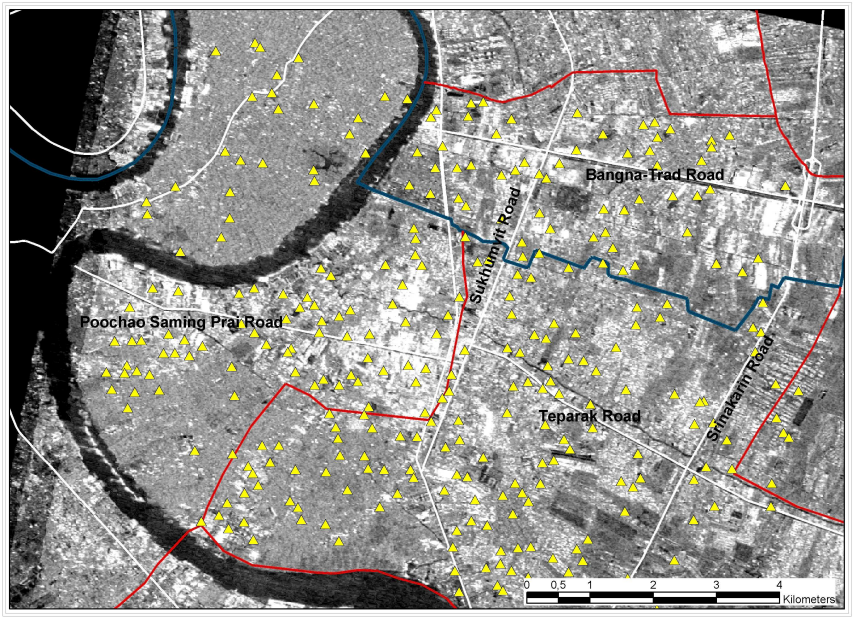

Figure 4.15: PSs at stable reference network on amplitude background - 15 IFGMs

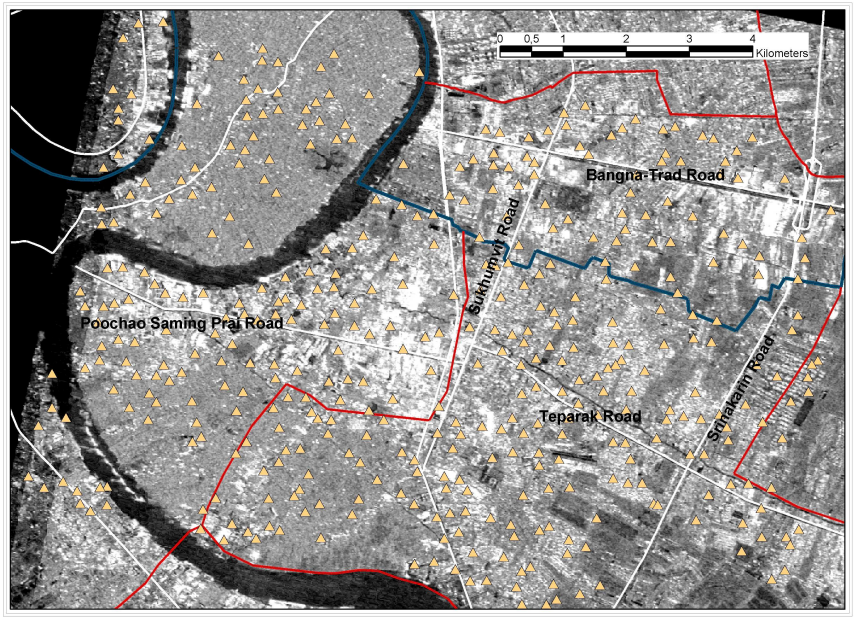

Figure 4.16: PSs at stable reference network on amplitude background - 19 IFGMs

Parameter estimation for other points

Once the parameters at PS points in the reference network were obtained, it is also possible to derive parameter estimates for other PS through the same procedure. First, other PS points will be connected to the known neighboring PS residing in the reference network. As a consequence, the wrapped phase difference between the known points and those of unknown points form the observation space for the parameter estimation. The next step, the ILS estimation, LS integration and testing procedure will be repeated for this extended network and the parameters at those new points can then be obtained. Compared to the PS in the reference network, the new connected PS could contain a higher level of noise as they were formerly omitted in the sparsification step due to high D_A value. Before continuing the next step, a set of reliable estimates will be selected based on a given criterion (overall model test: OMT) (Kampes et al., 2001) and be further exploited.

Spatial unwrapping of residual phase

Apart from the modeled phase component that was temporally unwrapped, the wrapped residual phase (typically expected to be less than π) in eq. 4.13 is also required to be unwrapped. Since PSs are normally irregularly distributed, the principle of phase unwrapping with sparse data based on Delauney triangulation have to be adopted (Costantini and Rosen, 1999). Generally, phase unwrapping is composed of two steps, firstly, the estimation of unwrapped phase difference between adjacent pixels and secondly, the integration of gradient using one of the known techniques e.g. minimum cost flow, weighted least mean square and branch cut etc. In our PS system, an algorithm of minimum cost flow is applied (Costantini, 1998; Eineder et al., 1998; Eineder and Holzner, 1999).

Estimation based on unwrapped phase

After both unwrapped phase terms are obtained, the weighted ILS estimation is then repeated using this unwrapped phase data on those selected reliable points to obtain the final parameters. The suitable parameters of interest can be defined depending on the purpose of study. As mentioned previously, the estimated parameters are DEM error and the mean displacement rate.

LOS to vertical displacement conversion

The SAR imaging system is capable of detecting the LOS displacement d_{LOS}. The conversion from LOS to the vertical displacement is required and can be carried out following the relationship.

$$d_{vertical} = d_{LOS} / \cos(\alpha) \tag{4.14}$$

in which $d_{vertical}$ represents the vertical displacement and α denotes the local incidence angle. In an ERS-SAR scene, the incidence angle varies from about 21 to 26 degree (Hanssen, 2001) across the range direction.

4.5.4 Factors influencing the estimates

Experiments were carried out to assess the success rate that could be expected from parameters (between points) estimation in relation to phase noise contained in PSs and the number of IFGMs. To simulate real data, the random phase (normally distributed) was generated with different noise levels at PSs using the PS distribution and baseline configuration of real data. The phase noise data range from 10-60 degree with 10, 16 and 20 IFGMs were simulated. Parameters estimated between points were DEM error and linear displacement rate differences. To assess the success rate, threshold criteria are required as a reference. The threshold of $\pm 2\,mm/y$ and $\pm 2\,m$ for the displacement and dem error parameters were set respectively. Arcs with the estimated values less than the given threshold are considered as a ' success ' estimate. The corresponding expected success rate (%) is simply computed as:

$$success\ rate = \frac{n}{N} \tag{4.15}$$

where n symbolizes the number of arcs above the set threshold, and N denotes total number of arcs. Fig. 4.17 visualizes the experimental result.

This assessment is particularly useful when the available number of interferograms is marginal. The estimated success rate indicates how probable it is to obtain the right estimate in relation to the noise level for a particular data configuration. In case sufficient IFGMs are available, this test can be used to determine whether or not a noisy interferogram can be eliminated from the estimation.

The result indicates a nonlinear inter-relationship between success rate and degree of noise. As it can be obviously observed the lower the noise level of a PS, the better the

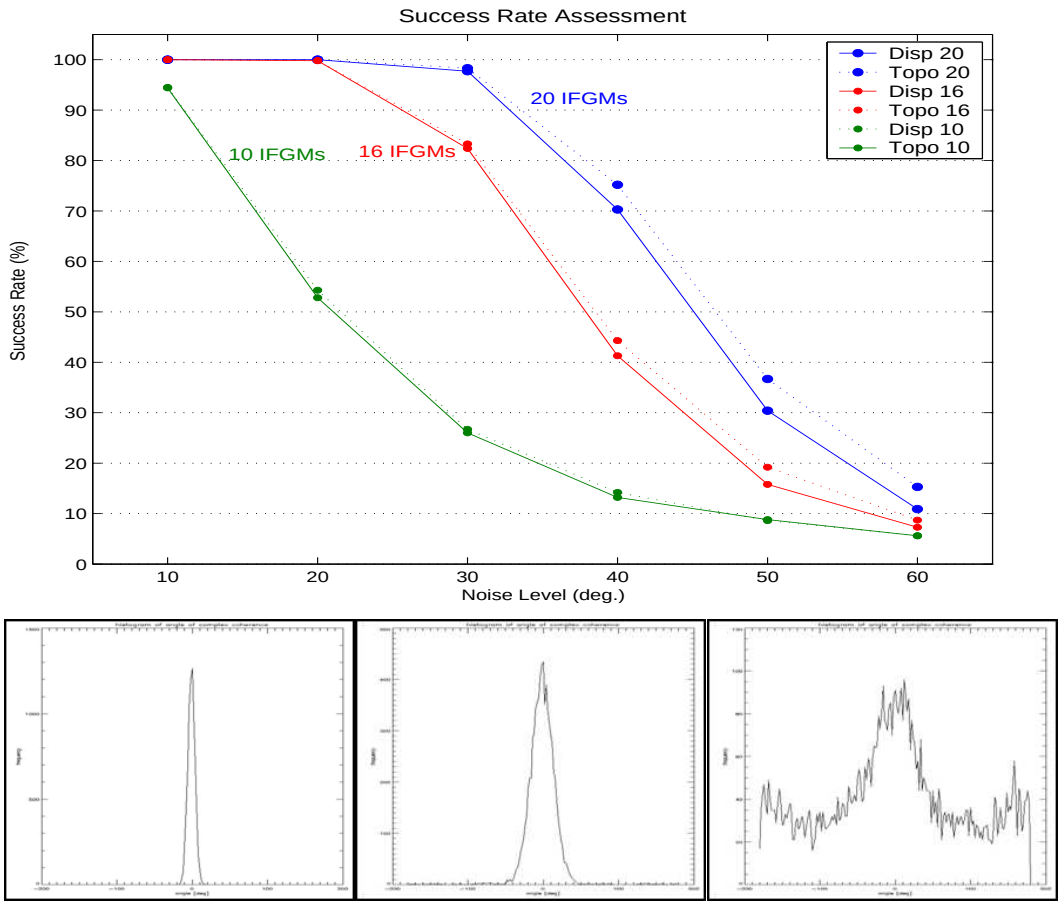

(a) 10 deg. Noise (b) 30 deg. Noise (c) 60 deg. Noise

Figure 4.17: Success rate assessment result based on actual data configuration and histograms of displacement estimates

success rate. When the degree of noise of PSs is low ($<$ 20 degree or 0.35 radian), estimation using a 20 or 16 IFGMs stack provide a relatively similar success rate approaching 100%. Similarly, when the quality of PSs are bad (containing phase noise of about 60 degree or more than 1 radian), the percent of success in case using 10, 16 or 20 IFGMs are very low and not so much distinguishable. It is in the moderate phase noise region (about 30-40 deg.) where we can find significant improvement when using 16 and 20 IFGMs for the estimation.

For the 10 IFGMs case, the success percentage is very high only when the selected PSs contain very little noise level ($\sim$ 10 deg. or 0.17 radian), which is the case for PS with a coherence value very close to 1. These PSs should possess SCR value more than 16 (see eq. 4.4) and are rarely found in suburban areas of Bangkok. When the number of IFGMs is fixed, increasing of noise level contained in PSs results in the noisier estimate. Sub-fig. 4.17 (a), (b) and (c) show histograms of the displacement estimate with different level of phase noise. The highest noise level (60 degree) provides the noisiest estimate (widest peak) that no longer has a normal distribution. Note that an estimation carried out with the marginal number of IFGMs i.e. 20 IFGMs can still achieve a high success rate (about 98 %) when the phase noise is not more than 30 degree ($\sim$ 0.5 radian). In this study, PSs were selected with an SCR threshold of 2 and $D_A$of about 0.5. Both cases were equal with phase noise of about 0.5 radian. In addition, it was referred to in section 4.4.2 that about 20 scenes are required for a reliable phase dispersion estimation. This empirical observation has demonstrated that under this data configuration (20 IFGMs), it is possible to expect for a reliable estimate (98% of success rate) provided that 1) the temporal unwrapping is correct 2) the expected accuracy is not higher than 2 mm/year for linear displacement rate parameter and 3) the PSs are carefully selected.

4.6 Estimation results

Fig. 4.18 and 4.19 visualize the estimated LOS displacement rate at PS in the reference network (after LS integration) . The color representation from red to blue represent the most subsiding (red) and uplifting (blue) locations in relation to their reference points (black asterisk). The displacement rate presented here are *still relative to the reference point*. In both estimation therefore, attempts were made to select PS located nearest to a known leveling point (DMR-13) as the reference point (marked as black asterisk in both figures) for LS estimation to facilitate the derivation of absolute displacement rate later on.

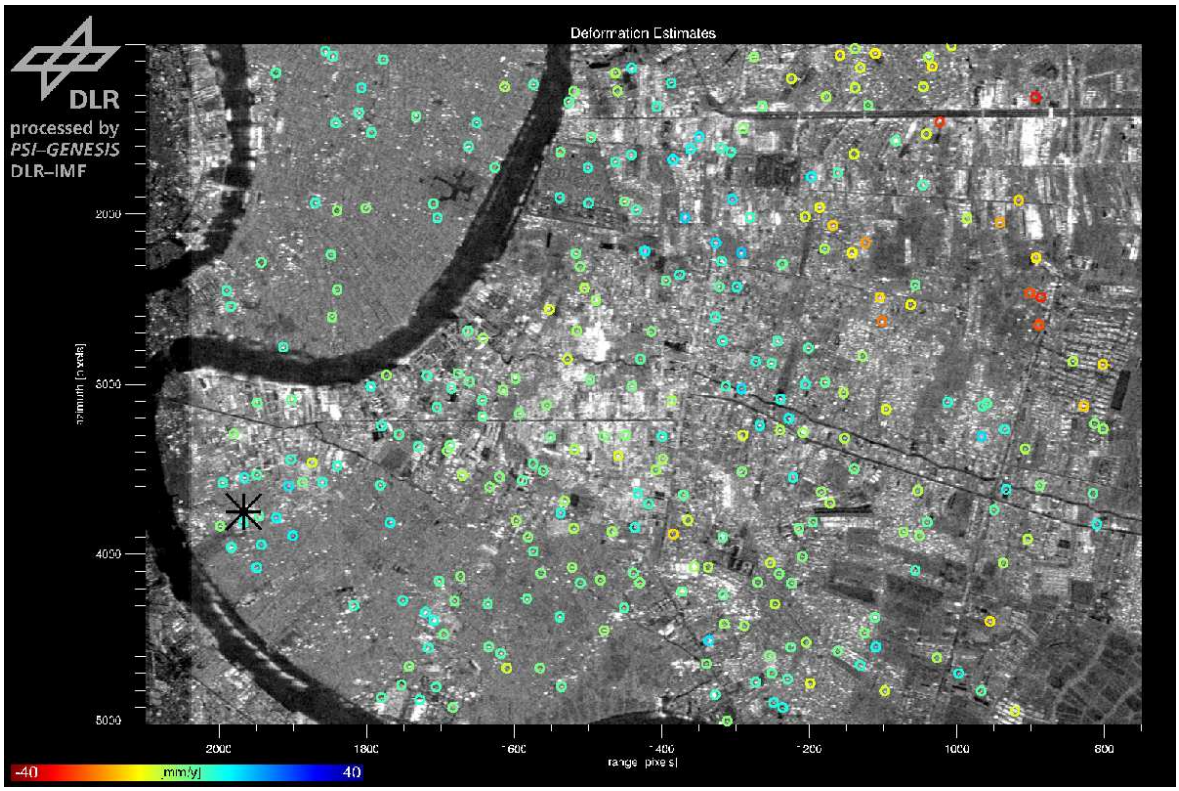

Figure 4.18: LOS displacement estimates at reference network (15 IFGMs)

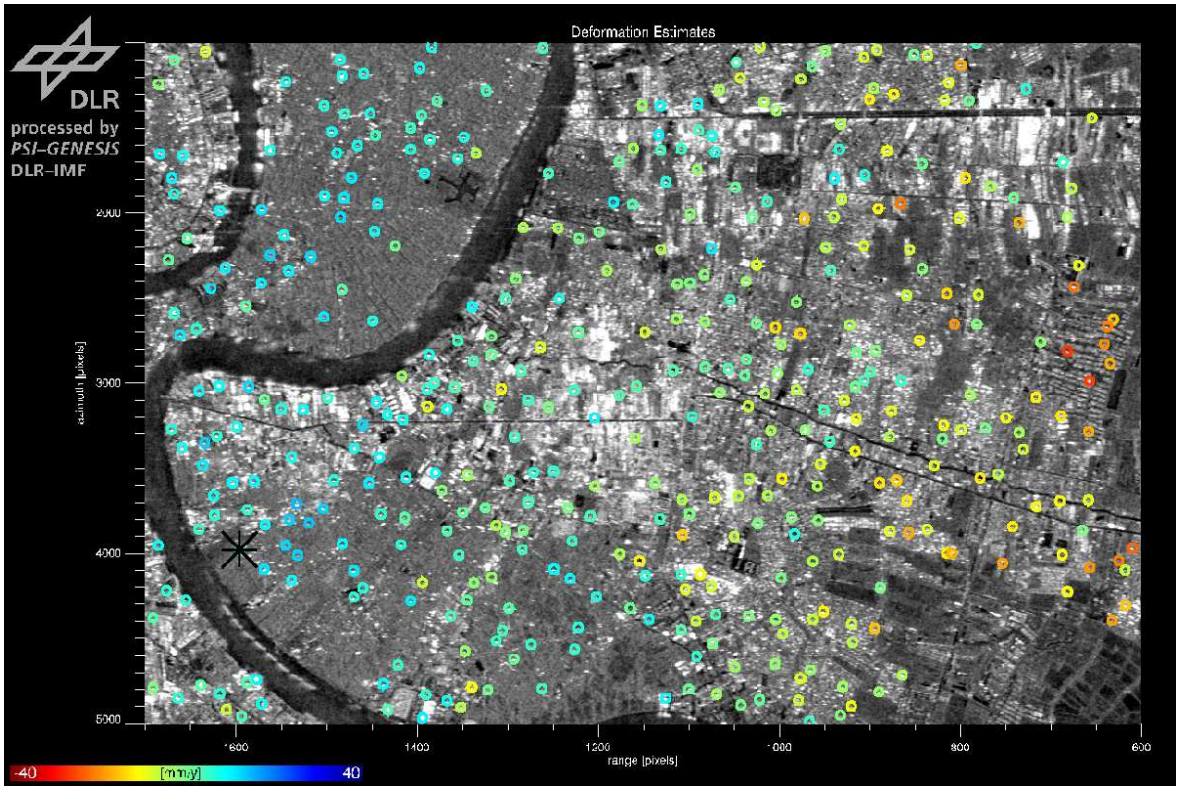

Figure 4.19: LOS displacement estimates at reference network (19 IFGMs)

By visual interpretation, the two estimates in fig. 4.19 and 4.18 provide similar overviews of the subsidence rate distribution in the area with the most critical subsiding area coinciding in the eastern part of the image. Displacement rate increases as we proceed from west toward the east. The color bar is centered at the mean displacement estimate (yellow-green) making two relative estimations comparable in color independent from their values. Most of the estimates (greenish points) resulting from the 15-IFGMs stack slightly deviate from their mean value (-3.85 mm/year; see table 4.2) . Most of the 19-IFGMs estimates (cyan color points) show higher deviation from their mean (-8.74 mm/year). The distribution of the remaining PSs (stable estimates) in the network is looser in the 15-IFGMs stack than in the 19-IFGMs stack with PS densities of about 3.1 PS/km^2 and 4.3 PS/km^2 respectively . Note that the original PS density (before LS estimation) of these 15-IFGMs was higher than the 19-IFGMs stack (see table 4.1). This implies that more unreliable estimates were contained in the 15-IFGMs data and were discarded during the estimation.

Fig. 4.20 and 4.21 illustrate a relative displacement estimate of the extended network resulting from conducting ILS estimation between these new PS points in relation to the established displacement network in fig. 4.18 and 4.19 . With a higher density of PS, the similar displacement trends are better noticeable. The visualized PS estimates are the subset of the entire PS and are considered reliable fulfilling the given threshold criteria e.g. Overall Model Test (OMT) value, the permitted minimum-maximum range of the estimate. From this, some obvious outliers can be discarded. Investigation of the spatial displacement estimate in these two figures indicate similar estimates to those from the reference network accompanied with a higher variance (refer to their statistics in table 4.2). At local positions (within hundreds of meters), the estimates from 15-IFGMs provide more heterogeneous results. Despite the fact that some thresholding criteria were applied to select good estimates, there still exist outliers within these two estimates. Up to this point, it is not feasible to decide which estimation result is more reliable. Further quantitative analysis is required and will be presented in section 4.10.

The succeeding fig. 4.22 presents the final LOS displacement estimate derived from unwrapped data. Statistics of the LOS displacement estimates (fig. 4.18 - 4.22) are summarized in table 4.2. Fig. 4.23 shows corresponding histograms of the LOS displacement estimates (a) to (e) in table 4.2. Within the same data set, the mean and standard deviation of the displacement rates of the extended network are slightly different from the reference network. Nevertheless, their histograms look relatively similar (compare fig.4.23 (a) to (c) and (b) to (d)).

Table 4.2: Statistics of LOS displacement estimates

Estimates	No.PS, Density (PS, PS/km^2)	[Min, Max] (mm/y)	Mean (mm/y)	STD (mm/y)
Reference network				
(a) 15IFGMs	299, 3.1	[-33.17, 9.79]	-3.85	±6.7
(b) 19IFGMs	417, 4.3	[-35.20, 5.95]	-8.74	±8.1
Extended network				
(c) 15IFGMs	3451, 35.9	[-37.85, 21.60]	-4.58	±7.9
(d) 19IFGMs	2739, 28.5	[-39.34, 26.30]	-9.44	±9.0
(e) 19IFGMs (unwrapped)	2739, 28.5	[-39.37, 26.26]	-9.36	±9.1

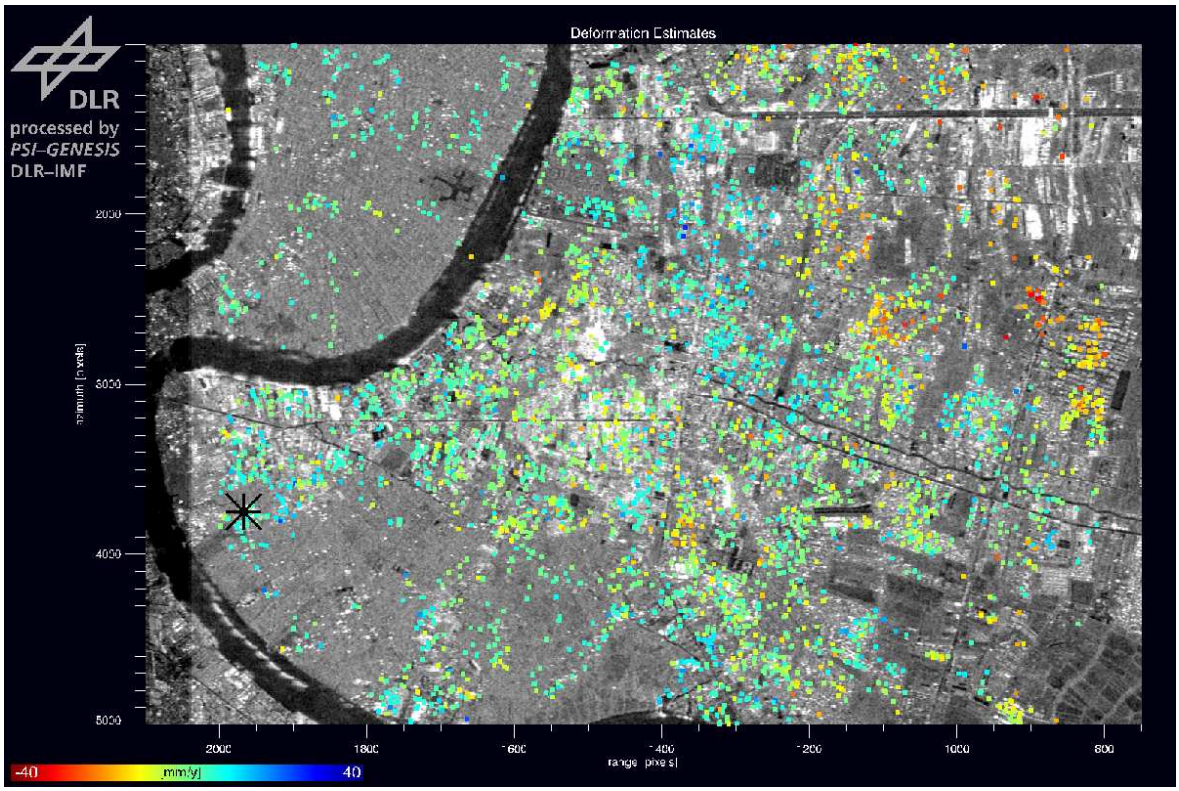

Figure 4.20: LOS displacement estimates at reliable points - 3451 PS (15 IFGMs)

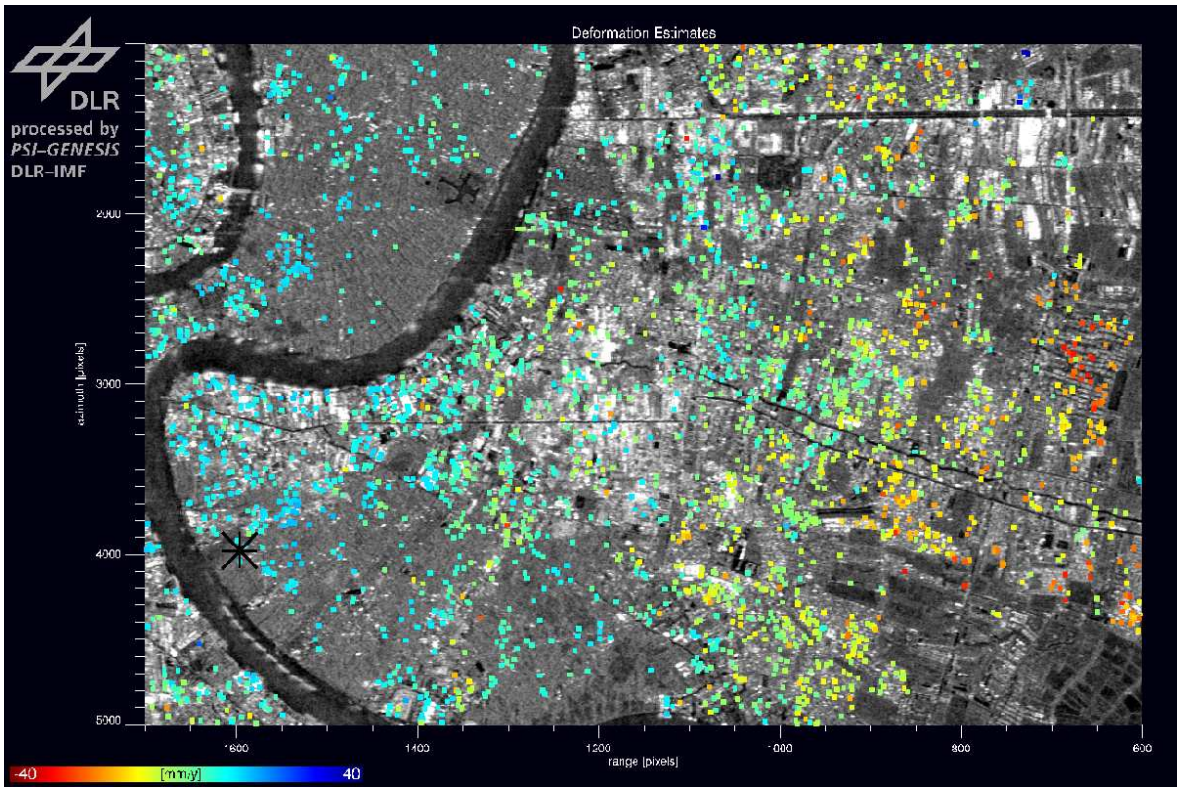

Figure 4.21: LOS displacement estimates at reliable points - 2739 PS (19 IFGMs)

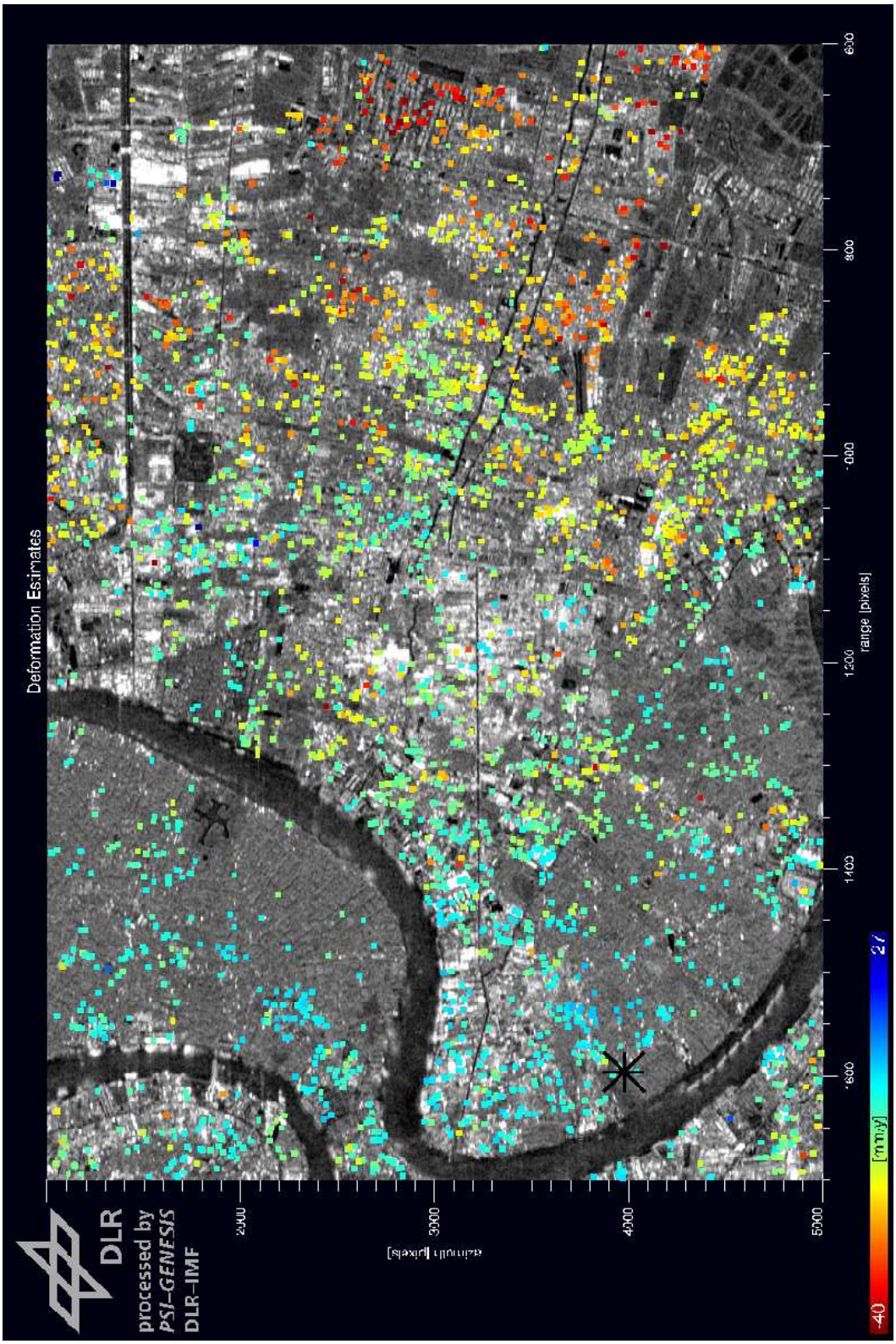

Figure 4.22: LOS displacement estimates based on unwrapped data (19 IFGMs)

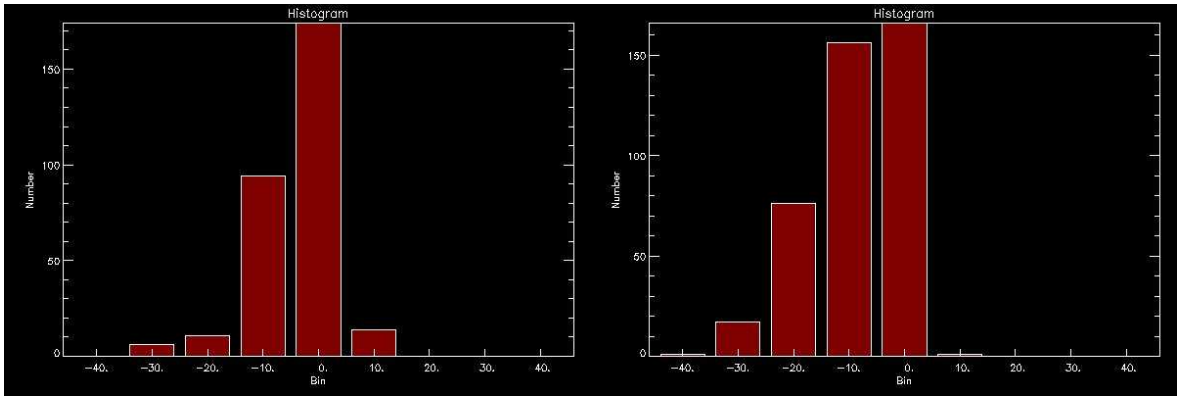

(a) reference network - 15 IFGMs (b) reference network - 19 IFGMs

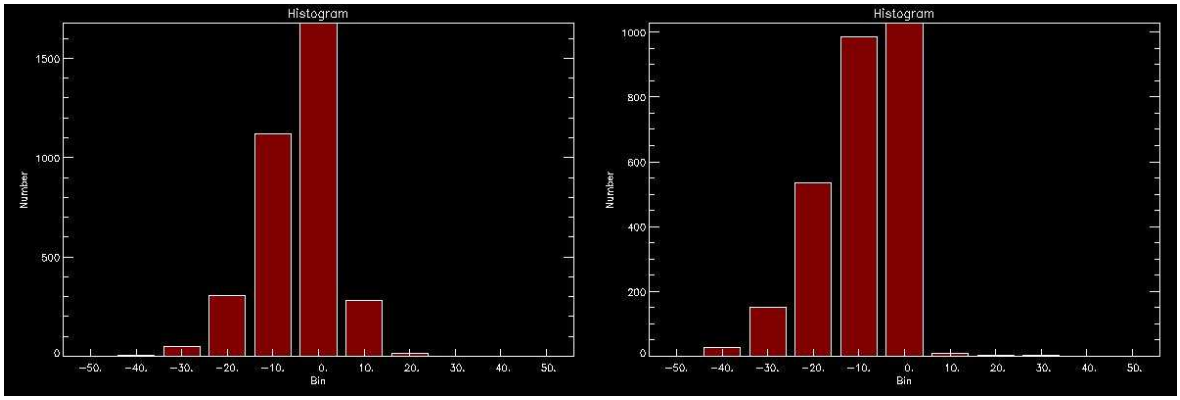

(c) 3451 PS - 15 IFGMs (d) 2739 PS - 19 IFGMs

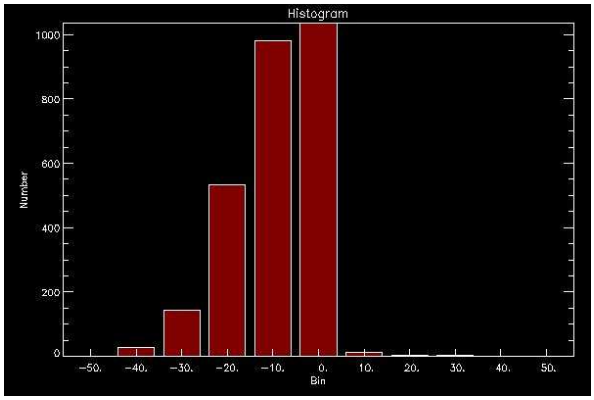

(e) unwrapped data - 19 IFGMs

Figure 4.23: Histograms of LOS displacement estimates

4.7 Post processing of estimates

The purpose of the post processing step is the separation of different phase terms contributing to the (unwrapped) residual phase. Recall eq. **??**, two parameters were estimated and the possible contribution to the resulting residual phase could be therefore

the atmospheric phase delay, orbit error and/or noise. The impact of orbit uncertainties for deformation analysis is less critical and the precise (PRC) orbit information can normally fulfil the accuracy requirement (Reigber et al., 1996). Since the precise orbit information was used in the processing, impact from orbit indetermination is strongly reduced (Scharoo et al., 1998). Also, it is difficult to separate this orbit error from the atmospheric phase screen (Colensanti et al., 2003a) therefore, I infer these two terms as the atmospheric contribution phase. The atmospheric delay term ($\bar{S}_{p,p'}$) in eq. 4.9 is the mean double difference of the atmospheric delay between points p and $p^{'}$ and between the master and all slave images. And the atmospheric delay difference in interferogram i $S^{i,0}_{p,p'} = \bar{S}_{p,p'} + (S^{i,0}_{p,p'} - \bar{S}_{p,p'})$ where $\bar{S}_{p,p'} = S^{0}_{p,p'} - \frac{1}{N}\sum_{i=1}^{N} S^{i}_{p,p'}$ (see eq. 4.10). In DLR PSI system, it is possible to estimate this $\bar{S}_{p,p'}$ term by assuming that $E\{S^{i,0}_{p,p'} - \bar{S}_{p,p'}\} = 0$ (Kampes and Hanssen, 2004).

Apart from these contributions, if a non-uniform movement of the ground surface exists during the observation time and is not estimated, e.g. in this case study, the phase component contributed by this *nonlinear movement* will also be retained in the residual phase. Past studies (Ferretti et al., 2000c; Colensanti et al., 2003a; Kampes and Hanssen, 2004) have shown that it is feasible to achieve with nonlinear (e.g. seasonal) movement estimation provided that large number of SAR images are available (normally more than 30 images). Alternatively, it might be possible to differentiate this nonlinear movement from other phase components by applying suitable filters. I have not estimated either the nonlinear motion or the atmospheric delay terms due to interferogram constraint. In this section instead, the feasibility of applying temporal and spatial filters to separate the signal of interest, i.e. nonlinear movement and atmospheric phase delay, is investigated. The main purpose is to investigate if it is possible to separate the nonlinear component from other components based on existing interferometric data configuration[9].

I applied a few filtering steps both spatially and temporally to the 19-IFGM data. A filtering scenario describing input and output data is illustrated in fig. 4.24. To validate the results, filtered phases were converted to range (in mm) and compared with the leveling measurement point by point. The obtained results are successively presented and discussed.

[9]Note that i have not applied any filtering to the 15 IFGMs estimates due to unsuitability of data configuration.

Table 4.3: Interferometric signal components and their characteristics

Phase Components	Space	Time
1. Linear (LN) displacement	correlated	correlated
2. DEM error	correlated	uncorrelated
3. $S^{i,0}_{p,p'}$	correlated	uncorrelated
4. $S^{0}_{p,p'}$	correlated	correlated
5. Nonlinear (NL) displacement	correlated	correlated
6. Orbit error	correlated	uncorrelated
7. Noise	uncorrelated	uncorrelated

Signal characteristic

It is necessary to know how the signal of interest behaves spatially and temporally. Depending on these characteristics, the corresponding filter can be applied. Different interferometric signal components and their behaviors are summarized in table 4.3.

The $S^{i,0}_{p,p'}$ symbolizes the atmospheric phase delay of interferogram i while $S^{0}_{p,p'}$ denotes the master atmospheric delay. In table 4.3, the phase components in items 1 and 2 were estimated while items 3 to 7 contributed to the residual phase.

The following diagram (fig. 4.24) illustrates the applied filtering steps used to obtain the nonlinear displacement component. As described in section 4.7, i therefore assume that there are 3 main contributions in the residual phase, namely nonlinear motion (NL), atmospheric phase delay ($S^{i,0}_{p,p'}$ *and* $S^{0}_{p,p'}$) and noise (NSE). Initially, the temporal averaging of residual phase was carried out to obtain the so called 'master atmospheric' contribution phase. It is based on an assumption that the master atmospheric phase has not changed over time (a to b in fig. 4.24). After the master atmospheric delay was removed, a spatial low-pass filter was applied to separate the correlated signal (low-frequency) from the uncorrelated signal (high-frequency). As a result, the nonlinear motion and the atmospheric phase screen for each interferogram were obtained as the low-pass component, and noise as the high-pass component (c to obtain d and e). Finally, the temporal low-pass filter was utilized to separate the nonlinear motion (f) from the interferometric atmospheric phase delay (g) as the former part is correlated in time while the latter part is temporally uncorrelated. In principle, half the size of the applied filter window should be at least equal to the correlated size of the signal of interest. I applied the filter size of 6 months and 1 km for the temporal and spatial low-pass filter respectively. All filters used are the triangulate filters. The red boxes in fig. 4.24 indicate the primary results that are interested in this study.

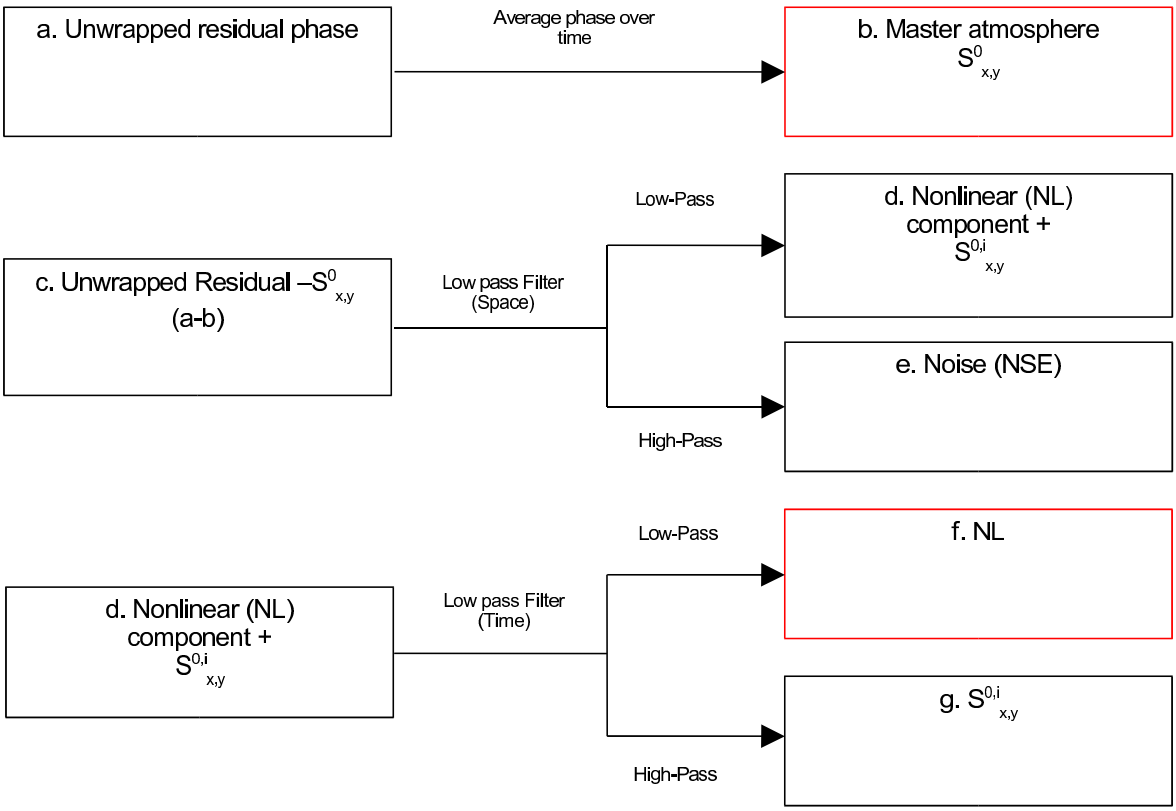

Figure 4.24: Filtering scenario to obtain NL displacement (d) and master APS (b)

Filtering results

Fig. 4.25 presents the master atmospheric phase estimates resulting from temporal averaging of the unwrapped residual phase value. Such image reveals the spatial variations of the estimated atmospheric contribution phases in the master scene in radian. The blue and red colors indicate PSs with relatively high atmospheric contribution. Note that these atmospheric contribution phases do not influence in the linear displacement estimation as they are treated as a contribution to the residual phase.

Table 4.4 summarizes mean and standard deviation of filtered phases, namely the nonlinear motion, the interferometric atmospheric phases and noise in degrees and ordered by slave acquisition time. The repeated acquisition times in the table indicate tandem[10] data. Observing the nonlinear component, large phase jumps can be recognized where the acquisition time gaps are greater than 6 months e.g. from 10.96 to 05.97 and from 06.98 to 12.99. Similar effects can be better observed from the temporal plot of subsidence measurements at PS presented in fig. 4.27 to 4.31.

Interferometric atmospheric phase delay are caused by the differences of the atmospheric contribution phases both in space and in time in an IFGM. The significant difference due to spatial and temporal variation in water vapour distribution between the two acquisition time is the main reason contributed to this atmospheric delay. Their phase statistics therefore vary with different mean and standard deviation depending on the difference of the weather conditions. The mean noise levels at PSs in all IFGMs are satisfactorily low (less than 1 radian), confirming that the selected PS are good point scatterers.

[10] 1 day satellite revisit time between 2 acquisitions

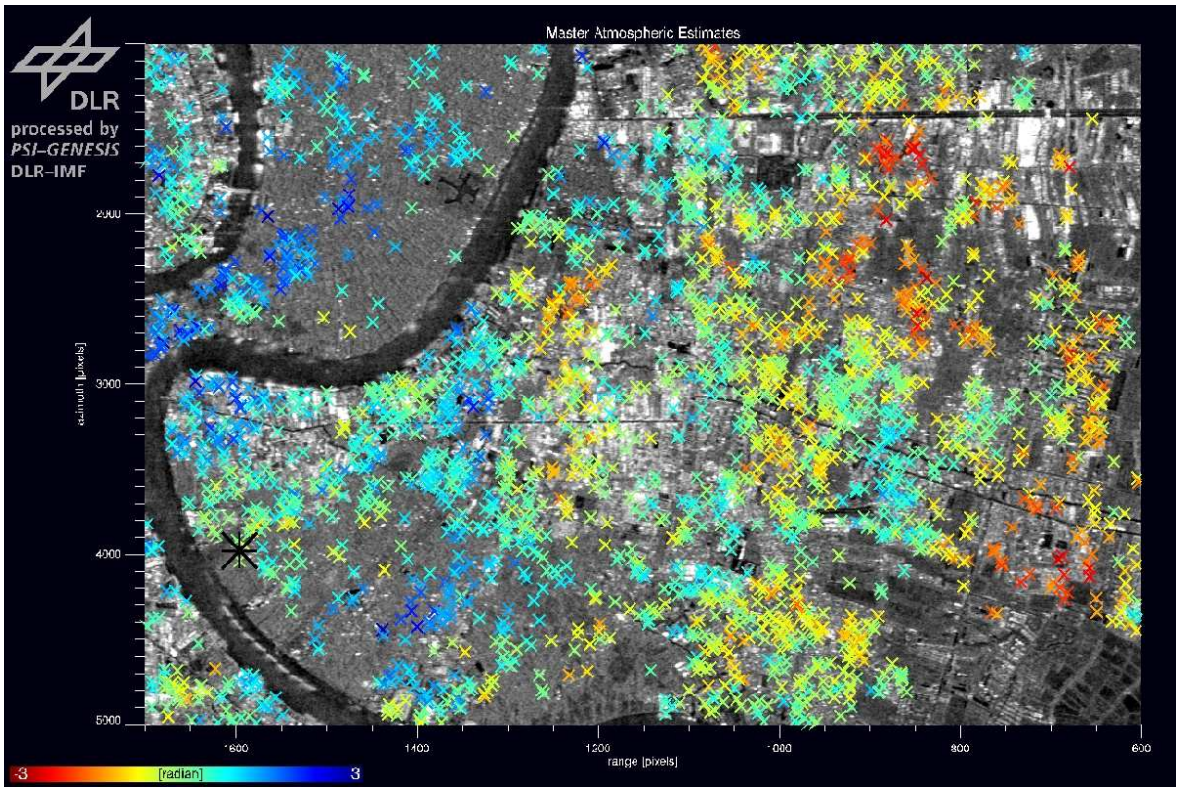

Figure 4.25: Estimated master atmospheric phase results from phase averaging (refer to product b in fig. 4.24) red: -3 radian, blue: +3 radian

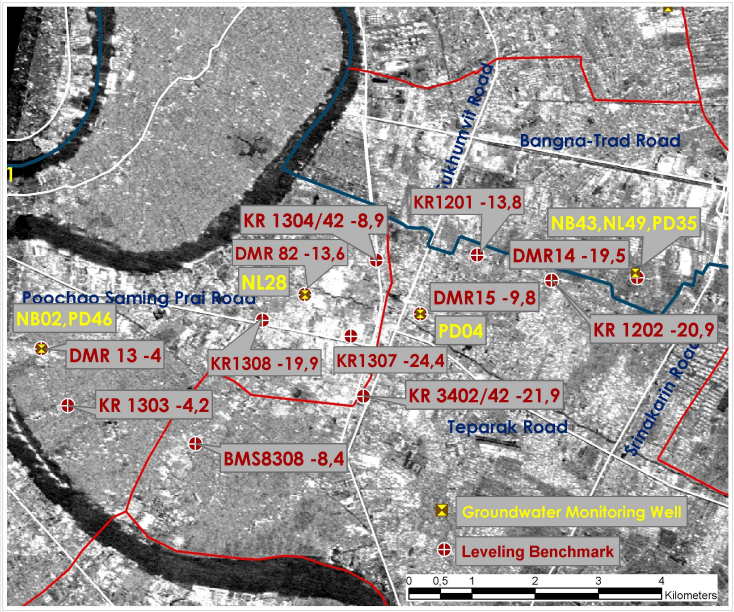

Figure 4.26: Location of benchmarks and their corresponding linear subsidence estimates are presented as reference for fig. 4.27 to 4.31.

Table 4.4: Statistics of filtered phase components (in degrees)

IFGM	NL	NL (SD.)	$S^{i,0}_{x,y}$	$S^{i,0}_{x,y}$(SD.)	Noise	Noise(SD.)
02.96	-22.9	15.9	-19.8	20.8	-2.3	24.3
02.96	-22.8	15.9	-2.4	16.4	-0.5	19.9
03.96	-20.3	15.2	-70.6	28.7	-3.9	36.3
03.96	-20.1	15.2	75.7	47.6	2.1	44.6
04.96	-17.1	13.0	47.4	27.6	1.0	41.2
05.96	-17.0	12.9	-72.3	38.8	-2.8	40.3
06.96	-10.7	9.7	34.7	40.7	-0.2	33.5
07.96	-5.7	8.4	-9.4	33.8	-0.9	37.0
08.96	1.5	8.3	-17.1	23.8	0.2	28.9
09.96	11.1	11.7	4.8	20.0	1.3	25.1
10.96	22.3	18.3	48.8	38.4	1.9	27.9
05.97	-60.0	36.9	-5.1	2.5	-1.7	28.3
11.97	40.1	25.8	17.5	26.4	3.5	34.3
01.98	38.0	24.1	-25.4	37.8	0.1	35.1
04.98	42.9	25.4	14.3	26.6	1.9	39.4
06.98	44.6	30.8	-0.3	21.6	1.9	42.7
12.99	-8.6	7.1	28.1	20.8	0.3	24.3
12.99	-8.7	7.1	-33.8	18.7	-1.6	14.8
01.00	-7.8	6.6	6.1	10.1	-0.2	16.9

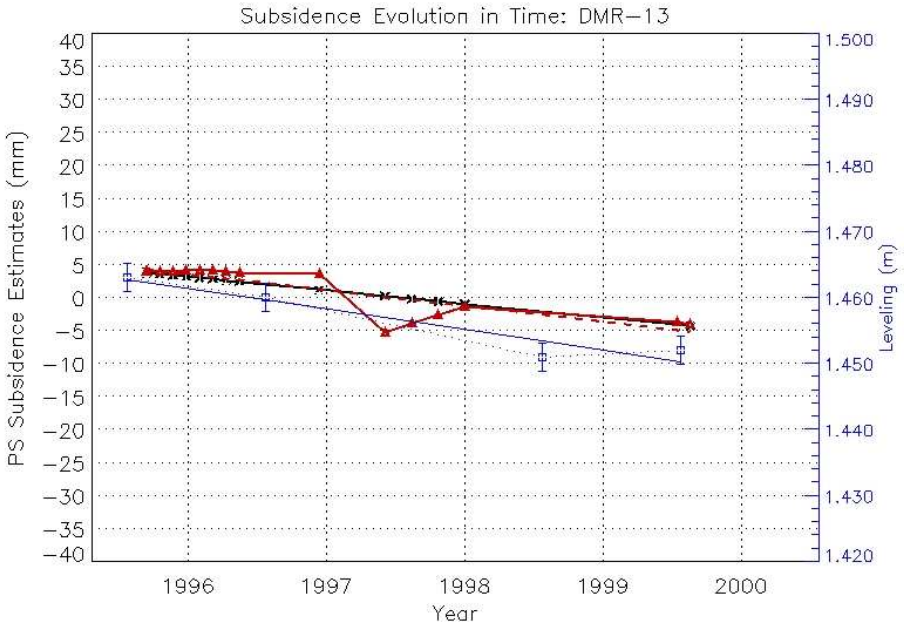

Figure 4.27: Subsidence evolution at a PS (PS23872) located 200 m away from the benchmark (BM-DMR13) shows the linear (black crosses) displacement estimates at the radar acquisition time (1996 - 2000) resulting from PS analysis and the nonlinear (red triangles) displacement estimates resulting from filtering. Their linear LS fits are presented in the corresponding colors. For comparison, leveling measurements (blue squares) at BM-DMR13 of the same time are also presented. Note that slopes of all the lines represent estimated subsidence rates. The plots use a relative scale, slopes are directly comparable. Forthcoming fig. 4.28 to 4.31 present subsidence evolution at other locations in the same way. Quantitative comparison of these subsidence rates is tabulated in table 4.5.

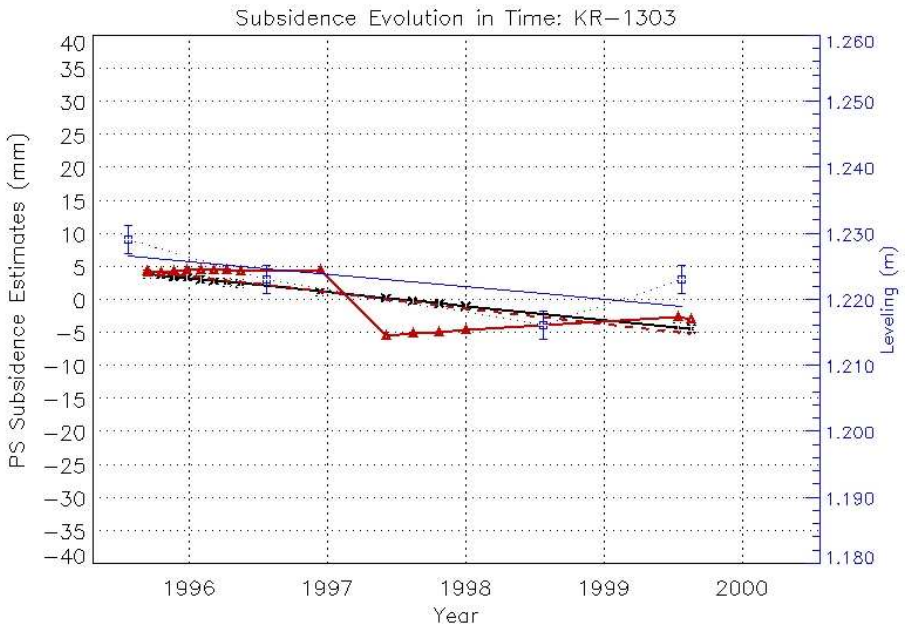

Figure 4.28: Subsidence evolution at a PS(PS26163) located 45 m away from the benchmark (BM-KR1303).

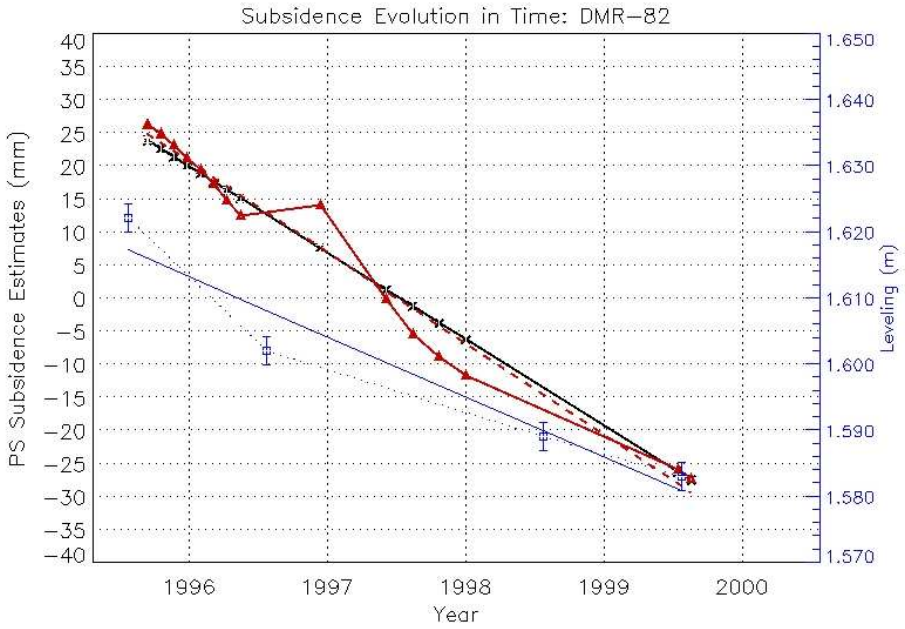

Figure 4.29: Subsidence evolution at a PS (PS18234) 170 m away from the benchmark (BM-DMR82).

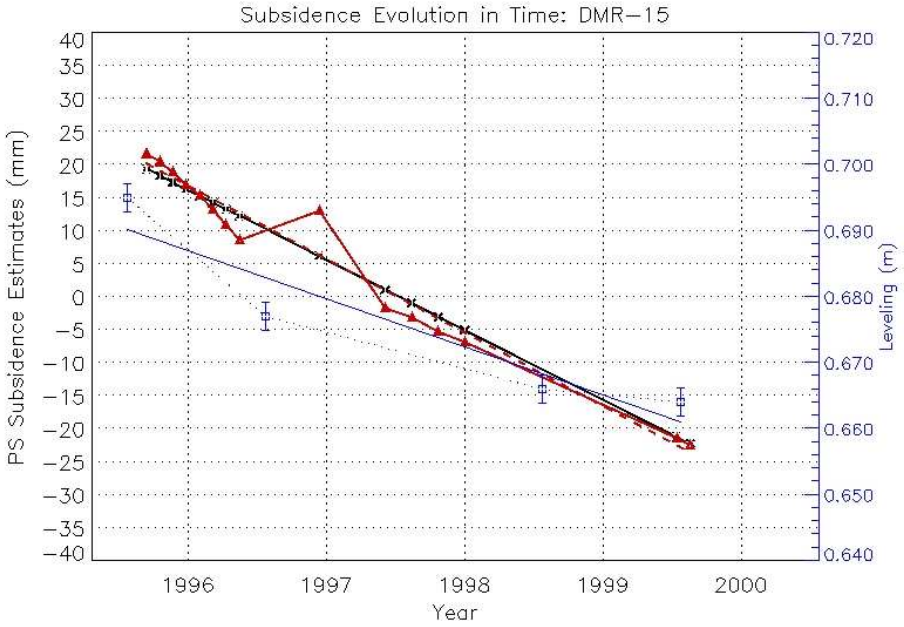

Figure 4.30: Subsidence evolution at a PS (PS17800) located 35 m away from the benchmark (BM-DMR15).

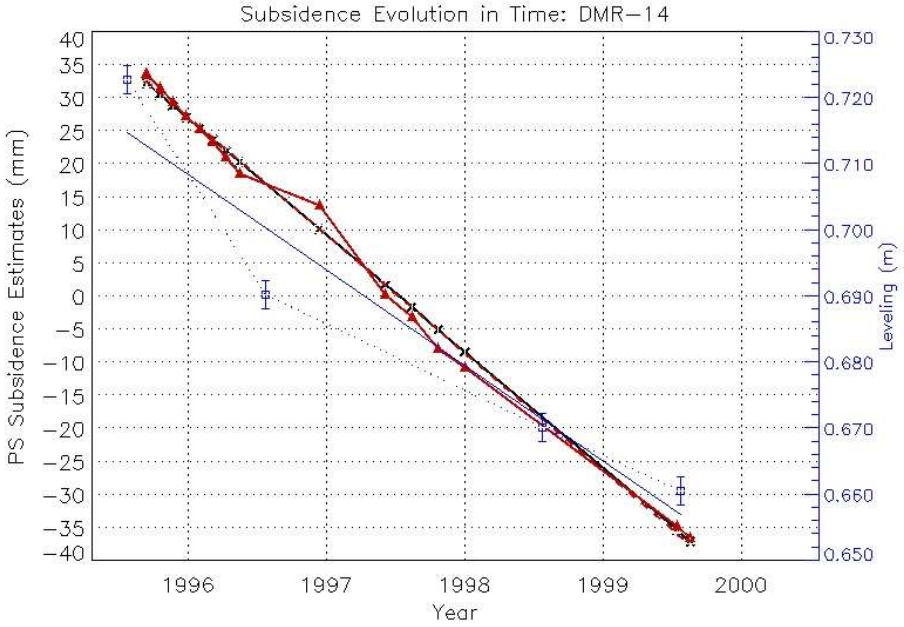

Figure 4.31: Subsidence evolution at a PS (PS14176) located 80 m away from the benchmark (BM-DMR14).

Fig. 4.27 to 4.31 visualize evolution of subsidence measurements at PS compared to the leveling benchmark measurements spanning the same time from 1996 to 2000. These PS are selected as they are the best estimates providing the highest coherence and are located nearest to the benchmark. The nonlinear motion rates were least-square estimated (red dashed line) in order to compare them with the PS linear subsiding rate (black-solid line) and the subsiding rates from the precise leveling (blue solid line). Additional to these figures, fig. 4.32 also presents the LS estimates of the PS actual (unwrapped) phase measurements (pink lines). This aims to demonstrate the influence of filtering process on the nonlinear motion component. Table 4.5 summarizes and compares the subsiding rates (coupling with their RMS differences) obtained from PS analysis (linear), from LS fits of nonlinear and from the linear+residual PS measurements against the benchmark leveling (used as reference).

My assumption was that if the nonlinear component separation process is robust, it should be able to improve PS measurements when compared to a leveling measurement especially at the nonlinear motion benchmarks. The correlation coefficient (R^2) in table 4.5 is presented as an indicator of degree of linearity of the leveling measurements at each benchmark. The comparison shows that the nonlinear and the linear+residual measurements can better approximate the leveling measurements at the nonlinear locations (DMR 13, KR 1303). At BM-KR 1303, the linear+residual PS measurements is the better estimates than the PS nonlinear measurements. Subsidence due to the compacting aquifer is a time-dependent process. Its temporal behaviour can be correlated over relatively short or long time determined by the aquifer sytem properties and the pumping behaviour at individual location. This correlation length and the temporal sampling of interferometric data strongly influence the filtering results. In a sense that, if the correlation length is longer than the interferograms sampling, the nonlinear signal can be constructed successfully and vice versa. Therefore, the highest sampling of SAR data in time (i.e. 35 days for ERS-1/2) is optimal for the extraction of the nonlinear displacement component. Nonetheless, results show that the nonlinear and the linear+residual measurements are the better estimates (than the PS linear estimates) at the nonlinear subsiding locations (fig. 4.32 (a) and (b)). At the linear displacement locations, the estimated linear displacement is the best estimate for subsidence rate at BM-DMR 15(fig. 4.32 (c)). At BM-DMR 14, the nonlinear estimates are found to be better than the linear estimates. Fig. 4.32 (d) explains that a highly linear subsiding location like DMR 14 (indicated by high R^2) can possess a certain degree of nonlinear behaviour. In such case, the nonlinear estimates perform the better result. Additionally, this implies that many locations in this area subside nonlinearly

with time.

Evaluation of results as shown in table 4.5 and fig. 4.32 can infer that the accuracy of the nonlinear estimates as a result from filtering is different from location to location depending on the correlation of the nonlinear behaviour in time at that particular location and the temporal sampling of the available interferograms.

Table 4.5: Comparison of subsidence rate (in mm/y) obtained by PS analysis using linear model(LN) , nonlinear, linear+residual and precise leveling

BM ID	(R^2)	Leveling	Linear(RMS*)	Nonlinear (RMS*)	LN+residual(RMS*)
DMR 13	0.72	-4.0	-2.1(2.7)	-2.4(2.3)	-2.0(2.7)
KR 1303	0.66	-4.1	-2.1(3.7)	-2.4(2.6)	-2.6(2.2)
DMR 15	0.94	-9.8	-10.6(10.0)	-11.1(10.6)	-11.3(10.8)
DMR 14	0.97	-18.8	-17.6(8.4)	-17.9(8.0)	-17.6(8.4)

* unit in mm

4.8 Derivation of subsidence surface

In this section, spatial subsidence field will be derived from the displacement estimates at PSs. The *Kriging* method is utilized due to two reasons; first, unlike other interpolation methods the surface is estimated by accounting for spatial variation of the data. Second, through semi-variogram modeling the method is able not only to produce a predicted surface but also to provide a measure of certainty or accuracy of the prediction. This interpolation method assumes that the distance or direction between sample points reflect a spatial correlation that can also be exploited to explain the variation in the predicted surface.

Kriging is a multi-step process consisting of

- statistical analysis of the data
- semi-variogram modeling
- surface prediction.

The estimated displacement rates at reliable PS points (see fig. 4.22) were converted into vertical displacement rates (using eq. 4.14) and georeferenced based on the local datum. The vertical displacement rates at PS points together with their coordinates were then used as the initial input for this derivation. The geostatistical software 'GSLIB' (Deutsch and Journel, 1998) was used for this purpose.

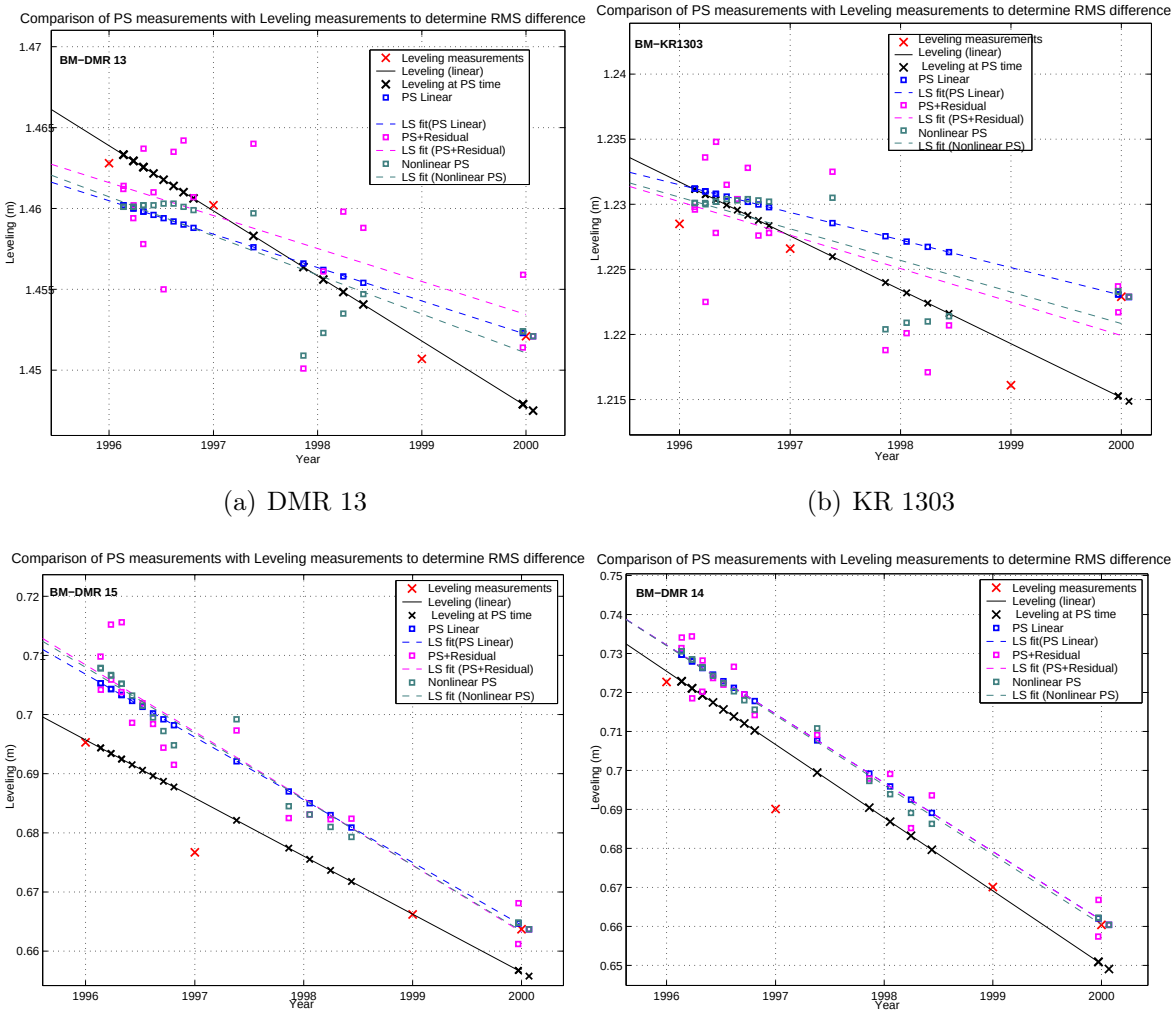

(a) DMR 13

(b) KR 1303

(c) DMR 15

(d) DMR 14

Figure 4.32: Linear least-squares fits of different PS measurements (linear: Blue, nonlinear: Green, linear+residual : Pink) compare to linear leveling measurements (Black) at nonlinear (a) and (b) and linear subsiding locations (c) and (d) . These figures show which PS measurements can better approximate the linear leveling measurements (the Black lines) at each location. The RMS differences for the comparison are presented in table 4.5.

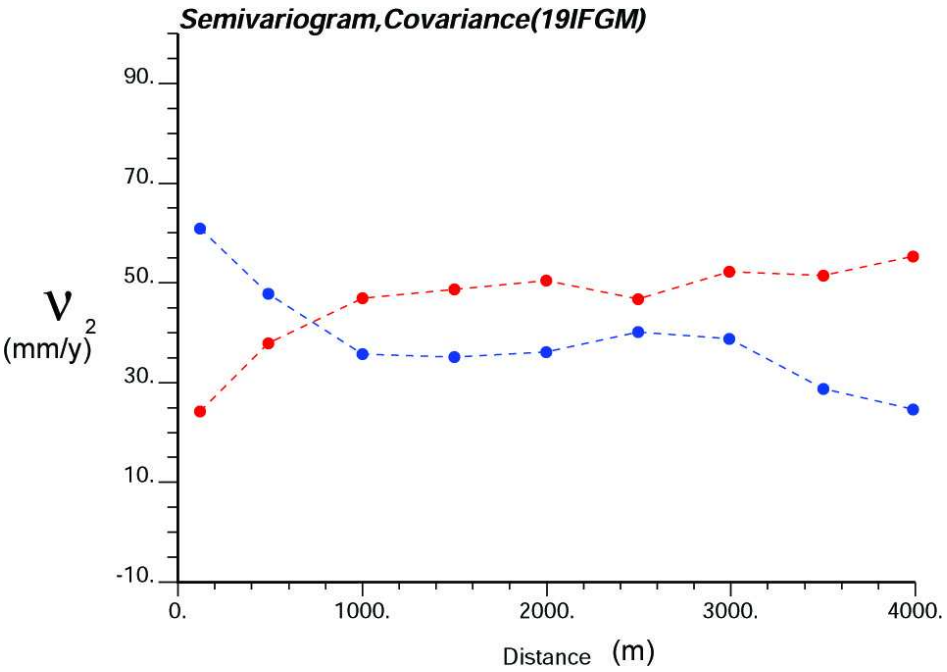

Figure 4.33: Semivariogram (red dashed line) and covariance (blue dashed line) plot of displacement rate derived from 19-IFGMs data

Statistical analysis of the data begins with the calculation of an empirical semi-variogram from the sampled points follows eq. 4.16

$$\nu(h) = \frac{1}{2n} \sum_{i=1}^{n} \{Z(x_i) - Z(x_i + h)\}^2 , \tag{4.16}$$

where n denotes the number of all sample pairs located at distance h away from each other. $Z(x_i)$ denotes data value at location x_i and $\nu(h)$ the average semi-variance. Eq. 4.16 states that semi-variance of a data set is half of the average of squared difference of Z of all pair locations located within h distance from each other. In this case, Z is the displacement rate. Fig. 4.33 illustrates a semi-variogram derived from the estimated displacement rates of 19-IFGMs.

The semi-variogram presents the average semi-variance $\nu(h)$ on the Y-axis and the distance (h) on the X-axis. It implies a certain characteristic of many geographical parameters in that the pair locations that are closer (far left on the x-axis) have more similarity (low on the y-axis) than the pair locations that are farther apart (high value in squared difference, high on y-axis). Eq. 4.17 defines the relationship between semi-variance and covariance $C(h)$. It can also be observed that when the distance increases, semi-variance increases but the covariance decreases (see fig. 4.33). This is because

$C(0)$ is variance ($h = 0$) and is a positive constant value (see eq. 4.17).

$$\nu(h) = C(0) - C(h) \tag{4.17}$$

The generated semi-variogram graph did not provide information for all possible distances and directions. To facilitate the interpolation, it is necessary to fit a continuous function to the generated semi-variogram. This is also known as *semi-variogram modeling.* This is a key step that connects between spatial description and spatial prediction (interpolation). There are several mathematical functions that could be utilized to model the semi-variogram. Among those functions, the spherical model and the exponential model are often used. Here, the exponential model was used, as the covariance function appears to reach zero at infinite distance. Fig. 4.34 presents a semi-variogram of the displacement rates with their exponential fit (black line) from two data sets (blue for 15-IFGMs and red for 19-IFGMs). From this plot, the range distance, where the semi-variance starts to level out, of 1000 and 1200 meters were chosen for the red and blue plots respectively. It implies that beyond this range distance, the displacement rate is no longer spatially correlated. This range distance is important during the interpolation process, i.e. the subsidence estimates located outside this range will be weighted (λ_i is weighting factor see eq. 4.18) equally. The semi-variance curves of the estimates from two different IFGM stacks look similar but with different mean semi-variance values (seen as a shift of the blue dashed line above the red dashed line as shown in fig. 4.34). The fact that these semi-variance values were derived from different set of PSs can be an explanation.

After a suitable model is fit to the empirical semi-variogram, the *subsidence surface can be predicted* by kriging. Eq. 4.18 reveals the kriging formula.

$$\hat{Z}(x_0) = \sum_{i=1}^{n} \lambda_i Z(x_i) \tag{4.18}$$

$Z(x_i)$ is the measured value at x_i location

λ_i is the weight factor for the measured value at x_i location following the applied model

x_0 is the predicted location

n is the number of measured values surrounding x_0 location

Kriging process assigns a value to the unsampled location x_0 according to the selected exponential model. Upcoming figures show the kriging interpolation results. It should be noted that the subsidence fields shown here represents rather an average (linear) subsidence rate over a time span from 1993 to 2000 (fig. 4.35) and from 1996 to 2000

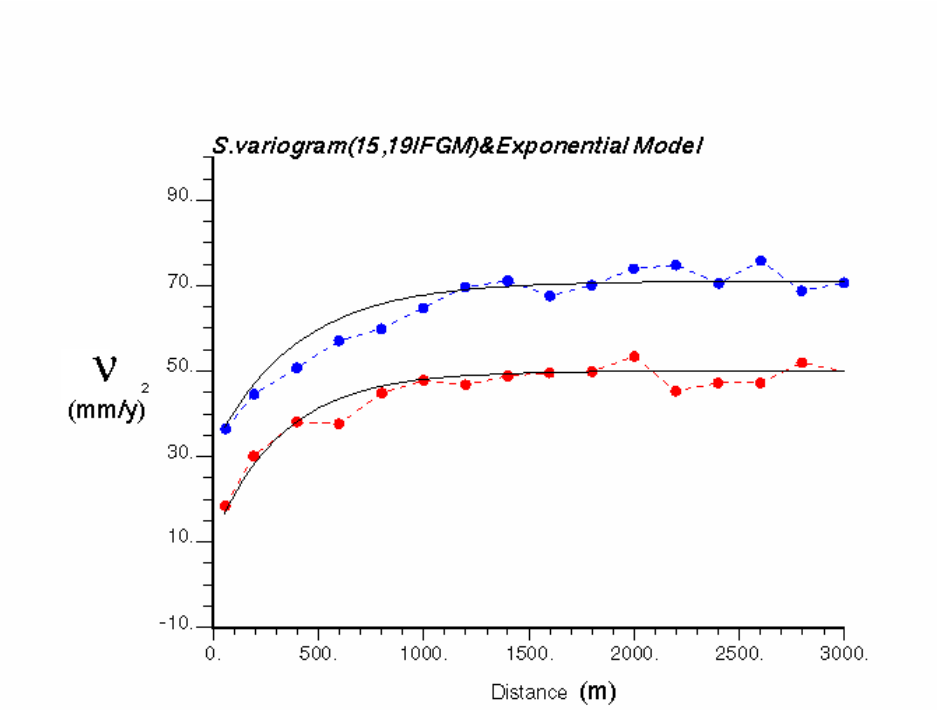

Figure 4.34: Semi-variogram plots of 15-IFGMs (blue dot) and 19-IFGMs (red dot) data modeled by exponential function (black solid line)

(fig. 4.36) than subsidence rate at a certain point of time. The higher mean semi-variance of subsidence estimates from 15 IFGMs implies that the derived subsidence pattern will also have a higher spatial variation than of the 19 IFGMs as shown by the results in fig.4.35 and 4.36. The subsidence pattern in the latter case is more uniform. The difference between these two interpolated subsidence estimates was calculated and presented in fig. 4.37. The dark blue and red colors indicate areas where significant differences were found. It was found that such differences were encountered at the location where PSs are not present (blue area in the northeast) or where spatial subsidence rates derived from 15 IFGMs are highly variated (red area). Validation of these interpolated displacement rates with the independent reference data of precise leveling will be carried out in subsection 4.10.2.

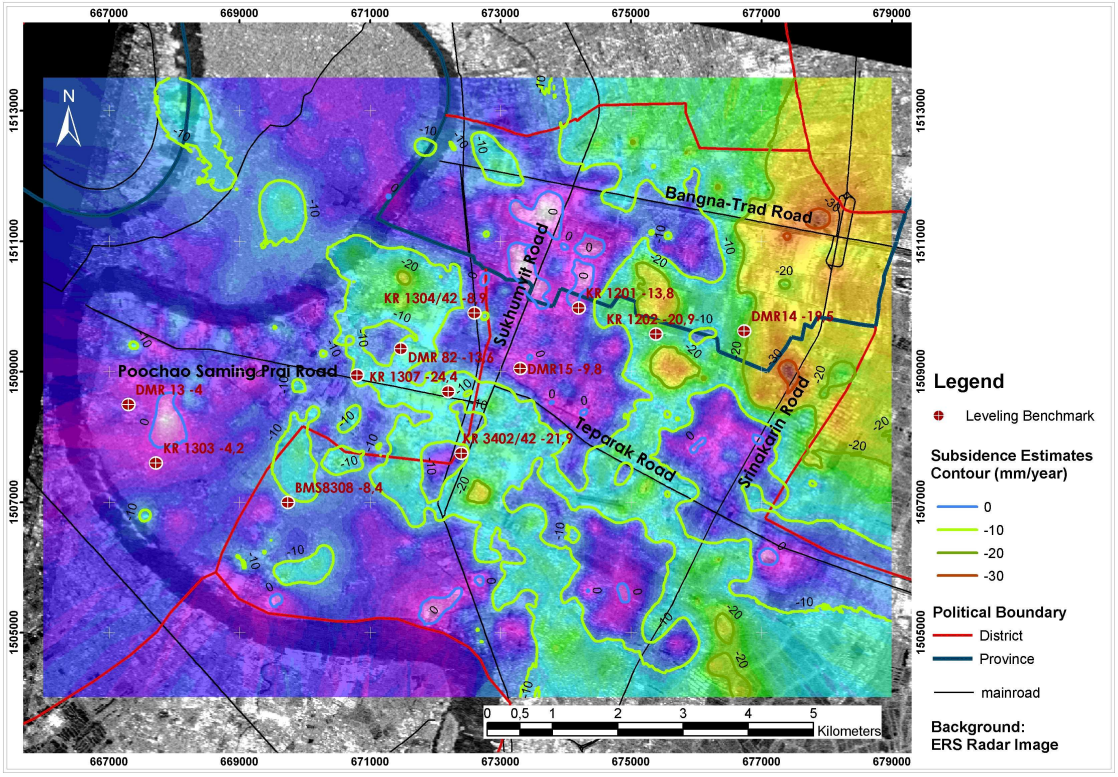

Figure 4.35: Derived subsidence field by kriging (15 IFGMs)

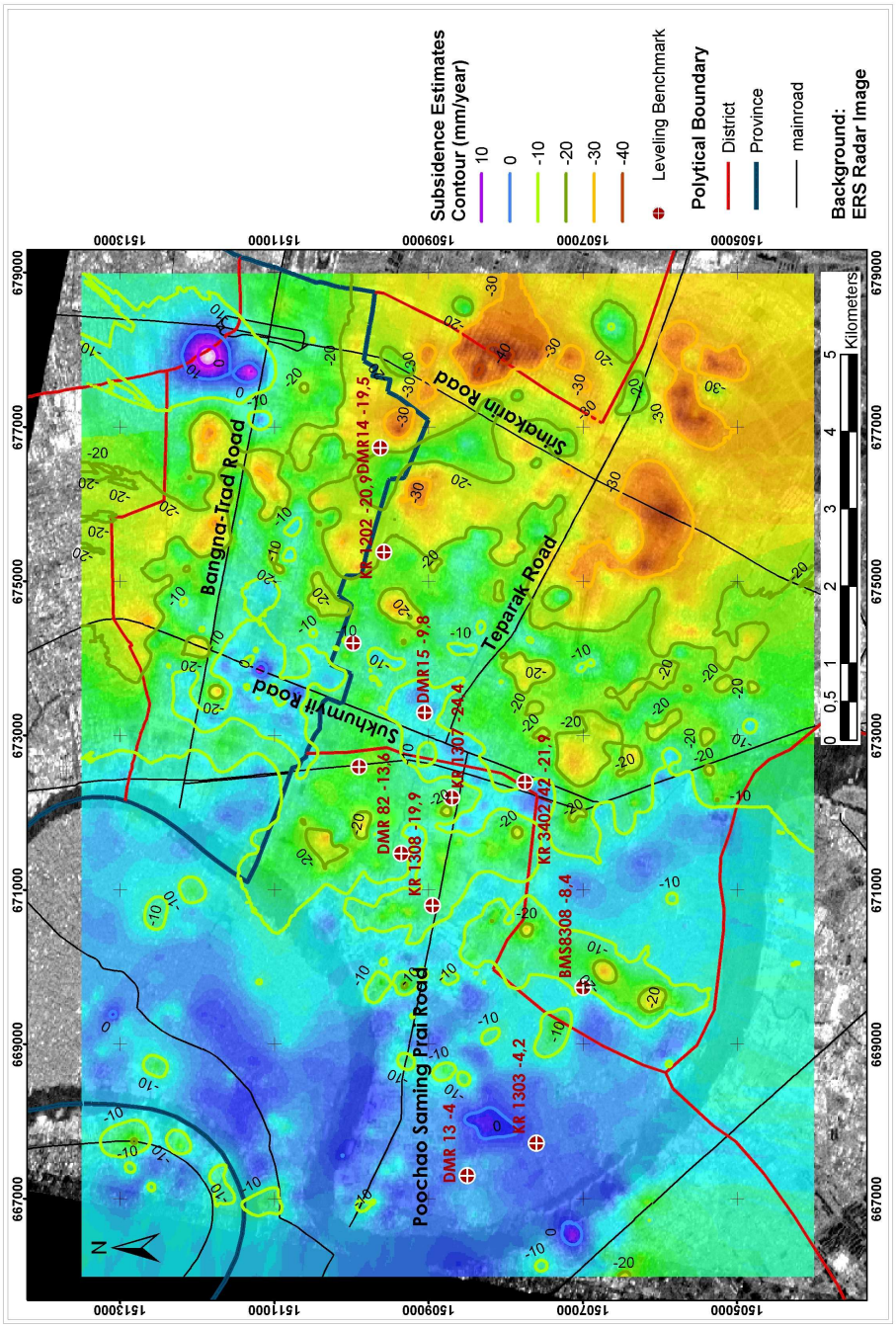

Figure 4.36: Derived subsidence field by kriging (19 IFGMs)

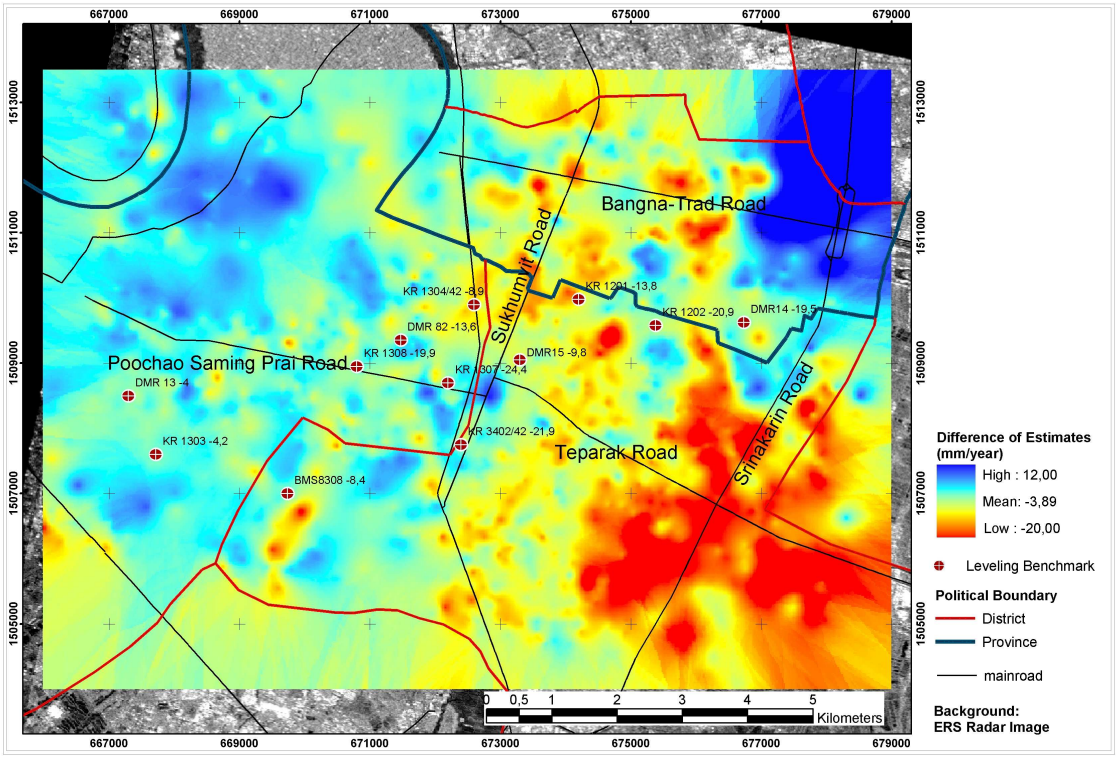

Figure 4.37: Difference of interpolated subsidence estimates (19 IFGMs - 15 IFGMs)

4.9 Quality description of the estimates

PS subsidence estimates

The precision of the unwrapped phase observations used in the final ILS estimation can be obtained by estimation of a final a posteriori variance factor $\underline{\hat{\sigma}^2}$ for any PS point: p. This factor is calculated using the least squares temporal phase residuals (difference) with respect to the reference point. Temporal phase residual is assumed to be zero at the reference point. The higher the temporal phase residuals, the lower the estimate precision. This posteriori variance factor is used to scale the a priori variance-covariance (vc) matrix Q_{ifg} of the double difference phase observations describing the quality of the unwrapped phase observations as (see Kampes, 2005):

$$Q_{ifg_p} = \underline{\hat{\sigma}^2} \cdot Q_{ifg}. \tag{4.19}$$

In a similar way, the precision of the PS subsidence estimates at point p can be described by the vc-matrix $Q_{\hat{b_p}}$ with respect to the reference point. It is performed by scaling

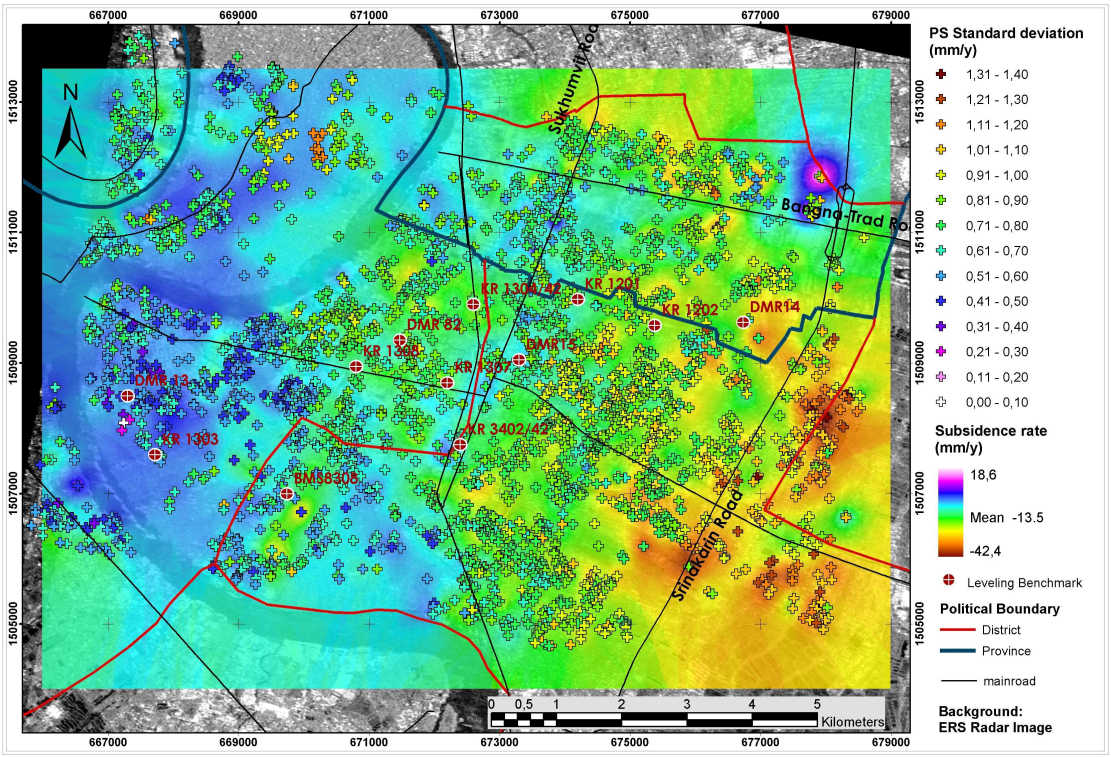

Figure 4.38: Standard deviation of the estimated displacement rates (PS analysis)

the propagated vc-matrix of the estimated parameters $Q_{\hat{b}}$ with the same a posteriori variance factor:

$$Q_{\hat{b_p}} = \underline{\hat{\sigma^2}} \cdot Q_{\hat{b}} \tag{4.20}$$

Detailed derivation of the posteriori variance factors and all related terms can be found in (Kampes, 2005).

The derived standard deviation obtained from the $Q_{\hat{b_p}}$ vc-matrix of the displacement estimates is shown in fig. 4.38. In the map, colors of each PS (plus sign) represent standard deviations in mm/year of the linear PS displacement estimates superimposed on the interpolated displacement estimates derived by the kriging method. It shows that the precision of the PS estimates is relatively high and is better than 1.4 mm/year. The relatively high precision of PS estimates shown here could be used to imply that significant differences in fig. 4.37 are mainly due to less reliable estimates from 15 IFGMs.

Precise leveling estimates

Comparison of precise leveling information with the derived linear subsidence rate from PS analysis requires conversion of leveling information into subsidence rate. This can be done through the linear least-squares fit to the leveling measurements. Slope of this straight line represents the linear subsidence rate occurring during that time frame.

A linear relationship between independent x and dependent y variables can be written as:

$$y_0(x) = a_0 + b_0 x \tag{4.21}$$

In our case, x is the time variable and y represents surface elevation at time t. We expect to estimate the parent coefficients a_0 and b_0 for a line that provide an optimum fit to our measured values y_i. In principle, it is possible to estimate y_0(parent population) from an infinite number of measured y_i values. In practice, we usually obtain one y_i corresponding to one x_i. The idea of the linear least-squares fit is to find the best estimate of a and b coefficients that maximize the probability for making N measurements of y_i with standard deviation σ_i for the observations about the actual value y_0. In other words, finding a and b that minimize the goodness of fit parameter χ^2. This can be expressed as:

$$\chi^2 = \sum \left[\frac{1}{\sigma_i} (y_i - a - bx_i) \right]^2 . \tag{4.22}$$

In general, there are two types of errors from a measurement. Systematic errors usually originate from instrument or observer. The statistical error is caused by the statistical fluctuation of the measurement. The precision leveling information used here was systematically corrected (DMR, 2002) and unfortunately the information is insufficient to derive accuracy for individual leveling data. The following conditions were applied in deriving the LS error for the linear fit:

1. The length of a leveling line is about 2-15 km.in the city area and more than 15 km. in the suburbs

2. In a leveling survey, the disclosure of a profile line is better than $\pm\, 2.33\sqrt{K}$, where K is the profile distance in km. I used $K = 15$ to derive the upper bound of the error.

3. All leveling measurements measured during the period 1993 - 2000 are derived

from the same parent distribution and therefore the same standard deviation from 2 can be applied.

I assumed the same standard deviation σ value for all leveling measurements. The linear fit to the data is calculated by the method of determinants described in (Bevington and Robinson, 1992) chapter 6 . Equations 4.23 to 4.27 describe how the linear coefficients a,b for leveling information can be derived.

$$a = \frac{1}{\Delta}\left(\sum x_i^2 \sum y_i - \sum x_i \sum x_i y_i\right) \tag{4.23}$$

$$b = \frac{1}{\Delta}\left(N \sum x_i y_i - \sum x_i \sum y_i\right) \tag{4.24}$$

$$\Delta = N \sum x_i^2 - (\sum x_i)^2 \tag{4.25}$$

$$\sigma_a^2 = \frac{\sigma^2}{\Delta} \sum x_i^2 \tag{4.26}$$

$$\sigma_b^2 = N \frac{\sigma^2}{\Delta} \tag{4.27}$$

Here, we are interested in the standard deviation of the estimated slope (see eq. 4.27 or *sigb* indicated in fig. 4.39) which is the uncertainty of the estimated linear subsidence rate obtained from leveling measurements. When x_i and the number of measurements N have not changed, σ_b^2 depends primarily on the variance of the leveling measurement σ^2 which is constant for all benchmarks in this case. As a result, error-bars for some leveling benchmarks can be identical. Fig. 4.39 shows an example of LS fit result of leveling survey data (red cross with black error bars) from benchmark DMR-82. The blue line is the best linear fit to the data, while the magenta line and the green-line indicate deviations of $\pm\sigma_b$ respectively. These standard deviation values are represented as error-bars in fig. 4.45 and 4.46.

Kriging Interpolation error

Error from kriging interpolation follows the applied statistical model, i.e. the exponential model. The error is induced by the deviation of the data points from the model. Standard deviation of PS and interpolated PS estimates are visualized in fig. 4.40.

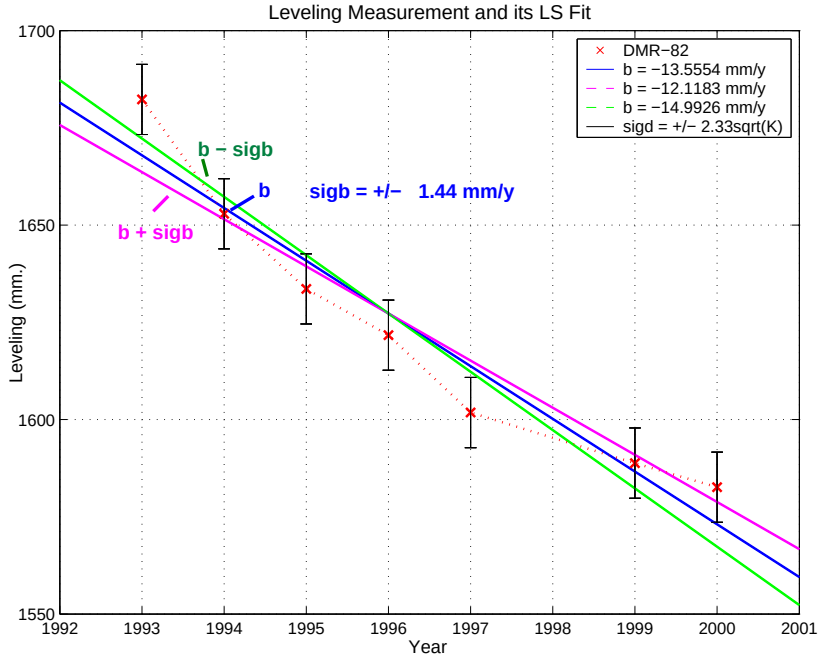

Figure 4.39: Leveling measurement and its LS fit

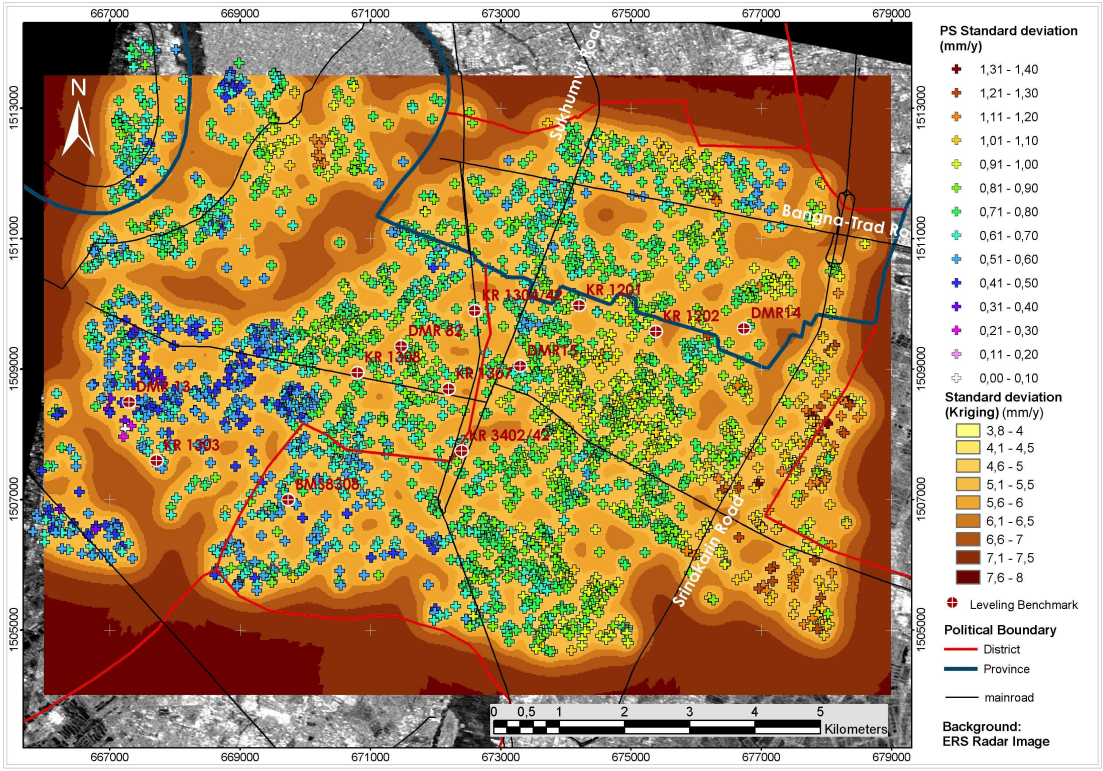

Figure 4.40: Standard deviation of PS and interpolated PS estimates. Standard deviations of the interpolated PS estimates are limited up to 4-5 mm/y (light yellow to orange) at locations near to PS.

4.10 Validation of estimates and discussions

4.10.1 Cross validation between two stacks estimates

For a cross validation between two independent sets (15 IFGMs and 19 IFGMs) of PS estimates, both LOS displacement estimates were converted to vertical displacement rates and georeferenced. The vertical subsidence rates were also adjusted with respect to a subsidence rate of a known point resulting in the absolute subsidence rates. All these steps facilitate spatial comparison between two independent displacement estimates in one image (fig. 4.41). The color scale represents a minimum displacement rate of -45 mm/y (red) to a maximum rate of +45 mm/y (blue). Note that only estimates from the reference network of the 15-IFGM stack (circle) were used in the comparison as the estimated results from the extended network (with more PS) are too noisy. In general, the two sets of estimates agree well with each other in the west side of the AOI. Nevertheless, discrepancies increase toward the east and the southeast. Fig. 4.42 shows a zoom-in of the estimates around the benchmarks that were used to observe the discrepancies visually. Visual investigations for every benchmark can detect differences between these two estimates at some locations, e.g. benchmark KR-1304/42 and DMR-15. The difference map (fig. 4.37) could provide a better spatial overview of these differences. The average difference of absolute subsidence estimates from both stacks is about 4 mm/y. I consider this difference significant. It also implies that the combination of these two estimates is not possible in practice or that the estimates are wrong. Statistics of the absolute subsidence rates from these two data stacks are summarized in table 4.6. At this point it is reasonable to assume that the 15-IFGMs estimate is likely to be less robust than the 19-IFGM estimate. This is due to the fact that the more IFGMs used in the estimation, the better precision we can expect. Results and discussion in the latter part of section 4.10 will be presented to justify this assumption.

Table 4.6: Statistics of absolute displacement estimates compared to relative LOS estimates

Estimates	No.PS, Density (PS, PS/km^2)	[Min, Max] (mm/y)	Mean (mm/y)	STD (mm/y)
(a) 15IFGMs (vert.)	3451, 35.9	[-44.53, 20.29]	-9.00	±8.7
(b) 19IFGMs (vert.)	2739, 28.5	[-45.96, 24.05]	-14.00	±9.7
(c) 15IFGMs (LOS)	3451, 35.9	[-36.53,21.83]	-4.5	±7.9
(d) 19IFGMs (LOS)	2739, 28.5	[-39.37, 26.26]	-9.36	±9.1

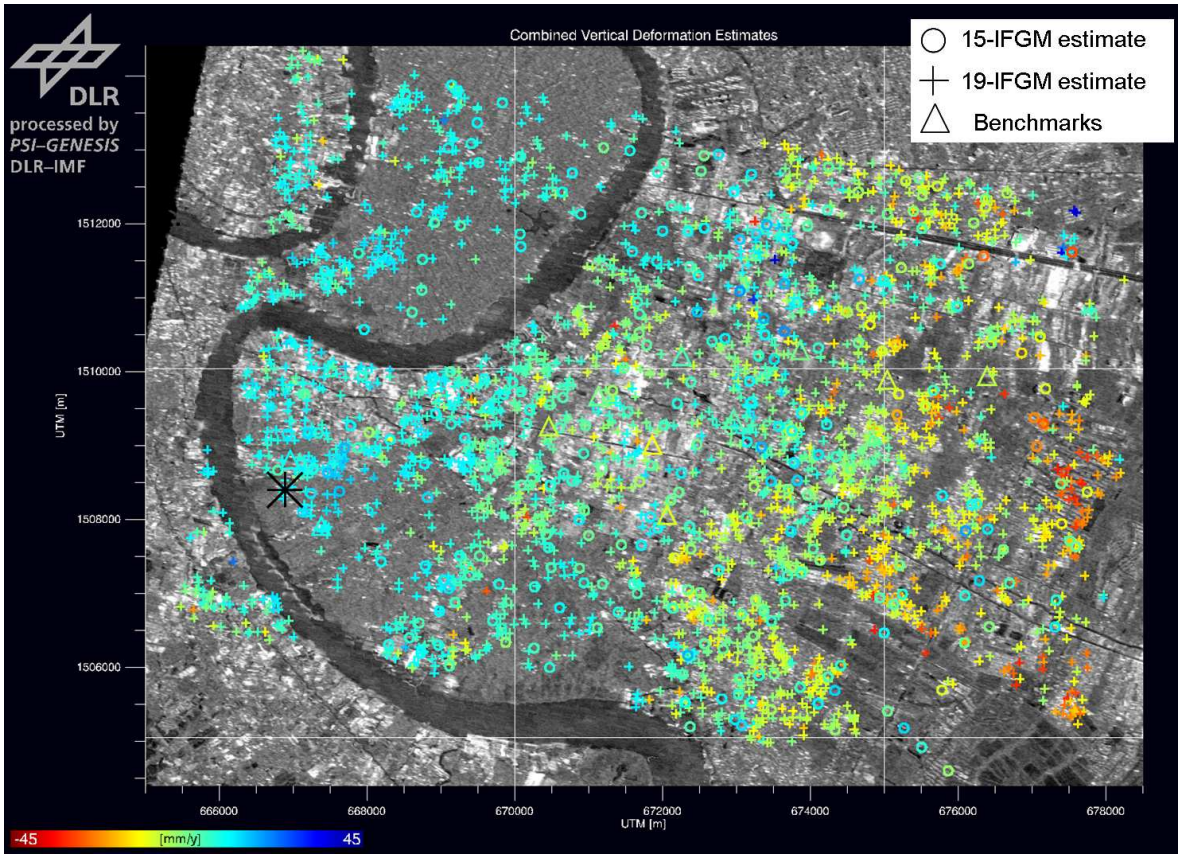

Figure 4.41: Cross validation result between two stacks of estimates

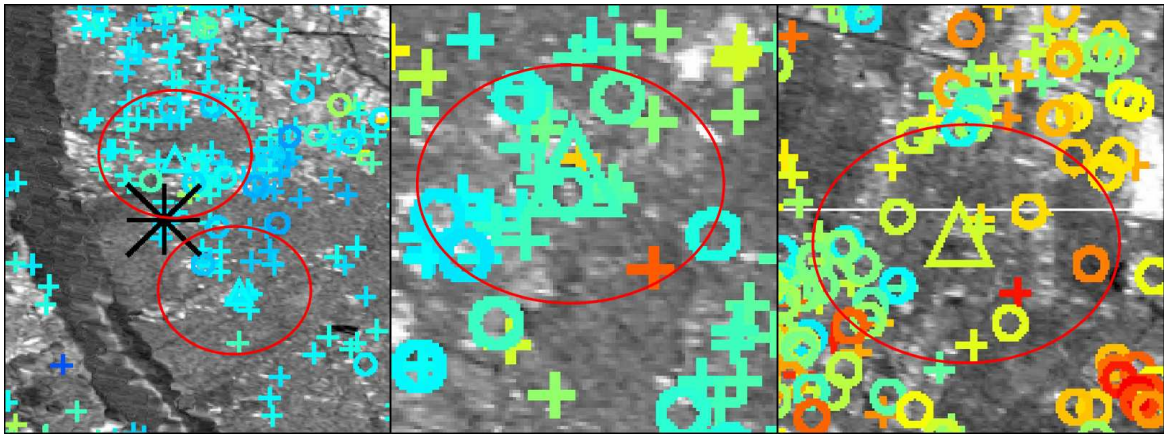

(a) DMR-13 and KR-1303 (b) BMS-8308 (c) DMR-14

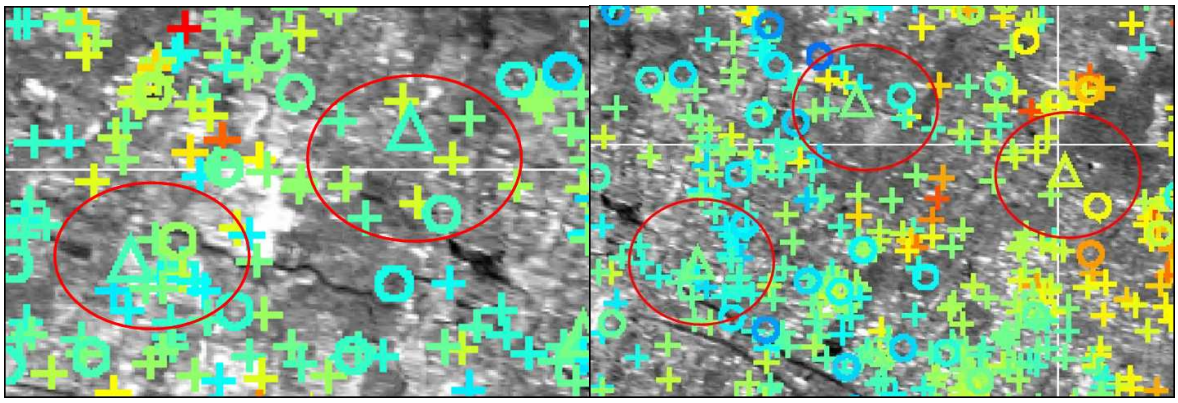

(d) DMR-82 and KR-1304/42 (e) DMR -15, KR-1201 and KR-1202

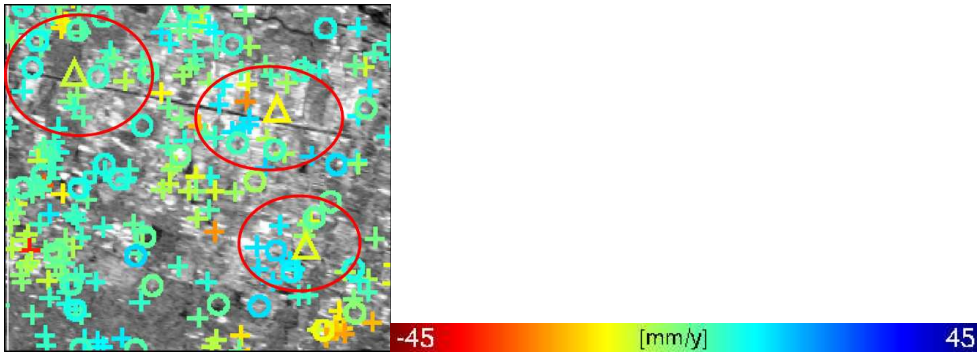

(f) KR-1308, KR-1307 and KR-3402/42

Figure 4.42: Visual investigations of displacement estimates around benchmarks in the AOI for cross-validation purposes.

4.10.2 Validation with leveling measurements

This subsection presents comparison results between PS estimate and the derived (linear) subsidence rate from surface leveling together with the discussion. Two comparison schemes were carried out. In the first scheme, the comparison will be carried out point-wisely. In this case, the best PS estimates around the benchmarks are required. The second comparison compares the interpolated estimate with leveling data. The relative displacement rate obtained from PS analysis was converted to an absolute displacement rate using the reference point's velocity information before comparison.

Based on PS point estimate

The estimate with the highest quality (highest coherence value) and nearest to the benchmark will be selected as the best estimate for that benchmark (nearest neighbor interpolation). This is based on the assumption that if the overall estimates are adequately reliable, then the PS nearest to the benchmark should be able to provide the closest estimate of the subsidence rate while also providing high coherence. Fig. 4.43 shows examples of the best estimate selected for benchmark BMS-8308 and DMR-14 that agree well with the subsidence rates from leveling. There are also locations where the subsidence rates from these two measurement methods do not agree. For all benchmarks, distances between the best PS estimates to the benchmarks varies from 30 to almost 500 meter. The average distance is about 180 m. Fig. 4.45 presents the result of the comparison between best PS estimate and leveling point-wisely along the W-E profile (indicated by the black dashed arrow in fig. 4.44).

Discussion

Fig. 4.45 shows the comparison along the W-E profile at the benchmark locations from two sets of PS subsidence estimates (15-IFGMs and 19-IFGMs) with the independent subsidence rates obtained from leveling surveys. Standard deviation (SD) (derived from vc-matrix in eq. 4.20) of the best PS estimates are indicated by error bars. The PS estimates provide relatively high precision (short error bar) with standard deviation ranging from 0.4-0.9 mm/year (19-IFGMs) and from 0.5-1.1 mm/year (15-IFGMs). The SD of leveling measurements vary depending on the number of measurements available during 1993-2000. Assuming that the leveling measurements were carefully carried out and their accuracies were correctly estimated, they can be used as reference values for this comparison. It can be observed from the plot that at most locations, the PS estimate from 19-IFGMs provides the closer estimate to the reference value than

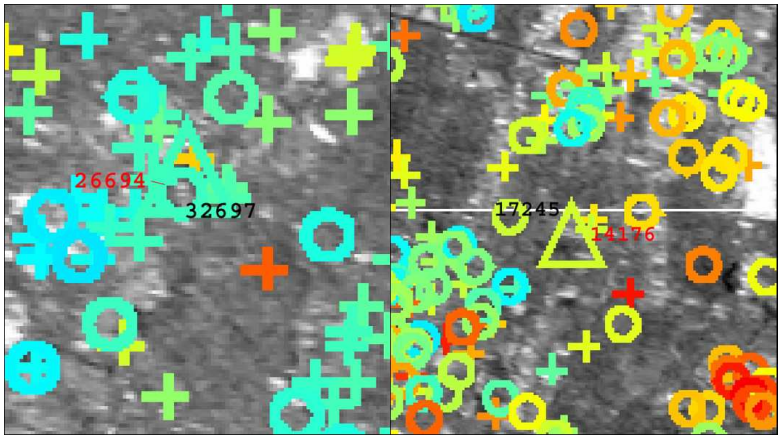

(a) BMS-8308 (b) DMR-14

(c)

Figure 4.43: Example of the selected best estimate around the leveling benchmarks (triangles), black: PS from 15-IFGMs stack, red: PS from 19-IFGMs stack

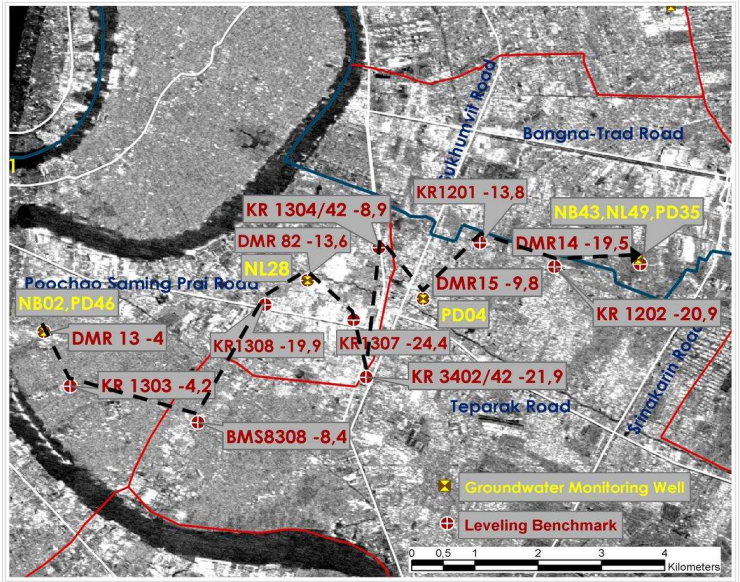

Figure 4.44: Benchmark (red circles) location and West-East profile for comparison (black dashed line)

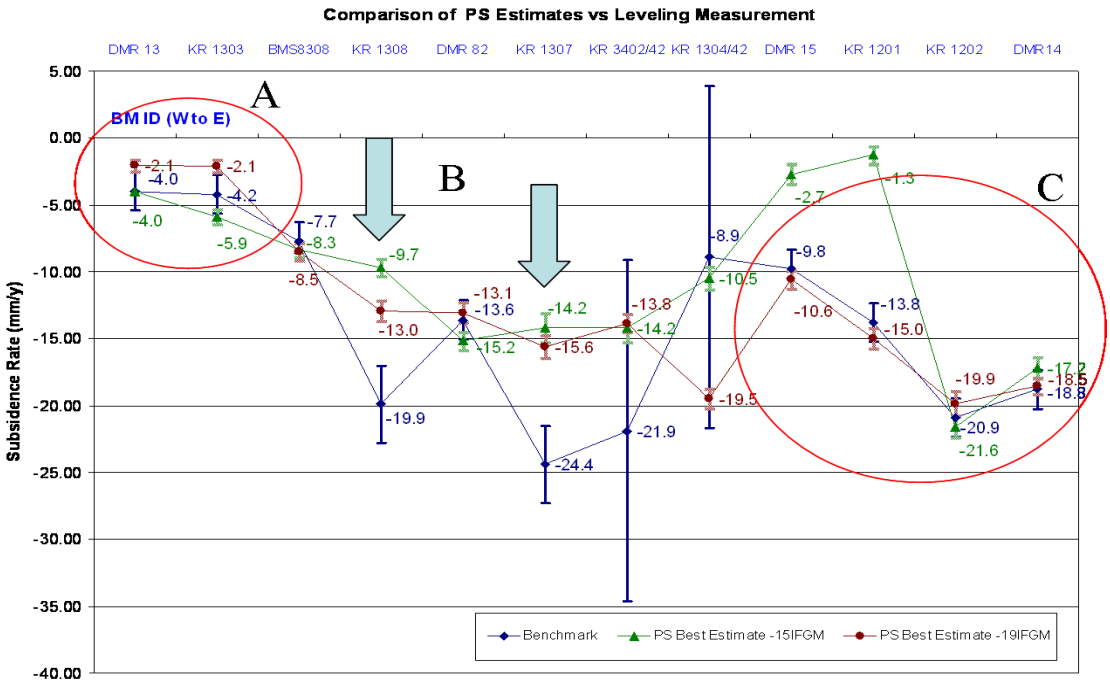

Figure 4.45: Point-wise comparison between the best estimate from PS analysis and the leveling measurement in the area of interest

from 15-IFGMs. Deviations of these PS estimates from the reference values vary in magnitude from small (0.3 mm/year) to considerable (8.8 mm/year). Estimates from 8 out of 12 benchmarks and 4 out of 12 benchmarks lie within 1 SD of the leveling data for 19-IFGMs and 15-IFGMs data set respectively. Careful consideration gives rise to a categorization of these deviations into three groups with small (C), medium (A) and large (B) discrepancies using 2 mm/year as the threshold value. Possible causes for these differences could be due to 1) unwrapping error or 2) suitability of the linear model to the displacement behavior in the test area. We shall investigate the sources of the differences further in subsection 4.10.3.

Based on interpolated estimate

Discussion

Standard deviation of the interpolated estimates for 19-IFGM is 4-6 mm/year while it is higher for the 15-IFGM (6-8 mm/year), as also suggested by the semi-variogram plot. Differences between the interpolated estimate and the best point estimate depends on the estimates around a benchmark, the set range distance and the number of

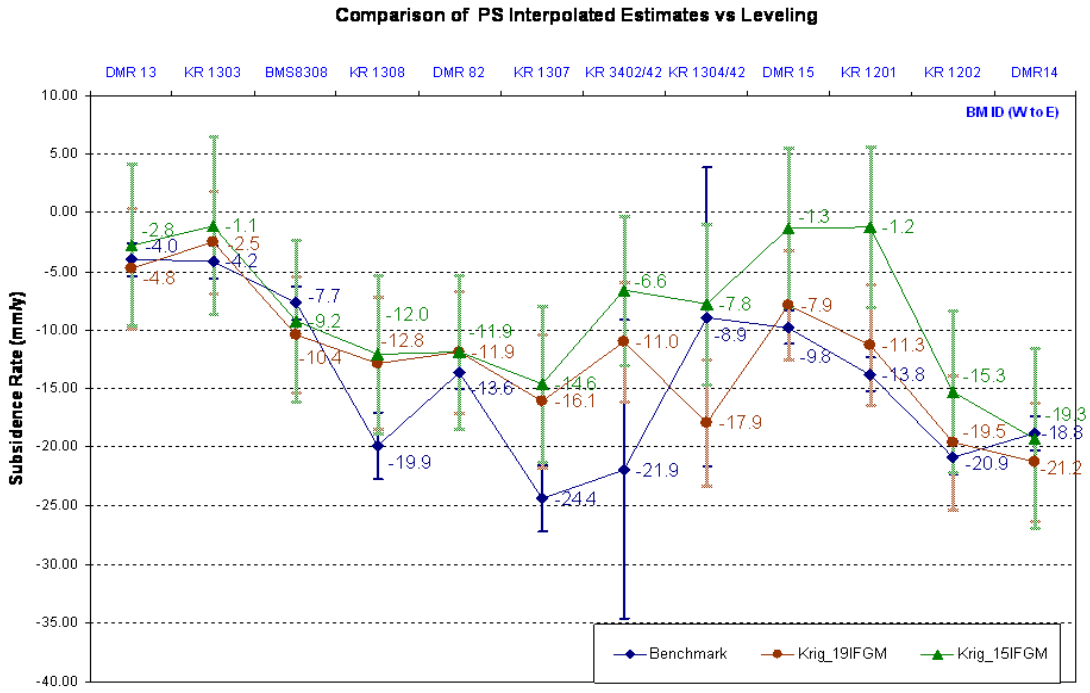

Figure 4.46: Comparison between interpolated estimate from PS analysis and leveling measurement

surrounding data points used for interpolation. Note that the derivation of subsidence surface from point estimate in this study is primarily aimed for subsidence monitoring purposes. And it is always reasonable to use an interpolation method by which the error is quantifiable. Therefore, while utilizing the interpolated estimate, one should keep in mind that they contain lower accuracy than the PS point estimate when the interpolated estimates are far away from the data points.

Spatial comparison of estimate

An attempt was made to compare two estimates spatially. *Subsidence contours* (every 5 mm/year) were generated from the subsidence rates measured during the year 1996-1997 at benchmark locations. The leveling survey points used to derive these contours are visualized in purple in fig. 4.47. If uniform subsiding rates are assumed in this area, the subsiding velocity will be constant over time. Therefore, in principle it is possible to use these subsidence contours to assess the average spatial displacement rate from the PS technique (estimated using data from 1996 - 2000). Comparison of the linear subsidence rate spatially reveals that both measurements provide the same increasing trend of subsidence rate from west to east direction. However, the local PS

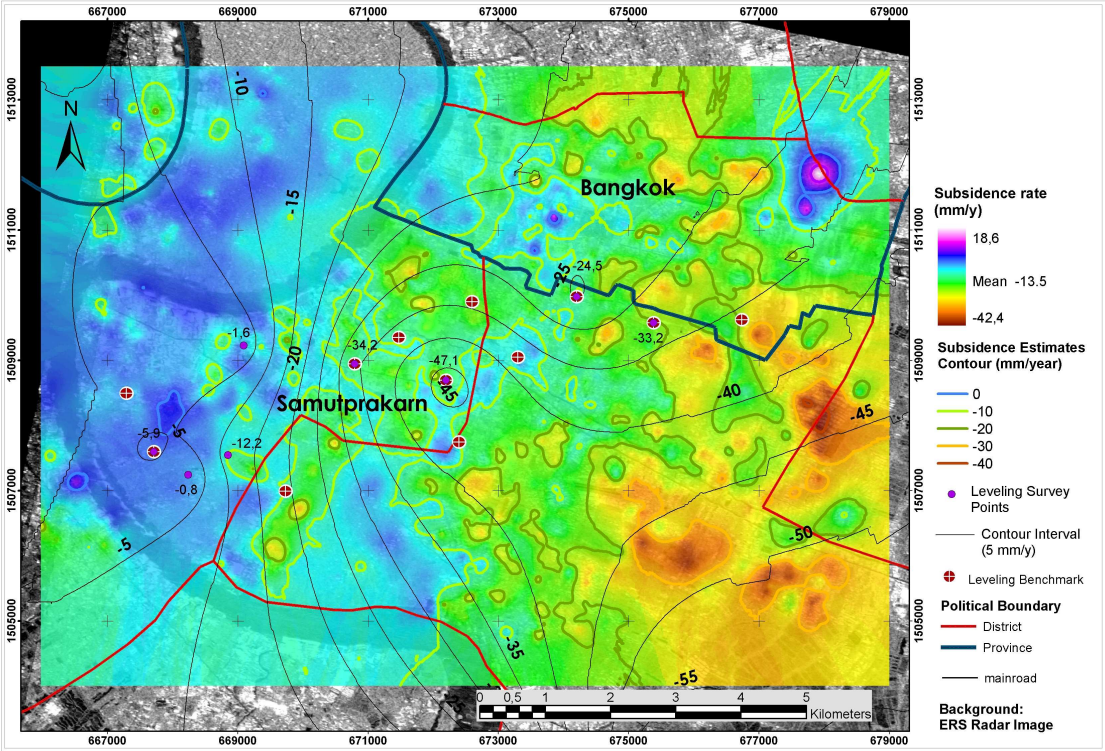

Figure 4.47: Spatial comparison between interpolated PS estimate and leveling contour estimated from leveling measurement in 1997

estimate is usually underestimated from the contour line. This confirms that subsidence behaviour in the area of interest is not linear with time. And the degree of nonlinearity varies spatially. Subsidence rate derived from a short period of time (leveling from 1996-1997) is therefore not sufficient for this assessment. Nevertheless, information from the PS estimates can be worthwhile to fill in the gap for the measurements of sparsely distributed leveling points both spatially (subsidence surface) and temporally (spanning a period of time: 1996-2000).

4.10.3 Analysis of estimates

Analysis of PS estimate were aimed to justify causes of the deviations of PS estimate from the reference leveling measurements. The possible error sources in this case could be the unwrapping process and the unsuitability of the linear model used.

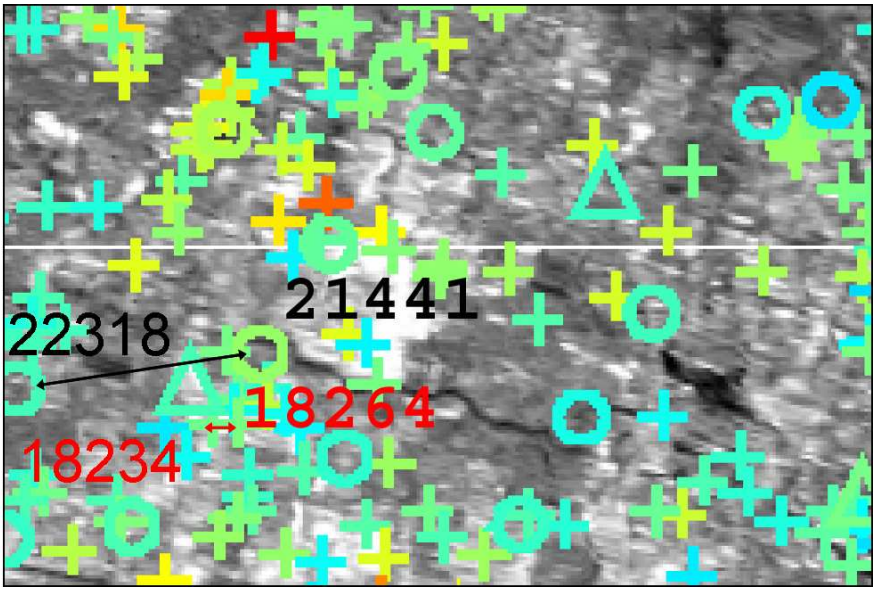

Figure 4.48: Arc locations near to DMR-82 (green triangle). Their PS analysis results are shown in fig. 4.49 and 4.50.

Unwrapping error

Detailed analysis at PS points can be performed in order to quality control the unwrapping results. An utility program called 'ps_analyze' developed as a part of the DLR PSI system was used for this purpose. The PS analysis program examines a pair estimate (difference of height error dh and of displacement rate dv between two points) simultaneously and calculates their fit to the model expressed in terms of coherence function. A clear peak (coherence value close to 1) of coherence function indicates a good fit and hence the best estimate (dh, dv) with lowest error (residual). On the other hand, having more than one peak indicates that many possible solutions of pair estimate provide the same quality result. In this case, a best estimate cannot be found and coherence value will be far below 1. Therefore, it is possible to use coherence magnitude $(0 \leq \gamma \leq 1)$ to indicate the quality of unwrapping results (Ferretti et al., 2000c; Colensanti et al., 2002).

According to coherence observations of PS estimate around 12 benchmarks, PS estimates from 19-IFGMs stack exhibit very high coherence with coherence values of 0.97-0.99 and can provide a clear peak (fig. 4.50) of coherence function. The coherence magnitudes of the estimates from 15-IFGMs are not so high ranging from 0.5-0.8 and containing many low identical peaks (see fig. 4.49). Fig. 4.48 shows example arcs connecting the estimate (black: 15-IFGMs, red: 19-IFGMs) used for coherence analysis. Their analysis result and coherence functions are shown in fig. 4.49 and 4.50.

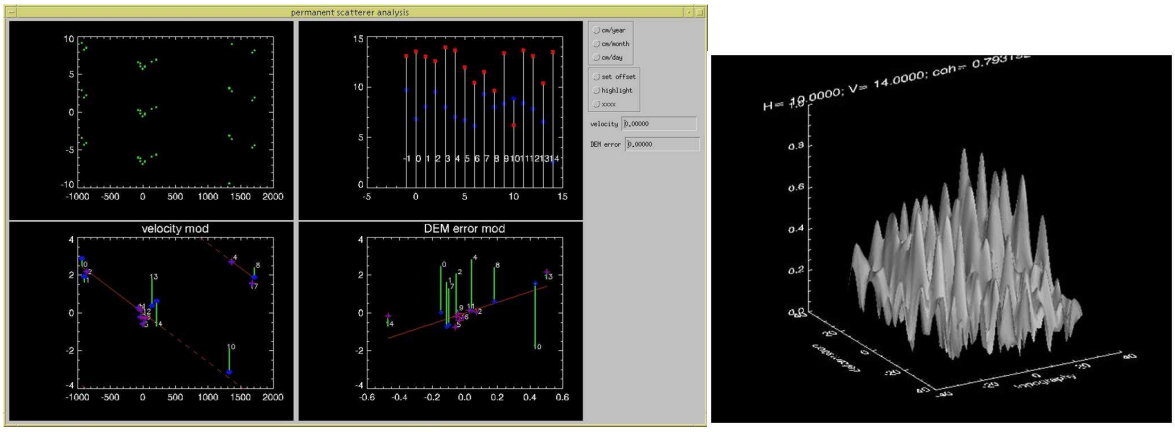

(a) PS analysis window (b) Coherence = 0.79

Figure 4.49: Coherence analysis result between PS 22318 and PS 21441 (black arc in fig. 4.48) of 15 IFGMs. The upper left (UL) window shows phase ambiguity plot for all IFGMs (topographic phase removed). The upper right window indicates amplitude evolution of each PS over time. The lower left window shows phase difference corrected for topography in blue diamond. The number indicates number of interferogram. The lower right window shows phase difference corrected for deformation. (b) Coherence function with many identical peaks indicates low quality of unwrapping result of 15-IFGMs data set

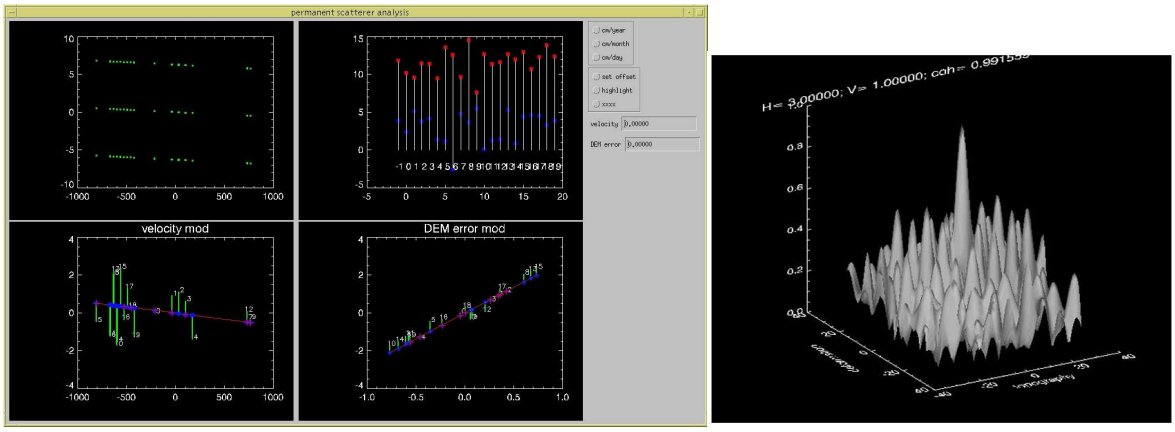

(a) PS analysis window (b) Coherence = 0.99

Figure 4.50: Coherence analysis result between PS 18234 and PS 18264 (red arc in fig. 4.48) of 19 IFGMs. (b) Coherence function with a clear peak indicates high quality (good) unwrapping result.

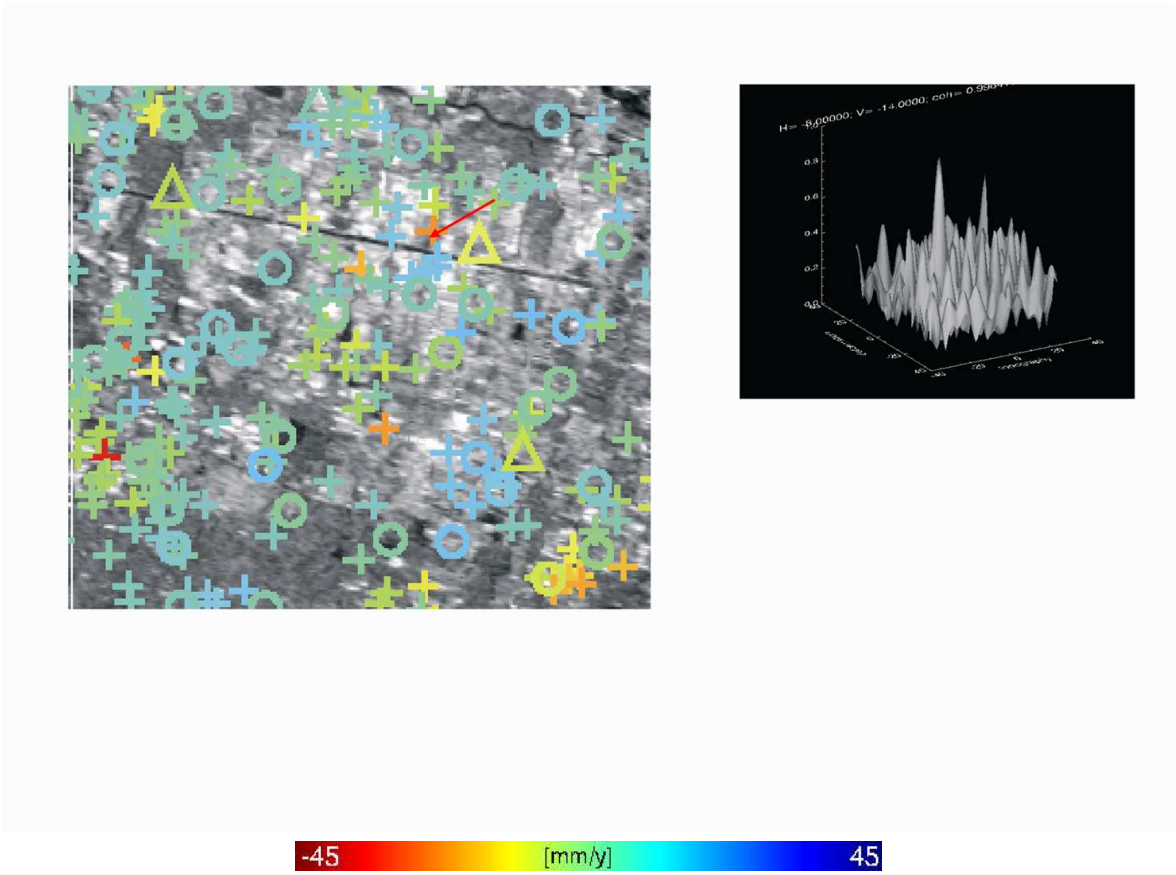

Figure 4.51: Estimate between arcs (red arrow) with high coherence (0.99) but more than one dominant peak around BM- KR1307 (green triangle)

Fig. 4.51 shows an exception observed around BM-KR 1307, where coherence value is high (0.99) but there are two dominant peaks. It is likely that an unwrapping error occurred for this estimate. This error could result in a large difference between PS estimate and the leveling at KR1307 (see fig. 4.45).

Discussion

A reason explaining why the 15-IFGM estimates possess lower quality than the 19-IFGM estimates could be an insufficient number of acquisitions. In Kampes (2005), the relation between the average temporal sampling $\triangle T/K$ (equidistant sampling) and the maximum displacement rate α_{max} that can be estimated unambiguously is shown. The relationship can be written as:

$$\alpha_{max} = \frac{\lambda}{4} \cdot \frac{K}{\triangle T}. \tag{4.28}$$

K denotes the number of interferograms and $\triangle T$ denotes time span of all acquisitions.

Considering interferometric temporal data sampling, the 19-IFGMs (19 IFGMs for 4 years) has a higher sampling rate than the 15-IFGMs (15 IFGMs for 7 years) (see fig. 4.52). Therefore, $\frac{K}{\triangle T}$(15-IFGM) = 15/7 and the resulting α_{max} is ∼30 mm/y . While $\frac{K}{\triangle T}$(19-IFGM) = 19/4 resulting in α_{max} of ∼67 mm/y. This implies that with this 15-IFGMs data configuration, the PS subsidence rates higher than 30 mm/y could be unwrapped or estimated incorrectly. The significant differences of estimates from these two data sets in fig. 4.37 found in the high subsidence rates area (red color) therefore are likely resulted from this. To estimate the minimum number of interferograms required for an unambiguous displacement rate or DEM error difference parameters estimation, following equations are used (Kampes, 2005).

$$K_{\alpha}^{min} = \frac{4}{\lambda} \cdot \triangle T \cdot \alpha_{max} \tag{4.29}$$

$$K_{\triangle h}^{min} = \frac{4}{\lambda} \cdot \frac{\triangle B_{\perp}}{r sin(\theta)} \cdot \triangle h_{max} \tag{4.30}$$

Baseline span $\triangle B_{\perp}$for 19 IFGMs data set is about 1000 m. For ERS case, $r = 850\,km$, $\theta = 21°$and $\lambda = 56.6\,mm$. For this test area, the maximum displacement rate between points is not higher than 50 mm/y and the DEM error is not higher than 10 m. Using these parameters, I get $K_{\alpha}^{min} = 15$ and $K_{\triangle h}^{min} = 3$. Hence in case of equidistant sampling data, minimum number of IFGMs required for this test area is = 15 + 3 = 18. The available 19 IFGMs with irregular sampling is therefore likely sufficient to obtain unambiguous estimation under this study condition.

From section 4.10.1 up to now, I have shown that PS estimate from 15-IFGMs possess different statistical characteristics (mean, variance and covariance) with a lower quality of estimates indicated by low coherency when comparing to the 19-IFGM estimates. In addition, the 19-IFGMs could provide the better estimate close to the measurement from surface leveling. Based on these facts, it has been proved that these estimates are not sufficiently reliable. At this point, i have been adequately convinced to discard these 15-IFGMs estimates from further analysis.

Suitability of linear model

Deviations of PS estimate from the actual leveling estimate can originate from the unsuitability of the linear model applied for PS analysis to the actual subsiding behavior at the measured location. A simple linear regression study of leveling measurements was carried out to investigate the linearity of the local subsidence behaviour. The

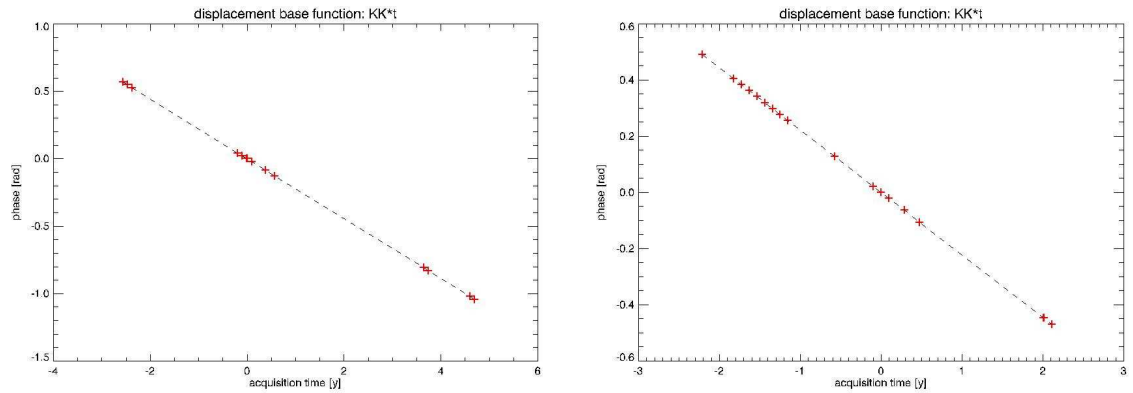

(a) 15-IFGM (b) 19-IFGM

Figure 4.52: shows linear base functions and the temporal data sampling of two data stacks. From this information, the average temporal data sampling: $\triangle T/K$ can be estimated and the maximum subsidence rate according to eq. 4.28 can then be determined. Each red plus represents an interferogram.

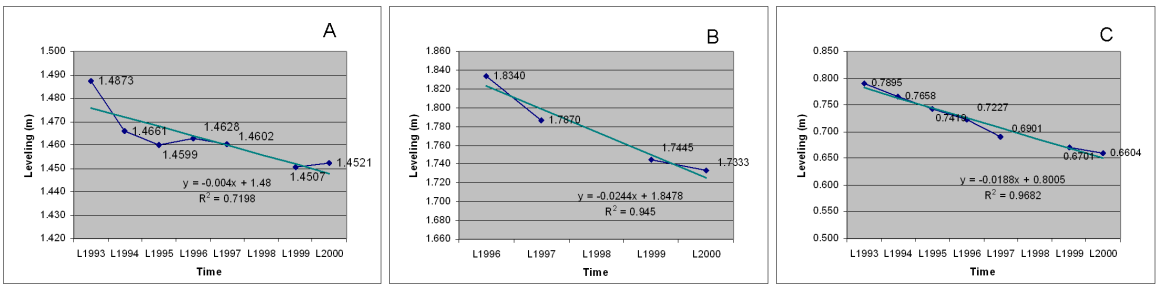

(a) BM-DMR 13 (b) BM-KR 1307 (c) BM-DMR 14

Figure 4.53: Linear regression of leveling data over time at 3 benchmarks

correlation coefficient (R^2) was used to imply the relationship between the leveling data and time. Correlation coefficients were calculated for all leveling benchmarks and three examples are shown in fig. 4.53 according to point category A, B and C in fig. 4.45. Slope of the regression line represents the average subsidence rate during that period of time. Additional plots for other benchmarks can be found in Appendix B. According to the calculated R^2, the order of linearity from max to min will be from point category C, B and A respectively. Table 4.7 summarizes the information on R^2, differences and number of measurements of all benchmarks ordered by R^2 value. Fig. 4.54 visualizes the relationship between R^2 and the differences of estimates (leveling estimate - 19 IFGMs estimate).

Table 4.7: Estimated correlation coefficients at benchmarks ordered by $R^2$and differences of estimates

BM_ID	R^2	Leveling-PS (mm/y)	No. of leveling measurements from 1993-2000
KR3402/42	1.00	-8.07	2
KR 1304/42	1.00	10.55	2
KR 1202	0.97	-1.05	7
DMR 14	0.97	-0.26	7
KR 1308	0.95	-6.95	4
KR 1307	0.95	-8.79	4
KR 1201	0.94	1.16	7
DMR 15	0.94	0.79	7
DMR 82	0.93	-0.53	7
BMS 8308	0.87	0.81	7
DMR 13	0.72	-1.95	7
KR 1303	0.66	-2.10	7

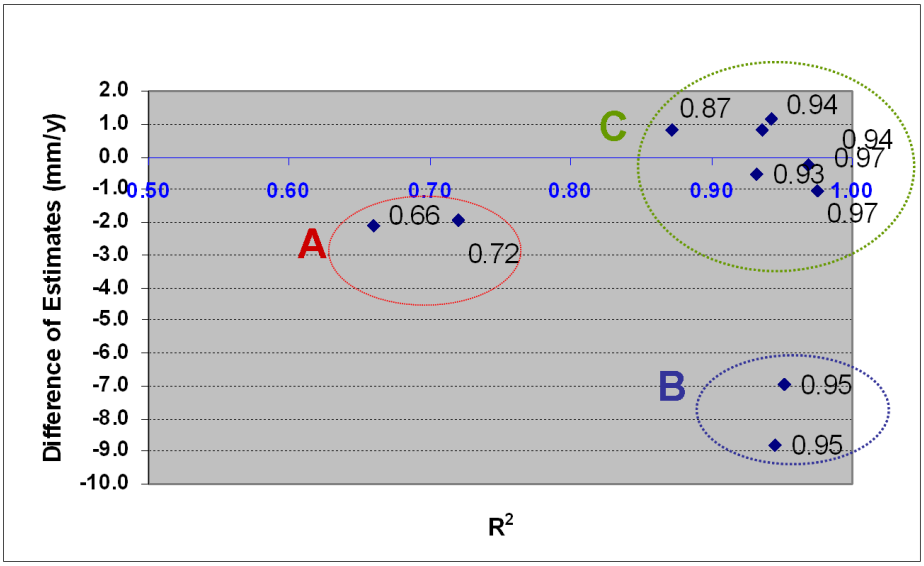

Figure 4.54: Relationship between R^2 and differences of estimates

Discussion

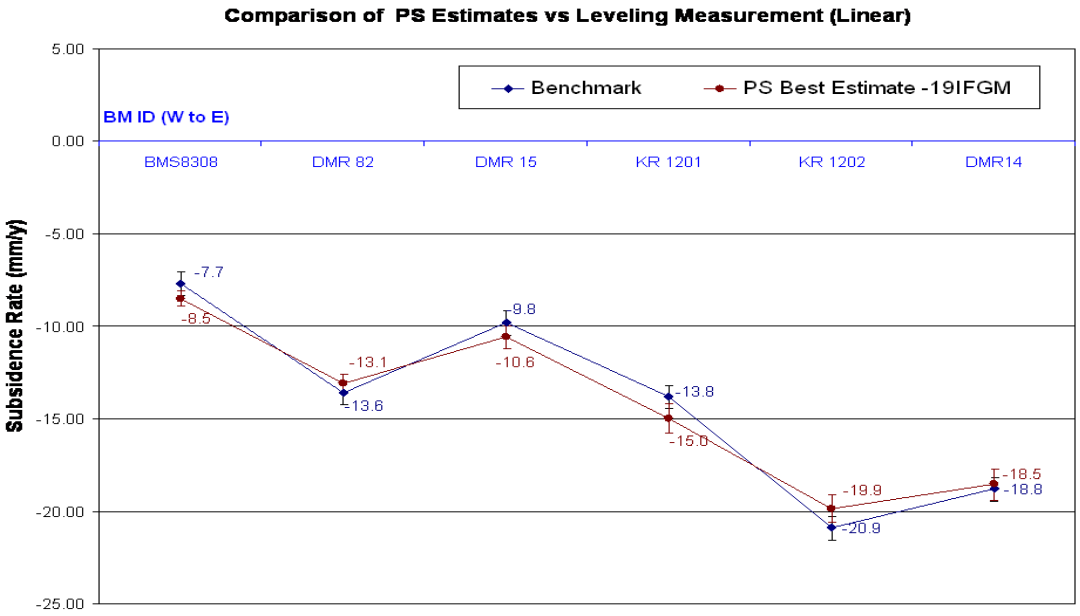

Figure 4.55: Comparison between PS estimates and leveling estimates at linear subsiding benchmarks shows very well agreement with each other. The precision is better than $\pm 1.5\, mm/y$.

Though comparisons along the profile either based on the best estimate or interpolated estimate with only 19 or 15 data sets have not yet shown very convincing results on the PS subsidence estimates. The plot in fig. 4.54 reveals a fact that the linearly subsiding locations, i.e. point category C, can be well predicted by PS analysis (difference close to zero). An increase of nonlinearity (R^2 decreases), i.e. point category A, also increases the deviation from the reference value. This is due to the fact that the linear model was used for the estimation. By point category B, with the information on hand it is not possible to provide a concrete answer. Even subsiding activities at these locations are considered linear suggesting a high R^2 value. A lower number of leveling measurements (4 times within 8 years) can reduce the reliability of the leveling estimate used as the reference (refer to error bar in fig. 4.45). In addition, those four measurements reflect a certain degree of nonlinearity among themselves (see also fig. 4.53(b). Notwithstanding, I can conclude that at the reliable benchmarks (except KR-1308,KR-1307,KR-3402/42, KR-1304/42), the differences of these two measurements increase as the nonlinearity of subsidence over time increase. Again, fig. 4.55 presents the comparison plot of measurements between PS estimate and leveling estimate along

the W-E profile. This time only linear subsiding benchmarks are plotted (point category C). Deviations of PS estimate from the actual leveling estimate for these locations are very limited and are better than $\pm 1.5\, mm/y$.

4.11 Summary

The important observations in this chapter can be summarized into three main aspects.

Concerning PSI technique :

- A number of methods can be applied for PS detection. Detectability and distribution of PS depend on the characteristics of the applied criteria and the sensor-target interaction geometry. The dispersion index approach provides phase stability information in time and therefore requires a sufficient number of images to retrieve a reliable estimate. The signal-to-clutter ratio thresholding considers the proportion between a signal from a PS compared to its clutter background, hence providing phase stability estimation in space. The technique is therefore less constrained by the number of images available. For a smaller number of images the SCR method is preferable.

- Density of the reliable PS in the suburban area of Bangkok is approximately $30 - 40\ PS/km^2$ which is theoretically sufficient for a reliable estimation and removal of the atmospheric phase contribution by applying the PS technique (minimum requirement is $5{-}10 PS/km^2$depending also on the number of available interferograms).

- Success rate assessment of the simulated data informs that the success rate of 98 % and 80 % can be expected for parameter estimation using 20 and 16 radar images respectively. Provided that the PS are carefully selected (noise level is not more than 30° or $SCR \geq 2$) and the expected displacement rate accuracy is not better than 2 mm/y. This assessment also confirms that high percentage of success (98%) can be expected from PS analysis of 20 images under these data configurations.

- Model's suitability study using simple linear regression confirms that the discrepancy between the PS estimate and the reference leveling increases as the degree of temporal variability of subsidence rates increases. More importantly, this implies that the PS algorithm for the estimation of linear motion under the existing data configuration functions correctly.

Concerning shortcoming from very limited and badly distributed data :

- Too few interferograms and high subsiding rates are main limitations for the derivation of reliable displacement estimates using 15-IFGM data set (subsection 4.10.3). The unreliable unwrapping results from the 15 IFGMs made the cross-combination of the two data sets infeasible.

- The quality of the nonlinear displacement estimates as a result from spatial-temporal filtering at a location varies depending on whether or not the correlation time of the nonlinear motion behaviour at that location is longer than the temporal sampling of the available interferograms. When the correlation time of the nonlinear motion is longer, filtering provides reliable result. At a location the nonlinear behaviour of subsidence is characterized by the aquifer system properties e.g. compressibility, interbeds thicknesses and the groundwater pumping behaviour.

Concerning measurement results :

- Despite the interferogram constraint, PS analysis of 20 radar scenes *is capable to provide a reliable linear displacement estimates.* The point-wise comparison result with precise leveling measurements show very promising and good agreement between these two methods with a discrepancy less than 1.5 mm/y at the linearly subsiding locations (as shown in fig. 4.55). At 6 out of 10 benchmarks, the PS subsidence estimates agree better than $\pm$1.5mm/y to the benchmark values. The primary result of this chapter, the PS mean displacement rates (at a larger scale) for the period 1996-2000 in the area of interest is attached at the back of this dissertation.

- A nature of spatial-temporal analysis of PSI enriches the derived subsidence information both spatially and temporally. The derived PS subsidence estimates represent the most detailed subsidence information in this area to date. While their derived subsidence field could provide an overview of subsidence status spanning the period of time 1996 to 2000.

Chapter 5

Subsidence analysis and applicability of PSI derived subsidence

5.1 Introduction

Temporal analysis of hydraulic head or piezometric head changes and the surface subsidence measurements leads to a determination of the *subsidence to head decline ratio*. This ratio can be used to predict the amount of subsidence regarding to change in hydraulic heads. It can be also used to infer the compressibility[1] property of an aquifer system for the time period from which the ratio is derived. In principle, it is possible to derive a subsidence to head decline ratio at the locations where the groundwater monitoring data and periodic leveling data are available. Derivation of this quantity at more locations can possibly be facilitated by using subsidence measurements derived from PSI. Feasibility to use PS subsidence estimates for this derivation will be examined. The derived ratios from PS are assessed by the ratios derived from leveling data. The usefulness of these ratios for an understanding of the aquifer system property and for the prediction of future subsidence will be also discussed.

Applicabilities of the PS mean subsidence estimates complementary to the monitoring purpose will be demonstrated in two areas. First, the *risk analysis* to identify the subsidence prone and subsidence critical areas. The resulting map will be visualized as *the subsidence zoning map* with a 25x25 meter grid resolution. This map serves well as base information for planners and decision makers tackling with subsidence related

[1] compressibility is a material property that describes the change in volume (strain) induced in a material under an applied stress

problems. Second, the empirical *prediction of subsidence* represented by *the predicted subsidence maps* in the next 25 years (between 2000-2025), and 50 years (between 2000-2050). For this prediction, the exponential model was assumed.

5.2 Subsidence due to aquifer system compaction

When water is removed from an aquifer, the piezometric level in that aquifer will drop unless there is sufficient recharge. Lowering the piezometric pressure or the hydraulic head in an aquifer (i.e. sand bed) below a clay stratum creates a hydraulic gradient between the sand and the clay. As a result, there exists a descending flow across the compressible clays and other soil strata between the sand and the clay layers, i.e. consolidation process takes place. Subsequently, the aquifer system compacts and surface subsidence occurs.

5.2.1 Soil compressibility

Geological materials constituting an aquifer system respond to an *effective stress*[2] that is induced by hydraulic head changes differently according to their compressibilities. Compressibility is a material's property that describes change in volume (strain) induced in a material in response to change in an applied stress. The expression for compressibility α of the sediments can be written as

$$\alpha = \frac{-dV_T/V_T}{d\sigma_e} \tag{5.1}$$

where V_T is the total volume of a soil mass and $d\sigma_e$ is the change in effective stress. The fine-grained sediments of clay commonly found in the aquitard layer have approximately a 1-2 order of magnitude larger compressibility than the compressibility of coarse-grained sediments, e.g. sand and gravel constituting an aquifer layer(Freeze and Cherry, 1979).

Compressibility is usually expressed as the slope in the $e - d\sigma_e$ curve. e is the void ratio of a soil which is defined as a ratio between the volume of the voids V_v and the volume of the solid portion V_s in a total unit volume V_T. And $V_T = V_v + V_s$. Fig. 5.1(a) visualizes the $e - d\sigma_e$ curve for compressibility of soil during compression (increase of effective stress) and expansion (decrease of effective stress) schematically. It implies that for soils having a compressibility that is significantly less (much lesser slope)

[2]Principle of effective stress is described in Appendix C.

in expansion than in compression, compactions that occur in response to increasing effective stress are largely irreversible. This compaction or the original void ratio e_0, cannot be recovered when the effective stresses subsequently decrease. For clays, the ratio between these two α's is usually about 10:1, for uniform sands, it approaches 1:1 (Freeze and Cherry, 1979). Fig. 5.1(b) depicts schematic curves of compressibility for two different soil types, clay and sand. The lesser slope for sand implies a smaller compressibility and its linearity implies that the compressibility remains constant over a wide range of σ_e.

Soil compressibility is in fact a function of the applied stress and depends on whether the effective stress exceeds the previous maximum effective stress, termed as preconsolidation stress (Jorgensen, 1980). In this case, the preconsolidation stress is the previous maximum hydraulic head. If the applied effective stress is less than the preconsolidation stress, small elastic compactions occur in both coarse and fine-grained sediments. Elastic compactions are recoverable when the effective stress returns to its initial value. If the applied effective stress is larger than the preconsolidation stress, many fine-grained sediments like clay compact inelastically. An inelastic compaction results from a physical rearrangement of the grains in the sediments and is largely permanent.

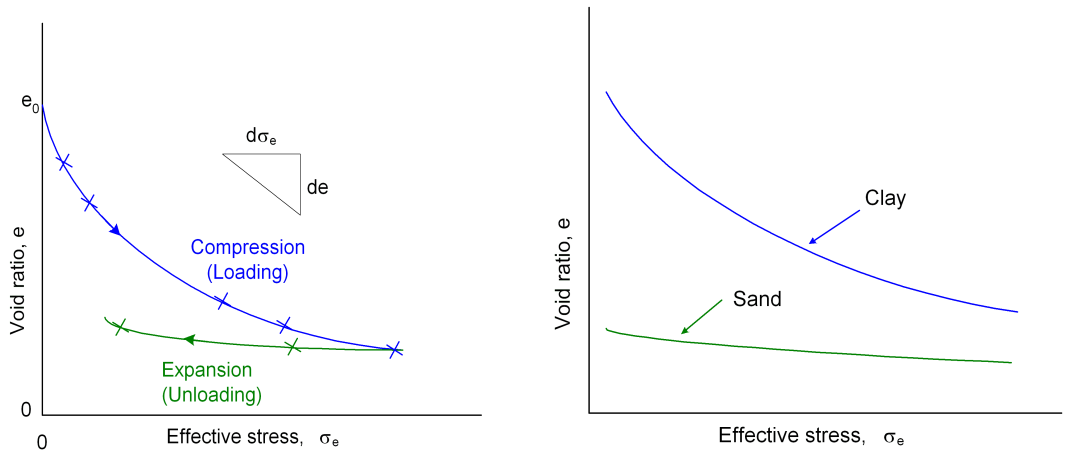

(a) (b)

Figure 5.1: Schematic curves of void ratio versus effective stress (a) when compression and expansion (b) for sand and clay (after Freeze and Cherry (1979))

5.2.2 Compaction of compressible aquifer system

The one-dimensional (vertical) compressibility, in the absence of horizontal displacement, can be written as

$$\alpha = \frac{-db/b}{d\sigma_e} \tag{5.2}$$

where db is change in thickness or compaction and b is the initial thickness. If the change in effective stress is induced only by change in pore pressure, the compaction db in eq. 5.2 can be expressed as

$$db = \alpha \cdot b \cdot d\sigma_e = \alpha \cdot b \cdot \rho g dh. \tag{5.3}$$

where $d\sigma_e = -\rho g dh$ (see eq. C.6 in Appendix C). ρ is mass density of water and g is gravity acceleration. Eq. 5.3 shows that apart from head changes, a compaction of soil also depends on its compressibility α and its thickness b. For an aquifer system with several pumping wells, the surface subsidence can be estimated using eq. 5.3 and is the summation of all the aquitard and aquifer compactions.

The storage coefficient S can be defined as the volume of water that an aquifer releases from storage per unit of aquifer surface area per unit decline in the component of hydraulic head normal to the surface (Freeze and Cherry, 1979). It can be related to compressibility α as

$$S = \rho g \alpha \cdot b, \tag{5.4}$$

where b is the aquifer thickness. The term specific storage S_s is closely related to S and can be defined as

$$S = S_s b. \tag{5.5}$$

As ρ , g and b are constant for an aquifer, the term storage coefficient and the specific storage are directly proportional to compressibility of an aquifer. Eq. 5.3 can be therefore rewritten in relation to S and S_s as

$$db = S \cdot dh = S_s \cdot b \cdot dh. \tag{5.6}$$

Two different terms are often used to account for the marked change of S_s when the effective stress exceeds the previous maximum effective stress $\sigma_{e(max)}$. These are

$$S_s = \begin{cases} S_{se} & \text{for } \sigma_e < \sigma_{e(max)} \\ S_{sv} & \text{for } \sigma_e \geq \sigma_{e(max)} \end{cases}$$

where S_{se} denotes the elastic specific storage and S_{sv} denotes the virgin or inelastic specific storage.

The relation expressed in eq. 5.6 will be used later in section 5.3 to derive subsidence to head decline ratio.

There are two fundamental differences concerning compaction of aquifers and aquitards. First, since the compressibility of clay is 1-2 orders of magnitude larger than that of the compressibility of sand, the total potential compaction of an aquitard is much greater than that for an aquifer. Second, since the hydraulic conductivity of clay is several orders of magnitude less than the hydraulic conductivity of sand, the compaction process is much slower in aquitards than in aquifers. This time-delay compaction of a clay interbed is usually expressed using the time constant τ_0 which represents the time during which 93% of the ultimate compaction for a given head decline occurs (Riley, 1969). The time constant τ_0 can be given as

$$\tau_0 = \frac{\left(\frac{b_0}{2}\right)^2 S_s^{'}}{K_v^{'}}, \tag{5.7}$$

where b_0 denotes thickness of the interbed, $S_s^{'}$ denotes specific storage and $K_v^{'}$ denotes vertical conductivity of the clay interbed.

5.3 Analysis of subsidence with geohydrological data

Temporal analysis of geohydrological data, the hydraulic head changes in conjunction with the PSI subsidence estimates (representing subsidence at the surface) is carried out to determine the *subsidence to head decline ratio* or *storage coefficient.* It is the ratio between the amount of subsidence and the head decline in the coarse-grained permeable beds of a compacting aquifer for a common time interval. This ratio is useful to predict subsidence magnitude in response to a step increase in virgin stress[3]. Apart from prediction, the ratio also represents a minimum value of storage coefficient component for virgin compaction of the aquifer system skeleton (Poland, 1984). Derivation of subsidence to head decline ratios will be carried out at three groundwater monitoring wells where groundwater monitoring data is available.

5.3.1 Analysis approach

In many cases of aquifer system compaction, change in the effective stress is typically small. Eq. 5.6 can then be linearized as (see also Hoffmann et al., 003a)

$$\triangle b = S \triangle h = S_s b \triangle h, \tag{5.8}$$

therefore,

$$\frac{\triangle b}{\triangle h} = \frac{subsidence}{head\ decline} = S = S_s b \tag{5.9}$$

where $\triangle b$ denotes changes in aquifer thickness and $\triangle h$ denotes change in hydraulic head.

In this analysis, the subsidence to head decline ratios, or in other words, the storage coefficients, of the aquifer system were determined according to eq. 5.9. Two points should be mentioned in the derivation of subsidence to head decline ratio. First, the derived ratio will be reliable only if the water levels used represent the average artesian head in the aquifers (coarse-grained beds) of the compacting system. Second, the derived ratio represents only the *transient* compressibility of the aquifer system for the period from which this ratio is derived. Unless the equilibrium of pore pressure in the compacting aquitards and adjacent aquifers is attained, compaction process stops, the ratio is then a true measure of the virgin compressibility.

[3]Virgin stress is the applied stress that exceeds the past maximum stress. For example, lowering of groundwater level below the historical groundwater level is equivalent to applying virgin stress to an aquifer.

The average head decline for the available aquifers was obtained as follows (see $\triangle h$ in table 5.1 and table 5.2). First, the annual minimum and the annual maximum heads were selected from the monthly observed hydraulic heads. Then for a period of interest e.g. t_0 to t_n, the head changes for annual maximum heads were obtained by computing $max\, h_{t_0} - max\, h_{t_n}$ and the head changes for annual minimum heads were obtained by computing $min\, h_{t_0} - min\, h_{t_n}$. The average of the minimum and maximum head changes was then used as the representative hydraulic head change for the computation of the ratio. The mean PSI subsidence estimates were used for computation of the ratio for the period 1996-2000. Subsidence to head decline ratios computed from subsidence measurements of periodic leveling surveys during the same period were used for result assessment. For the period of 1992-1995 where InSAR observations were not available, the subsidence observations from leveling surveys were used to derive subsidence to head decline ratio.

5.3.2 Interpretation of results and discussion

Fig. 5.2(a), (b) and (c) show piezometric head changes of aquifers over time. The corresponding subsidence measurements, the PSI (1996-2000) and the leveling data (1992-2000), used to derive $\triangle b / \triangle h$ are presented in table 5.1 and table 5.2. Locations of the benchmarks and corresponding monitoring wells for which the $\triangle b / \triangle h$ have been derived are presented in fig. 5.3. Computation of $\triangle b / \triangle h$ led to a determination of subsidence to head decline ratio of the compacting aquifer. When $\sigma_e \geq \sigma_{e(max)}$, $\triangle b / \triangle h$ represents subsidence to head decline ratio. When $\sigma_e < \sigma_{e(max)}$, $\triangle b / \triangle h$ represents storage coefficient and is a measure of (elastic) compressibility during aquifer expansion. Using mean PS subsidence rates, the $\triangle b / \triangle h$ at three groundwater monitoring stations (corresponding locations with BM DMR-13, DMR 14, and DMR 15) were computed and are shown as in table 5.1. For an assessment of the result the derived ratios from geodetic leveling data using the same approach are also shown. Note that this ratio represents the storage coefficient or elastic compressibility during aquifer expansion as the hydraulic heads increased during this period and were not lower than the previous maximum stress (see fig 5.2). A value of $\triangle b / \triangle h = 0.0032$ means that for an hydraulic head change of +1 m, a rebound of 3.2 mm can be expected. It can be observed that for the aquifer system at a particular location, the higher head change results in the lower $\triangle b / \triangle h$ estimate e.g. $\triangle b / \triangle h$ for NL is lower than for PD at DMR 14. This comparison shows that the ratios derived from PSI estimates can provide reasonable agreement to the estimates from periodic leveling. Discrepancies of the derived ratios by both means are relatively small with the maximum discrepancy not more than 3

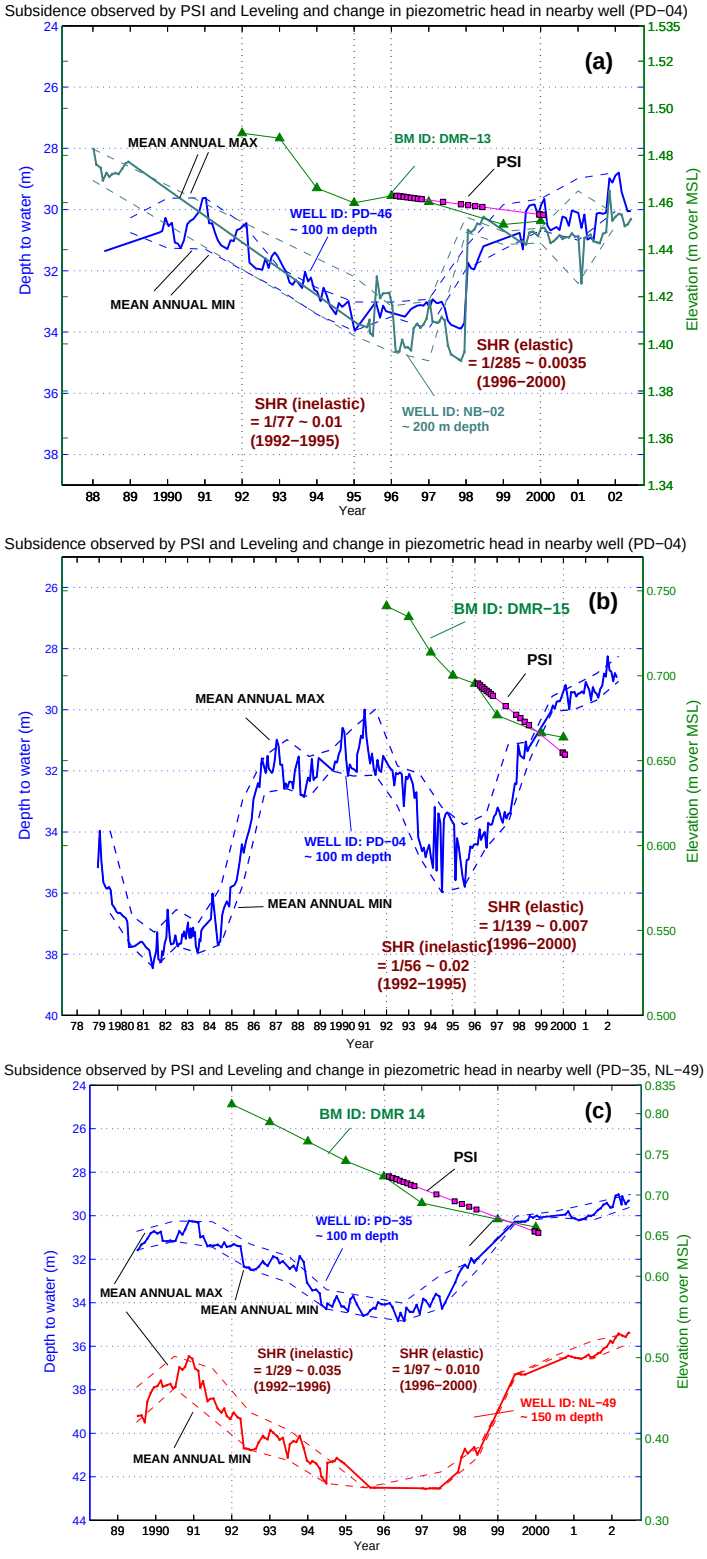

Figure 5.2: Temporal analysis of hydraulic head change and subsidence measurements from PSI and leveling survey data to determine $\triangle b / \triangle h$ at three groundwater monitoring wells.

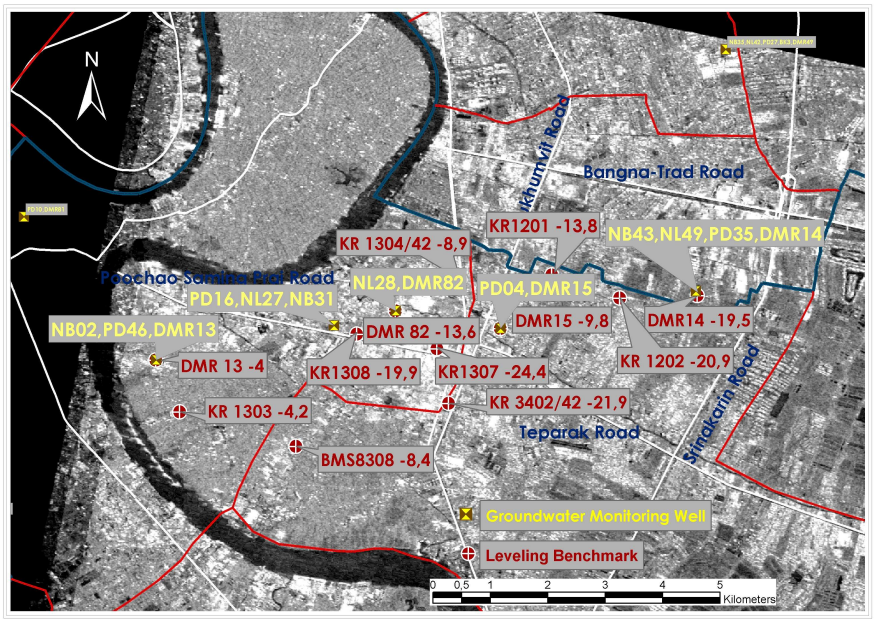

Figure 5.3: The map shows the locations of groundwater monitoring wells

millimeters per 1 meter of hydraulic head change. It should therefore be possible to use the PSI estimates to approximate the $\triangle b/\triangle h$ ratios for the locations where the leveling data does not exist and where PS estimates are sufficiently reliable (see section 4.10).

Since PSI estimates are not available for the period 1992-1995, the subsidence to head decline ratios were derived using leveling data. These ratios can be exploited to predict the subsidence magnitude in response to head decline. They also represent the storage coefficients of the compacting bed during inelastic compaction. During this period, the hydraulic heads exceed the preconsolidation stress therefore, the compressible beds compact inelastically. (see fig. 5.2). Results of these derivations are presented in table 5.2. At DMR-13, the subsidence to head decline ratio of 0.01 or $\triangle b/\triangle h = 1/77$ means that the head decline of 77 m can produce 1 m of subsidence. The $\triangle h$ values presented in column 5 of table 5.2 are relatively identical (e.g. DMR 14). They reveal that the $\triangle h$ used provide a good representation of the average artesian head of the system. Thus the derived ratios could be expected to be reliable. Interpretation of the derived $\triangle b/\triangle h$ for the period 1992-1995 implies that the aquifer system underneath BM DMR-13 is the least susceptible to subsidence ($\triangle b/\triangle h \sim 0.01$), followed by BM DMR-15 ($\triangle b/\triangle h \sim 0.02$) and BM DMR-14($\triangle b/\triangle h \sim 0.04$) respectively. During elastic compaction, the calculated ratios are 0.002-0.003 (BM DMR-13), 0.007 (BM DMR-15) and 0.010-0.014 (BM DMR-14). For example, at DMR-13, the (elastic)

compressibility of 0.004 or $\triangle b/\triangle h = 1/289$ means that an increase in piezometric head of 289 m is required to generate 1 meter of expansion (table 5.2). These expansion ratios also convey the fact that even the groundwater levels are restored to their initial values. The ground surface cannot be returned to their original levels i.e. the ground surfaces were permanently subsided. The ratios between aquifer compressibility during compression and expansion are 2.5:1, 3:1 and 2.5:1 respectively.

Historical groundwater level changes information was obtained from past studies. It is mentioned in AIT (1981) that as of the year 1959 groundwater level in the deep zones (usually refer to a depth below 30 m) were still only reduced to a maximum of 9 m. Groundwater level conditions in the PD aquifer during 1969 to 1982 were obtained by interpreting the available historical piezometric maps (1969-1982) (Sungkhaburana, 1983). They revealed that piezometric drawdowns have occurred with the rate of ∼2-3 m/year during 1969-1974, ∼ 2-2.5 m/year during 1974-1979 and ∼1-2.6 m/year during 1979-1982. Between 1992 and 1995 (1996 for DMR-14), the piezometric head has fallen at the slower rate of about 0.6-1.0 m/y and gradually resumed to the rate of 0.7-1.2 m/y (1995-2000) in the following years (refer to fig. 5.2). The slower drawdown's rates could probably result from the launch of implementation regulations for groundwater withdrawal charge in 1994 (UNEP, 2001). Interpretations of PD groundwater level change over time at all locations reveal subsidence of more or less similar trends. This indicates that the aquifer has suffered from permanent compactions (probably since late 1960s - 1981 and during 1989-1995) alternating with small elastic compactions.

Although the piezometric heads have increased (expansion state) at these sampled locations since 1995, the subsiding process has still taken place (at least until 2000) but with a lower subsiding rate indicated by leveling measurements during the same time. This delay effect could be due to the residual compaction of the highly compressible clay aquitards in attaining pore pressure equilibrium with its adjacent aquifers. The time constant for the NB clay bed was estimated according to eq. 5.7 using $S_s = 1.15E-4$ 1/m , $k_v^{'} = 8.4E-12$ m/s (JICA et al., 1995; Giao, 1996) and $b = 20$ m. The estimated time constant is approximately 43 years indicating 93% of the ultimate compaction time of clay. Continuation of subsidence even with groundwater increase after 1995 is likely due to this delay compaction.

In practice, the use of $\triangle b/\triangle h$ derived estimates for subsidence prediction is relatively limited due to the fact that the present groundwater level change indicates no further head decline. The derived ratios represent rather the temporary compressibility than the virtual compressibility. In addition, at a location there are other possible causes contributing to surface subsidence that could not be modeled with the information

in hand e.g. local subsidence due to loading of the construction and the time delay compaction of the clay beds.

Table 5.1: Shows the estimated storage coefficients S (eq. 5.9) using PSI and leveling data for three groundwater monitoring stations corresponding to three leveling benchmark locations (DMR 13, DMR 14 and DMR 15) for the period 1996 to 2000.

Benchmarks	Well ID	$\triangle b/\triangle h$ (elastic) PSI	$\triangle b/\triangle h$ (elastic) Leveling	$\triangle b$ PSI (mm)	$\triangle b$ Leveling (mm)	$\triangle h$ $\sigma_e < \sigma_{e(max)}$ (m)
DMR-13	PD46	0.0027	0.0035	8.4	10.69	3.10
	NB02	0.0028	0.0035	8.4	10.69	3.05
DMR-15	PD04	0.0097	0.0070	42.40	31.61	4.38
DMR-14	PD35	0.0165	0.0139	74.00	62.30	4.49
	NL49	0.0123	0.0104	74.00	62.30	6.02

Table 5.2: The derived storage coefficients (inelastic) or subsidence to head decline ratios at three benchmarks presented from the West to the East for the period 1992 to 1995 (to 1996 for DMR 14).

Benchmarks	Well ID	$\triangle b/\triangle h$ (inelastic)	$\triangle b$ Leveling (mm)	$\triangle h$ $\sigma_e \geq \sigma_{e(max)}$ (m)	$\triangle b/\triangle h$ (elastic) Leveling
DMR-13	PD46	1/77 (∼0.01)	29.54	2.29	1/289 (∼0.004)
	NB02	-	-	-	1/285 (∼0.004)
DMR-15	PD04	1/56 (∼0.02)	40.88	2.28	1/139 (∼0.007)
DMR-14	PD35	1/29 (∼0.035)	88.80	2.53	1/72 (∼0.014)
	NL49	1/29 (∼0.034)	88.80	2.59	1/97 (∼0.010)

The findings of this analysis according to the interpretation of the available data are:

- At all sample locations the subsidence follows the same trends which indicate inelastic compaction of the aquifer in the early years (1988-1995) and subsequent elastic compaction due to an increase in the hydraulic head in the later years (after 1995 or 1996).
- Among these locations, the lowest piezometric head for PD aquifer was found at BM DMR-15 in 1981 and recorded at 38 meters below ground level. The

groundwater levels in the PD aquifer have been ascending since 1995 or 1996. This trend has been maintained at least until 2002.

- The analysis of temporal changes of hydraulic heads in a PD aquifer imply that the inelastic compactions of the underlying aquifer system had occurred in the past (probably since the late 1960s - 1981 and during 1989-1995) alternating with lesser elastic compactions resulting from an increase in hydraulic heads. These irreversible compactions created permanent surface subsidence in the area. The ratios between the aquifers' compressibilities during compression and expansion are 2.5:1, 3:1 and 2.5:1 which demonstrates that it is impossible to recover the original surface elevations even though the piezometric heads are returned to their initial levels.

- The derived subsidence to head decline ratios do not represent the virtual compressibility of the aquifer. They are only the transient values since the compaction process has not yet stopped. This is indicated by the continuation of surface subsidence after 1996 at all locations where leveling data was measured.

- A subsidence estimate from PSI can be utilized in approximating a transient subsidence to head decline ratio where surface leveling is not available. This provides reasonable agreement with the estimate derived from leveling measurements of the same time. The maximum discrepancy is about + 3 mm. per 1 m. of hydraulic head change.

5.4 Application of PSI estimates

5.4.1 Risk analysis

Effective mitigation of the adverse effects caused by subsidence requires an up-to-date pool of subsidence information. Information on geographical, geohydrological and groundwater resource, geological and political aspects of the area in concern needs to be gathered. One piece of the indispensable information serving as fundamental information for urban planners and decision makers is the subsidence risk map. Based on the 1996-2000 averaged subsidence rate map derived by PS analysis (see also page 149), the area of interest was classified into different subsidence zones with high (more than 20 mm/year), medium (more than 10 mm/year) and low (less than 10 mm/year) subsidence rate. To provide ready-to-use information for strategic planners, the administrative boundary at the district level was used and the subsidence risk map for each

district was produced (see fig. 5.5). Note that the average subsidence rate for each district was derived where the InSAR mean subsidence rate is available as depicted in fig. 5.4. Therefore, the mean subsidence rates shown for some districts might not be the actual average for the entire district. Information on the local subsiding rate can be acquired by interpreting the InSAR subsidence map alone.

Two districts of Bangkok- Bang Na and Phra Khanong- and four districts in Samut Prakarn province- Phra Pradaeng, Phra Samut Chedi, Muang Samut Prakarn, and Bang Plee- are classified. Based on PSI estimates, Phra Pradaeng and Phra Samut Chedi districts have been categorized as low subsiding areas with a rate of less than 10 mm/year. Bang Na, Phra Khanong and Muang Samut Prakarn have been considered as medium subsiding areas with the average subsidence rate of more than 10 mm/year. The Bang Plee district has been considered as a critical zone having the highest subsidence rate of more than 20 mm/year (see fig. 5.5). This subsidence risk map shows that subsidence rate increases from west to east in the study area or southeast of downtown Bangkok.

Subsidence risk map provides the basic information on severity of subsidence for an individual district based on PS estimates. Such an abstracted information may be useful for urban planners or administrative bodies to support their decision concerning subsidence mitigation. Its application in conjunction with historical data on groundwater pumpage, production well locations, geological and geohydrological properties of subsoils etc. can improve our understanding of the past subsidence status and may support in anticipating future subsidence. In addition, subsidence magnitude can usually be related to the decline of piezometric level or the amount of groundwater withdrawal in the affected areas. Utilizing all these information, a more systematic way to understand the complex subsidence mechanisms can be drawn.

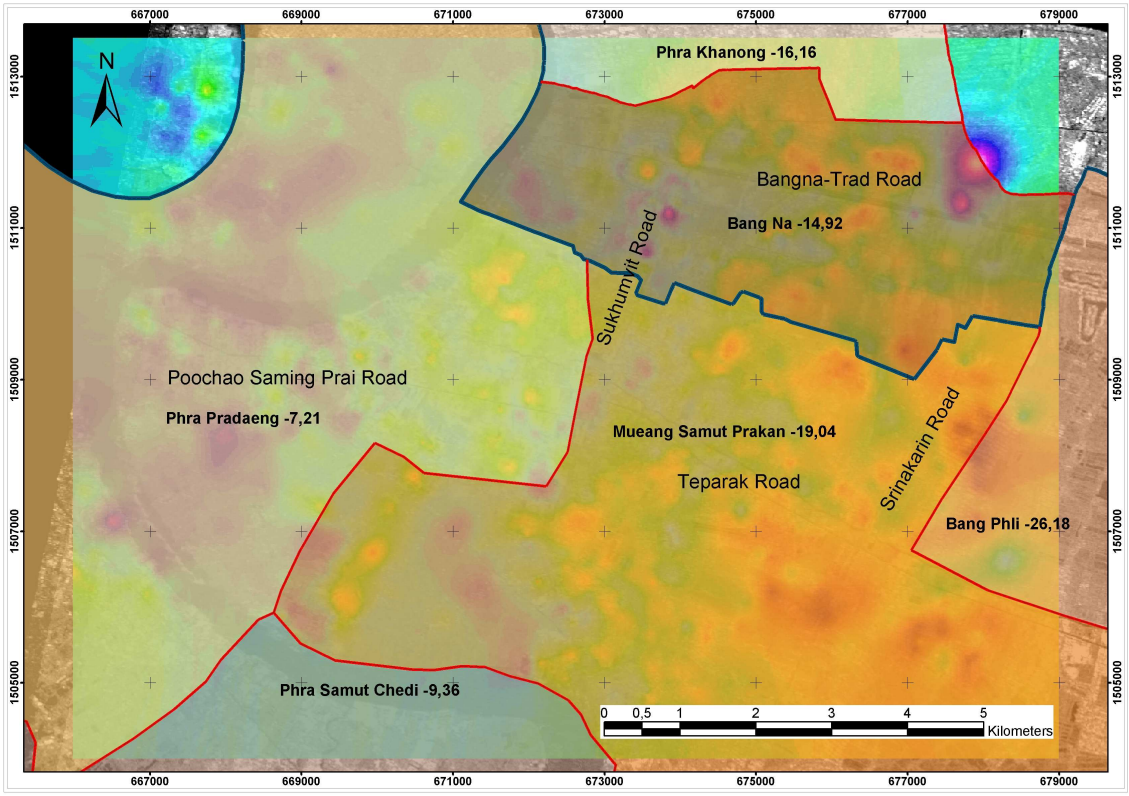

Figure 5.4: Zoning of subsiding areas based on the derived mean PS subsidence estimates

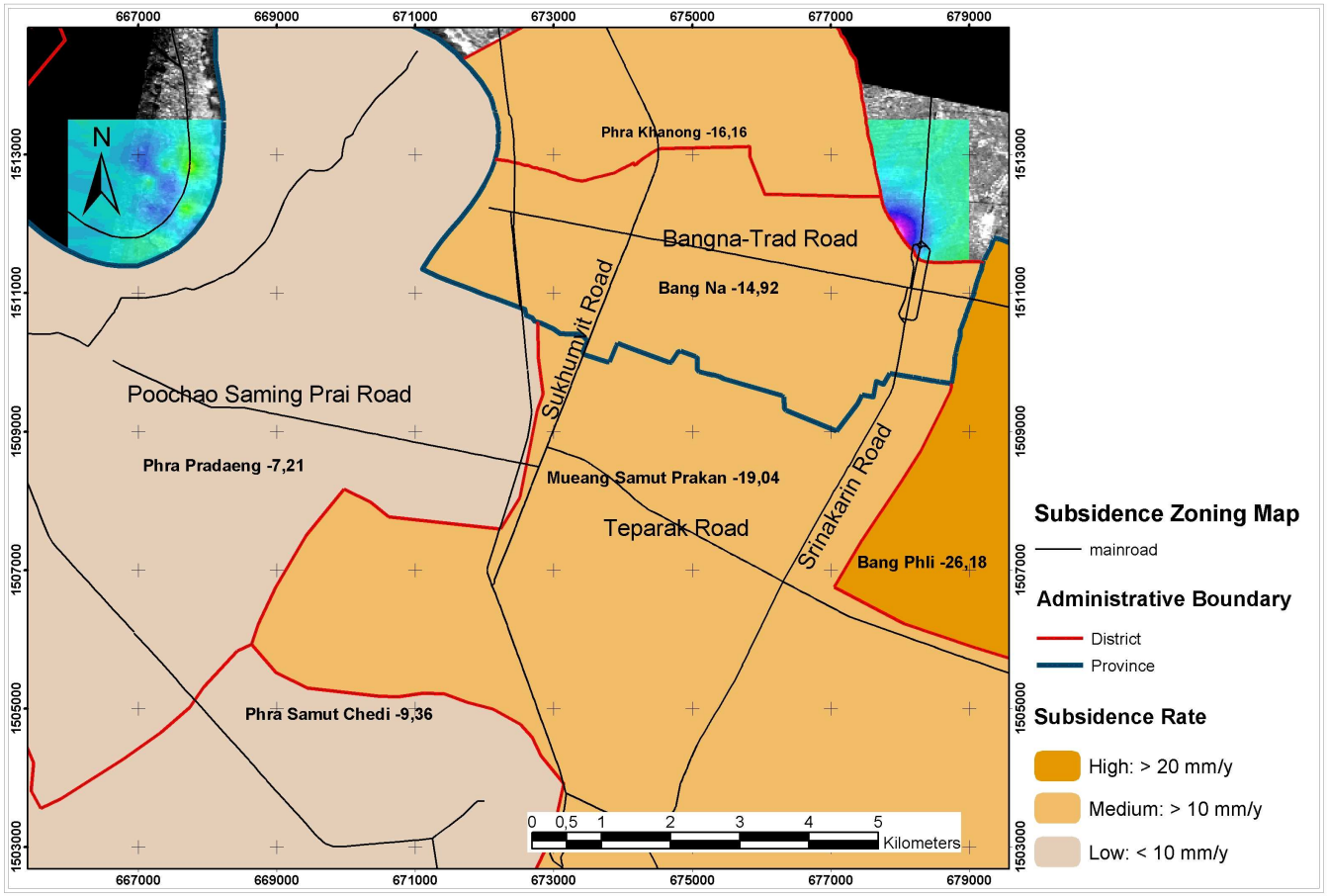

Figure 5.5: Map of subsidence zones in the study area. Here, the Bang Plee district (farthest most right) is considered the most critical subsiding zone with an averaged subsidence rate of more than 20 mm/year.

5.4.2 Prediction of subsidence

Time series analysis of InSAR observations as described in chapter 4 results in an estimate of the mean subsidence rate over a period of time where InSAR data is available. An empirical mean to predict subsidence can be carried out by extrapolating these PSI subsidence measurements to derive a future trend. The primary goal of this approach is to anticipate the future surface elevation changes due to subsidence based on the known time-series subsidence measurements.

Past studies (Giao, 1996; Duc, 1999; Thepparak, 2001; Phienwej et al., 2004) applied empirical, semi-theoretical or theoretical means to predict land subsidence . Prediction results were usually presented as the evolution of subsidence over time at a local point. Using PSI subsidence measurements for this prediction is appealing due to its frequent observations and high spatial resolution. The average time sampling of the InSAR observations used is approximately 5 observations per year (19 interferograms in 4 years). Fitting a model using more measurements should provide a better characterization of subsidence and thus its subsequent prediction results.

Prediction assumption and model assessment

The prediction assumes that surface elevations caused by subsidence decrease exponentially with time. This assumption is applied for two reasons. First, the hydraulic head dissipation over time for the interbed that is related to subsidence can be described by an exponential model. And second, investigations of the past periodic leveling measurements at several benchmarks showed nonlinear behavior of subsidence with time. The results in fig. 5.6 and table 5.3 justify why the exponential assumption was applied for the prediction. Fig. 5.6 shows the time, t and $\log(D)$ plot of a benchmark, where D represents leveling measurements. An approximate linear relationship of this $\log(D)$ plot implies that D is more or less decreasing exponentially. In addition a good fit of the linear and exponential models were evaluated by estimating root mean square (RMS) differences between the actual leveling and the predicted values from the models (see table 5.3). Comparison of RMS at these three locations showed that the exponential model of the leveling is the best fit (lowest RMS) for the actual leveling. Among PS measurements, the nonlinear PS measurements provide the best fit.

The following exponential model was used for the prediction.

$$D = D_0 k^t \tag{5.10}$$

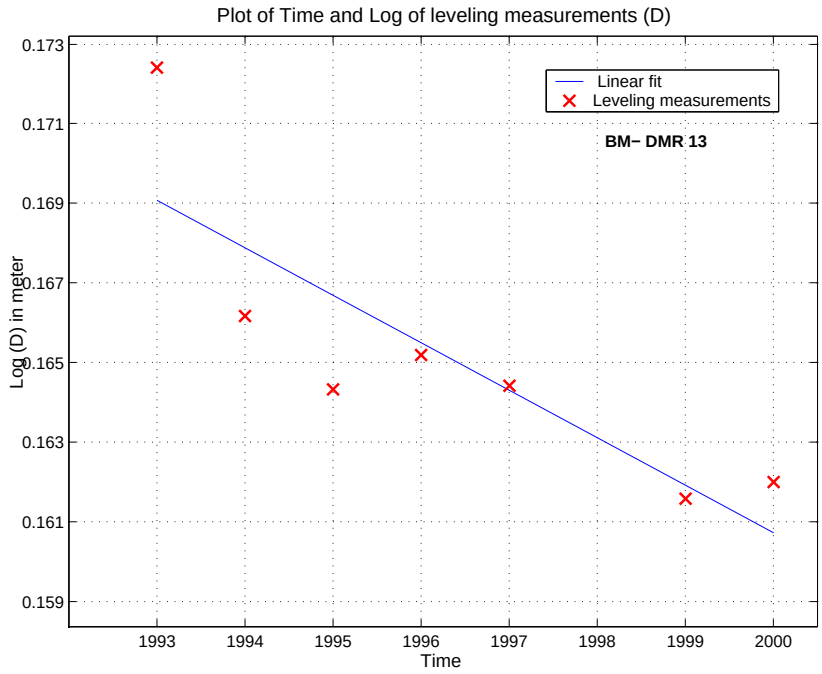

Figure 5.6: Plot of time and log(D) shows an approximate linear relationship

Table 5.3: RMS differences between the actual leveling measurements and the estimates from linear and exponential models at three benchmark locations

Benchmarks	Leveling (Linear) (mm)	Leveling (Exp*) (mm)	PS (Linear) (mm)	PS+residual (Exp*) (mm)	Nonlinear PS (Exp*) (mm)
DMR 13	5.9	6.0	3.4	3.6	2.9
DMR 14	8.1	7.1	9.2	8.5	8.7
DMR 15	6.1	5.8	6.6	8.5	7.7

* Exponential model

where D denotes surface elevation at time t that decreases exponentially due to subsidence.

D_0 denotes surface elevation at time t_0; in this case t_0= 1996 was assumed.

t denotes the elapsed time of interest.

k is a parameter of the exponential function representing its slope and is to be determined.

At the PS reference point, the PS measurement was compared to the leveling of the corresponding benchmark of the same time (DMR 13) and adjusted. This same amount of adjustment was then applied to all other PSs. These adjusted measurements at reliable PSs (PS density $\sim 27 PS/km^2$) were the starting point of the model calculation. At each PS, the nonlinear measurements between 1996-2000 were used to determine parameters $D_0$and k using a program written in IDL. Hence, the year 2000 is the starting point of the prediction. Surface elevation D in the year 2025 and 2050 were determined. The predicted subsidence was then estimated by subtracting the surface elevations during the time frame of interest (between 2000-2025 and between 2000-2050).

Predicted subsidence - Results

The prediction results demonstrate varieties of subsidence magnitudes experienced at PSs. They indicate that PSs located in the east of the area are about to subside more than those in the west. Subsidence magnitude ranges from a minimum of 5 mm to a maximum of 73 cm within 25 years. For the same period, an average subsidence of 26 cm is predicted for this area (fig. 5.7). For the longer period of 2000-2050, the anticipated subsidence ranges from a minimum of 8 mm to a maximum of 1.1 m with an average of 43 cm (fig. 5.8). Such subsidence prediction maps (fig 5.7 and fig 5.8) demonstrate an advantage of using PS measurements for this prediction. It has potential of deriving a highly detailed subsidence prediction. The predicted subsidence from exponential extrapolations of leveling measurements and of PS measurements are compared in table 5.4.

Table 5.4: The comparison of predicted subsidence obtained from exponential extrapolation of leveling and PS measurements at 8 benchmark locations

Benchmarks	SS*(Leveling) (cm) 2000-2025	SS*(PS) (cm) 2000-2025	SS*(Leveling) (cm) 2000-2050	SS*(PS) (cm) 2000-2050
DMR 13	10.0	6.0	19.0	11.6
DMR 14	32.1	33.2	48.4	52.8
DMR 15	20.2	24.8	34.0	45.0
DMR 82	30.5	27.6	54.5	46.4
KR 1303	10.5	6.1	19.5	11.8
KR 1201	28.7	30.0	48.7	49.2
KR 1202	40.6	40.6	66.6	68.9
BMS 8308	19.2	19.5	36.2	36.1

* An abbreviation for subsidence

5.5 Summary

Important findings from this chapter are:

- Temporal analysis of hydraulic head change and surface subsidence at three sampled locations equally revealed the same response trends. The permanent compactions of the compressible aquifer occurred around 1988-1995 due to continuously lowering of the drawdown. Their expansions have taken place since 1995 until at least 2000 due to the ascending of the drawdown. These behaviours can be reflected at the ground surface as the precise leveling data at approximately the same time showed the slow down of subsidence (see fig. 5.2).

- The calculated $\triangle b/ \triangle h$ inferring a compressibility during compaction of the aquifer increases spatially from west to the east from 0.01, 0.02 and 0.04 respectively. It indicates that the areas in the east side are the most susceptible to subsidence. This increasing trend also corresponds to the subsidence trend estimated by PSI.

- A subsidence estimate from PSI is found to be useful in approximating a transient subsidence to head decline ratio where surface leveling is not available. This provides reasonable agreement with the estimate derived from leveling measurements of the same time. The maximum discrepancy is about + 3 mm. per 1 m. of hydraulic head change.

- Due to recent trends of the rebound of hydraulic heads (1995 and beyond) at all sampled locations, it is not realistic to use subsidence to head decline ratios for predicting subsidence.

- Despite a scarcity of supported data during analysis, it was realized that effective monitoring of dynamic and complex phenomenon like subsidence requires indispensably a regular monitoring system to acquire adequate data to better characterize the subsurface compaction mechanisms. Regularly monitored groundwater data and the corresponding surface leveling data (yearly or every second year depending on the subsidence rate) are the minimum requirement. Additional observations from compression indicators installed at different depths are preferable in characterizing and understanding subsurface compression.

- The mean subsidence rates derived from PS analysis during 1996-2000 were utilized to identify the subsidence zones based on their potential risk to subsidence. This spatial subsidence risk map provides an overview of subsidence status over the 4-year period and can be used as fundamental information in planning and prioritizing appropriate strategies for alleviation of subsidence problems.

- The predicted subsidence maps between 2000-2025 and 2000-2050 which are based on the exponential extrapolation of PS measurements anticipate the average subsidence magnitude of 26 cm and 43 cm in the next 25 and 50 years for this area. These maps demonstrate the potential of PS to derive highly detailed future subsidence information.

- In this study, the empirical (section 5.4.2) and semi-theoretical approaches (section 5.3) were used for subsidence analysis and prediction. Concerning the prediction of the amount of subsidence, it is preferable to use several methods e.g. empirical, semi-empirical and theoretical approaches, whenever possible, to reach a conclusion based on an overall judgement. Detailed information on the stratigraphication of the aquifer-aquitard system, their geohydrological properties, regional groundwater flow model, when available, could be exploited to conduct a subsidence analysis based on the theoretical approach.

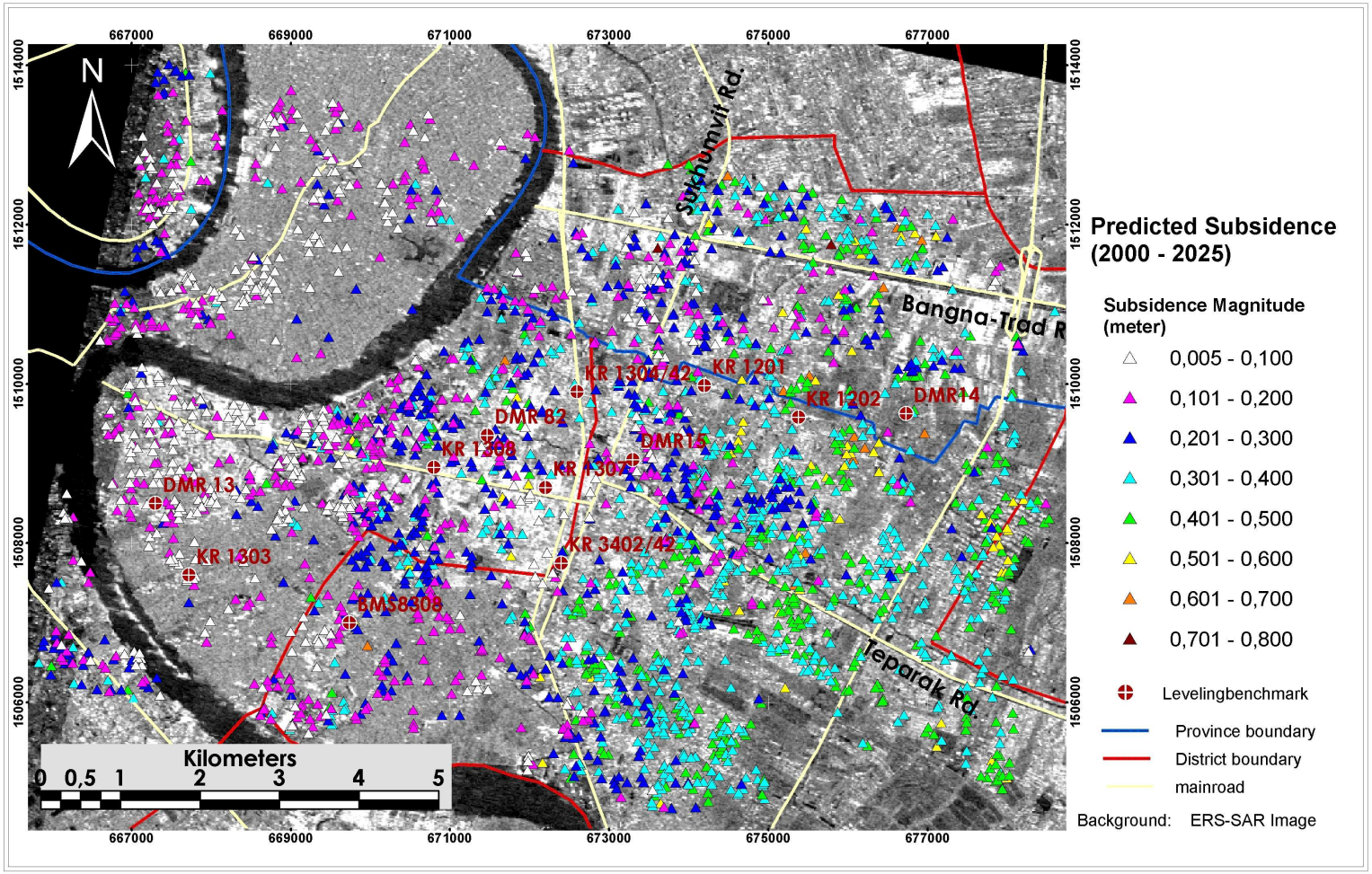

Figure 5.7: Predicted subsidence (2000 - 2025) estimated by exponential modelling

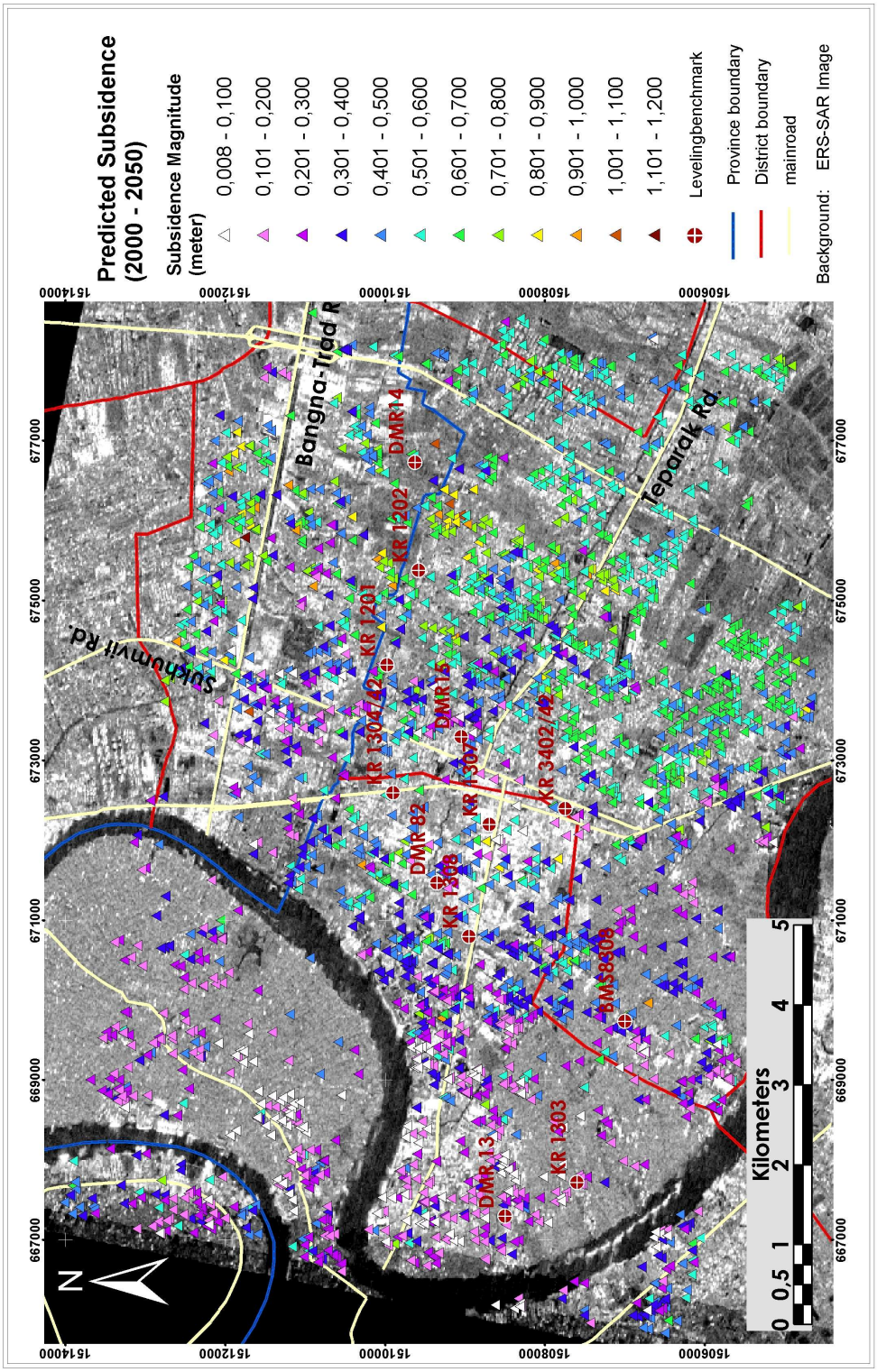

Figure 5.8: Predicted subsidence (2000 - 2050) estimated by exponential modelling

Chapter 6

Conclusions and perspectives

6.1 Implications of this work

Employing PS analysis of 20 SAR images, I have quantified the averaged subsidence rates for the Bangna-Samrong area in the Bangkok Metropolitan area during the period 1996-2000. The subsidence estimates agree well with reference levelling data. The precision achieved was better than $\pm 1.5\,mm/y$ at locations subsiding at approximately constant rates. This study has identified several factors influencing the application of PS analysis. These can be grouped into three groups. The first group consists of factors related to data configuration, the second includes those concerned with the processing, and the last contains those dependent on the study site and subsidence mechanism. The number of SAR acquisitions available for PS analysis strongly influences the attainable precision of the resulting estimate. The more images are used in the analysis, the higher the precision that can be expected. Irregular temporal sampling may induce difficulties in temporal filtering, e.g. in extracting nonlinear displacement signals. Different PS detection algorithms or different subsidence models are examples of important processing factors. I used the Signal-to-Clutter-Ratio (SCR) approach to select PS since this selection criteria proved superior for the small number of images. I have found that the linear subsidence model applied during the PS analysis is not generally appropriate to describe subsidence behaviour in the study area. The degree of non-linear movement of a point can be observed in the difference between the PS estimate and the reference levelling measurement. The observations available from levelling benchmarks confirmed that many benchmarks do not subside linearly with time, but follow a more complex time-varying subsidence behaviour. However, the small number of images available for this study prevented the use of more complicate subsidence models.

Factors related to the study area most importantly include the high rate of subsidence and subsidence rate gradients, and an insufficient distribution of the number of PS detected. High subsidence rates can induce ambiguous phase unwrapping, particularly when the number of images is small. The density of PS in the study area largely determines the stability of the difference phase observations and thus the detectable spatial gradients in subsidence rates or atmospheric phase contributions. The number of interferograms available is important for the reliability of the PS identification and the temporal statistics for estimating and correcting - the atmospheric phases. Optimizing these factors should lead to practically successful applications of PSI for surface displacement estimation.

Where only a few images are available, a few preparatory considerations are useful. Knowledge of the maximum subsidence rate in the study area is necessary to anticipate whether or not the interferometric data sets in hand are able to provide unambiguous estimates. A success rate assessment with simulated data, as presented in section 4.5.4, is useful to anticipate the success of the PSI subsidence estimation. These procedures can support the decision whether or not the available data is sufficient to enable reliable subsidence estimates through PSI.

I have found that irregular temporal sampling strongly restricts the extraction of the temporal signal, i.e. the nonlinear motion. The quality of the non-linear PS estimates resulting from the spatial-temporal filtering depends on both the temporal sampling of the interferometric data and the correlation time of the subsidence signal. Meaningful non-linear estimates may be obtained where the signal correlation time exceeds the InSAR sampling interval. The non-linear subsidence behaviour in the study area varies spatially and is determined primarily by aquifer system properties, i.e. compressibility and thickness of compacting interbeds, and the water level changes. The paucity of data to fully characterize the aquifer mechanics restricts the reach of a further interpretation of the non-linear subsidence estimates. Nonetheless, the PS estimates' applicability for non-linear subsidence monitoring is constrained primarily by the unfavourable data configuration in this case and does not represent a fundamental limitation of the potential of the InSAR technique. The temporal sampling of 35 days is sufficient for the characterization of dynamic subsidence processes in many situations.

With PS density of 28 PS/km^2, the main result of this study is the most detailed subsidence map of the area under study to date. Compared to the levelling measurements, its denser estimates provide an improved characterization of spatial varying subsidence. The improvement of the understanding of the complex subsidence mechanism related to aquifer system compaction is therefore less restricted by a lack of detail in subsidence

information.

In addition, PS mean subsidence estimates were employed for the first time to derive elastic storage coefficients for the Bangkok aquifer system. The results agree with estimates derived from levelling data of the same period. This implies that PS estimates are useful for the derivation of elastic storage coefficients in the absence of the levelling data. However, a derivation of storage coefficient estimates at PS resolution is restricted by the unavailability of the hydraulic head information.

Persistent Scatterer Interferometry has been demonstrated to be a feasible tool for deriving robust surface subsidence magnitudes even under difficult conditions in this study. Its ability to provide subsidence information with great spatial detail is unprecedented by other means available to date. While conventional DInSAR can sense small displacements at resolutions on the order of ten meters, temporal decorrelation and atmospheric influences in tropical conditions have prevented a successful displacement detection in Bangkok. The density of levelling measurements is limited by the number of distributed benchmarks, which is approximately 1 BM per 100 km^2 in Bangkok and vicinity. The advance in InSAR technology such as PSI now makes spatially detailed subsidence mapping in Bangkok possible.

Beyond being a feasible tool of providing detailed subsidence information, PSI was demonstrated to be useful for monitoring and mitigating subsidence through two example applications - risk analysis and subsidence prediction. The obtained subsidence risk map provides information on the severity of subsidence classified within district boundary. The map can be used by urban planners or the administrative bodies to support their decision making. The empirical extrapolation of the PS subsidence estimates based on an exponential model results in predicted subsidence maps for the year 2025 and 2050 at PS resolution demonstrating potential of PS estimates in delivering detailed subsidence prediction information. These results anticipate a maximum subsidence of 0.73 m and 1.14 m in this area by the year 2025 and 2050, respectively.

Reliable subsidence information constitutes a critical part in establishing a systematic subsidence monitoring system that is indispensable for subsidence control and mitigation. PSI can contribute by providing spatially detailed subsidence patterns for large areas. PSI is considered to be the most cost effective means for determining subsidence over extensive areas. SAR data from existing and future missions will likely suffice to provide for the continuity of subsidence observations by InSAR. Periodic levelling surveys (with observation frequencies dependent on the subsidence rate) and regular water level observations in wells are useful additions to provide precise measurements locally, validate PS measurements, and analyze the subsidence cause-effect relations.

From my point of view, these data are the minimum requirements for an effective monitoring system. Information from compression indicators installed at different depths could add further understanding of subsurface compaction mechanism of the aquifer system. Unfortunately, the cost of maintaining field instruments and obtaining regular data are foreseen to be the major obstacles in obtaining adequate data.

6.2 Perspectives

- Using L-band SAR data in a Persistent Scatterer analysis would be very interesting. The reduced sensitivity to noise would likely avoid some of the difficulties in interpreting C-band measurements. Also, the use of PSI in non-urban areas might become more interesting. JERS-1 data archived by the Japanese Earth Resource Satellite or planned future missions like ALOS(JAXA, 2005) may be of use for this experiment.

- The joint exploitation of SAR data acquired by the ENVISAT satellite together with ERS-SAR data can extend the image archive for Bangkok. This provides possibilities for a more robust PS analysis.

- The first German radar satellite for earth observation, TerraSAR-X (DLR, 2005), scheduled to launch in 2006 will also be highly interesting for quantifying time-varying subsidence. Its high spatial resolution and short revisit cycle of 11 days might enable exciting perspectives for dynamically changing urban environments in particular.

- The understanding of the complex surface subsidence and subsurface compaction mechanisms can only be improved through a continuous and long-term monitoring of related data. Apart from benefiting from repeat-pass InSAR technology, periodic geodetic surveying and regular observations at wells are necessary.

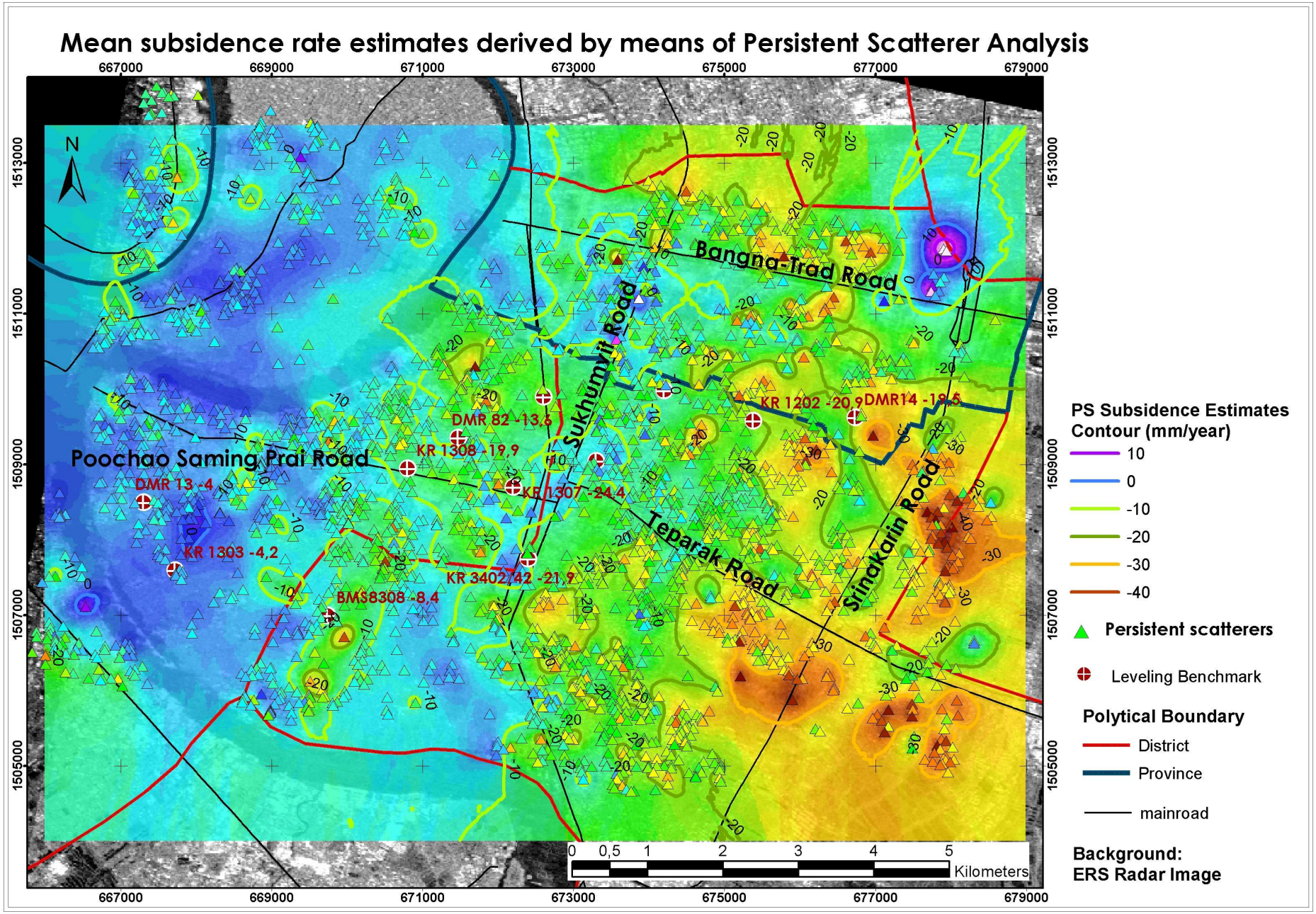
Mean subsidence rate estimates derived by means of Persistent Scatterer Analysis
667000
669000
671000
673000
675000
677000
679000
1513000
1511000
1509000
1507000
1505000
N
Bangna-Trad Road
Sukhumvit Road
Poochao Saming Prai Road
Teparak Road
Srinakarin Road
DMR 82 -13,6
KR 1308 -19,9
DMR 13 -4
KR 1303 -4,2
KR 1307 -24,4
KR 3402/42 -21,9
BMS8308 -8,4
KR 1202 -20,9
DMR14 -19,5
0 0,5 1 2 3 4 5
Kilometers
PS Subsidence Estimates Contour (mm/year)
10
0
-10
-20
-30
-40
Persistent scatterers
Leveling Benchmark
Polytical Boundary
District
Province
mainroad
Background:
ERS Radar Image

Appendix A

Satellite SAR Missions

Table A.1: List of past, present and future satellite SAR missions

Mission	Year	ΔT	H_{sat}	f_0	B_R	θ_{inc}	Swath
		(day)	(km)	(GHz)	(MHz)	(deg)	(km)
Seasat*	1978	3	800	1.275	19.00	20(23)26	100
SIR-A	1981	-	235	1.278	19.00	(50)	50
SIR-B*	1984	-	235	1.282	12.00	(15)-(64)	10-60
Cosmos 1870	1987-89	var	250	3.000	*	(30)-(60)	20-45
ALMAZ	1991-92	-	300	3.000	uncoded	(30)-(60)	20-45
Magellan*	1989-92	var	290-	2.385	2.26	(17)-(45)	20
			2000				
ERS-1*	1991-92	3	790	5.300	15.55	21(23)26	100
	1992-93	35	790	5.300	15.55	21(23)26	100
	1993-94	3	790	5.300	15.55	21(23)26	100
	1994-95	168	790	5.300	15.55	21(23)26	100
	1995-2000	35	790	5.300	15.55	21(23)26	100
ERS-2*	1995-	35	790	5.300	15.55	21(23)26	100
JERS-1*	1992-98	44	568	1.275	15.00	26(39)41	85
SIR-C/X-SAR	Apr.1994	-	225	1.240	20	(55)	21-42
	Apr.1994	-	225	5.285	20	(55)	21-42
	Apr 1994	-	225	9.600	10-20	(15)-(45)	15-45
SIR-C/X-SAR*	Oct 1994	1	225	1.240	20	(55)	21-42
	Oct 1994	1	225	5.285	20	(55)	21-42
	Oct 1994	1	225	9.600	10-20	(15-45)	15-45
Radarsat*	1995-	24	792	5.300	11-30	(20)-(49)	10-500
SRTM*	2000	0	233	5.300	9.50	(52)	225
	2000	0	233	9.600	9.50	(52)	50
ENVISAT*	2001	35	800	5.300	14.00	(20)-(50)	100-500
Radarsat-2*	2003	24	798	5.300	12-100	(20)-(60)	20-500
ALOS	Summer 2005 (delayed)	45	700	1.270	28/14	(8)-(60)	40-350
TerraSAR-X	June 2006	11	514	9.65	5-300	(20)-(45)	30-100

ΔT repeat period; H_{sat} satellite altitude; f_0,B_R range bandwidth; θ_{inc} incidence angle (values between parentheses denote nominal mid-incidence angles). * Missions capable of interferometry. * Unknown ; Not applicable. SIR-A/B/C, X-SAR and SRTM are instruments flown on-board the space shuttle. (modified after Hanssen, 2001)

TerraSAR-X will be the first German's radar satellite for earth observation `www.caf.dlr.de/tsx/main/mission.ge.htm`.

Appendix B

Additional Information relates to Persistent Scatterer Analysis

B.1 Example of persistent scatterers in reality

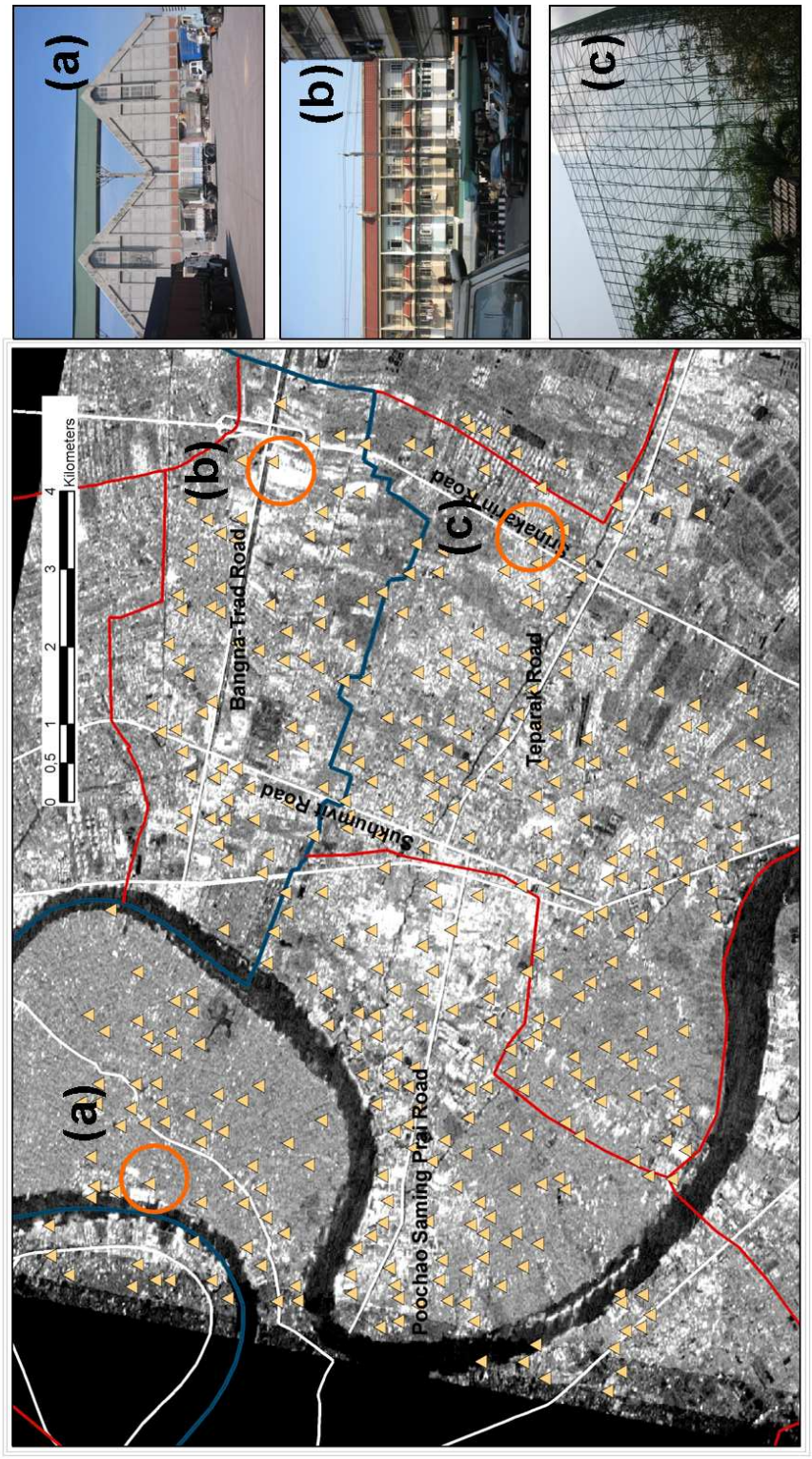

Figure B.1: Persistent scatterers in reality

B.2 Plots of leveling measurements versus time

Subsidence evolution over time of benchmarks which are not presented in fig. 4.53.

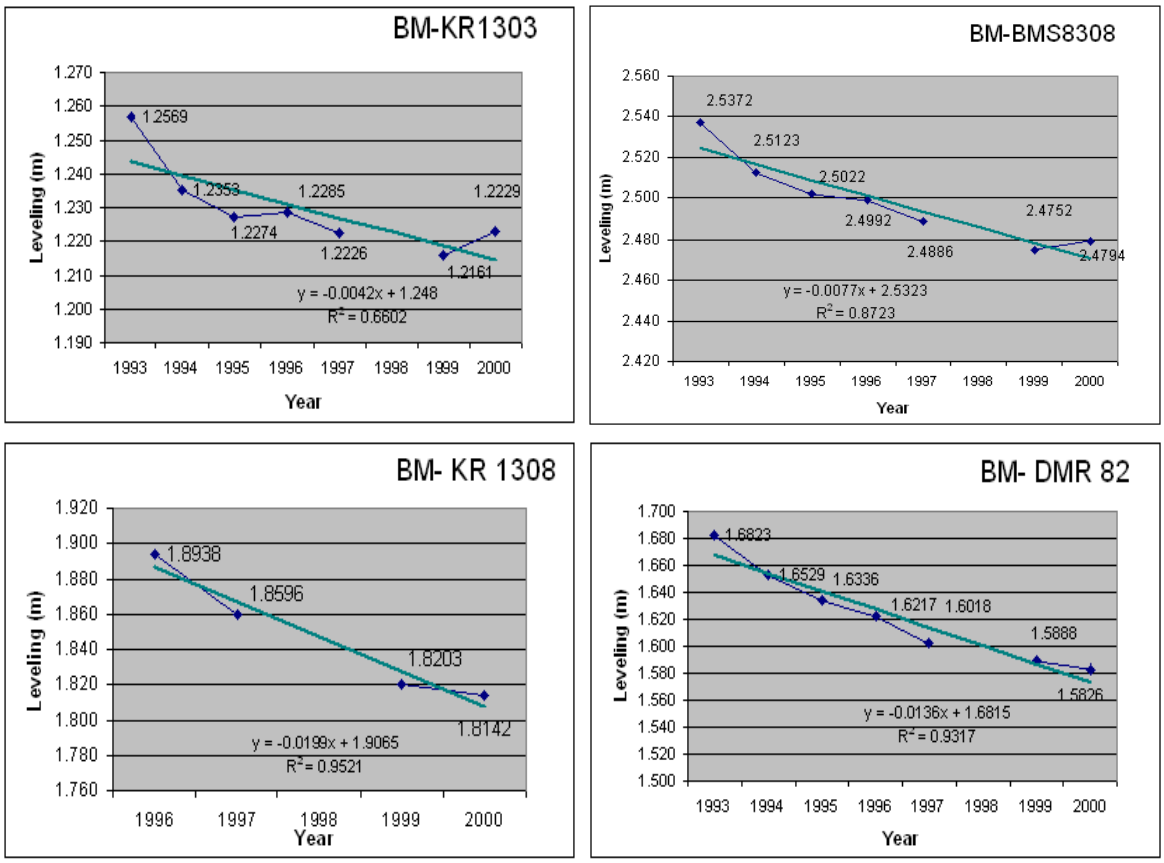

Figure B.2: Plots of leveling measurements versus time at benchmarks for the period 1993-2000.

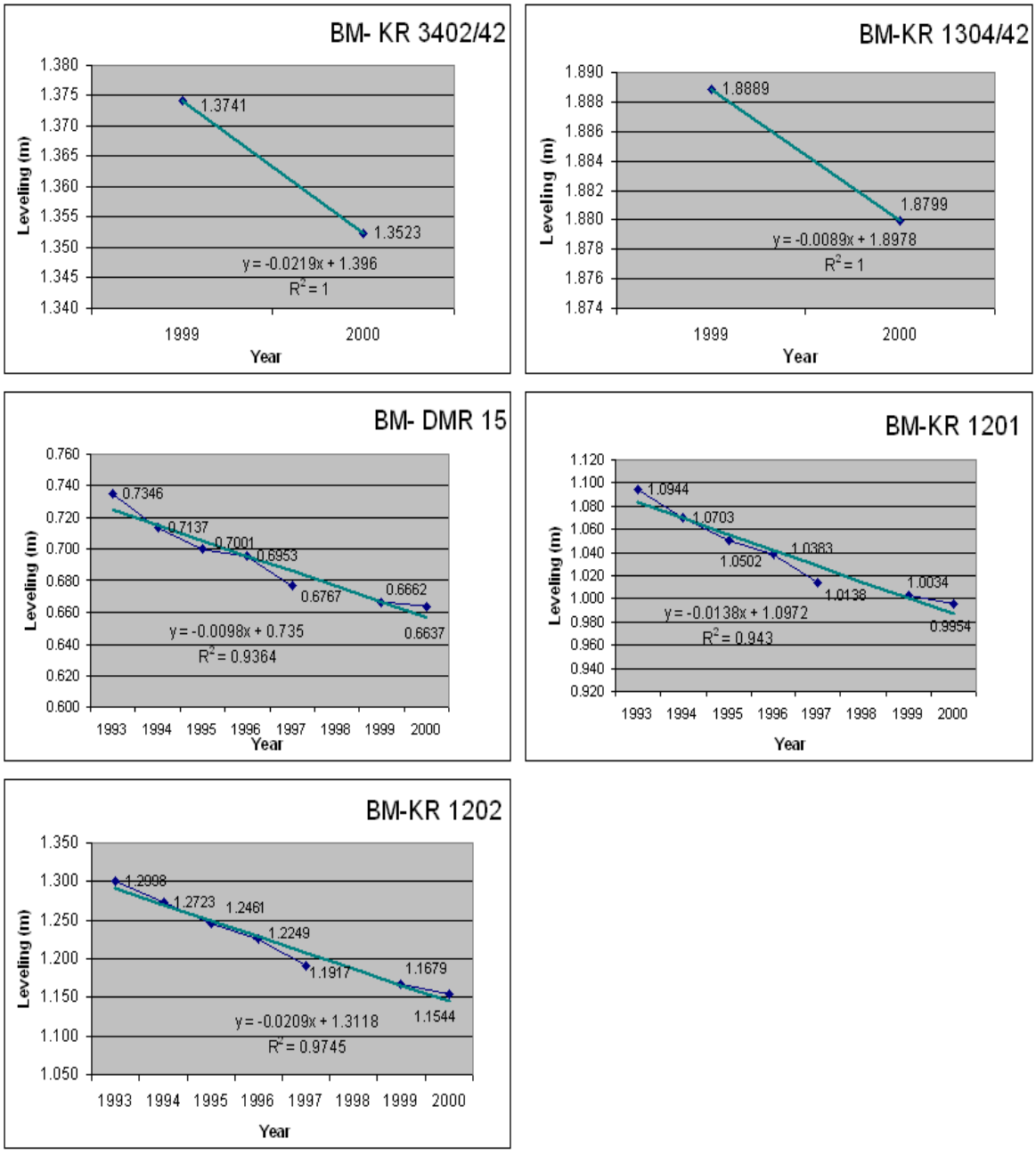

Figure B.3: Plots of leveling measurements versus time at benchmarks for the period 1993-2000 (continued from fig. B.2).

Appendix C

Effective Stress and the Hydraulic Head

C.1 Principle of effective stress

The principle of *effective stress* was developed by Terzaghi (1925). For an easy understanding of the concept (fig. C.1), consider a stress equilibrium on an arbitrary plane through a saturated geologic formation at depth. σ_T denotes the total stress and is the stress due to the weight of overlying rock and water. One part of this stress is borne by the granular skeleton of the porous geologic material and the other part is borne by the fluid pressure p of water in the pores. The portion of total stress that is not borne by the fluid is called *effective stress* σ_e. It is this stress that is applied to the grains of the porous medium. Rearrangement of the soil grains and the resulting compression of the granular skeleton is caused by changes in the effective stress, not by changes in total stress.

Fig. C.1 illustrates the concept of effective stress σ_e in relation to total stress σ_T and fluid pressure p. Their simple relationship can be expressed as

$$\sigma_T = \sigma_e + p \tag{C.1}$$

An expression of this relationship in term of changes can be written as:

$$d\sigma_T = d\sigma_e + dp \tag{C.2}$$

The analysis of transient subsurface flow problems usually do not involve a change in total stress, as the weight of the overlying rocks and water often remains constant over

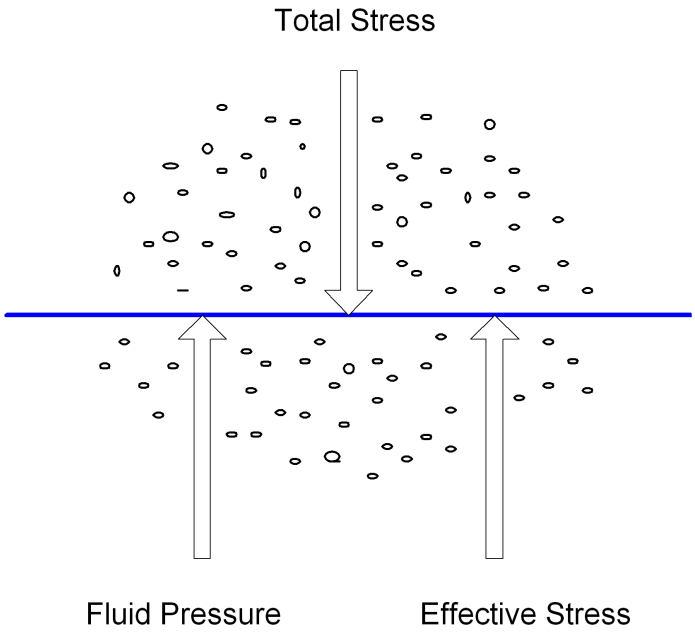

Figure C.1: Total stress, effective stress, and fluid pressure on an arbitrary plane through a saturated porous medium (after Freeze and Cherry (1979))

time (Freeze and Cherry, 1979). Therefore, $d\sigma_T = 0$ and equation C.2 can be rewritten as:

$$d\sigma_e = -dp \tag{C.3}$$

The relation (eq. C.3) implies that when fluid pressure decreases, the effective stress increases by an equal amount. When groundwater is removed from the pores in an aquifer, the fluid pressure decreases and as a result the effective stress borne by the granular skeleton increases by the same amount.

C.2 Change in effective stress and change in hydraulic head

Using equations C.3 to C.5, change in effective stress $d\sigma_e$ can be expressed in relation to hydraulic head change as shown in eq.C.6.

$$p = \rho g \Psi \tag{C.4}$$

$$\Psi = h - z \tag{C.5}$$

$$d\sigma_e = -\rho g dh \tag{C.6}$$

where ρ denotes water density

g denotes gravity acceleration

Ψ denotes pressure head

z denotes elevation head and it is constant at a point under interest

h denotes the hydraulic head.

Detail derivation of each of the equations C.4 to C.6 can be found in (Freeze and Cherry, 1979). Eq. C.6 implies that a change in effective stress at a point in the system is governed by a change in the hydraulic head at that point.

Bibliography

C. Achalabuti (1974) Petroleum geology of the Gulf of Thailand. In Circum-Pacific Energy and Mineral Resources.

N. Adam, B. M. Kampes and M. Eineder (2004) The development of a scientific persistent scatterer system: Modifications for mixed ERS/ENVISAT time series. In ENVISAT and ERS Symposium. 6-10 September 2004, Salzburg, Austria. CDROM.

N. Adam, B. M. Kampes, M. Eineder, J. Worawattanamateekul and M. Kircher (2003) The development of a scientific permanent scatterer system. In ISPRS Joint Workshop on High Resolution Mapping from Space. 6-8 October 2003, Hannover, Germany.

AIT (1981) Investigation of land subsidence caused by deep well pumping in the Bangkok area. Comprehensive report 1978-1981. Submitted to Office of National Environmental Board by the Division of Geotechnical and Transportation Engineering of Asian Institute of Technology, Bangkok, Thailand.

AIT (1982) Investigation of land subsidence caused by deep well pumping in the Bangkok area: Phase IV Extension of subsidence observation network. Final report. Submitted to Office of National Environmental Board by the Division of Geotechnical and Transportation Engineering of Asian Institute of Technology, Bangkok, Thailand.

AIT (1992) Simulation study of Bangkok aquifer system. Research report 251, Asian Institute of Technology, Bangkok, Thailand.

AIT (1995) Artificial recharge subsidence control, Bangkok Thailand. Final technical report, School of Civil Engineering, Asian Institute of Technology, Bangkok, Thailand. Submitted to the International Development Research Centre.

AIT (2004) Workshop on Geo-Engineering in Groundwater, Land subsidence, Exploration Geophysics and Underground rock engineering. Workshop document, EIT-Japan-AIT, Bangkok, Thailand. 20-21 September 2004.

AIT and DMR (1982) Groundwater resources in the Bangkok area: Development and management study. Comprehensive report 1978-1981. Research Report 91, Asian Institute of Technology, Bangkok, Thailand.

R. Bamler and P. Hartl (1998) Synthetic aperture radar interferometry. *Inverse Problems*, 14, R51–R54. IOP Publishing Ltd., UK.

P. Berardino, G. Fornaro, R. Lanari and E. Sansosti (2002) A new algorithm for surface deformation monitoring based on small baseline differential SAR interferograms. *IEEE Transactions on Geoscience and Remote Sensing*, 40(11), 2375–2383.

P. R. Bevington and D. K. Robinson (1992) Data reduction and error analysis for the physical science. McGraw-Hill Inc., 2nd edition. 328 p.

M. Bontenbal (2001) Land subsidence in Bangkok: An overview of changes in land subsidence over the last 25 years. Master's thesis, Free University of Amsterdam, The Netherlands.

G. F. Brown, S. Buravas, J. Charaljavanaphet, N. Jalichandra, W. J. Johnson, V. Shesthaputra and G. Taylor (1951) Geological reconaissance of the mineral deposits of Thailand. USGS Bulletin 984, U.S. Geological Survey.

C. Colensanti, A. Ferretti, F. Novali, C. Prati and F. Rocca (2003a) SAR monitoring of progressive and seasonal ground deformation using the Permanent Scatterers Technique. *IEEE Transactions on Geoscience and Remote Sensing*, 41(7), 1685–1701.

C. Colensanti, A. Ferretti, C. Prati and F. Rocca (2003b) Monitoring landslides and tectonic motion with permanent scatterers technique. *Engineering Geology*, 68, 3–14.

C. Colensanti, R.Locatelli and F. Novali (2002) Ground deformation monitoring exploiting SAR permanent scatterers. In International Geoscience and Remote Sensing Symposium. 24-28 June, 2002. Toronto, Canada. CDROM.

C. Colensanti, J. Wasowski and A. Fumagalli (2004) Monitoring landslide activity with SAR interferometry. In ENVISAT and ERS Symposium. 6-10 September 2004, Salzburg, Austria. CDROM.

M. Costantini (1998) A novel phase unwrapping method based on network programming. *IEEE Transactions on Geoscience and Remote Sensing*, 36(3), 813–821.

M. Costantini and P. A. Rosen (1999) A generalized phase unwrapping approach for sparse data. In International Geoscience and Remote Sensing Symposium. 28 June -2 July 1999, Hamburg, Germany. CDROM.

M. Cotelli, G. Fornaro, G. Franceschetti, R. Lanari, M. Migliaccio, J. Moreira, K. P. Papatanassiou, G. Puglisi, D. Riccio and M. Schwaebisch (1996) SIR-C/X-SAR multifrequency multipass interferometry: A new tool for geological interpretation. *Journal of Geophysical Research*, 101(E10), 23127–23148.

J. B. Cox (1968) A review of Engineering properties of the recent marine clays in Southeast Asia. Research report 6, Asian Institute of Technology, Bangkok, Thailand.

C. V. Deutsch and A. G. Journel (1998) GSLIB: Geostatistical Software Library and User's Guide Applied Geostatistics Series., 2nd edition. Oxford University Press, 368 p.

DLR (2001) Shuttle Radar Topygraphy Mission: X-SAR/SRTM. Technical report, German Aerospace Center. URL `http://www.dlr.de/srtm/index_en.html`.

DLR (2005) TerraSAR-X Website. German Aerospace Center (DLR). URL `http://www.caf.dlr.de/tsx/main/mission.ge.htm`, accessed September, 2005.

DMR (1997) Statistical records on groundwater usage. Technical report, Department of Mineral Resources, Bangkok, Thailand.

DMR (2002) Precise leveling measurements at groundwater monitoring stations and benchmarks in Bangkok and vicinity. Annual report, Department of Mineral Resources (DMR), Bangkok, Thailand.

N. A. Duc (1999) Updating and analysis of Bangkok land subsidence caused by deep well pumping with emphasis on shallow soil settlement. Master's thesis, School of Civil Engineering, Asian Institute of Technology, Bangkok Thailand. 237 p.

M. Eineder and J. Holzner (1999) Phase unwrapping of low coherence differential interferograms. In International Geoscience and Remote Sensing Symposium. 28 June -2 July 1999, Hamburg, Germany. CDROM.

M. Eineder, M. Hubig and B. Milcke (1998) Unwrapping large interferograms using the minimum cost flow algorithm. In International Geoscience and Remote Sensing Symposium. 6-10 July , Seattle, USA. CDROM.

C. Elachi, T. Bicknell, R. L. Jordan and C. Wu (1982) Spaceborne Synthetic Aperture Imaging Radar: Applications, Techniques and Technology. *IEEE Transactions on Geoscience and Remote Sensing*, 70(10), 1174–1209.

A. Ferretti, F. Ferrucci, C. Prati and F. Rocca (2000a) SAR analysis of building collapse by means of the permanent scatterers technique. In International Geoscience and Remote Sensing Symposium. 24-28 July, 2000. Honolulu, Hawaii. CDROM.

A. Ferretti, C. Prati and F. Rocca (1999) Permanent scatterers in SAR interferometry. In International Geoscience and Remote Sensing Symposium. 1528–1530. 28 June -2 July 1999, Hamburg, Germany. CDROM.

A. Ferretti, C. Prati and F. Rocca (2000b) Analysis of permanent scatterers in SAR interferometry. In International Geoscience and Remote Sensing Symposium. 24-28 July, 2000. Honolulu, Hawaii. CDROM.

A. Ferretti, C. Prati and F. Rocca (2000c) Nonlinear subsidence rate estimation using permanent scatterers in differential SAR interferometry. *IEEE Transactions on Geoscience and Remote Sensing*, 38(5), 2202–2212.

A. Ferretti, C. Prati and F. Rocca (2001) Permanent scatterers in SAR interferometry. *IEEE Transactions on Geoscience and Remote Sensing*, 39, 8–20.

R. A. Freeze and A. J. Cherry (1979) Groundwater. Prentice-Hall Inc., Englewood Cliffs, New Jersey.

B. Fruneau, P. J. Rudant, D. Obert and D. Raymond (1999) Small displacements detected by SAR interferometry on the city of Paris (France). In International Geoscience and Remote Sensing Symposium. 28 June -2 July 1999, Hamburg, Germany. CDROM.

G. A. Gabriel, R. M. Goldstein and H. A. Zebker (1989) Mapping small elevation changes over large areas: Differential radar interferometry. *Journal of Geophysical Research*, 94, 9183–9191.

F. Gatelli, M. M. Gaurnieri, F. Parizzi, P. Pasquali, C. Prati and F. Rocca (1994) The wavenumber shift in SAR interferometry. *IEEE Transactions on Geoscience and Remote Sensing*, 32(4), 855–865.

P. H. Giao (1996) Artificial recharge of Bangkok aquifer system for mitigation of land subsidence. Ph.d. thesis, Asian Institute of Technology (AIT).

R. Goldstein (1995) Atmospheric limitations to repeat-track radar interferometry. *Geophysical Research Letters*, 22(18), 2517–2520.

R. M. Goldstein, H. A. Zebker and C. L. Werner (1988) Satellite radar interferometry: two-dimensional phase unwrapping. *Radio Science*, 23(4), 713–720.

L. C. Graham (1974) Synthetic interferometer radar for topographic mapping. In Proceeding of IEEE, volume 62. 763–768.

R. F. Hanssen (1998) Atmospheric heterogeneities in ERS tandem SAR interferometry. Delft university press, Delft, the Netherlands.

R. F. Hanssen (2001) Radar Interferometry: Data Interpretation and Error Analysis. Kluwer Academic Publishers, Dordrecht, The Netherlands.

R. F. Hanssen, T. M. Weckwerth, H. A. Zebker and R. Klees (1999) High-resolution water vapor mapping from interfeometric radar measurements. *Science*, 283, 1295–1297.

M. F. Henderson and J. A. Lewis (1998) Principles and applications of imaging radar, volume 2 of *Manual of Remote Sensing*. John Wiley & Sons Inc., USA, 3rd edition.

E. W. Hoen and H. A. Zebker (2000) Penetration depths inferred from interferometric volume decorrelation observed over the Greenland Ice Sheet. *IEEE Transactions on Geoscience and Remote Sensing*, 38(6), 2571–2583.

J. Hoffmann, S. A. Leake, D. L. Galloway and W. M. Wilson (2003a) MODFLOW-2000 ground-water model - User guide to the subsidence and aquifer system compaction (SUB) package. Open-file report, U.S. Geological Survey.

JAXA (2005) ALOS Mission. Website, Japan Aerospace Exploration Agency. URL `http://alos.jaxa.jp/2/alos_mission-e.html`, accessed October, 2005.

JICA (1993) The study on management of groundwater and land subsidence in the Bangkok Metropolitan area and its vicinity. Project interim report submitted to, DMR and PWD, Kokusai Kogyo Co., Ltd, Tokyo Japan.

JICA, DMR and PWD (1995) The study on management of groundwater and land subsidence in the Bangkok metropolitan areas and its vicinity. Final report, JICA, DMR and PWD, Kokusai Kogyo Co., Ltd, Tokyo, Japan.

D. G. Jorgensen (1980) Relationships between basic soils-engineering equations and basic ground-water flow equations. Water-Supply Paper 2064, U.S. Geological Survey. 40p.

B. M. Kampes (2005) Displacement parameter estimation using Permanent Scatterer Interferometry. Ph.d thesis and dlr research report 2005-16, Delft University of Technology. 168p.

B. M. Kampes and N. Adam (2003) Velocity field retrieval from long term coherent points in radar interferometric stacks. In International Geoscience and Remote Sensing Symposium. 21-25 July, 2003, Toulouse, France. CDROM.

B. M. Kampes and N. Adam (2004) Deformation parameter inversion using permanent scatterers in interferogram time series. In European Conference on Synthetic Aperture Radar. Ulm, Germany, 341–344.

B. M. Kampes and R. F. Hanssen (2004) Ambiguity resolution for permanent scatterer interferometry. *IEEE Transactions on Geoscience and Remote Sensing*, 42(11), 2446–2453.

B. M. Kampes, R. F. Hanssen and L. M. Swart (2001) Strategies for non-linear deformation estimation from interferometric stacks. In International Geoscience and Remote Sensing Symposium. 9-13 July 2001, Sydney, Australia. CDROM.

M. Kircher, N. Adam, J. Hoffmann, B. M. Kampes, H. J. Neugebauer and A. Roth (2003) Application of permanent scatterers on mining induced subsidence. In International Workshop on ERS SAR Interferometry 'Fringe03'. ESA. 1-5 December 2003, Frascati, Italy. CDROM.

R. K. Koch (1999) Parameter estimation and hypothesis testing in linear models. Springer-Verlag, New York., 2nd edition.

F. Kuehn, A. Margane, T. Tatong and T. Wever (2004) InSAR-based land subsidence map for Bangkok, Thailand. *Zeitschrift fuer Angewandte Geologie*, 1/2004, 74–81.

R. Lanari, G. Fornaro, D. Riccio, M. Migliaccio, J. Moreira, M. Schwaebisch, L. Dutra, G. Puglisi, G. Frannceschetti and M. Coltelli (1996) Generation of Digital Elevation Models by using SIR-C/X SAR multifrequency two-pass interferometry: the Etna case study. *IEEE Transactions on Geoscience and Remote Sensing*, 34(5), 1097–1114.

F. Li and R. M. Goldstein (1987) Studies of multi-baseline Spaceborne interferometric Synthetic Aperture Radars. In International Geoscience and Remote Sensing Symposium. Ann Arbor, 18-21 May 1987.

F. Li and R. M. Goldstein (1990) Studies of multi-baseline spaceborne interferometric Synthetic Aperture Radars. *IEEE Transactions on Geoscience and Remote Sensing*, 28(1), 88–97.

P. Lundgren, S. Usai, E. Sansosti, R. Lanari, M. Tesauro, G. Fornaro and P. Berardino (2001) Modeling surface deformation observed with SAR interferometry at Campi Flegrei Caldera. *Journal of Geophysical Research*, 106, 19355–19367.

U. Marschalk, A. Roth, M. Eineder and S. Suchandt (2004) Comparison of DEMs derived from SRTM/X- and C-Band. In International Geoscience and Remote Sensing Symposium. 4531–4534. Anchorage, Alaska, 20-24 September 2004.

D. Massonet, K. Feigl, M. Rossi and F. Adragna (1994) Radar interferometric mapping of deformation in the year after the Landers earthquake. *Nature*, 369, 227–230.

D. Massonet, M. Rossi, C. Carmona, F. Adragna, G. Peltzer, K. Feigl and T. Rabaute (1993) The displacement field of the Landers earthquake mapped by radar interferometry. *Nature*, 364, 138–142.

O. Mora, J. Mallorqui and J. Duro (2002a) Advanced differential interferometric techniques using stable targets for generation of terrain displacement maps. In European Conference on Synthetic Aperture Radar.

O. Mora, J. Mallorqui and J. Duro (2002b) Generation of deformation maps at low resolution using differential interferometric SAR data. In International Geoscience and Remote Sensing Symposium. 24-28 June, 2002. Toronto, Canada. CDROM.

MWA (2003) The performance report of the year 2003. Annual report, The Metropolitan Waterworks Authority (MWA), Thailand. URL `http://www.mwa.co.th/annual_content_i8_e.html`.

NASA (2005) Shuttle Radar Topographic Mission: The Mission to Map the World. Website, Jet Propulsion Laboratory. URL `http://www2.jpl.nasa.gov/srtm/index.htm`, last updated October 2005.

P. Nippitavasin (1989) Artificial recharge in Thailand - A case study of Ban Rong Khao, San Kampang district, Chiang Mai province. In "Bangkok Land Subsidence-What's next?" Symposium. 22-23 June 1989, Bangkok, Thailand.

P. Nutalaya, N. R. Yong, T. Chumnakit and S. Buapeng (1989) Land subsidence in Bangkok during 1978-1988. In "Bangkok Land Subsidence-What's next?" Symposium. 22-23 June 1989, Bangkok, Thailand.

D. Odijk, F. Kenselaar and R. F. Hanssen (2003) Integration of leveling and InSAR data for land subsidence monitoring. In International symposium on Deformation Measurements. URL `http://www.geo.tudelft.nl/fmr/research/insar/dig/bibliography/papers/odijkfig.pdf`, 23-28 May 2003, Santorini, Greece.

N. Phienwej, S. Thepparak and P. H. Giao (2004) Analysis of differential settlements induced by land subsidence from deep well pumping. In Workshop on Geo-Engineering in Groundwater, Land subsidence, Exploration Geophysics and Underground rock engineering. The Engineering Institute of Thailand (EIT), 20-21 September, Bangkok, Thailand.

C. Piancharoen and S. Buapeng (1973) Groundwater Bulletin No. 4. Department of Mineral Resources, Bangkok, Thailand.

J. F. Poland (1984) Guidebook to studies of land subsidence due to ground-water withdrawal. Technical report, United Nations Educational, Scientific and Cultural Organization (UNESCO), Michigan, USA.

J. Premchit (1978) Analysis and simulation of land subsidence with special reference to Bangkok. Dissertation no. d37, School of Civil Engineering, Asian Institute of Technology, Bangkok, Thailand.

J. Premchit and A. D. Gupta (1981) Simulation of a complex groundwater system and an application. *Water Resources Research*, 17(3), 673–685.

V. Ramnarong (1989) Subsurface injection of storm water runoff into an underground storage of Bangkok. In "Bangkok Land Subsidence-What's next?" Symposium. 22-23 June 1989, Bangkok, Thailand.

V. Ramnarong and S. Buapeng (1992) Groundwater resources of Bangkok and its vicinity: Impact and Management. In National Conference on Geological Resources of Thailand.- Potential for Future Development. DMR, Bangkok, Thailand, 172–184.

C. Reigber, X. Ye, H. Kaufmann, H. F. Massmann, L. Timmen, J. Bodechtel and M. Frei (1996) Impact of precise orbits on SAR interferometry. In Workshop on Applications of ERS SAR Interferometry 'Fringe96'. Remote Sensing Laboratories,

University of Zurich. URL `http://www.geo.unizh.ch/rsl/fringe96/papers/reigber-et-al/`, 30 September to 2 October 1996 ,Zurich, Switzerland.

F. S. Riley (1969) Analysis of borehole extensometer data from central California. International Association of Scientific Hydrology Publication 89. 423-431.

F. Rocca, J. Allievi, C. Prati, G. Savio, M. Arrigoni and L. Zanoletti (2004) Combined use of artificial and permanent scatterers. In ENVISAT and ERS Symposium. 6-10 September 2004, Salzburg, Austria. CDROM.

P. A. Rosen, S. Hensley, H. A. Zebker, F. H. Webb and E. Fielding (1996) Surface deformation and coherence measurements of Kilauea Volcano, Hawaii, from SIR-C radar interferometry. *Journal of Geophysical Research*, 101(E10), 23109–23125.

RTSD (2002) Subsidence surveys of Bangkok and its surrounding cities. Annual report, The Royal Thai Survey Department.

R. Scharoo, P. Visser and G. J. Mets (1998) Precise orbit determination and gravity field improvement for the ERS satellites. *Journal of Geophysical Research*, 103(C4), 8113–8127.

S. Sinsakul (2000) Late Quarternary geology of the Lower Central Plain, Thailand. *Journal of Asian Earth Sciences*, 18, 415–426.

E. K. Smith and S. Weintraub (1953) The constants in the equation for atmospheric refractive index at radio frequencies. In Proceeding of I.R.E., volume 41. 1035–1037.

T. Strozzi, U. Wegmueller, K. Graf, C. Werner and A. Wiesmann (2004) Analysis of the displacement along a Funicular with large baseline interferograms on point targets. In ENVISAT and ERS Symposium. 6-10 September 2004, Salzburg, Austria. CDROM.

S. Sungkhaburana (1983) Site investigation of land subsidence in the Samut Prakarn area due to deep well pumping. Master thesis gt-82-12, School of Civil Engineering, Asian Institute of Technology, Bangkok, Thailand. 108 p.

T. Suzuki (1991) Recent trend of land subsidence and government response in the cities of Asia. Master thesis gt-90-27, School of Civil Engineering, Asian Institute of Technology, Bangkok, Thailand. 131p.

K. Terzaghi (1925) Principle of soil mechanics, IV- Settlement and consolidation of clay. *Eng. News-Rec.*, 95(3).

P. G. J. Teunissen, P. J. de Jonge and C. C. J. M. Tiberius (1995) A new way to fix carrier-phase ambiguities. *GPS World*, 58–61.

K. Thammakumpee (1978) Instrumentation for the measurement of subsidence in Bangkok. Master thesis no. 1290, School of Civil Engineering, Asian Institute of Technology, Bangkok Thailand.

S. Thepparak (2001) Analysis of settlement and compression of shallow soil strata due to drawdown of groundwater in an underlying aquifer from well pumping in the Bangkok area. Master thesis no. ge-00-1, School of Civil Engineering, Asian Institute of Technology, Bangkok Thailand. 104 p.

F. T. Ulaby, R. K. Moore and A. K. Fung (1982) Microwave remote sensing: active and passive., volume 2 Radar remote sensing and surface scattering and emission theory. Addison-Wesley, Reading.

UNEP (2001) Bangkok: State of the environment. Technical report, United Nations Environment Programme, Regional Resource Centre for Asia and the Pacific (RRCAP).

S. Usai (2001) A new approach for long term monitoring of deformations by differential interferometry. Ph.d. thesis, Delft University of Technology, Delft Univ. Press, Delft, the Netherlands.

S. Usai and R. F.Hanssen (1997) Long time scale InSAR by means of high coherence features. In Third ERS Symposium- Space at the Service of our Environment. 225–228. Florence, Italy, 17-21 March, 1997.

S. Usai and R. Klee (1999) SAR interferometry on very long time scale: A study of the interferometric characterisitcs of man-made features. *IEEE Transactions on Geoscience and Remote Sensing*, 37(4), 2118–2123.

D. Walter, J. Hoffmann, B. M. Kampes and A. Sroka (2004) Radar interferometric analysis of mining induced surface subsidence using permanent scatterer. In ENVISAT and ERS Symposium. 6-10 September 2004, Salzburg, Austria. CDROM.

C. A. Wiley (1954) Pulse Doppler Radar Methods and Apparatus. United States Patent 3196436.

D. Woodrooffe (2000) Deltaic and estuarine environments and their late Quarternary dynamics on the Sunda and Sahul shelves. *Journal of Asian Earth Sciences*, 18, 393–413.

J. Worawattanamateekul (2002) Field observations in the Bangkok and surroundings. Field surveys.

J. Worawattanamateekul, J.Hoffmann, N. Adam and B. M. Kampes (2003) Urban monitoring in Bangkok metropolitan (Thailand) using permanent scatterers and differential interferomery technique. In International Workshop on ERS SAR Interferometry 'Fringe03'. 1-5 December, Frascati, Italy.

K. Worayingyong (1975) Preliminary prediction of subsidence in Bangkok Metropolitan area. Master's thesis, School of Civil Engineering, Asian Institute of Technology, Bangkok, Thailand.

H. A. Zebker and R. M. Goldstein (1986) Topographic mapping from interferometric Synthetic Aperture Radar observations. *Journal of Geophysical Research*, 91(B5), 4493–4999.

H. A. Zebker, P. A. Rosen, R. M. Goldstein, A. Gabriel and C. L. Werner (1994) On the derivation of coseismic displacement fields using differential radar interferometry: The Landers Earthquake. *Journal of Geophysical Research*, 99(B10), 19617–19634.

H. A. Zebker, P. A. Rosen and S. Hensley (1997) Atmospheric effects in interferometric synthetic aperture radar surface deformation and topographic maps. *Journal of Geophysical Research*, 102(B4), 7547–7563.

H. A. Zebker and J. Villasenor (1992) Decorrelation in interferometric radar echoes. *IEEE Transactions on Geoscience and Remote Sensing*, 30(5), 950–959.